Seismic Behavior Of Circular Reinforced Concrete Bridge Columns Under Combined Loading Including Torsion

by

Suriya Prakash Shanmugam

Disclaimer

The contents of this report reflect the views of the author(s), who are responsible for the facts and the accuracy of information presented herein. This document is disseminated under the sponsorship of the Department of Transportation, University Transportation Centers Program and the Center for Infrastructure Engineering Studies UTC program at the Missouri University of Science and Technology, in the interest of information exchange. The U.S. Government and Center for Infrastructure Engineering Studies assumes no liability for the contents or use thereof.

Technical Report Documentation Page

1. Report No. UTC R159	2. Government Accession No.	3. Recipient's Catalog No.
4. Title and Subtitle Seismic Behavior Of Circular Reinforced Concrete Bridge Columns Under Combined Loading Including Torsion		5. Report Date December 2009
		6. Performing Organization Code
7. Author/s Suriya Prakash Shanmugam		8. Performing Organization Report No. 00010496
9. Performing Organization Name and Address Center for Infrastructure Engineering Studies/UTC program Missouri University of Science and Technology 220 Engineering Research Lab Rolla, MO 65409		10. Work Unit No. (TRAIS)
		11. Contract or Grant No. DTRS98-G-0021
12. Sponsoring Organization Name and Address U.S. Department of Transportation Research and Innovative Technology Administration 1200 New Jersey Avenue, SE Washington, DC 20590		13. Type of Report and Period Covered Final
		14. Sponsoring Agency Code
15. Supplementary Notes		

16. Abstract

Reinforced concrete (RC) columns of skewed and curved bridges with unequal spans and column heights can be subjected to combined loading including axial, flexure, shear, and torsion loads during earthquakes. The combination of axial loads, shear force, and flexural and torsional moments can result in complex failure modes of RC bridge columns. This study carried out experimental and analytical studies to investigate the seismic performance of circular RC columns under combined loading including torsion. The main variables considered here were (i) the ratio of torsion-to-bending moment (T/M), (ii) the ratio of bending moment-to-shear (M/V) or shear span (H/D), and (iii) the level of detailing for high and moderate seismicity (high or low spiral ratio). In particular, the effects of the spiral reinforcement ratio and shear span on strength and ductility of circular RC columns under combined loading were addressed. In addition, the effects of torsional loading on the bending moment-curvature, ductility, and energy dissipation characteristics were also considered. The analytical investigation examined the development of existing models for flexure and pure torsion. Interaction diagrams between bending, shear and torsional loads were established from a semi-empirical approach. A damage-based design approach for circular RC columns under combined loads was proposed by decoupling damage index models for flexure and torsion. Experimental and analytical results showed that the progression of damage was amplified by an increase in torsional moment. An increase in the transverse spiral reinforcement ratio delayed the progression of damage and changed the torsional-dominated behavior to flexural-dominated behavior under combined flexural and torsional moments.

17. Key Words Design, Economic Development, Education, Finance, Future Transportation Professionals, Management, Materials, Operations, Safety, Security, Policy	18. Distribution Statement No restrictions. This document is available to the public through the National Technical Information Service, Springfield, Virginia 22161.		
19. Security Classification (of this report) unclassified	20. Security Classification (of this page) unclassified	21. No. Of Pages 335	22. Price

Form DOT F 1700.7 (8-72)

SEISMIC BEHAVIOR OF CIRCULAR REINFORCED CONCRETE

BRIDGE COLUMNS UNDER COMBINED LOADING INCLUDING TORSION

by

SURIYA PRAKASH SHANMUGAM

A DISSERTATION

Presented to the Graduate Faculty of the

MISSOURI UNIVERSITY OF SCIENCE AND TECHNOLOGY

In Partial Fulfillment of the Requirements for the Degree

DOCTOR OF PHILOSOPHY

in

CIVIL ENGINEERING

2009

Approved by:

Abdeldjelil Belarbi, Advisor

Roger A. LaBoube

John J. Myers

Oh-Sung Kwon

K. Chandrashekhara

ABSTRACT

Reinforced concrete (RC) columns of skewed and curved bridges with unequal spans and column heights can be subjected to combined loading including axial, flexure, shear, and torsion loads during earthquakes. The combination of axial loads, shear force, and flexural and torsional moments can result in complex failure modes of RC bridge columns. This study carried out experimental and analytical studies to investigate the seismic performance of circular RC columns under combined loading including torsion. The main variables considered here were (i) the ratio of torsion-to-bending moment (T/M), (ii) the ratio of bending moment-to-shear (M/V) or shear span (H/D), and (iii) the level of detailing for high and moderate seismicity (high or low spiral ratio). In particular, the effects of the spiral reinforcement ratio and shear span on strength and ductility of circular RC columns under combined loading were addressed. In addition, the effects of torsional loading on the bending moment-curvature, ductility, and energy dissipation characteristics were also considered. The analytical investigation examined the development of existing models for flexure and pure torsion. Interaction diagrams between bending, shear and torsional loads were established from a semi-empirical approach. A damage-based design approach for circular RC columns under combined loads was proposed by decoupling damage index models for flexure and torsion. Experimental and analytical results showed that the progression of damage was amplified by an increase in torsional moment. An increase in the transverse spiral reinforcement ratio delayed the progression of damage and changed the torsional-dominated behavior to flexural-dominated behavior under combined flexural and torsional moments.

ACKNOWLEDGMENTS

TABLE OF CONTENTS

LIST OF ILLUSTRATIONS

LIST OF TABLES

Page

1. INTRODUCTION

1.1. BACKGROUND

The elements of structural system can be subjected to combined actions including bending, shear, and torsion irrespective of their material composition (steel, concrete, or wood),. This loading results in a complex internal force flow due to geometrical conditions or complex load combinations. However, no matter how complex, no loading involves more than four basic load types: axial loads, shear forces, bending; and torsional moments. In case of members made of perfect isotropic materials such as steel, analysis of behavior in the elastic region under combined actions is cumbersome. The inelastic behavior of quasi-brittle materials such as concrete can make such analyses even more complex. In a reinforced concrete, the relative contribution of steel reinforcement and concrete and their interaction under combined loads make the analysis even more difficult. In spite of their complexity, the behavior of reinforced concrete sections needs to be understood to make rational provisions in design and analysis.

Combined loadings including torsion with axial load, shear force, and bending moment can occur in reinforced concrete (RC) elements such as arch ribs, L-shaped bridge piers, spiral stair cases, and bridges with outrigger bents. In particular, torsional moments occur in RC structure elements (i) due to eccentric loads caused by traffic conditions in bridge box girders, (ii) when a spandrel beam meets at a corner without a column, and (iii) in curved beams, staircases, and girders with horizontal projections (Figure 1.1). In spite of the significant effect of combined actions including torsion, most studies performed during the early twentieth century focused mainly on axial force, flexure, pure shear, or pure torsion without considering their interactions.
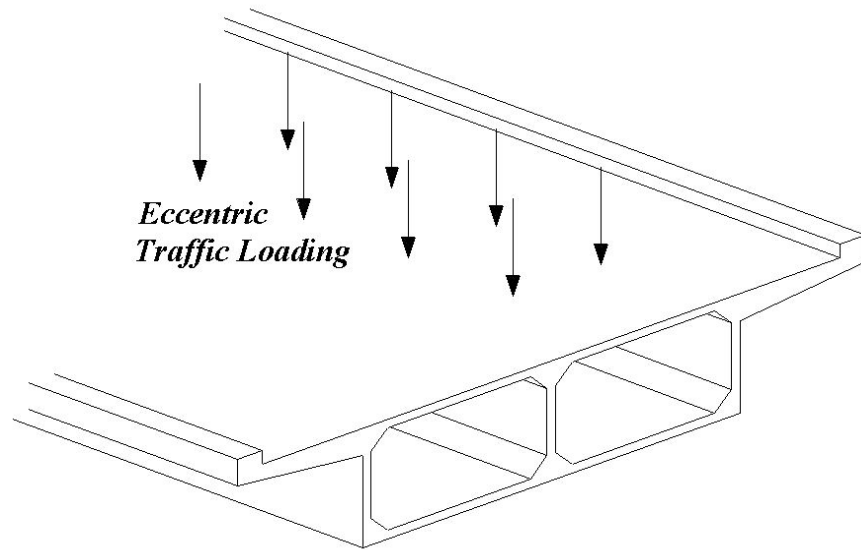
(a) Equilibrium Torsion in Box Girders
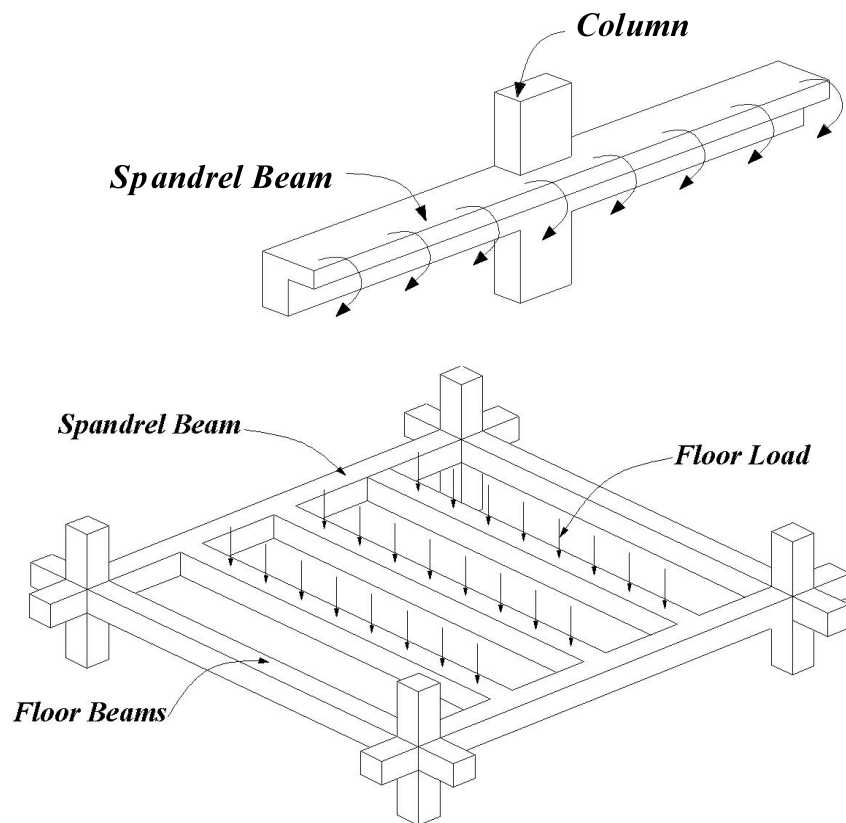
(b) Compatibility Torsion in Spandrel Beams

Figure 1.1 Examples of Torsion in Reinforced Concrete

The compression behavior of plain concrete is well understood [Whitney 1937; Hognestad 1951; Mattock 1961 and Rusch, 1961], as is that of RC [Kent 1969; Park and Paulay 1975, Ahmad and Shah 1982, Mander and Cheng, 1984 and Mander et al., 1988]. Research on shear and torsional behavior of RC began in the nineteenth century. The first theoretical models for shear behavior in cracked RC members date back to the turn of the century when Ritter (1899) and Mörsch (1902) formulated the 2-D plane truss concept. By extending this model, Rausch (1929) developed three-dimensional space truss model for torsion; this model assumed longitudinal and hoop steel reinforcement to resist tension and concrete struts to resist compression. It also assumed that the shear flow path would follow the centerline of the hoop steel reinforcement.

Researchers, in the second half of the twentieth century, investigated the behavior of RC beams under combined bending and torsion [Lampert and Thürlimann 1969; McMullen and Warwaruk 1970; Onsongo 1978] and under combined torsion and shear [Klus 1968; Rahal 1993]. Recently, a few studies have also investigated the behavior of combined bending, shear, and torsion [Hsu and Wang 2000; Hsu and Liang 2003; Otsuka et al., 2004; Tirasit and Kawashima, 2007, Greene and Belarbi, 2009a]. However, all these studies were limited to rectangular or square sections. In addition, the cyclic behavior under combined loading is not yet clearly understood. To date, no studies have reported on the behavior of circular sections under combined bending, shear; and torsional static and cyclic loads. The combination of torsion and compression is the least studied in spite of its occurrence in bridge columns during earthquakes [Peir 1973; and Pandit and Mawal 1973]. Studies on the behavior of RC subject to combined loading including torsion have been limited because (a) torsion is usually considered a secondary

effect in concrete structures, (b) the members can be usually arranged in a structure so that they are subject to only very small torsional moments, and (c) torsion tests require special equipment and instrumentation.

At this time, the behavior and ultimate strength of RC members subject to various combinations of shear force, axial compression, and bending moment are well understood based on several experimental studies [Mander and Cheng, 1984 and Mander et al., 1988; Stone and Cheok 1989; Wong et al. 1990&1993; Priestley et al. 1996; Kawashima et al. 1994, Kawano and Watanabe 1997]. Accordingly, recent analytical models have focused primarily on inelastic flexural hysteresis behavior without considering the effects of shear and torsion [Kent 1969; Park and Ang 1985; Priestly and Benzoni 1996; Priestly et al., 1996 and Lehman et al., 1998]. A few studies have considered flexure and shear interaction; however, this interaction is not yet fully understood [Ang et al., 1989; Wong et al., 1990; Ozcebe and Saaticoglu 1989; Galal and Ghobarah 2003; and Zhang and Xu, 2008]. Torsional loadings with flexure and shear can significantly affect the flow of internal forces of RC members, as well as their deformation capacity. The presence of torsion with shear and flexure increases the possibility of shear-dominated failure. At present, the knowledge of the interaction between flexural and torsional moment with various levels of shear and compression in RC elements is very limited [Tirasit et al., 2008 and Greene and Belarbi, 2009a &2009b]. No analytical models include the effect of interaction among flexure, shear, and torsion and in their assessment of seismic performance of RC members with axial loads. Due to the paucity of experimental results on the cyclic and dynamic behavior of RC columns under combined loadings, a reliable hysteresis model has not yet been developed. Knowledge on the effects of torsion with

various levels of compression, shear, and bending moment is necessary to make rational

design provisions for RC columns under combined loading.

1.2. COMBINED LOADING IN RC BRIDGE COLUMNS

The addition of torsional moment is more likely in skewed and horizontally

curved bridges, bridges with unequal spans or column heights, and bridges with outrigger

bents. Construction of bridges with these configurations is often unavoidable due to site

constraints imposed by rivers, railroad tracks, and other obstacles that do not necessarily

cross a bridge perpendicular to its alignment. Accordingly, bridge members are often

built in a skew or in a curved fashion to accommodate such obstacles. In addition,

multidirectional earthquake motions including significant vertical motions, structural

constraints due to a stiff deck, movement of joints, abutment restraint, and soil conditions

may also lead to combined loading effects. Because, the responses of curved bridges

under longitudinal and transverse motions are coupled, the columns can be subject to

multidirectional deformation with torsion. This combination of seismic loading can have

significant effects on the force and deformation capacity of RC columns and influences

the performance of the bridge system as a whole. Torsion may also occur due to the

eccentricity of inertial force transferred from superstructures in bridges with outrigger

bents.

In skewed bridges, a collision between the bridge deck and the abutment may

cause in-plane rotation of superstructures; consequently inducing torsion in the bridge

columns (Tirasit and Kawashima, 2005), as illustrated in Figure 1.2. A 2008 analytical

study by Tirasit and Kawashima carried out to investigate the seismic torsion response of

skewed bridge piers showed the possibility of significant torsional loading. Using the finite element method, this work conducted a time history analysis of a four-span continuous skewed bridge considering several parameters such as skewness, pounding, cable restrainer system, and locking of steel bearing movement after damage. The results show that pounding occurs between a skewed bridge deck and abutments; resulting in in-plane deck rotation and increase of the seismic torsion in skewed bridge piers. The results also show clearly that torsional moments in the columns closest to abutments in a skewed bridge are higher than those in a straight bridge. Other columns are subject to significantly lower torsion-to-bending moment (T/M) ratios of almost 0.08 at maximum response. The work of Tirasit and Kawashima also demonstrated the possibility of significant deck rotation due to the seismic torsional response of skewed bridge piers. Moreover, it showed that locking of bearing movement after failure could significantly amplify seismic torsion in skewed bridge piers.
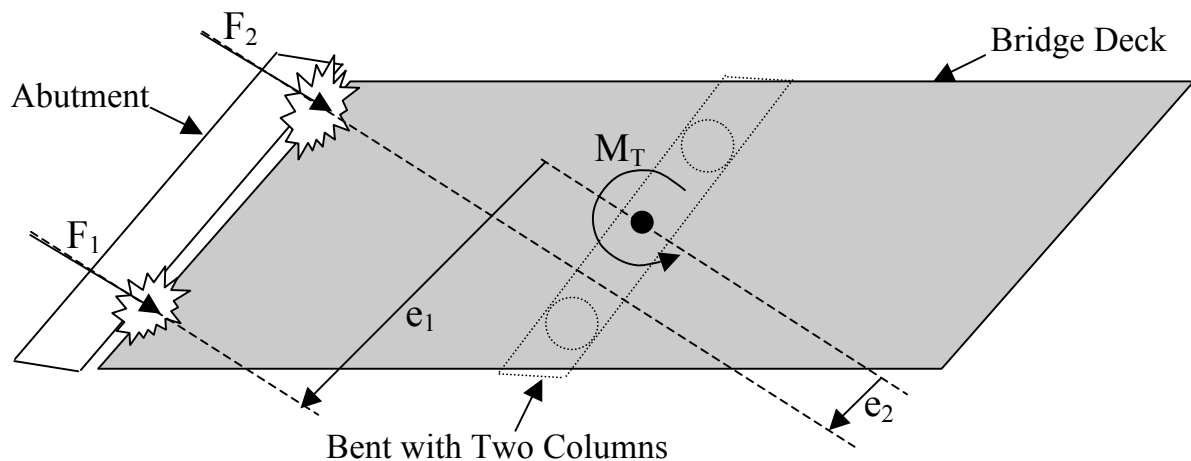
Figure 1.2 Torsional Moment in Columns due to Deck Rotation
(Plan View of a Skewed Bridge)

Due to the deformation of the deck under the shear force, columns will be subjected to compatibility torsion inducing torsional moment. Figure 1.3 shows a segment of bridge superstructure between movement joints contains one short column and one long column. As a result, the center of rigidity is displacement from the centre of mass towards the shorter columns. The bridge columns are subjected to torsional moments due to eccentricity between center of mass and stiffness during an transverse earthquake motion as shown in Figure 1.3.
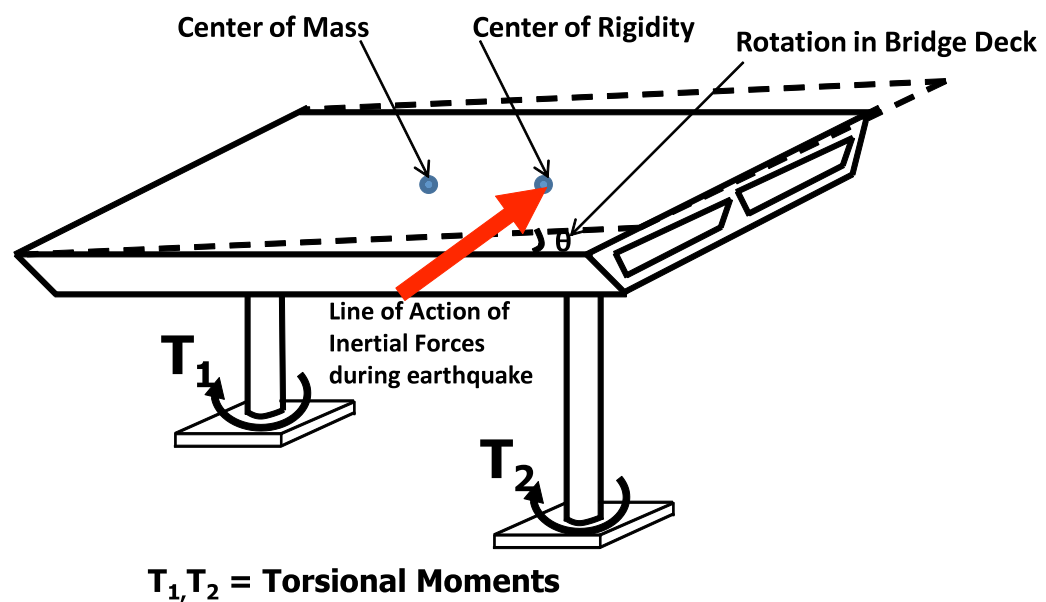
Figure 1.3 Torsional Moment in Bridge Columns During an Earthquake

Belarbi et al. (2008) investigated the presence of torsion in bridge columns by analyzing a bridge structure model (Figure 1.4). Figure 1.5 presents the results of their seismic analyses for various earthquake motions. As this figure indicates, a supporting bent of a bridge under complex deformation, is subjected to a combination of axial loads, bending moments, shearing forces, and potentially to torsional rotations as well. Torsion

is more evident, however, in columns farther from abutments that are under deformation restraints from the abutment keys (e.g., pier line 3 in Figure 1.4). Torsion effects due to rotation of the superstructure can be significant when shear keys restrain the bridge superstructure at the abutments, or when there is a significant decrease in torsion stiffness relative to the bending stiffness of the column.

In general, the force produced in bridge columns due to dead and live loads is primarily axial. During an earthquake, the inertial forces cause longitudinal loads in the direction of the bridge, transverse loads in a horizontal plane, and orthogonal loads to the bridge centerline causing shear and torsional loads in bridge columns. The results of seismic analyses clearly show that the bridge columns in the bents closest to the bridge abutments are subject to a T/M of between 0.52 and 0.33, significantly higher than that for the bents closest to the center of the bridge. The other columns are subject to significantly lower T/M ratios of almost 0.08 at maximum response.

(a) Longitudinal Section

(b) Analytical Model

Legend:
——○—— Undeformed Shape
– –○– – Deflected Shape of Unrestrained Structure at the Abutment
——○—— Deflected Shape of Restrained Structure at the Abutments
★ Center of Rotation of Restrained Structure at the Abutments
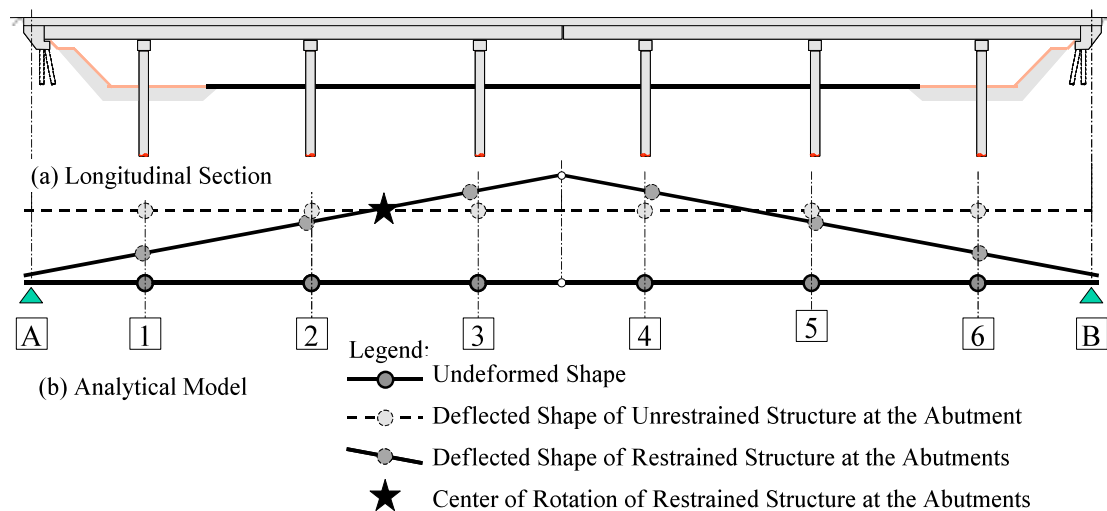
Figure 1.4 Bridge Transverse Seismic Response
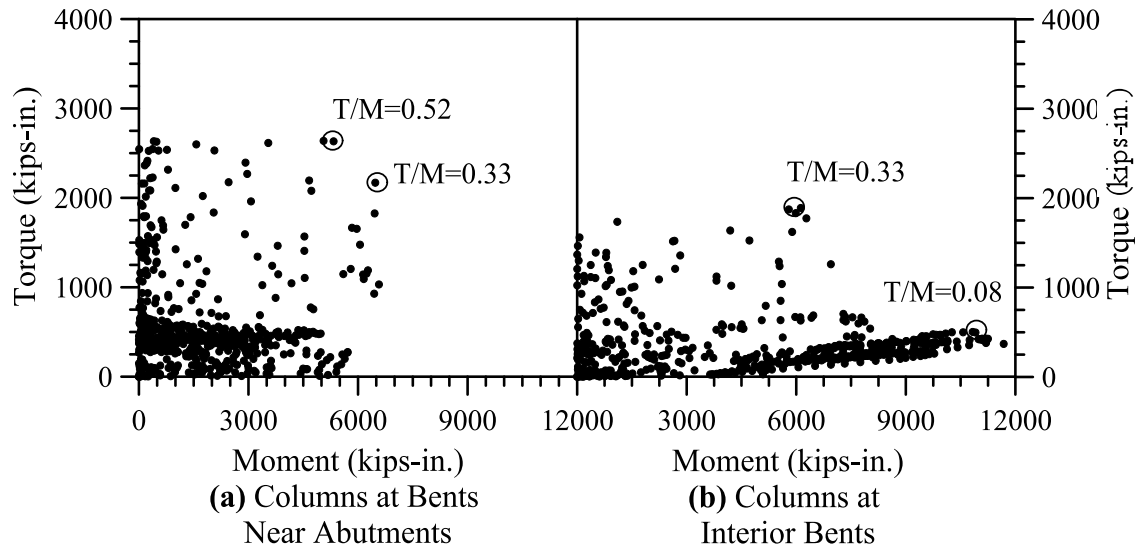
Figure 1.5 Interaction between Bending and Torsion
(1 kip-in. = 0.11299 kN-m).

During the design of bridge systems, columns are typically selected to provide effective dissipation of seismic energy. To improve the ductility and energy dissipation capacity of the columns, therefore, suitable and properly detailed plastic-hinges are provided at the end region of the column where the moments are at a maximum under lateral response. In addition, the presence of torsion loadings can change the formation of plastic-hinge zones. The detailing of RC columns under combined loadings including torsion has not been studied in depth. Most codes include confinement requirements based on the assumption that the compressive strength of the confined core of a column after spalling should be equal to the strength of the gross section of the column before spalling. However, the presence of torsion amplifies the occurrence of spalling and also softens the core concrete, resulting in a reduction of the confinement effect in the core concrete. Accordingly, the detailing requirements for transverse reinforcement must be examined more carefully under combined loading. Moreover, local ductility contributing

to the overall displacement ductility is ensured for columns primarily by modifying and arranging the lateral transverse reinforcement. Thus, the existing plastic-hinge model assumes that the length of the plastic zone in a member is proportional to the level of detailing of the transverse reinforcement and the member's shear span. In other words, a member with a shorter shear span has a smaller plastic-hinge zone; hence detailing should be modified based on consideration of factors mentioned above.

1.3. OBJECTIVES AND SCOPE

Most research on the behavior of RC under combined loading has relied on small-scale beams. A review of previously published studies indicates that very few investigations have examined the behavior of RC columns under combined loading. Moreover, information is scarce on the effect of increasing the transverse reinforcement ratio or on the effect of aspect ratio on the behavior of RC columns under combined loading. Thus, the research presented here on RC circular columns under combined bending, shear, and torsion loadings with various aspect ratios and spiral reinforcement ratios can provide valuable information that was unavailable previously. The results of this study will also support the development of analytical models and design detailing guidelines. In addition, they will provide the basis for further development of interaction surfaces and design guidelines for circular RC columns subjected to combined loading including torsion.

The objective of this research program is to characterize and quantify the seismic performance of circular RC bridge columns under combined loading including torsion. The primary objectives of this research can be summarized as follows:

(i) To investigate the effect of full-reversal cyclic pure torsion, cyclic bending and shear, and torsion combined with shear and bending loads on the behavior of circular RC bridge columns.

(ii) To investigate the effect of spiral reinforcement ratio on the failure modes and ductility characteristics of circular RC columns under combined loading including torsion.

(iii) To understand the effect of shear span or moment-to-shear ratio on the failure mode and energy dissipation characteristics

(iv) To improve tools for the analysis of RC members under combined loadings at service and ultimate-load levels. This includes modifying the existing mechanical and damage models for combined loading.

(v) To establish interaction diagrams and propose equations for various failure modes of circular RC columns with various aspect and spiral ratios.

1.4. RESEARCH PLAN AND METHODOLOGY

The experimental portion investigated the response of circular RC columns under full-reversal cyclic torsional, bending; shear, and combined loadings with constant axial load. The specific objective was to determine the effect of cyclic loads on the stiffness degradation stiffnesses under pure flexure and torsion as well as combined loading. The experimental work focused on (i) the interaction between torsional and bending moment and the damage progression of the specimen resulted from the diagonal cracking in two orthogonal directions, (ii) the characteristics of the shear-flow zone and the impact of the

concrete softening, and (iii) the occurrence and severity of concrete cover spalling and estimation of plastic-hinge lengths.

The analytical portion of this investigation consists of (i) development of mechanical models such as the existing plastic-hinge-based model for flexure, (ii) improvement of softened truss model for pure torsion, and (iii) establishment of interaction surfaces using semi-empirical methods. The mechanical models developed here can predict the load-deformation behavior of RC columns subject to flexural loads and torsional moment-twist curves under pure torsion. The semi-empirical model can be used to establish interaction curves to predict the failure of RC members under combined loading. This work also contributes to the development of damage index models that can be used to predict the damage behavior under combined loadings from a performance-based design point of view.

In summary, the specific scope of the work includes:

(i)   To investigate the effect of torsion by varying the torsion-to-bending moment (T/M) ratio on strength and stiffness degradation, failure modes; and deformation characteristics.

(ii) To establish interaction diagrams of RC circular columns between torsion, bending, and shear through an experimental study based on two aspect ratios (H/D=6 and H/D=3) and two spiral ratios (0.73% and 1.32%).

(iii) To develop the decoupled damage index models for flexure and torsion and study the interaction between torsional and flexural damage indices for various levels of T/M ratios based on aspect ratios of 6 and 3 and spiral ratios of 0.73% and 1.32%.

(iv) To establish the limits of various damage states based on the level of cross sectional details such as longitudinal and transverse reinforcement ratios and loading conditions.

1.5. ORGANIZATION OF THE DISSERTATION

Section 2 presents background information and a review of literature related to this research. It also describes existing models and code provisions for combined loadings. Section 3 presents the details of the experimental program, including design, construction, and testing procedures. Section 4 discusses the results of experiments and assesses the performance of test specimens with respect to hysteresis behavior, displacement and twist components, strain plots, and interaction diagrams. Section 5 suggests modifications of existing models for flexure and pure torsion and includes the diagrams of interaction between flexural, shear, and torsional loads. Section 6 offers damage index models and validate experimental results for various test parameters. Finally, Section 7 summarizes the conclusions of this study and recommends some directions for future research.

2. REVIEW OF STUDIES ON BEHAVIOR OF REINFORCED CONCRETE UNDER COMBINED LOADING INCLUDING TORSION

2.1. INTRODUCTION

The existence of torsion significantly alters the behavior of concrete members. Although, a number of studies have addressed flexure, pure shear, and pure torsion, independently, investigations on such loads in combinations are scarce. Among them, the combination of torsion and axial loads is the least studied until now in spite of its frequent occurrence in bridge columns during earthquakes (See Section 1 above for a discussion of torsion in bridge columns). The development of rational design provisions requires a clear understanding of the effect of torsion when combined with bending, shear, and axial loads on the behavior of bridge columns. The following discussion addresses, the state of research on the behavior of RC members under various combinations of bending moment, shear force, and torsional loads. In particular, it reviews the literature on the behavior of RC columns under combined loading in detail.

2.2. BEHAVIOR UNDER FLEXURE AND AXIAL LOADS

In general, parameters such as member sectional details, material properties, and loading conditions characterize the behavior of RC columns under flexure, as shown in Figure 2.1.

Geometry and Sectional Details	⇄	Material Properties	⇄	Loading Details
Length of Column, Aspect Ratio, Cover, Transverse Reinforcement ratio, Longitudinal Ratio, Diameter of Longitudinal Bar		Stress Strain Relationship of Unconfined Concrete, Transverse and Longitudinal Steel, Spacing and Configuration of Transverse Reinforcement Ratio (Confinement)		Amount of Compression, Loading History, Type of Loading (Psuedocyclic, Psuedodynamic), Earthquake Simulator Tests

Figure 2.0 Factors Affecting the Behavior of RC Columns under Combined Flexure and Axial Compression

2.2.1. Experimental Studies. Several experimental studies have examined the response of concrete elements under flexure and axial compression. A number of tests have been carried out to determine the cyclic behavior of RC columns under flexure, with or without axial compression. The earliest tests on bridge columns under seismic loading were carried out in New Zealand and Japan. Several studies have provided valuable information on the behavior of RC columns under cyclic uniaxial flexural loads (Kent, 1969; Ang et al., 1989; Mander et al., 1988; Stone and Cheok, 1989; Wong et al., 1990 and 1993; Priestley et al., 1996; Kawano and Watanabe, 1997; Kawashima et al., 1994; Kowalsky and Priestley 2000, and Kunnath, 1997). The following review of these studies classifies the behavior of RC columns according to the effect of aspect ratio, confinement, axial load, and other parameters.

2.2.1.1 Effect of aspect ratio. The behavior of RC columns can be classified as flexure-dominated or shear-dominated or as having significant flexure-shear interaction. The aspect ratio of a column determines the level of flexure-shear interaction. A number

of researchers have studied the effect of aspect ratio, namely Iwasaki et al., (1985), Davey and Park (1975), Stone (1989), McDaniel (1997), and Vu (1999). Most significantly, these studies have found that (i) displacement ductility capacity decreases with a decrease in moment-to-shear ratio and (ii) shear demand increases with a reduction in the moment-to-shear ratio. The failure modes of flexure-dominated columns are similar to those of conventional beams under flexure. However, the failure mode under the interaction of flexure and shear is intricate owing to complex shear transfer mechanism at crack interfaces. This results in variation of local stresses in concrete and steel from section to section along the length of the shear span and the depth of the cross section. A number of failures have been reported due to inadequate shear strength and a lack of ductile response under shear. The load transfer mechanisms and failure modes of shear-dominated columns are shown in Figure 2.1. A few studies address this area of flexure and shear interaction; however, a full understanding is yet lacking (Ang et al., 1989; Wong et al., 1990 and 1993; and Kowalsky and Priestley, 2000).
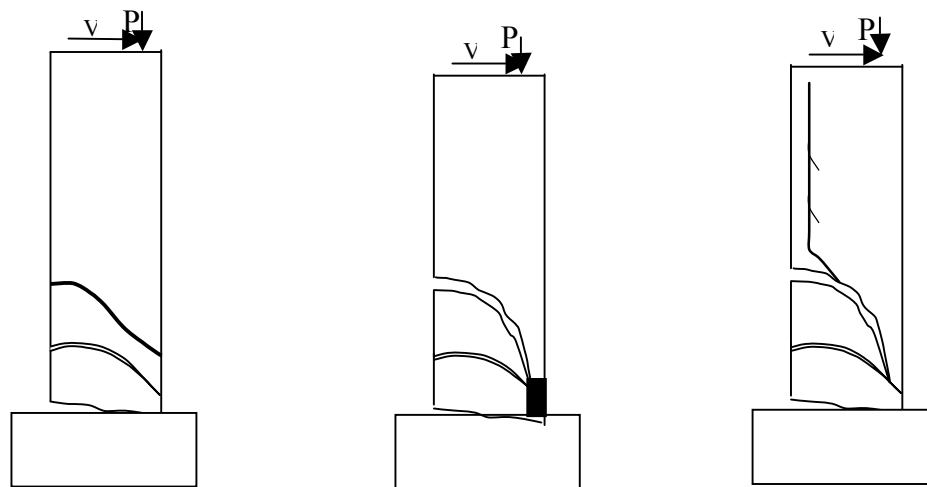
(a) Shear Tension Failure   (b) Shear Compression Failure   (c) Shear Bond Failure

Figure 2.1 Failure Modes of Shear-Dominated Column

2.2.1.2 Effect of confinement. Several researchers have studied the effect of confinement by testing columns under monotonic and cyclic axial loads (Mander et al., 1988; Sheikh and Uzumeri, 1982; Calderone et al., 2001). The role of confinement reinforcement is well documented in Razvi and Saatcioglu (1994). The effect of confinement also depends on the amount and configuration of transverse reinforcement and the level of axial load ratios. Wong et al. (1990) tested columns with a smaller aspect ratio and found that those with a smaller transverse reinforcement have a smaller curvature demand. Similarly, several researchers have examined the effect of spiral reinforcement ratio on circular columns (Potangaroa, 1979; Ang, 1981; Zhan, 1986; Stone, 1989). The increase in transverse reinforcement confines the concrete core more effectively and improved shear resistance. However, the effect of transverse reinforcement on shear dominated behavior is not very well understood.

2.2.1.3 Effect of axial load. Previous research has shown that an increase in axial compression reduces displacement capacity (Atalay, 1975; Saatcioglu, 1989; and Sheikh, 1993). The increase in axial compression increases the shear strength by enhancing the aggregate interlock and increasing shear transfer across the compression zone. Also, when the axial loads are in tension there is a decrease in shear strength, which most of codes take into account. However, with increasing displacement ductility demands, shear strength decays significantly within the plastic end regions of columns and this effect has not yet been studied in depth. Axial loads may vary during an earthquake due to vertical ground motions. The literature has reported failures due to significant vertical motions (Hachem et al., 2003); therefore, the effect of axial-flexure-shear interaction in the presence of very high vertical motions must be evaluated.

However, tests on RC columns under dynamic loadings with various vertical ground motions have been limited.

2.2.1.4 Other parameters. Other important parameters that influence the behavior of RC members (in particular columns) are concrete cover thickness, longitudinal reinforcement ratio, bar diameter, and loading patterns. No experiments have addressed the hysteresis characteristics of RC columns with a combination of load patterns. Nonlinear time history analyses are, therefore, difficult. Also, dynamic and pseudodynamic test data are not currently available to clarify the dynamic behavior of RC columns.

2.2.2. Analytical Studies. Several analytical models have been developed for predicting the behavior of reinforced concrete member under flexure and axial load. They are classified into mechanical models and plastic-hinge based models and discussed in the following sections.

2.2.2.1 Mechanical models. As noted in the Section 2.2.1 above, extensive investigation has revealed the strength and deformation capacities of RC members under flexure and axial load. Bernoulli's model assuming that plane sections remain plane accurately predicts the behavior of RC sections under flexure. This model satisfies all three principles of the mechanics of materials, namely equilibrium of forces, planar strain compatibility; and the uniaxial constitutive laws of concrete. For flexural behavior, traditional section analysis considering axial-flexural interaction gives acceptable predictions of ultimate strength and yielding displacement (Mostafaei and Kabeyasawa, 2007). However, the determination of shear strength and deformation characteristics of shear-dominated columns remains controversial. Past mechanical models for RC columns

have focused primarily on inelastic flexural behavior; usually decoupled from axial, shear, and torsion behavior. Various models have been proposed to predict the shear strength prediction under monotonic loading (ASCE–ACI, 1973; Ang et al., 1989; Watanabe and Ichinose, 1991; Priestley et al., 1994) and shear force-shear deformation response (Collins, 1978; Vecchio and Collins, 1986; Hsu, 1993; Pang and Hsu, 1992). Models for cyclic shear or flexure and shear are still in development. Recently, however, Ozcebe and Saatcioglu (1989) have reported that shear displacement can be significant even in RC members not governed by shear failure. They also indicated that RC members with much higher shear capacity than flexural capacity do not guarantee elastic behavior in shear deformation. Their observations suggest that RC members governed by flexural behavior may still have significant shear displacement and hence should not be ignored in inelastic stage. The presence of torsion along with shear force increases the shear deformation and should be considered in predictions. Thus, an accurate mechanical model for RC members must consider a combination of the axial and lateral behaviors.

A number of experimental studies at the University of Toronto and the University of Houston have generated rational models such as compression field theory (CFT) and the softened truss model (STM), respectively, to predict the behavior of RC square/rectangular sections under combined loading. Among these, the CFT developed by Collins (1978) and the STM developed by Hsu (1988) are particularly significant. Hsu's model predicted the shear and torsional strength as well as the force-deformation response of RC members (Hsu and Mo 1985a &1985b; Hsu et al. 1987); however, it could not predict the concrete contribution to shear behavior. This contribution was clarified by Pang and Hsu (1996) who developed an improved STM employing fixed-

angle model. This model demands considerable effort to solve the complex equations needed to derive the concrete contribution. Similarly, at the University of Toronto, Vecchio and Collins (1986) proposed the modified compression field theory (MCFT), which is capable of predicting not only the shear strength of both reinforced and prestressed concrete members, but also the force-deformation response of those members. The theory proved the accuracy of the predictions when compared to test results (Vecchio and Collins 1986; Bhide and Collins 1989; Vecchio and Emara 1992). Detailed descriptions of MCFT and STM are presented in the later Sections (2.4.2.2, 2.4.2.3) below which describe analytical models for combined loading including torsion.

2.2.2.2 Plastic-hinge models for lateral load-displacement behavior. Seismic evaluation of RC members under flexural loads requires a detailed representation of the complete hysteretic load-displacement relationship. Available models for hysteresis analysis include fiber, lumped-plasticity, and multilinear force-displacement. Simplified model to approximate the displacement capacity of RC member includes the plastic-hinge method. Moment-curvature analyses commonly form the basis for assessing the nonlinear force displacement response of a particular RC cross section. Plastic-hinge analyses require assumptions about the plastic zone in a structural member to calculate plastic rotations and displacements based on plastic curvatures. They can be enhanced by accounting for shear displacements and end rotations resulting from strain penetration into the footing or bentcap. The equivalent plastic-hinge analysis (Park and Paulay, 1975; Priestely et al., 1996) is a popular method for assessing plastic rotation which strongly influences ductile seismic design This method assumes a given plastic curvature lumped in the center of an equivalent plastic-hinge. The plastic-hinge length is the length over

which this plastic curvature is integrated to solve the total plastic rotation by assuming to be constant (Figure 2.2).
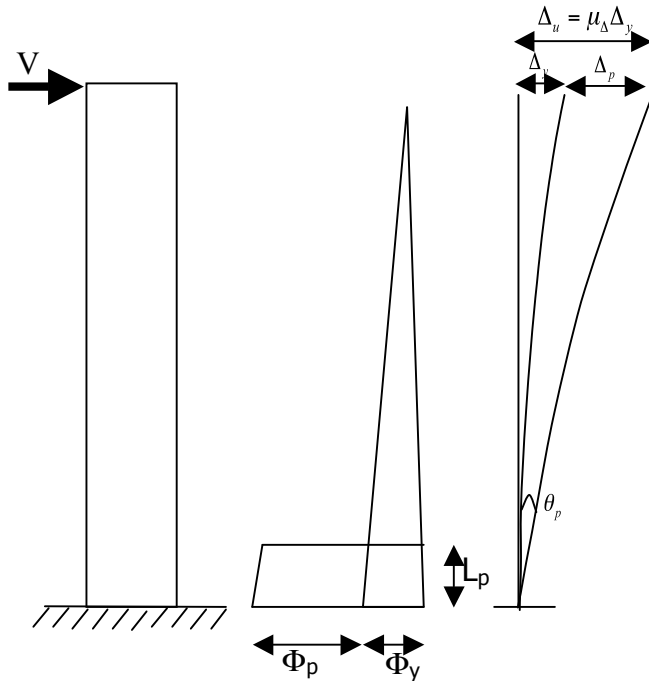
(a) Loading and Curvature Distribution
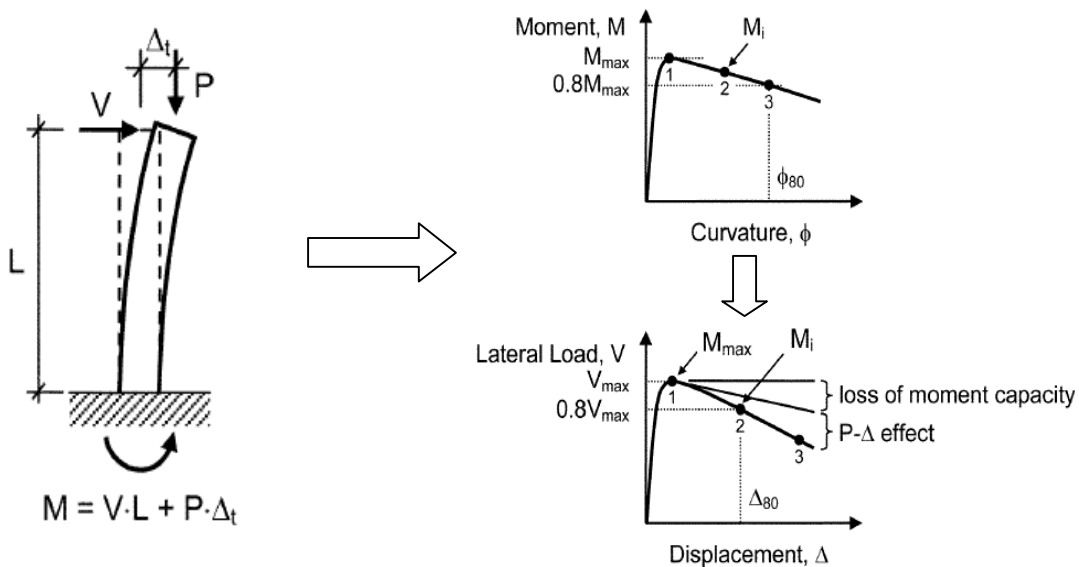
(b) Moment Curvature and Load-Displacement

Figure 2.2 Lateral Load-Displacement Curve using Plastic-Hinge Method

Under flexure, the displacement ductility can be derived using the moment curvature relationship and the assumed length (Priestley et al., 1996). Using a plastic-hinge concept and the second moment area theorem, Park and Paulay proposed an expression for the tip displacement of a column, which is expressed in Eq. 2.1. From this equation, they further derived a relationship between curvature ductility and displacement ductility, as shown in Eq. 2.2. The latter equation indicates a linear relationship between the curvature and displacement ductilities of the columns. The plastic-hinge length l_p and the column height L are two important factors influencing this relationship. The flexural displacement distribution is essentially linear until the yielding of the longitudinal bars on the tension side; thereafter, it becomes nonlinear. The yielding of longitudinal reinforcement and the subsequent crushing of cover concrete result in the formation of a flexural plastic-hinge. Well confined columns tested under flexure (single curvature) typically form a plastic-hinge in the bottom portion where the bending moment is greatest, as shown in Figure 2.2. The total flexural displacement of the column under flexure can be expressed as the sum of yield displacement and plastic displacement:

$$\Delta_t = \Delta_y + \Delta_p = (\phi_u - \phi_y)l_p(L - 0.5l_p) \qquad\qquad \text{Eq. 2.1}$$

where Δ_t is the total displacement, Δ_y is the yielding displacement, Δ_p is the plastic displacement, l_p is the length of the plastic-hinge, L is the length of the column, Φ_u is the curvature at ultimate moment, and Φ_y is the curvature at yield moment.

As demonstrated by Priestely et al. (1996), the displacement ductility can be expressed in terms of curvature ductility:

$$\mu_{\Delta} = 1 + 3(\mu_{\phi} - 1)\frac{l_p}{L}(1 - 0.5\frac{l_p}{L})$$

Eq. 2.2

where μ_{Δ} is the displacement ductility and μ_{Φ} is the curvature ductility. Further, the estimation of flexural displacement using the above equations depends on the accuracy of the plastic-hinge length calculations.

2.2.2.2.1 Empirical equations for plastic-hinge length. Baker (1956) proposed the following equations for plastic-hinge length based on experiments:

$$l_p = k_1 k_2 k_3 (\frac{z}{d})^{\frac{1}{4}} d$$

Eq. 2.3

where k_1 is equal to 0.7 for mild steel or 0.9 for cold-worked steel, and

$$k_2 = 1 + 0.5\frac{P_u}{P_0}$$

Eq. 2.4

where P_u represents the axial compressive force in a member, P_0 represents the axial compressive strength of the member without bending moment, k_3 is equal to 0.6 when f'c is 5100 psi (35.2 N/mm2) or 0.9 when $f'c$ is 1700 psi (11.7 N/mm2) (assuming $f'c$ is equal to 0.85 cube strength of concrete), z is the distance from the critical section to the point of contra flexure, and d is the effective depth of member.

Baker indicated that l_p lies in a range between *0.4d* and *2.4d* for practical range of span/d and *z/d* ratios. Later, Baker (1964) proposed an expression of l_p for members confined with transverse steel as follows:

$$l_p = 0.8k_1k_3(\frac{z}{d})c \qquad\qquad \text{Eq. 2.5}$$

where c is the neutral axis depth at the ultimate moment, and the other terms are define as for Eq. 2.5. Eq. 2.5 are valid only when concrete strain, the steel ratio is restricted.

From the results of tests on simply supported beams, Corley (1966) proposed the following expression for the equivalent length of the plastic-hinge:

$$l_p = 0.5d + 0.2\sqrt{d}\,(\frac{z}{d}) \qquad\qquad \text{Eq. 2.6}$$

He also suggested the following conservative estimate for maximum concrete strain:

$$\varepsilon_c = 0.003 + 0.02\frac{b}{z} + \left(\frac{\rho_s f_y}{20}\right)^2 \qquad\qquad \text{Eq. 2.7}$$

where z represents the distance from the critical section to the point of contra-flexure, b is the width of beam, d is the effective depth of the beam in inches (1 in. = 25.4 mm), ρ_s is the ratio of the volume of confining steel (including the compression steel) to the volume of concrete core, and f_y is the yield strength of the confining steel in kips per square inch (1 kip/in.2 = 6.89 N/mm). In discussing Corley's work, other investigators have proposed simplified equations that fit the data with reasonable accuracy. These include:

$$l_p = 0.5d + 0.05z \qquad\qquad \text{Eq. 2.8}$$

and

$$\varepsilon_c = 0.003 + 0.02\frac{b}{z} + 0.2\rho_s \qquad\qquad \text{Eq. 2.9}$$

This modification to the equation for ε_c makes it more conservative for high values of ρ_s.

Priestley and Park (1987) proposed a plastic-hinge length considering the strain penetration into column footings which is dependent on the rebar diameter and column length. This plastic-hinge length is:

$$l_p = 0.08l + \xi f_y d \qquad\qquad \text{Eq. 2.10}$$

where l is the length of the column, ξ is a coefficient equal to 0.15 in. (0.022 mm), f_y is the steel stress in the furthest rebar, and d is the diameter of the main rebar.

If the curvature distribution within the elastic range is assumed to be linearly distributed, D_e can be calculated as follows at yield point:

$$\Delta_e = \frac{1}{3}\phi_y(l_t - l_p)^2 \qquad\qquad \text{Eq. 2.11}$$

where

$$l_t = l + \xi f_y d \qquad\qquad \text{Eq. 2.12}$$

The plastic deflection is:

$$\Delta_e = \phi_p l_p (l_t - \frac{l_p}{2}),$$

Eq. 2.13

and the total deflection is the sum of the elastic and plastic deflections:

$$\Delta = \Delta_e + \Delta_p.$$

Eq. 2.14

2.2.2.2.2 <u>Discussion of plastic-hinge model.</u> The formulation described in Section 2.2.2.2.1 above is limited to well confined columns with flexure-dominated failures. The validity of these formulations is questionable for the shear-dominated behavior of columns subject to combined loading including torsion. In addition, in recent years, the focus of research has shifted toward performance-oriented seismic design (ATC 32, 1996; Lehman et al., 1998) to improve the methods to evaluate the performance of bridge columns over the range of performance levels. As part of the performance-based-design (PBD) approach, bridge columns are designed to reach a particular damage level depending on the magnitude of an earthquake. Therefore, this approach requires that inelastic response to be assessed in the presence of combined loading including torsion. Specifically, the designers must determine the strength of the concrete shear resistance mechanism across a wide range of ductility so that the structure can be protected against shear- and torsion-dominated failure. Further, they must quantify flexural response so that the dependability of flexural hinges can be assessed under combined loading.

2.3. BEHAVIOR UNDER PURE TORSION WITH AXIAL LOADS

Pure torsion loading is rarely present in structural members, and it usually occurs in combination with other actions such as bending and shear. However, understanding the behavior of members subject to pure torsion is necessary for further analysis of a structural member under combined loading. The torsional strength of an RC column depends mainly on the amount of transverse and longitudinal reinforcement, the sectional dimensions including clear cover, and the concrete strength. In terms of reinforcement ratios, the failure modes of RC columns under pure torsion can be categorized into under-reinforced (when both the longitudinal and transverse reinforcement yield before ultimate failure), completely over-reinforced (when neither longitudinal nor transverse reinforcement yields before ultimate failure), and partially under-reinforced (when either longitudinal or transverse reinforcement yields before ultimate failure). Few studies have reported the behavior of RC columns under pure torsion (Pandit and Mawal, 1971; Bishara and Pier, 1984).

2.3.1. Experimental Studies. Very few investigations have focused on pure torsion and pure torsion combined with axial loads. Experimental studies and general behavior or RC members under pure torsion and pure torsion combined with axial compression is described in the following sections.

2.3.1.1 Pure torsion. Under pure torsional loading, diagonal cracks begin to develop from near mid-height on the column due to the boundary conditions of the foundation and top loading block. These diagonal cracks spread continuously in the form of inclined spirals at an increased level of twisting. Soon after diagonal cracking, the stiffness drops significantly. After significant yielding of transverse reinforcement, a plastic zone forms near the mid-height of the column. The post-yield stiffness and

strength depends mainly on the amount of transverse reinforcement in the cross section. Figure 2.3 plots the variation in torsional strength with respect to the transverse reinforcement ratio based on the existing literature (Hindi et al., 2005). This plot clearly shows that an increase in the transverse reinforcement ratio increases torsional strength.
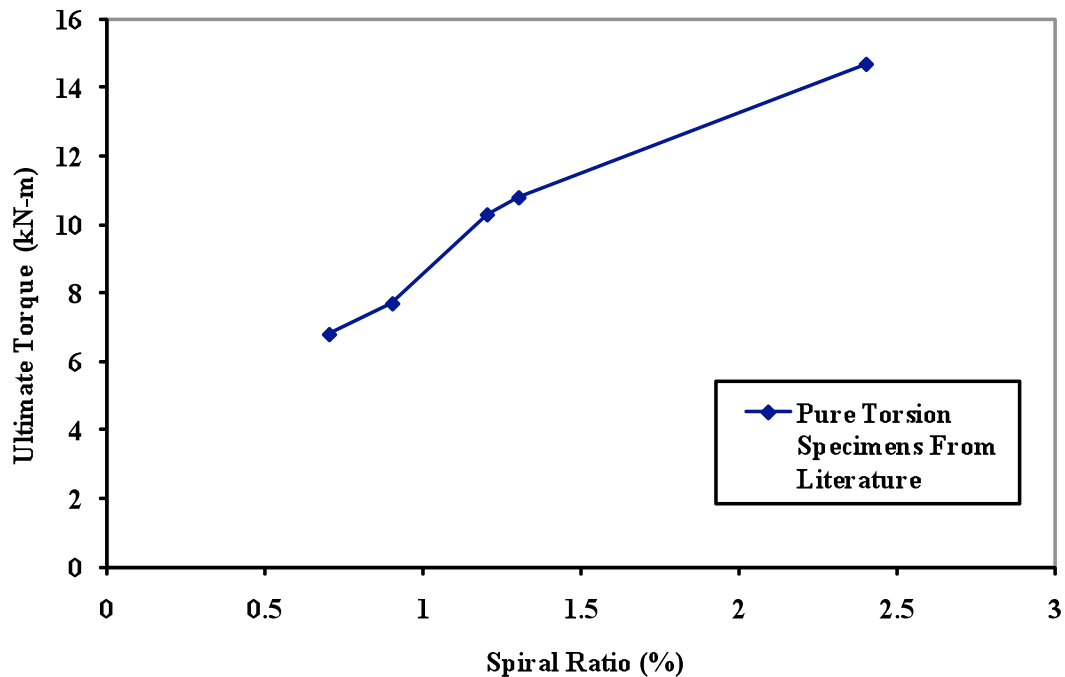
Figure 2.3 Variation of Torsional Strength with Increase in Spiral Reinforcement Ratio

The occurrence of spalling is important from a torsional design point of view. The occurrence of spalling before or after peak load determines whether effective cross sectional dimensions must be used in the design calculations. If spalling occurs before the member reaches the peak load, then the concrete cover must be subtracted from the actual dimensions during design. Researchers have investigated spalling in several ways for RC rectangular and box sections. Hsu and Mo (1985a) have suggested a simple equation based on cover thickness and shear flow thickness to determine the effect of spalling. In a study by Rahal and Collins (1995a) of members under combined shear and torsion, the

potential for spalling was assumed to be proportional to several factors as follows; the compressive force in the concrete cover, to the cover thickness, and to the area of the splitting plane occupied by the reinforcement, and inversely proportional to the concrete tensile strength and the size of the section. In addition, spalling can depend on a number of factors such as reinforcement ratio, and section type (square/rectangular/circular). These factors have not been investigated adequately under pure torsion and combined loading including torsion.

Seismic design relies heavily on the ductility of RC members, which in turn depends on the transverse reinforcement ratio. Circular columns may have either hoop or spiral as transverse reinforcement. A spirally reinforced column under pure torsion has a direction bias. In one loading direction, the spiral locks itself, which produces more confinement in the concrete core, thereby increasing strength and stiffness. In the other direction, the spiral unwinds or unlocks itself, which results in lower strength and stiffness. To eliminate the locking and unlocking effect of spiral reinforcement under pure torsion, Hindi et al. (2005) proposed the use of two cross-spirals to enhance the strength and ductility characteristics Columns confined with cross spiral reinforcement have been studied under increasing axial load and combined axial and flexural loads (Turechek and Hindi, 2006). Browning et al. (2007) found that cross spirals (two spirals crossing opposite to each other at 45º) reduce strength deterioration, increase the ductility, and reduce the directional bias when the same spiral reinforcement ratio remains constant. In post-peak behavior, the dowel action of longitudinal bars has also been reported to increase load resistance significantly at higher cycles of loading.

2.3.1.2 Torsion with axial load. Experimental research on RC columns under torsion combined with axial compression is extremely limited. There is no experimental data available for the combination of torsion and axial tension. Bishara and Peir (1973) and Pandit and Mawal (1973) have reported the results of few tests on rectangular sections under torsion combined with axial compression. Their results show that axial compression improves torsional strength linearly up to an axial stress level of $0.7f_c'$. The maximum increase in torsional strength was 210%, measured when compressive stress was about 65% of the cylinder strength. Various researchers have also proposed a number of empirical equations to predict the torsional strength. Figure 2.5 illustrate the interaction between torsion and compression. Interaction between torsion and axial tension is not a common load combination; however, the model proposed by Rahal (2006) has shown that the presence of axial tension considerably reduces the torsional strength.
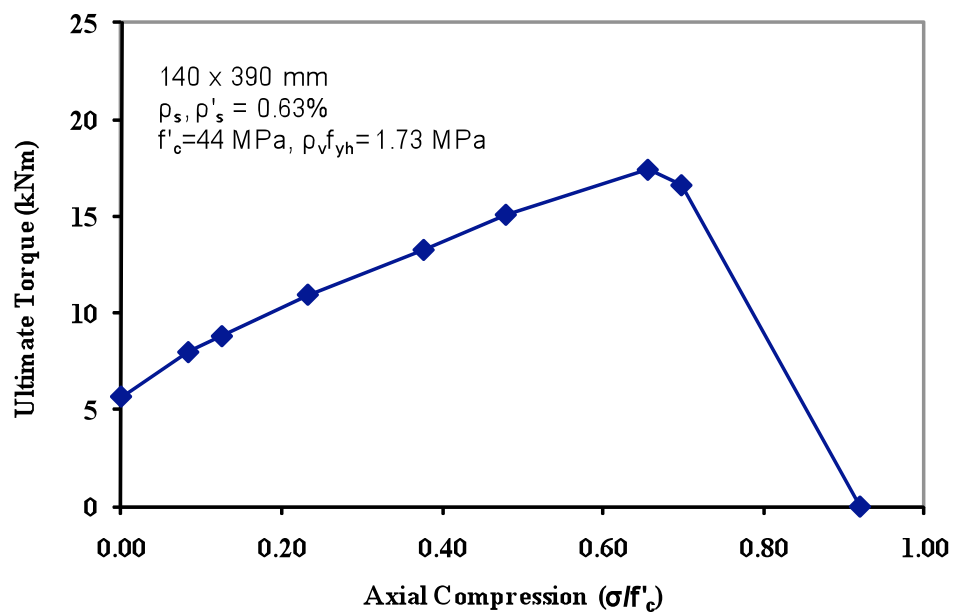
Figure 2.4 Torsion Moment-Axial Compression Interaction Diagrams
[Using Results from Bishara and Peir, 1973]

2.3.2. Analytical Studies. Many theories predict the cracking and peak torsional strength of non-circular RC members. Early theories for predicting cracking torsional moment were based on the assumption that an RC member would behave as a homogeneous member of plain concrete before cracking. Theories for the torsion of plain concrete include the elastic theory (Saint-Venant, 1856), the plastic theory (Nylander, 1945), and the skew bending theory (Elfgren, 1974). There are several theories capable of estimating the ultimate strength of RC members under torsion such as skew bending theory (Lessig, 1959; Yudin, 1962; Collins et al., 1968; Hsu, 1968; Elfgren, 1974) and the well-known truss models developed by Mitchell and Collins (1974) and Hsu and Mo (1985a).

Bredt (1896) derived the thin-tube theory with simple equations for describing torsional behavior. According to Bredt's theory, the constant shear stress, τ, can be converted to a shear flow, q, by multiplying by the tube's thickness, h (e.g., $q = \tau h$). Collins (1972) estimated the thickness of thin tube or "shear flow zone," in an uncracked concrete member. Mitchell and Collins (1974) developed the first theory to satisfy equilibrium, strain compatibility, and material laws; this theory is known as compression field theory (CFT). Later, Hsu and Mo (1985) formulated the softened truss model (STM) and included the material laws of biaxial loaded RC.

A basic concept of both theories is that the stress and strain are averaged, or smeared. Both theories adopted force equilibrium and strain compatibility obtained from a shear panel, in an idealized wall of a member's cross section. Additional equilibrium and compatibility equations are necessary to assemble the membrane elements (shear panel) to a closed noncircular torsional member. These additional equations are derived

from the Bredt's thin tube theory; they include specific equations that relate twist to shear strain and twist to the curvature in the concrete strut (Figure 2.5). Out-of-plane warping in the walls of noncircular sections causes curvature in the concrete struts. This curvature in turn causes flexure in the concrete strut. The angle of the diagonal cracks to the member's longitudinal centerline, α, is variable in both CFT and STM (Figure 2.6). The use of variable-angle truss models has several implications: the use of the variable α allows a unified treatment of shear and torsion. Further, it allows the interaction of torsion, shear, bending, and axial load to be treated rationally. The equations of Bredt's thin tube theory are shown below:

$$T = q \oint r_0 dt \qquad\qquad \text{Eq. 2.15}$$

$$\oint r_0 dt = 2 A_0 \qquad\qquad \text{Eq. 2.16}$$

$$T = 2 A_0 q \qquad\qquad \text{Eq. 2.17}$$

$$t_d = \frac{3}{4} \frac{A_0}{p_0} \qquad\qquad \text{Eq. 2.18}$$
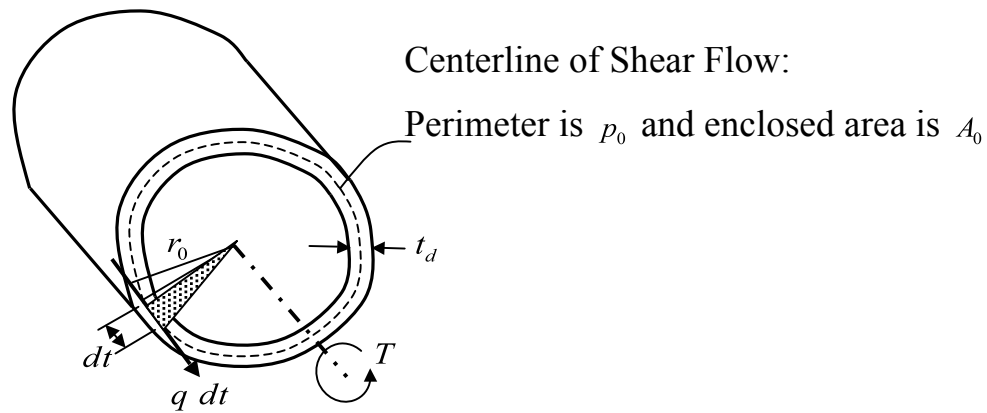
Figure 2.5 Schematic Representation of a Tube under Pure Torsion
(Greene, 2006)
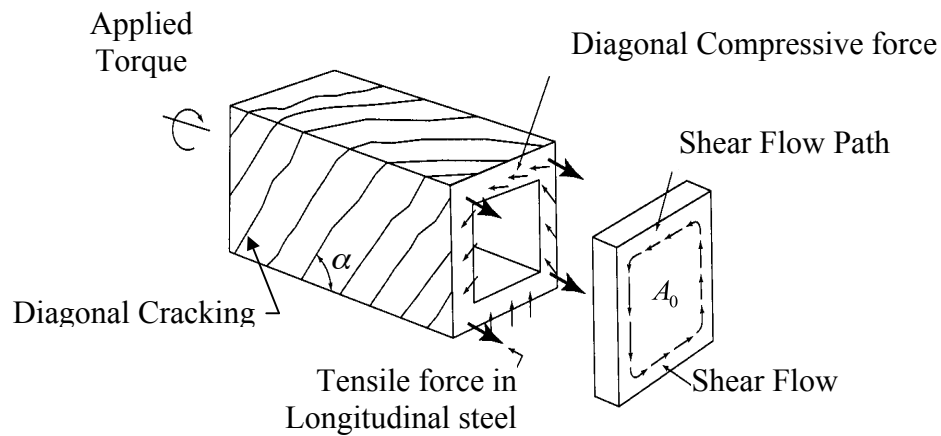
Figure 2.6 Truss Model for RC Section under Pure Torsion

2.3.2.1 Compression field theory (CFT). Many aspects of CFT and STM are similar; however, they differ significantly in their treatment of the shear flow zone and the stress-strain relationship for concrete in compression. Mitchell and Collins (1974) assumed the member was in a completely spalled condition. Under pure torsion, the concrete at the corners was under compression, and the interface at the transverse steel

reinforcement and concrete cover was under tensile stresses resulting in spalling. At higher torsional moments, the concrete cover and core interface do not have adequate tensile strength to keep them from spalling off. Based on the assumption of complete spalling, the outer cross section dimensions are assumed to be at the centerline of the transverse steel reinforcement, meaning that the shear flow zone is entirely contained in the enclosed transverse steel reinforcement. The uniaxial stress-strain relationship used in the CFT for concrete in compression followed the famous parabolic Hognestad (1951) equation. The concrete stress in the compression strut was then approximated using the same concept of equivalent stress block used in flexure. The assumption of a uniaxial stress-strain relationship for concrete overestimates the compressive stress developed in the concrete. However, the assumption of a spalled section causes a smaller "moment arm" and compensates the overestimation of concrete stress (Hsu, 1984). Accordingly, combined these two assumptions accurately predict the torsional capacity. Vecchio and Collins (1986) later quantified the reduction of compressive strength and stiffness in shear panels due to lateral tensile stress, a phenomenon known as compression softening. The effect of softening is also present in the walls of a torsional member.

  2.3.2.2 Softened truss model (STM). The STM incorporates the softening effect and makes several new assumptions about the shear flow zone. Calculation of the average compressive stress in the concrete strut is altered to include the proportional stress and strain softening of concrete. Eq. 2.19 gives the average compressive stress in terms of the peak compressive stress in the concrete strut. Equations Eq. 2.20 and Eq. 2.21 give the expression for k_1 in the ascending and descending branches of the σ_d-ε_d curve. Figure 2.7 shows the stress and strain distribution in the concrete strut assumed by

STM. It also shows the equivalent stress profile defined by Eq. 2.19. The STM was originally presented (Hsu and Mo, 1985a) using the softening coefficient developed by Vecchio and Collins (1982). The version described later (Hsu 1993) uses the softening coefficient developed at the University of Houston. Unlike the CFT, the STM assumes that the average compressive strain occurs at the mid-depth of the shear flow zone (e.g., $\varepsilon_d = \varepsilon_{ds}/2$), and as a result, the centerline of the shear flow is assumed to coincide with ε_d, as shown in Figure 2.7. In addition, the formulas for A_0 and p_0, Equations Eq. 2.22 and Eq. 2.23, include the full section dimensions instead of the spalled dimensions. The formulas for A_0 and p_0 given as shown in Figure 2.5 are assumed to be valid for any arbitrary bulky cross section.

$$\sigma_d = k_1\sigma_p = k_1\zeta f_c' \qquad\qquad \text{Eq. 2.19}$$

for $\varepsilon_{ds}/\varepsilon_p \leq 1$

$$k_1 = \frac{\varepsilon_{ds}}{\varepsilon_p}\left(1 - \frac{\varepsilon_{ds}}{3\varepsilon_p}\right) \qquad\qquad \text{Eq. 2.20}$$

for $\varepsilon_{ds}/\varepsilon_p > 1$

$$k_1 = \left[1 - \frac{\varepsilon_p^2}{\left(2\varepsilon_0 - \varepsilon_p\right)^2}\right]\left(1 - \frac{\varepsilon_p}{3\varepsilon_{ds}}\right) + \frac{\varepsilon_p^2}{\left(2\varepsilon_0 - \varepsilon_p\right)^2}\frac{\varepsilon_{ds}}{\varepsilon_p}\left(1 - \frac{\varepsilon_{ds}}{3\varepsilon_p}\right) \qquad\qquad \text{Eq. 2.21}$$

(a) Strain   (b) Stress   (c) Equivalent Stress
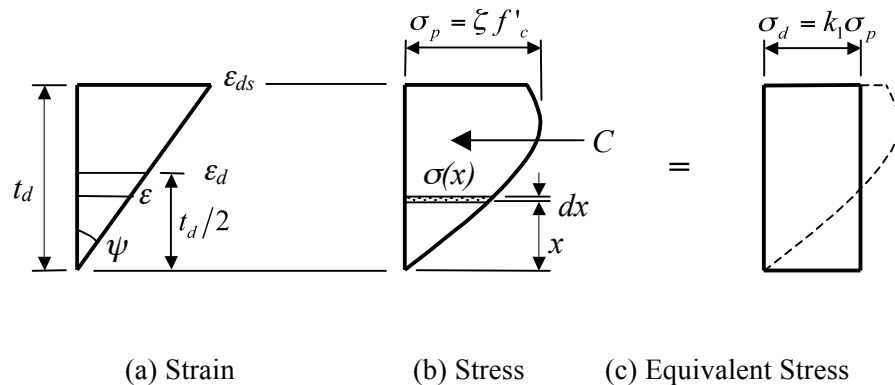
Figure 2.7 Stress and Strain Distributions in the Shear Flow Zone of the Concrete Strut

$$A_0 = A_{cp} - 0.5p_c t_d + t_d^2 \qquad\qquad \text{Eq. 2.22}$$

$$p_0 = p_c - 4t_d \qquad\qquad \text{Eq. 2.23}$$

2.3.2.3 Limitations of space truss models. The variable angle truss model theories for RC torsional members discussed in Sections 2.3.2.1 and 2.3.3.3 can reasonably predict the behavior up to the peak torsional moment. In under-reinforced members, the peak torsional moment typically occurs with the onset of the reinforcement yielding, or soon after. The STM defines failure at concrete crushing, which is assumed to occur when the principal compressive strain at the surface, ε_{ds} reaches -0.0035 mm/mm. This can occur after both longitudinal and transverse reinforcement yield (under-reinforced), after the reinforcement in only one direction yields (partially over-reinforced), or before yielding occurs in either direction (over-reinforced). However, the post-peak behavior in under-reinforced members can be affected by spalling or the Poisson effect.

2.3.2.3.1 <u>Spalling effect.</u> There is considerable debate over the occurrence of spalling in torsional members (Mitchell and Collins, 1974; Hsu and Mo, 1985a; Hsu and Mo, 1985b; Rahal and Collins, 1995). The debate focuses on when spalling occurs during the load-deformation response and what effect it has on peak and post-peak behavior. Among nine torsional beams tested by Mitchell (1974) at the University of Toronto, only one specimen showed spalling phenomenon before peak torsional moment. McMullen and El-Degwy (1985) tested 13 prestressed beams with varying aspect ratios. They

concluded that the full cross section should be used to calculate the member's torsional capacity because spalling occurred either at or soon after the maximum torsional moment. Researchers have modeled spalling in several ways. Hsu and Mo (1985b) have suggested that the concrete cover be disregarded when analyzing a member if $\overline{c}/t_d$ exceeds 0.75. The term $\overline{c}$ is defined as the distance from the centerline of the steel cage to the surface of the member, and t_d is the depth of the shear flow zone. According to this model, a member is assumed to be spalled when a factor for potential spalling exceeds the empirical factor of spalling resistance.

       2.3.2.3.2 <u>Poisson effect.</u> Due to the Poisson effect, loading along a principal direction induces strain not only in that direction but also in the lateral direction. Belarbi and Hsu (1994) have shown that beyond the peak stress, the shear stress (τ_{LT}) versus shear strain (γ_{LT}) curve exhibits a descending trend that is not predicted by the STM. Sengupta and Belarbi (2001) have postulated that post-peak, as τ_{LT} is decreasing and γ_{LT} is increasing, the reinforcement would have to relieve stress to maintain equilibrium. However, after yielding, the stress in the reinforcement is either constant with increasing strain or increasing due to strain hardening. This anomaly arises because the effect of Poisson's ratio in a panel element under a bi-axial stress state is disregarded. In STM and CFT, the strains along the direction of a stress are generated only by that stress in that direction. The lateral strain generated by stress acting in the normal direction due to the Poisson effect is ignored. As a result, the truss models described above cannot accurately predict the post-peak behavior.

2.4. BEHAVIOR OF RC COLUMNS UNDER COMBINED FLEXURE, SHEAR,

AND TORSION

Experimental and analytical studies on the general behavior of RC members under combined flexure, shear force and torsion is described in the following sections. The analytical studies also describe the variable angle truss models and their limitations in detail.

2.4.1. Experimental Studies. Many experimental investigations have tested RC members under combinations of torsion, flexure, and shear loads. Previous investigations have focused on the failure modes, the effect of asymmetric longitudinal reinforcement, and the inclination angle of diagonal cracking. The effect of varying the ratio of applied torsion-to-bending moments and shear forces has also been studied. However, very little research has focused on the hysteretic behavior of RC members under cyclic torsion and torsion combined with other actions (Collins and Chockalingam, 1979; Tirasit et al., 2005). The following discussion describes existing experimental studies of RC members under torsion and flexural moments, torsional moment and shear forces, and combined bending moment, shear force and torsional moment.

2.4.1.1 Torsional and bending moment. Under pure torsional moment, all longitudinal bars in a RC member are subject to tensile strains. However, under flexure there is a linear strain variation with tensile strains on the bottom and compression strains at the top as shown in Figure 2.9. In a section with symmetrically arranged reinforcement, the strains due to torsion are nearly equal across the cross section. Due to a combination of strains from torsion and bending, the curvature does not change if reinforcements are distributed symmetrically (Figure 2.9a). However, if the section is asymmetrically reinforced, the curvature changes due to the effect of additional torsional

loading (Figure 2.9b). In a member with symmetrically arranged reinforcement, the torsional moment needed to cause failure decreases as the ratio of torsion-to-bending moment decreases. The addition of bending moment has a minimal effect on post-cracking stiffness (McMullen and Warwaruk 1970).
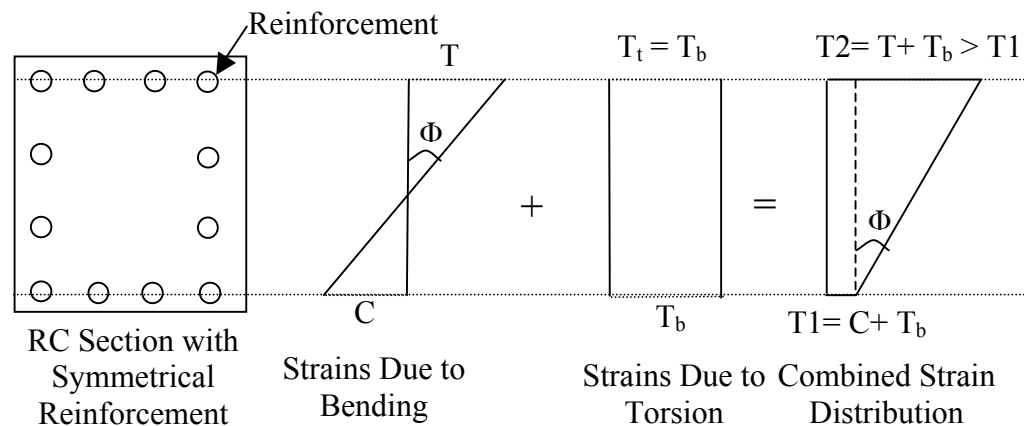
(a) Strain Distributions in a Symmetrically Reinforced Section
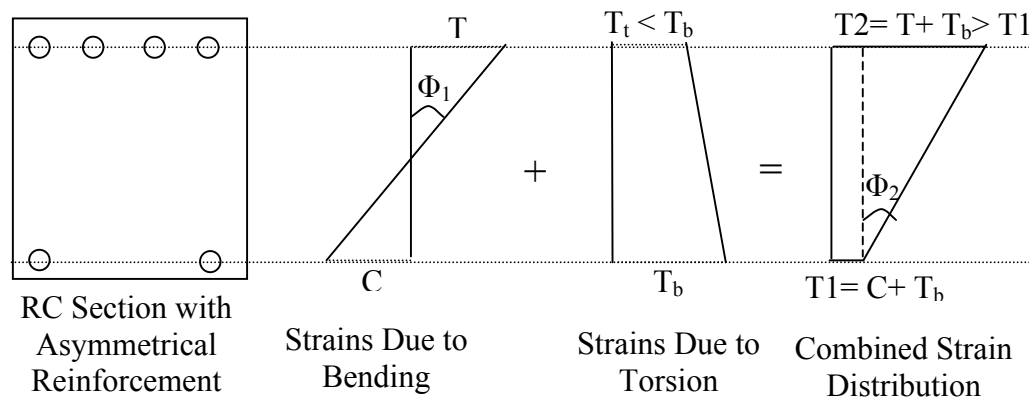
(b) Strain Distributions in an Asymmetrical Reinforced Section

(T= Tensile Strain, C= Compressive Strain, Φ = Curvature)

Figure 2.7 Strain Distributions in an RC Section under Combined Bending, and Torsional Moment, and Shear Force

In general, RC members with asymmetric reinforcement have additional reinforcement in tension side. In a member with asymmetrical reinforcement under pure torsion, the face with less longitudinal reinforcement, known as the weak face, yields first

and controls the member's capacity. Therefore, the addition of a small bending moment increases a member's torsional capacity (Lampert and Thürlimann, 1969; McMullen and Warwaruk, 1970; Onsongo, 1978). Such an addition of bending moment, also reduces the net tensile stress in the weak face, and increases the member's capacity. Another effect of asymmetrical reinforcement is that the additional strain in the weak face may cause a difference in curvature profile and deflection. Hence, this effect must be clarified for column members subjected to axial loads and shear forces combined with bending and torsional moment.

  2.4.1.2 Torsional moment and shear forces. Due to torsional moment and shear forces, shear stresses are produced across the cross section. Test results have shown that outer parts of the cross section are more effective in resisting the torsional loads (Collins et al., 1972). After cracking, core concrete in the center of the RC member has little effect on the torsional strength of the cross section and can be disregarded. The shear flows due to an applied torsional moment and shear forces are shown in Figure 2.8. The shear flow due to an applied torsional moment, q_T , circulates around the section as shown in Figure 2.8a. A vertically applied shear force induces a vertical shear flow. A member under combined shear and torsion has shear flows like those shown in Figure 2.8c, i.e., additive near one wall and subtractive near the wall on the opposite side of the cross section. Concrete cover spalling is more likely in the side where shear stresses are additive.

(a) Applied Torsion   (b) Applied Shear Force   (c) Combined Torsion and Shear
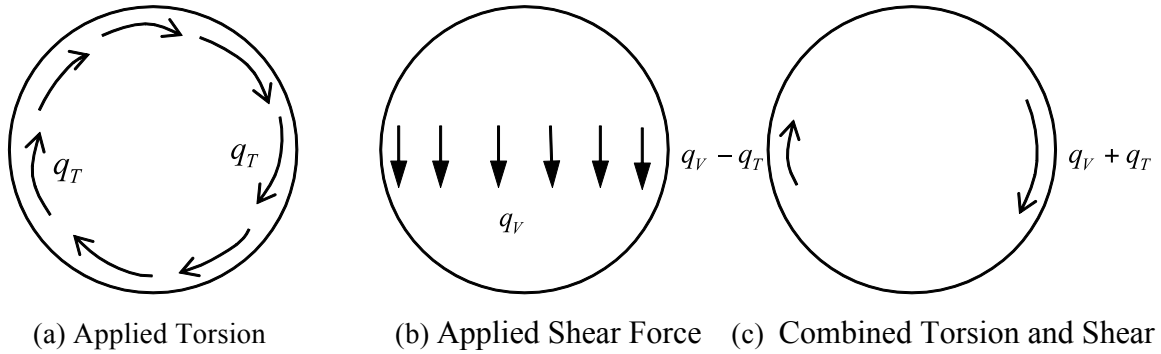
Figure 2.8 Shear Flow in a Member under Combined Loading

Klus (1968) has reported tests on combined actions of shear, torsion, and relatively low bending moment. He suggests a bilinear interaction curve for torsion and shear. Pritchard (1970) and Badawy (1977) have also reported tests on beams under different shear forces and torsional moment. Their results were bounded by the linear and circular interaction (Rahal, 1993). In an RC member under pure torsion, the cracks will spiral around a member in a helical pattern. The angle of the inclined cracks is near 45° from the longitudinal axis of the member, depending on the relative amounts of longitudinal and transverse reinforcement. If a small shear force is applied to a similar member, the angle of the inclined cracks on the face where the shear stresses are subtractive increases and becomes more vertical. If the applied torsional moment and shear force induce shear flows that are nearly equal in magnitude, then the cracks on the subtractive face nearly vertical. In specimens tested at higher ratios of shear force to torsional moment, the shear stresses on the subtractive face approached the "pure shear" case, and the cracks were oriented closer to the angle on the additive side.

Many researchers have reported on the characteristics of the shear flow zone for members under pure torsion (Mitchell and Collins, 1974; Alkhrdaji and Belarbi, 2001). However, very little information has been published regarding the effect of an additional applied shear force on the thickness of the shear flow zone and the variation in

compressive strain in the concrete strut. However, uniform q_V cannot be created in a prismatic member without inducing a bending moment in the section by static equilibrium. Thus, all experimental work investigating combined torsional moment and shear force might be influenced with a small amount of bending moment.

2.4.1.3 Combined bending moment, torsional moment and shear force. For a member reinforced with longitudinal and transverse reinforcement, three failure modes are possible under combined bending and torsional moment, and shear forces: completely under-reinforced (when both longitudinal and transverse steel yield), partially over-reinforced (when only longitudinal steel or only transverse reinforcement yields), and completely over-reinforced (when concrete crushing begins before steel yields). Figure 2.9 illustrate the possible failure sequences under combined flexural and torsional moment and shear force.

The first tests on combined bending, shear, and torsion were reported by Nylander (1945). He tested beams reinforced only with longitudinal bars and found that the bending moment exerted a favorable influence on the torsional strength. Later, Cowan (1953) confirmed this result. Lessig (1959) suggested two possible failure modes and derived equations for the torsional strength of beams. However, his equations suggested that the addition of bending moment could reduce the torsional strength of a beam. Much of the experimental work involving members under combined loading has focused on the failure modes and derived equations to define a three-dimensional interaction surfaces (Lessig 1961; Yudin 1962; Gesund and Boston 1964). These failure modes and interaction surfaces have typically been described using the skew bending theory. Elfgren (1972) proposed a torsion-shear-flexure interaction by using the skew bending theory.

Ewida and McMullen (1981) concluded that predictions using the skew bending theory agreed well with the available results.

```
┌─────────────────┐      ┌─────────────────┐      ┌─────────────────┐
│  Bending/Shear  │ ───▶ │  Bending/Shear/ │ ◀─── │     Torsion     │
│                 │      │     Torsion     │      │                 │
└─────────────────┘      └─────────────────┘      └─────────────────┘
        │                        │                        │
        ▼                        ▼                        ▼
┌─────────────────┐      ┌─────────────────┐      ┌─────────────────┐
│    Flexural     │      │    Flexure/     │      │  Shear Cracks   │
│     Cracks      │      │  Shear Cracks   │      │                 │
└─────────────────┘      └─────────────────┘      └─────────────────┘

┌─────────────────┐      ┌─────────────────┐      ┌─────────────────┐
│  Longitudinal   │      │   Spiral /Long  │      │     Spiral      │
│   Bar Yielding  │      │     Yielding    │      │     Yielding    │
└─────────────────┘      └─────────────────┘      └─────────────────┘

┌─────────────────┐      ┌─────────────────┐      ┌─────────────────┐
│  Cover Spalling/│      │  Cover Spalling/│      │     Cover       │
│   Crushing of   │ ───▶ │ Crushing of Cover│ ◀── │    Spalling     │
│    Concrete     │      │   Concrete or   │      │                 │
└─────────────────┘      │  Diagonal Strut │      └─────────────────┘
                         └─────────────────┘

┌─────────────────┐      ┌─────────────────┐      ┌─────────────────┐
│     Spiral      │      │   Severe Core   │      │  Longitudinal   │
│     Yielding    │      │   Degradation   │      │   Bar Yielding  │
└─────────────────┘      └─────────────────┘      └─────────────────┘

┌─────────────────┐      ┌─────────────────┐      ┌─────────────────┐
│   Long. Bar     │      │    Long. Bar    │      │   Severe Core   │
│    Buckling     │      │ Buckling/Spiral │      │   Degradation   │
└─────────────────┘      │     Rupture     │      └─────────────────┘
                         └─────────────────┘
```

Figure 2.9 Possible Failure Sequences under Combined Loadings

Otsuka et al. (2004) studied nine rectangular columns under pure torsion, flexure, and various ratios of combined bending and torsion. They concluded that the pitch of the hoop significantly affects the hysteresis loop of torsion. They found that the energy dissipation under combined loading increases with a decrease in hoop spacing. Although a number of experimental studies have been reported; there is disagreement with regard to the behavior of RC members subject to combined loading. Before a unified design

approach can be suggested, it is essential to obtain a better understanding the behavior at cracking, yielding, and ultimate failure for RC members under combined loading.

The literature reports very little experimental work on the behavior of rectangular columns under combined loading; and no studies have examined circular RC columns under combined loading. Hsu and Wang (2000) and Hsu and Liang (2003) have reported the performance of composite columns with H-steel sections under combined loading. They found that the flexural capacity and ductility of composite columns decreases when constant torsion is simultaneously applied. Tirasit and Kawashima (2007) have since reported tests on RC columns under three loading conditions: cyclic uniaxial bending and shear, pure torsion, and combined cyclic bending, shear and torsional loads. They introduced a parameter called the rotation-drift ratio (r) to represent the level of combined cyclic bending and torsion. However, this ratio will not necessarily be the same as T/M ratio after cracking. The authors reported that the flexural capacity of an RC column decreases and that the damage tends to occur above the flexural plastic-hinge region as the rotation-drift ratio increases. In the Figure 2.10, the interaction of bending and torsional moment is represented. Both the 2003 and 2007 studies had the same cross section dimensions (200 mm x 200 mm) and nearly the same longitudinal reinforcement ratio (1.27% and 1.33%). The transverse reinforcement ratio in the study by Tirasit and Kawashima was 0.79%, and those in the study by Otsuka et al. (2004) were 0.54% and 1.08% respectively. The concrete strength also varied among tests by a maximum of 10%. Figure 2.10 shows the interaction diagram based on the normalized ultimate bending and torsional moments from flexure and pure torsion respectively. It should be noted that the peaks of torsional and bending moments may not occur simultaneously. In

principle, the interaction diagram should be drawn both at peak bending and torsional moments. The results from the studies show that the simultaneous application of bending and torsional moments reduce the strength of both. Although few experimental studies have been reported, there is disagreement over the behavior of RC columns subjected to combined loading.
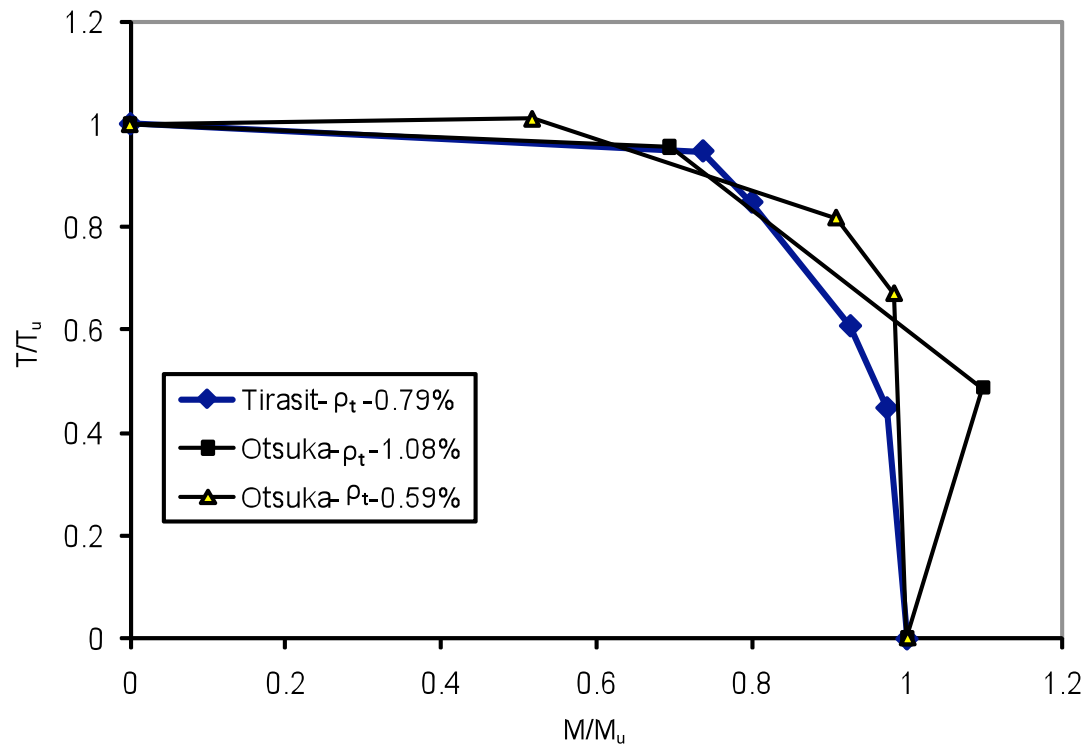
Figure 2.10 Interaction between Normalized Torsional and Bending Moments

2.4.2. Analytical Studies. Several analytical models have been developed to predict the behavior of RC sections such as the skew bending theory and truss models. They are briefly discussed in the following sections

2.4.2.1 Skew bending theory. Many researchers have proposed skew bending theories for members under combined loading including torsion, bending, and shear

(Lessig, 1959; Yudin, 1962; Collins et al., 1968; Hsu, 1968; Elfgren, 1974). Skew bending theory assumes that cracks form around the member in a helical pattern and create a skew failure surface with the compression zone inclined at an angle to the member's longitudinal axis. Sketches of three possible skew bending failure modes are shown in Figure 2.11.

(a) MODE 1 FAILURE

(b) MODE 2 FAILURE

(c) MODE 3 FAILURE
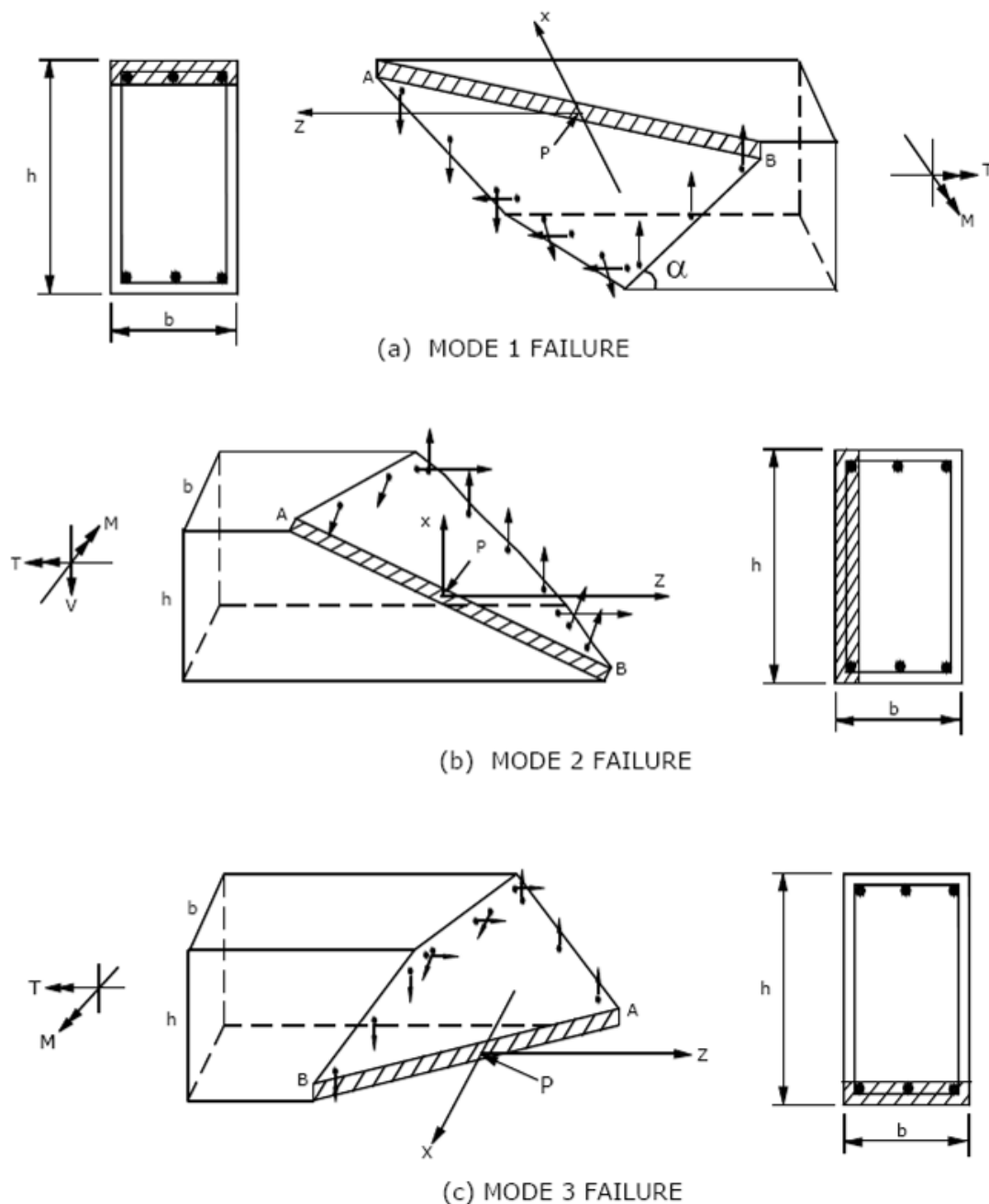
Figure 2.11 Skew Bending Failure Modes
(Adapted from Elfgren, 1974)

Internal torsional and bending resistance is calculated by assuming a failure mode, and then equilibrium equations are derived by summing moments along the failure surface. The assumptions of this theory are (i) shear stress in the compression zone does not affect concrete strength, (ii) both the longitudinal and transverse reinforcement that intersect the failure surface are yielding, and (iii) there are no applied loads or changes in transverse reinforcement spacing in the failure zone. It also neglects the effects of tension stiffening and dowel action of the reinforcement. In these sketches, the crack angle along a face of the member either was assumed to be 45° or was calculated based on the relative force developed in the longitudinal and transverse reinforcement assuming yield stresses in both.

Elfgren et al. (1974) developed a three-dimensional interaction surface for members under combined torsion, bending, and shear. The Elfgren model idealized a rectangular member as a box with reinforcement lumped into the four corners as "stringers." The components of axial force in the stringers induced by an applied torsional moment, T, bending moment, M, and shear force, V, were combined using superposition method. Warping in the cross section due to torsion was disregarded. Failure of the concrete before the longitudinal reinforcement yields was also not considered, so over-reinforced or partially over-reinforced sections could not be evaluated with this theory. Equations [Eq. 2.24, Eq. 2.25, Eq. 2.26] give the nondimensional interaction relationships for three modes of failure. The capacity of a member under pure torsional moment, bending moment, or shear force is denoted by T_0,

M_0, and V_0, respectively. The term d_v is the centerline distance between the top and bottom stringers, and p_0 is the perimeter around the member measured along the centerline of the stringers. The parameter r is the ratio of the force in the top stringers at yielding to the force in the bottom stringers at yielding accounting for an asymmetrical arrangement of longitudinal reinforcement in a member. This term has the effect of shifting the interaction surface along the M/M_0 axis. The inclusion of r allows the model to predict an increase in torsional capacity for members with a small bending moment and asymmetrical reinforcement. The interaction surface described by the Elfgren equations is shown in Figure 2.12 for $r = 1/3$ as presented by Hsu (1993).
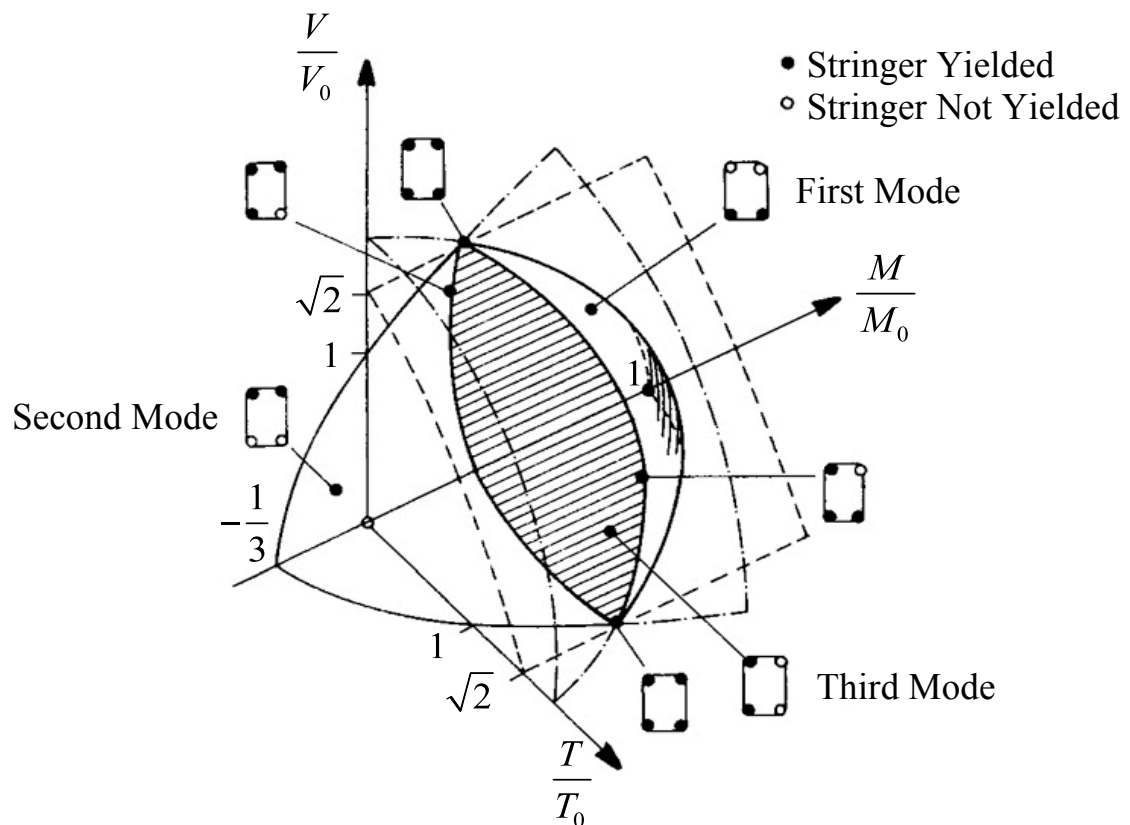
Figure 2.12 Interaction Surface for Torsion, Bending, and Shear
(Adapted from Hsu, 1993)

The skew bending theory is limited to calculation of a member's strength capacity because skew bending considers only the equilibrium of forces. It cannot predict the corresponding deformation because it does not consider the strain compatibility. Variable-angle truss models discussed in the following section overcome this limitation by including strain compatibility.

$$\text{Mode 1: } \frac{M}{M_o} + r\left(\frac{V}{V_o}\right)^2 + r\left(\frac{T}{T_o}\right)^2 = 1 \qquad\qquad \text{Eq. 2.24}$$

$$\text{Mode 2: } -\frac{1}{r}\left(\frac{M}{M_o}\right) + \left(\frac{V}{V_o}\right)^2 + \left(\frac{T}{T_o}\right)^2 = 1 \qquad\qquad \text{Eq. 2.25}$$

$$\text{Mode 3: } \left(\frac{V}{V_o}\right)^2 + \left(\frac{T}{T_o}\right)^2 + 2\left(\frac{VT}{V_oT_o}\right)\sqrt{\frac{2d_v}{p_o}} = \frac{1+r}{2r} \qquad\qquad \text{Eq. 2.26}$$

2.4.2.2 Variable-angle truss models. As in the case of pure torsion, space truss models consider strain compatibility in addition to force equilibrium and can therefore be used to predict a member's load-deformation behavior as well as its capacity. The angle of the compression strut is calculated based on the compatibility of strains, rather than by assuming an angle or using a function of force in the reinforcement at yielding. Several theories have used different constitutive relationships for concrete under uniaxial compression and for softened concrete. The concept of modeling different geometries of a RC member and the ways of accounting for out-of-plane warping effect to concrete

strut induced by torsion also varies in each of the models.

Rabbat (1975) developed the variable-angle space truss (VAST) model to account for combined loading, and it envisions a RC member with four chords and four wall panels. The chords consist of longitudinal reinforcement encased in a concrete block, and the applied bending moments and axial force are resisted by developing uniform tension or compression in the chord. Warping in the member due to an applied torsion is also assumed to induce axial forces in the chords. The wall panel resists applied torsional moments and shear forces as a uniform shear stress. Both the concrete and reinforcement resist compressive stress in the chord, and the reinforcement alone resists tension stresses. The wall panels are of a consistent thickness and are assumed to remain plane even when a torsional moment is applied to the member. The angle of the diagonal cracks could be calculated for each face and is affected by the applied load and the amount of reinforcement. This model uses an elastic, perfectly plastic stress-strain relationship for the reinforcement. For compression, the uniaxial stress-strain relationship of a concrete cylinder is assumed, and tension stiffening is disregarded.

2.4.2.2.1 CFT for combined torsion, bending, and axial load. The model developed by Onsongo (1978) conceives of an RC member as a series of wall panels. Equations for equilibrium, compatibility, and stress-strain relationships are satisfied at each longitudinal reinforcing bar. Concrete strut curvature can also be induced by longitudinal and transverse curvature in the wall panel. Equations were developed to maintain the compatibility of strain in the longitudinal reinforcement. Shear strain calculated at each longitudinal reinforcing bar affects twist in the member. Compressive stresses are assumed to be resisted only by the concrete and tensile stresses only by the

reinforcement. In the model, the uniaxial stress-strain relationship of a concrete cylinder is assumed for concrete in compression, and the concrete cover is disregarded.

2.4.2.2.2 <u>MCFT for combined shear force and torsional moment.</u> A more recent model by Rahal and Collins (1995a) incorporates the softening behavior of concrete under biaxial stress into models previously developed by Mitchell and Collins (1974) and Onsongo and Collins (Onsongo 1978). The model conceives of the member as four wall panels and assumes that the applied loads, torsional moment, and shear force act as shear stresses in each panel. It also adopts the strain compatibility equations developed by CFT and the equations for longitudinal strain compatibility and curvature of the concrete struts. However, the authors did not discuss the method used in the model to calculate the twist in a member resulting from an applied torsional moment.

This model includes tension stiffening and introduces an empirical coefficient to predict spalling. When the model predicts the initiation of spalling, the concrete cover is disregarded on the faces with high shearing stress. As part of tension stiffening, the model assumes that the tension at a crack is transmitted across the crack through local shear stresses after the reinforcement yields, In the context of this assumption, the model considers shear stress at the cracks, and the cracks are defined as being normal to the principal tensile direction. However, the assumption of a shear stress at the cracks violates the defined crack direction. Shear due to torsion was assumed to flow around the member, and the model adopts Bredt's expression for torsion in a thin tube, given by Eq. 2.15 was adopted. As in CFT, the shear stress in the walls induces tensile stresses in the longitudinal and transverse reinforcement, and compressive stress in the diagonal compression struts. Mitchell and Collins (1974) showed previously shown that for a

member under pure torsion, the strain distribution in the concrete strut is linear. However, s Rahal and Collins (1995a) offers no similar experimental justification for the distributions presented in this model.

2.4.2.3 Softened truss models for combined loadings. Various versions of STM have been extended from their original versions for shear and torsion to combined loadings. They are briefly discussed in the following sections.

2.4.2.3.1 <u>Tension stiffening-softened truss model (TS-STM).</u> The original STM neglects the tensile strength of concrete. That model has since been expanded to include the tension stiffening of concrete (Greene and Belarbi, 2009a&2009b). This modification is important because it permits an improved prediction of the service-level twist. It accounts for the concrete in tension with a stress-strain relationship and adjusts the shear flow zone to account for the transition between an uncracked and fully cracked member. This model has been validated using test data available in the literature.

The TS-STM assumes that a member has uniformly spaced reinforcement in the longitudinal and transverse directions. It uses average stress-strain relationships to model the constitutive material laws for concrete and reinforcement. For concrete under tension, these relationships model cracked concrete as a continuum. The alignment of the crack rotates to remain normal to the principal tensile stress and the contribution of concrete in shear is disregarded. Dowel action too is disregarded and a perfect bond between the concrete and reinforcement is assumed. The model has been validated by comparing the predicted and experimental behavior of members loaded under pure torsion and having a symmetric distribution of longitudinal reinforcement and normal

strength concrete. However, the only behavior predicted by the model is torque, which causes either spalling or ultimate failure.
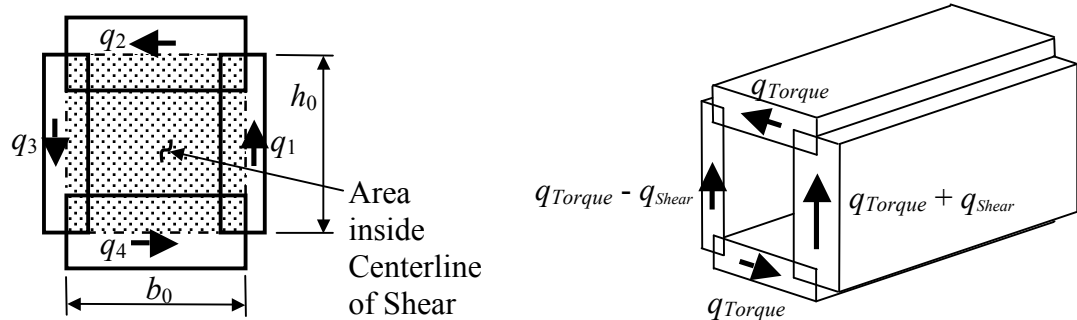
(a) Definition of Positive Shear Flow and A_0 (b) Combined Shear Flows
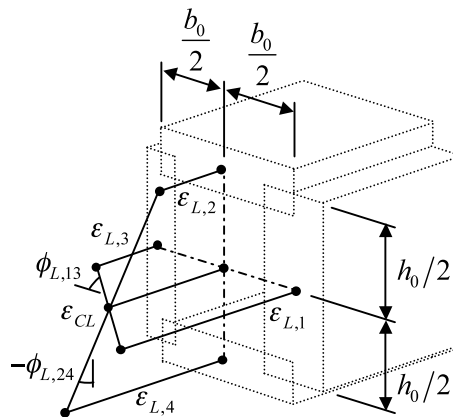
(c) Compatibility of Strain in Longitudinal Direction

Figure 2.13 Combined Actions-Softened Truss Model (CA-STM)
(Adapted from Greene, 2006)

2.4.2.3.2 Combined actions-softened truss model (CA-STM). The CA-STM developed by Greene (2006) assumes, as does that of Rahal and Collins (1997) that the walls of an RC member are as shear panels (Figure 2.13). The inclusion of tension stiffening effect is a significant improvement. Warping in the shear panels due to the member's twist is assumed to induce bending in the concrete struts. The effective

thickness of each panel is equal to the depth of the shear flow zone in the panel. Loads applied on the member act uniformly along the edges of the wall panels as normal and shear stresses. Equilibrium and strain compatibility are maintained in each panel, and strain compatibility in the longitudinal direction is maintained at the center of each panel. The member's twist is dependent on the shear strain in each panel. Also, the curvature in the concrete struts of a panel is dependent on the strain in the longitudinal and transverse directions of the other panels.

2.5. CODE PROVISIONS FOR COMBINED LOADINGS

Most code provisions are based on the pure shear, pure torsion, and pure flexure cases and there is no unified approach to the design of section subject to combined shear, torsion, and bending. This section discusses the development of ACI and AASHTO code provisions and their limitations. Structural standards and codes of practice are reviewed continuously, and changes are implemented as research findings require provisions for combined loading should be improved to include the softening of concrete and the spalling of concrete cover. The following section briefly presents, various limitations and their background.

2.5.1. ACI. Most shear and torsion provisions of the ACI code are based on the modified 45°-truss model. Shear resistance is divided between the concrete contribution (V_c) and the steel contribution (V_s). Torsion design provisions were first introduced into the ACI building code in 1971. The early provisions assumed that torsional resistance is divided between concrete and steel. In 1995, concrete contribution to torsional resistance was removed, and the influence of torsion on shear strength of concrete was disregarded.

2.5.1.1 Pure torsion. The ACI design provisions for torsion are based on thin tube, space-truss models. The RC members can be conceptualized as thin tubes. Soon after cracking, the tube becomes a space truss consisting of closed stirrups with longitudinal bars in the corners, and the concrete compression diagonals approximately centered on the stirrups. The diagonals are formed at angle 'θ', generally understood as 45° for reinforced concrete members. For prestressed concrete members, ACI recommends a value of 37.5°.

2.5.1.1.1 <u>Cracking torque (T_{cr}).</u> The cracking torsional moment is given by

$$T_{cr} = 4\sqrt{f_c'}\left(\frac{A_{cp}^{\,2}}{P_{cp}}\right)\text{(psi)} \qquad\qquad \text{Eq. 2.27}$$

where P_{cp} is the perimeter of the concrete section and A_{cp} is the area enclosed by this perimeter. The tensile strength of concrete in biaxial tension-compression is taken as $4\sqrt{f_c'}$ (psi). If the design torsional moment is less than the one quarter of T_{cr}, then torsional moments need not be considered in design. The presence of torsional moment at or below this limit has a negligible effect on the flexural and shear strength. Similarly, the torsional cracking strength to include the effect of prestress on the principal tensile stress, derived using the Mohr's circle:

$$T_{cr,p} = \phi\sqrt{f_c'}\left(\frac{A_{cp}^{\,2}}{P_{cp}}\right)\sqrt{1+\frac{f_{pc}}{4\sqrt{f_c'}}} \ \text{(psi)} \qquad\qquad \text{Eq. 2.28}$$

2.5.1.1.2 Minimum torsional reinforcement. The provisions of minimum torsional reinforcement are based mainly on the tests by Hsu (1968). He found that beams with same transverse and longitudinal yield strengths should have a minimum volumetric ratio of reinforcement in the order of 0.9 to 1 percent. Hence, for torsional design, the provisions of minimum reinforcement should be around 1 percent.

2.5.1.1.3 Torsion reinforcement. Based on the hollow tube analogy, the steel contribution Ts to the torsional resistance is:

$$T_s = 2A_0 \frac{A_t f_{yt}}{s} \cot \theta \qquad\qquad \text{Eq. 2.29}$$

where A_t represents the area of one leg of closed torsion reinforcement within a spacing s, A_0 represents the area enclosed by the shear flow path (taken as $0.85A_{oh}$) and A_{oh} is the area enclosed by the centerline of the outermost closed transverse reinforcement. According to ACI, the angle θ may assume any value between 30º and 60º. The required cross sectional area of one stirrup leg for torsion is calculated as follows:

$$A_t = \frac{T_u s}{2\phi A_0 f_{yt} \cot \theta} \qquad\qquad \text{Eq. 2.30}$$

The code limits f_{yt} to 60000 psi for the reasons of crack control.

2.5.1.2 Combined shear and torsion. The reinforcement provided for torsion must be combined with that required for shear. Based on a typical two-leg stirrup, this may be expressed as shown below.

$$\left(\frac{A_{v+t}}{s}\right) = \frac{A_v}{s} + 2\frac{A_t}{s}$$

Eq. 2.31

The code mentions that transverse stirrups used for torsional reinforcement must be of a closed form to provide the required tensile capacity across the diagonal cracks of all the faces. Because the concrete outside the reinforcing cage tends to spall off under torsional loading, the code requires the transverse reinforcement to be anchored within the concrete core. The ACI code requires that for T or L-shaped beams closed torsional stirrups must be provided in the flanges.

2.5.1.3 Combined torsion and bending moment. Torsion leads to an axial force 'N' that must be resisted by longitudinal reinforcement. If torsion occurs in a RC beam where moment also acts, the corresponding longitudinal torsion reinforcement is added to flexural reinforcement. This longitudinal reinforcement should be placed around the perimeter of the section for a torsional moment. In a flexural compression zone, the tension produced by torsion is counteracted by the compression resulting from bending. This effect allows a reduction in the area of longitudinal torsional reinforcement in the compression zone by the area of steel corresponding to the flexural compressive force. Based on a performance evaluation relying on previous research, the ACI code requires that A_l be no less than the value calculated using Eq. 2.32.

$$A_{l,\min} = \frac{5\sqrt{f_c'}A_{cp}}{f_{yl}} - \left(\frac{A_t}{s}\right)p_h\frac{f_{yv}}{f_{yl}}$$

Eq. 2.32

The spacing of the longitudinal bars should not exceed 300 mm, and the bars should be distributed around the perimeter of the cross section to control cracking. The code allows reinforcement required for torsion to be combined with other forces provided that the area furnished is equal to sum of the individually required areas and that the most restrictive requirements of spacing and placement are met.

2.5.2. AASHTO LRFD. The AASHTO provisions are based on the modified compression field theory. Similar to the ACI provisions, the general method allows a concrete and steel contribution to the shear resistance and only a steel contribution to the torsional resistance. The general method allows for variable concrete contribution stress depending on numerous factors (such as prestressing, axial force, bending moment, and amount of longitudinal reinforcement).

2.5.2.1 Shear. The shear resistance of a section is given by:

$$V_n = V_c + V_s + V_p \qquad\qquad \text{Eq. 2.33}$$

where V_c represents the concrete contribution provided by the stirrups, V_s is the shear contribution provided by the stirrups, and V_p is a component of effective prestressing force in direction of applied shear force. The concrete contribution to the shear resistance V_c is given as:

$$V_c = 0.083\beta\sqrt{f_c'}b_v d_v \quad (\text{MPa}) \qquad\qquad \text{Eq. 2.34}$$

where β is a factor that depends on the ability of concrete to transmit the tensile stresses; f_c' is the specified compressive strength of concrete at 28 days; b_v is the effective web

width; d_v is the effective shear depth taken as 0.9d; and d= the distance from extreme compression fiber to the centroid of tension reinforcement.

The contribution of vertical stirrups is given by:

$$V_s = \frac{A_v f_{yt} d_v}{s} \cot\theta \qquad \text{Eq. 2.35}$$

where A_v represents the area of the stirrups within a spacing s; S is the spacing of the stirrup measured along the length of beams, f_{yt} is the yield strength of the stirrups; θ is the angle that the principal compressive stresses and strains make with the longitudinal axis of the beam. Diagonal cracks are assumed to be oriented at angle θ.

2.5.2.2 Pure torsion. The AASHTO provisions disregard the concrete contribution to torsional resistance T_n. Based on the hollow tube analogy, the steel contribution T_s to the torsional resistance is given by:

$$T_s = 2A_0 \frac{A_t f_{yt}}{s} \cot\theta \qquad \text{Eq. 2.36}$$

where A_t is the area of one leg of closed torsion reinforcement within a spacing 's', A_0 is the area enclosed by the shear flow path (taken as 0.85 A_{oh}); and A_{oh} is the area enclosed by centerline of outermost closed transverse reinforcement

2.5.2.3 Combined shear and torsion. The parameters required to calculate V_c, V_s, and T_s are β and θ. These factors depend on the level of strain in the section ε_x and on the level of applied shear stress v/f'_c. The level of the longitudinal strain indicator as

conservatively taken at the level of the centroid of the flexural tension reinforcement.
This term is calculated as:

$$\varepsilon_x = \frac{0.5N + 0.5\cot\theta\sqrt{V^2 + \left(\frac{0.9p_hT^2}{2A_0}\right)} + \frac{M}{d_v} - A_{ps}f_{p0}}{E_sA_s + E_pA_{ps}}$$

Eq. 2.37

where A_s is the area of the nonprestressed steel in the section's flexural tension zone; A_{ps}
is the area of presressed steel in the section's flexural tension zone; E_s is the modulus of
elasticity of nonprestressed steel; E_p is the modulus of elasticity of prestressed steel; N
represents the applied axial load; M is the applied bending moment, and F_{po} is average
stress in prestressing steel when stress in surrounding concrete is 0.0; and this later term
can be conservatively taken as the effective prestress.

If the calculated strain is negative (i.e., the section is in compression), the general
method requires that it be multiplied by a factor F_e that accounts for the area and modulus
of elasticity of concrete in compression. This factor is calculated as follows:

$$F_\varepsilon = \frac{E_sA_s + E_pA_{ps}}{E_sA_s + E_pA_{ps} + E_cA_c}$$

Eq. 2.38

Again, the adequacy of the longitudinal reinforcement for the resisting stresses are
given by

$$A_sf_{yl} + A_{ps}f_{ps} \geq \frac{M_u}{\phi d_v} + \frac{0.5N_u}{\phi} + \cot\theta\sqrt{\left(\frac{V_u}{\phi} - 0.5V_s - V_p\right)^2 + \left(\frac{0.45p_hT_u^2}{2A_0}\right)}$$

Eq. 2.39

The shearing stress 'v' due to shear and torsion in hollow sections is given by

$$v = \frac{V_u - \phi V_p}{\phi b_v d_v} + \frac{T_u p_h}{\phi A_{oh}^2} \qquad \text{Eq. 2.40}$$

In solid sections, redistribution of the shearing stress is possible. Hence, the combined shearing stresses are given by:

$$v = \sqrt{\left(\frac{V_u - \phi V_p}{\phi b_v d_v}\right)^2 + \left(\frac{T_u p_h}{\phi A_{oh}^2}\right)^2} \qquad \text{Eq. 2.41}$$

To prevent the over-reinforcement of a section and to ensure yielding of the transverse reinforcement, an upper limit is proposed to normalized shear stress; this limit is represented by

$$\frac{v}{f_c'} \le 0.25 \qquad \text{Eq. 2.42}$$

2.5.3. Comparison of Code Provisions. For torsional design, the ACI and AASHTO code provisions disregard the concrete contribution and rely only on the steel contribution. Torsion reinforcement is required to in addition to the reinforcement required for shear. The angle 'θ' of the compression diagonal is assumed to be 45° for nonprestressed members and as low as 30° for the prestressed concrete members. In many ways, the AASHTO provisions are similar to ACI provisions. However, in the AASHTO provisions the θ is determined based on the longitudinal strain conditions of the section. The AASHTO provisions are based on the variable angle truss model, which

allows variable concrete contribution based on the amount of prestressing, and the longitudinal reinforcement as well as axial load and bending moment. Both the ACI and AASHTO code provisions have been checked for the cases of pure shear, pure torsion, and combined torsion and bending cases. However, for both prestressed and nonprestressed members, they have not been thoroughly checked for combined torsion, bending, and shear (Rahal, 2005). Although the AASHTO provisions are conservative for rectangular sections, their applicability to circular sections of bridge columns is uncertain.

The equations for cracking torque and minimum torque that must be considered in design, and the checks on minimum reinforcement and crack width limitation have not been adequately verified by experimental results. Further, there is some inconsistency for pure torsion and combined torsion and shear. Under pure torsion, the ACI code underestimates the cracking torque by as much as 30% for rectangular sections (Koutchkali and Belarbi, 2001; Ghoneim and MacGregor, 2003). Moreover, the design provisions are based on the assumptions that sections are under-reinforced or balanced. The effect of parameters such as size, reinforcement ratios, and delimits for combined loadings have not yet been established. Also, no analytical models are yet available to predict spalling behavior under combined torsion, bending and shear. Changes to the current specifications can be based only on the inferences from the limited experimental studies on combined loadings. To validate current design provisions for combined bending, shear and torsion, more experimental research should focus on RC columns of different sectional shapes.

2.6. SUMMARY OF REVIEW

This Section has presented the background information on experimental investigations of the behavior of RC columns. In addition, it has surveyed the models available to predict the behavior under bending-shear, pure torsion, and a combination of bending, shear, and torsion. Finally, it has addressed the limitations of various models and it discussed possibilities for further improvement. This review suggests, the following possibilities for further work related to the development of analytical models and code provisions.

2.6.1. Experimental Studies. Experimental results are needed to improve the knowledge of hysteresis characteristics of RC columns with combined loading. The lack of such results imposes difficulties for conducting the nonlinear time history analyses. Also, no dynamic or pseudodynamic test data are currently available to clarify the dynamic behavior of RC columns under combined loadings.

2.6.2. Analytical Models. No analytical models are available to predict the behavior of circular sections under combined loadings. Development of such model has been hindered by (i) a lack of sufficient information on concrete softening due to torsion and on combined loadings including torsion, (ii) the effect of confinement of transverse reinforcement in circular members, and (iii) an improper understanding of effectiveness of concrete cover and spalling mechanisms.

- Constitutive models are essential to describe behavior under combined loadings, knowledge that is also essential for finite element modeling. Simplified models must be developed incorporating the interaction of combined loadings.

- Analytical expressions need to be developed to quantify limit states such as cracking, spalling, residual drift, yielding, and ultimate state under combined loadings.

- Softening of concrete strength in the presence of shear and torsional loads and confinement of concrete due to transverse reinforcement play a major role in determining the ultimate strength of concrete sections under combined loadings. Simplified models must be developed incorporating these effects.

- Simplified plastic-hinge models available to predict the behavior under axial and bending loads are not applicable in the presence of significant torsional loading. The length, location, and distribution of plastic-hinge zone changes depending on the amount of torsional loading.

2.6.3. Code Provisions. AASHTO provisions are conservative for rectangular and square sections; however, their applicability to circular and interlocking sections of bridge columns is uncertain. Unlike rectangular columns, the circular columns have longitudinal reinforcement uniformly distributed along the cross section. Under torsion, rectangular sections are subject to warping but circular sections are not. Given these differences, the failure mode of circular sections under combined loadings will be significantly different from that of rectangular sections. These differences have not been considered in most code provisions.

3. EXPERIMENTAL PROGRAM

3.1. INTRODUCTION

Several parameters influence the inelastic cyclic behavior of an RC bridge column. Among these, spiral reinforcement ratio, column shear demand, axial load ratio, column aspect ratio, and the quantity of longitudinal reinforcement are particularly important. Codes and standards restrict the range of these parameters in modern construction. However, no studies have yet examined the ranges and limitations established for these parameters or their effect on the seismic performance of RC columns under combined loading including torsion. The paucity of experimental data is the main reason for the present inadequate understanding of the behavior of RC columns subjected to combined loading.

Previous research on the seismic behavior of RC columns has focused on uniaxial behavior with some biaxial bending, but has not included a significant torsional component (Yudin, 1962; Collins et al., 1965, Hsu, 1968; Ewida, 1981; Kawashima et al., 1994; Hsu and Wang, 2000; Rahal, 2000). Also, most previous research on biaxial loaded columns has used specimens where the moment is applied using eccentric verical point loads (Wang and Hsu, 1992). These tests are not capable of quantifying the detrimental effect of the induced torsional moment on flexural and axial capacilies. Effect of torsion on behavior of bridge columns has not been investigated with any detail at either small-scale or large-scale level. It is essential to take torsional effects into consideration in seismic design of bridge columns. This Section explains the objectives of the experimental program and describes the test setup designed to apply combined

shear force, flexural, and torsional moment. It also describes the instrumentation used to measure applied loads, strains, and displacements.

3.2. OBJECTIVES

Most of the interaction force diagrams developed to date is based on theoretical derivation with little to no experimental validation. The purpose of this investigation was to clarify the mechanisms of load resistance under combined loading and establish interaction diagrams. The experiments in this study were intended to provide data for calibration of models to predict behavior under combined loading including torsion. In particular they were intended to provide additional information on:

i. Effects of torsional moments on the flexural and shear capacities on the column and impact of torsion on ductility of the column.

ii. Localization of column plastic-hinges under combined loading including torsion. Torsion could shift the location of the plastic-hinge under large rotations.

iii. Proper detailing and plastic-hinges under torsional loadings.

iv. Effect of softening and loss of concrete cover due to torsion combined with shearing forces and thereby reduction in column capacity.

v. Effects of warping and additional bending of diagonal concrete struts in non-circular cross-sections.

vi. Development of reliable torsional hysteresis model for the analysis of RC columns subjected to combined cyclic bending and torsion and other actions.

The above list of issues has not been investigated with any detail at either small-scale or large-scale level. It is essential to take torsional effects into consideration in

seismic design of bridge columns. This work also explored the behavior of columns under combined loading with regard to (i) strength, loading and unloading stiffness degradation, (iii) extent of damage due to diagonal cracking in the orthogonal directions, and (iv) concrete softening, (v) plastic-hinge formations, and (vi) spalling and its significance for combined loading. The major variables were the ratio of torsional moment-to-bending moment (T/M), bending moment-to-shear or aspect ratio (H/D) and the change in spiral reinforcement ratio. The analytical investigation presented in Section 6 has as one of its goals to validate the existing and develop new design interaction equations. The interaction surface shown in Figure 3.1 was used as a guide for selection of test specimens for the experimental investigation. The points on the interaction surface relate to the loading combination. Key points on the curve were tested and linked to the analytical models presented in Section 6.

Various points for the test specimens were considered as the test parameter. Points "a" and "b" in Figure 3.1 lie on the biaxial failure line. Point "a" represents a shear dominated failure in a column with a small aspect ratio and point "b" represents flexure failure. Two points along the shear-torsion line are indicated by a moderate level of torsion at a *T/V* ratio of 125 mm and a high level of torsion at a *T/V* ratio of 500 mm. Several tests on reduced scale RC girders without axial loads have been carried out along this interaction curve (Rahal and Collins, 1995; Belarbi and Greene, 2009a). Line c-d maintains a constant *T/V* of 500 mm and line e-f maintains a constant *T/V* ratio of 125 mm. The amount of applied torsion starts at zero and increases along lines a-e-c and b-f-d. A column failing at point "e" would exhibit a failure due to low bending and torsional moment and high shear, whereas failure at point "d" would be due to high

bending and torsional moments and low shear. Similarly, failure at point "c" would be due to high shear and torsion, and low bending moment, and at point "r' there would be low shear and torsion, and a significant bending moment. The four points, c, d, e, and f, represent four reasonable combinations of bending moment, shear force, and torsional moment in combination of two levels of axial loads.

The relationship between moment and shear force were varied by changing the height of the cantilever columns and yet keeping the moment capacity constant. To limit the scope of work, the bending moment-to-shear ratio, torsion-to-bending moment ratio and spiral reinforcement ratio were chosen as the study parameters.
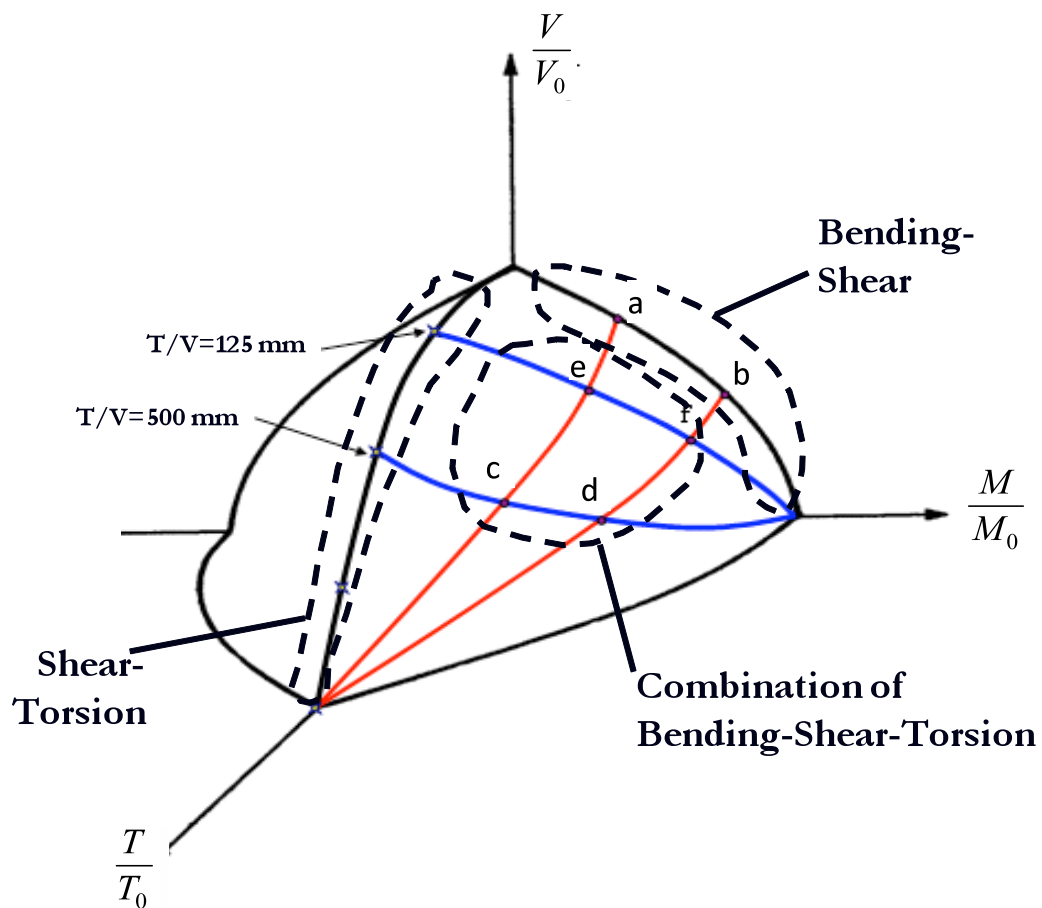
Figure 3.1 Schematic of Normalized Moment Shear and Torsion Interaction Diagram

3.3. TEST MATRIX

The experimental program was developed to establish the interaction diagrams between shear force, flexural, and torsional moments for a given cross section with specific longitudinal and spiral reinforcement ratios. To obtain more information about this behavior, this work tested 14 RC columns subjected to combined bending, torsion, and shear. This experimental program was designed to investigate the influence of several parameters on the response and failure of modern bridge columns. Due to the limitations of testing equipment and cost considerations, few tests are usually carried out at full scale. The specimens used in these tests were constructed at a reduced scale. Typically, bridge columns vary in diameter from 1.2 m to 2.4 m. The diameter of the columns used here was 610 mm (24 in.) representing a scaling factor 0.5. All of fourteen specimens, each with a circular cross section, were tested under various loading conditions, specifically, pure torsion, flexure, and combined flexure, shear, and torsion. The specimens were named according to the test parameter, spiral ratio and aspect ratio. For example, the specimen H/D(6)-T/M(0.0)/0.73% indicates, it had an aspect ratio (H/D) of six with a spiral reinforcement ratio of 0.73% and tested at a torsion-to-bending moment (T/M) ratio of '0.0'. All the columns had a constant axial load of 592 kN except for H/D(3)-T/M(0.2)/1.32%-A2, which had an axial load of 890 kN. The test setup applied cyclic loads on the loading block of each column to simulate the combined loading including torsional moment. The columns were heavily instrumented to measure their local and global behavior and their internal strain distribution. Fourteen specimens were tested in two series, one with a height of 3.66 m and other with a height of 1.83 m. The use of two series was intended to reduce the M/VD or H/D ratio from 6 to 3. Among

the columns in first series, the spiral reinforcement ratio was increased from 0.73% for the first six columns to 1.32% for the remaining two columns. For columns in the second series, the spiral reinforcement ratio was kept constant at 1.32%. The nominal strength of concrete for all the columns was 34 MPa; however, the concrete strength varied by approximately 5 MPa on the day of testing. All columns had a diameter of 610 mm. Details of all the specimens are provided in Table 3.1.

Table 3.1 Test Matrix

Specimen Name	ρ_l (%)	ρ_t (%)	Ht. (meter)	Scale	Spiral Design For Torsion	H/D	Axial (kN)
H/D(6)-T/M(0.0)/0.73%	2.1	0.73	3.67	1:2	Low	6	592
H/D(6)-T/M(∞)/0.73% w/H	2.1	0.73	3.67	1:2	Low	6	592
H/D(6)-T/M(0.1)/0.73%	2.1	0.73	3.67	1:2	Low	6	592
H/D(6)-T/M(0.2)/0.73%	2.1	0.73	3.67	1:2	Low	6	592
H/D(6)-T/M(0.4)/0.73%	2.1	0.73	3.67	1:2	Low	6	592
H/D(6)-T/M(∞)/0.73%	2.1	0.73	3.67	1:2	Low	6	592
H/D(6)-T/M(0.2)/1.32%	2.1	1.32	3.67	1:2	Moderate	6	592
H/D(6)-T/M(0.4)/1.32%	2.1	1.32	3.67	1:2	Moderate	6	592
H/D(3)-T/M(0.0)/1.32%	2.1	1.32	1.83	1:2	Moderate	3	592
H/D(3)-T/M(0.2)/1.32%	2.1	1.32	1.83	1:2	Moderate	3	592
H/D(3)-T/M(0.4)/1.32%	2.1	1.32	1.83	1:2	Moderate	3	592
H/D(3)-T/M(0.6)/1.01%	2.1	1.01	1.83	1:2	Moderate	3	592
H/D(3)-T/M(∞)/1.32%	2.1	1.32	1.83	1:2	Moderate	3	592
H/D(3)-T/M(0.2)/ 1.32%- A2	2.1	1.32	1.83	1:2	Moderate	3	890

3.3.1. Design Requirements. Reinforced concrete bridge systems subject to seismic loading are expected to sustain inelastic action. Therefore, the seismic design of

bridge columns requires the formation of plastic-hinges at column ends. However, the joint regions in the foundation beam and top cap beam are designed to limit the inelastic response, forcing the formation of a plastic-hinge. Brittle response mechanisms, including inelastic response in shear and bond, should be repressed; and the joint region should remain essentially elastic. The column and joint regions were designed in accordance with the Caltrans Bridge Design Specification (Caltrans, 2004). The joint region studied here was designed to meet the Caltrans standard requirements and to limit inelastic response, although inelastic strain in the embedded longitudinal reinforcement was expected. The longitudinal bars were embedded approximately 52 diameters into the joint and the embedment length was approximately 25% greater than by Caltrans specifications. The response of the specimen footing was not expected to model an actual footing in the field. The footings in the test specimens were intended to remain elastic under the demand that results from full inelastic action of the column. The maximum allowable tensile strain demands in the main longitudinal reinforcement of the footing were limited to 75% of the yield strain.

3.3.2. Geometry and Reinforcement. The specimens were constructed at one half scale of the typical column sizes ragning from 1.2 to 1.5 m. The longotudonal and spiral reinforcement bar sizes were not scaled and were selected as used in the practical construction. However, the longitudinal and spiral reinforcement ratios were maintained as observed in the typical bridge construction. Column and joint details of the test specimens are shown in the Figure 3.2. The column diameter was 610 mm modeling the prototype column of 1.22 m diameter. The columns were reinforced longitudinally with No. 8 bars (25.4 mm) and spaced evenly around the column. The longitudinal

reinforcement was embedded to a joint depth of 560 mm approximately to 22 bar diameters. The bars terminated with a 90º hook that extended 18 bar diameters parallel to the bottom of the footing. The column spiral reinforcement ratio was 0.73%. The spiral was 10 mm in diameter and spaced at 70 mm on center. Each of the columns with a spiral reinforcement ratio of 1.32% had a spiral of diameter 12.5mm spaced at 70 mm on center. The spiral reinforcement was continuous throughout the column height and joint depth. The longitudinal and spiral reinforcement ratios were 2.1% and 0.73%, respectively. The volumetric reinforcement ratio of longitudinal and spiral reinforcement is calculated as shown in Eq. 3.1 and Eq. 3.2, respectively. To permit evaluation of the effectiveness of the spiral reinforcement ratio under combined torsion and bending moments, the ratio was increased from 0.73% to 1.32% by increasing the spiral size from 9.5 mm (0.37 in.) to 12.7 mm (0.5 in.) in diameter while keeping the same spacing. The volumetric spiral reinforcement ratio (ρ_t) was chosen to satisfy the confinement criteria of CALTRANS (2004) according to Eq. 3.3. This requirement also satisfies the minimum required spiral reinforcement ratio according to AASHTO (1998) and ACI (2008).

$$\rho_l = \frac{100A_l}{A_g}$$

Eq. 3.1

$$\rho_t = 100\frac{\pi d_c A_{sp}}{sA_c}$$

Eq. 3.2

$$\rho_{t,\min} = 0.45(\frac{A_g}{A_c} - 1)\frac{f_c'}{f_y}\left(0.5 + \frac{1.25P}{f_c'A_g}\right)$$

Eq. 3.3

Figure 3.2 Geometry and Reinforcement

In the above expressions, ρ_t is the spiral reinforcement ratio, ρ_l is the longitudinal reinforcement ratio, $\rho_{t,\min}$ is the minimum required spiral reinforcement ratio, P is the applied axial load, f_y is the specified yield strength of the spiral reinforcement, f_c' is the specified compressive strength of concrete, A_l is the total area of longitudinal bars, A_g is the gross cross sectional area, A_c is the confined area enclosed by the centerline of the

spiral reinforcement, d_c is the diameter of the confined core of the concrete section measured with respect to the centerline of the spiral reinforcement, s is the spacing of the transverse reinforcement, and A_{sp} is the cross sectional area of the spiral reinforcement.

3.4. TEST SETUP

The test setup was designed such that various amounts of bending and torsion moments can be applied cyclically. Also, the amount of axial compression could be varied by up to 890 kN. The test setup is shown in Figure 3.3. The flexural and torsional moments were applied to the column by means of two servo-controlled hydraulic actuators connected to the loading frame, which was attached in turn to the column specimen. The base of the column was anchored to a strong floor by means of Dywidag bars, then prestressed.

3.4.1. Applying Axial Load. A hydraulic jack on top of the column was used to apply the axial load. The hydraulic jack transferred the load to the column via seven unbonded high-strength prestressing steel strands running through a duct in the center of the column and anchored to a plate underneath the test specimen. Typically, the axial load due to the superstructure dead weight to bridge columns varies between 5% and 10% of the concrete capacity of the columns. A target 7% of the concrete capacity (7%f'$_c$ Ag) was applied to simulate the dead load on the column in a bridge situation [Caltrans, 2002].
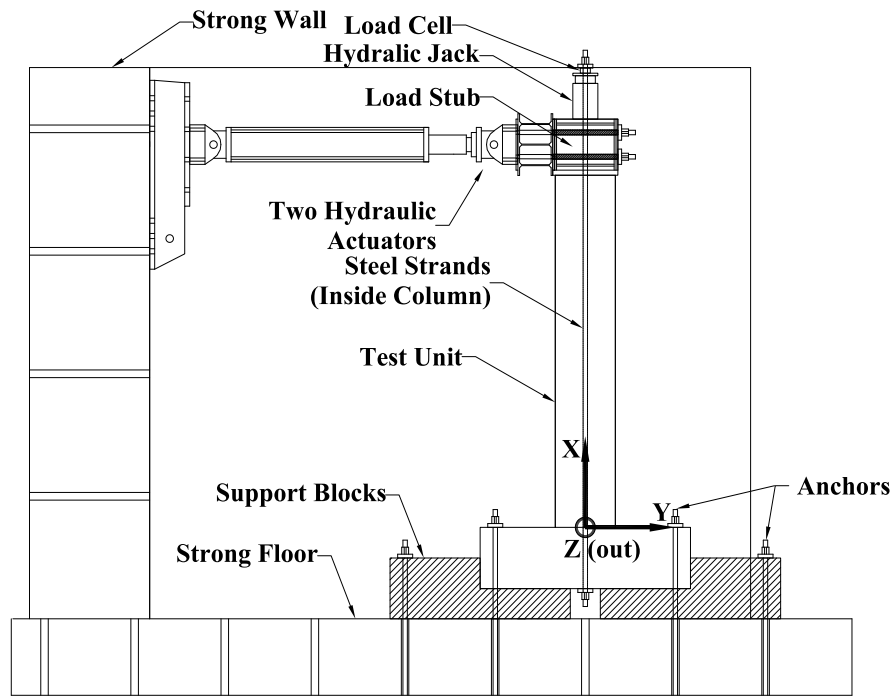
(a) SIDE ELEVATION
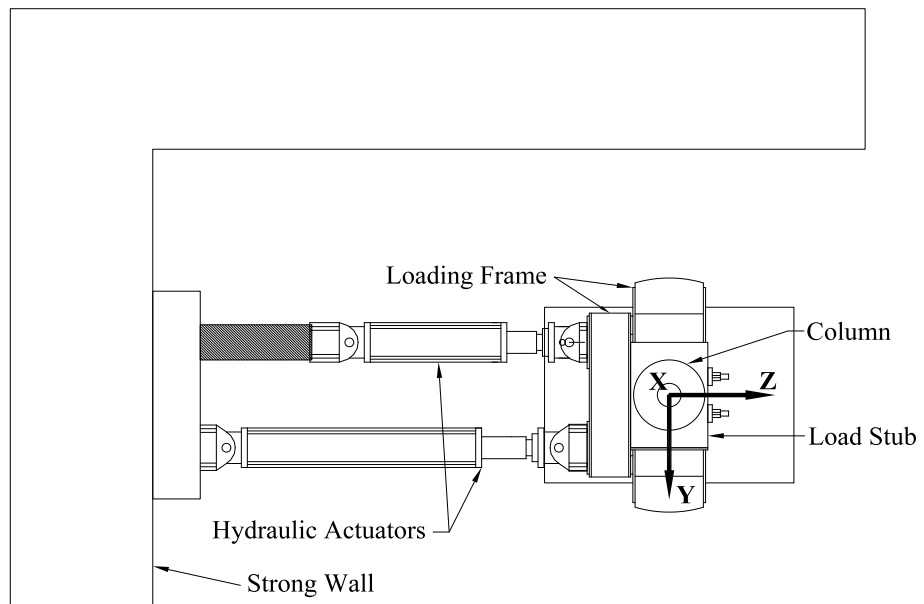
(b) PLAN

Figure 3.3 Test Setup

The unbonded external prestressing in the axial load system should be treated as an internal redundant force that makes a system internally indeterminate. An accurate analysis for this system, which is different from the uniform compressive stresses applied to the column by the hydraulic jack, must consider this internal indeterminate system. However, relatively broader and thicker steel plates were used to distribute loads from the jack to the loading block. Similarly, a thicker and broader steel plate was used to distribute the load beneath the foundation, resulting in a more uniform distribution of compressive stresses in the test portion of the column member (i.e., from top of foundation to the center of the loading block). Moreover, the strands ran through a duct that was closer to the neutral axis under flexure. In torsion, the outer portion of the concrete column is more effective, and the strands for prestressing do not influence behavior. In terms of overall behavior, therefore, the structural differences between unbonded prestressing strands and a hydraulic jack are not significant. Moreover, the p-delta effect is eliminated, thus simplifying the analysis.

3.4.2. Applying Shear Force, Flexural, and Torsional Moment. Shear force, flexural, and torsional moments were applied to each column member using two servo-controlled hydraulic actuators. Both actuators were manufacture by MTS corporation, are in the 243.45T series and in the243.7T series. The 243.45T series actuator had a total stroke of 508 mm and was capable of 650 kN in compression and 445 kN in tension at a maximum fluid pressure of 20.7 MPa. The 243.7T series actuator had a total stroke of 712 mm and was capable of 1460 kN in compression and 961 kN in tension at a maximum fluid pressure of 20.7 MPa. The actuators were controlled using a FlexTest GT digital controller made by MTS. The controller is capable of real-time closed-loop

control and load protocol function generation. The loadings were imposed in load control mode until the first yielding of the spiral or longitudinal bar. Thereafter, the loadings were imposed with a pattern of three cycles at each displacement level to provide information related to strength and stiffness degradation characteristics. The actuators used to apply the torsional and bending moment had built in linear variable displacement transformers (LVDTs) to measure the piston displacements and load cells to measure the axial forces produced by the actuator. The twist calculated from the displacements measured by the LVDTs in the actuators could not be used as an accurate measure of the twist in the specimen for several reasons: (i) Due to connections with the loading frame, the twist from the actuator displacement will not be the same as applied at the center of the column, and (ii) as the stiffness of the actuators was different and resulted in different piston movements. As shown in the Figure 3.4, one end of each actuators was connected to the steel referred to as loading frame, which was clamped to the specimen, and the other end of each actuator was connected to a large steel plate post-tensioned to the strong wall. Cyclic uniaxial flexure, pure torsion, and combined bending, shear, and torsion were generated by controlling the servo-controlled hydraulic actuators shown in Figure 3.4. Cyclic uniaxial flexural loading was created by applying equal forces with the two actuators. Pure torsion was created by applying equal but opposite forces with the two actuators. Combined cyclic flexural and torsional moments, and shear forces were imposed by applying different forces with each actuator depending on the test parameters. The ratio of T/M was controlled by maintaining the ratio of the forces in the two actuators in the load control mode until the first yielding of the transverse or longitudinal reinforcement.

Figure 3.4 Photo of the Test Setup for Column under Flexure

In the displacement control mode, the displacements of the actuators were adjusted to maintain the desired T/M ratio. The actuators applied the torsional moment by applying displacements in the opposite directions. When the actuators applied the displacements of unequal magnitude, torsional and bending moment were applied to the column. The actuator forces measured are directly used in the calculation of torsional and bending moments. Eq. 3.4 and Eq. 3.5 give the torsional moment (T) and bending moment (M) based on the actuator forces. The terms P_1 and P_2 represent the forces in the west and east actuators, respectively, and d is the distance between the vertical centerlines of the actuators. This distance was 0.914 m. The height h of the column was 3.66 m for columns with an H/D of 6; whereas it was 1.83 m for the columns with a low H/D of 3.

$$T = \left(P_1 - P_2\right) * \frac{d}{2} \qquad\qquad \text{Eq. 3.4}$$

$$M = \left(P_1 + P_2\right) * H \qquad\qquad \text{Eq. 3.5}$$

3.5. INSTRUMENTATION

The specimens were instrumented in order to measure their global and local behavior and their internal strain distribution. Twist and horizontal displacement were measured at multiple locations along the height of the column specimens using a system of string transducers. The instrument pairs were located at five points along the height of the column, as shown in Figure 3.5. Horizontal displacement was measured by averaging the displacements measured by the string transducers. Twist was measured by taking difference between the string transducer measurements and divided by the distance between transducers. Instrumentation also included a system of LVDT rosettes to calculate the curvature, shear, and principal strains. The LVDT rosettes were placed at the bottom of the column where the combined effects of torsion and bending moments would be greatest. To evaluate the internal strain distribution, the average strain distribution in the expected plastic-hinge zone was estimated using a system of LVDT rosettes (Figure 3.6).
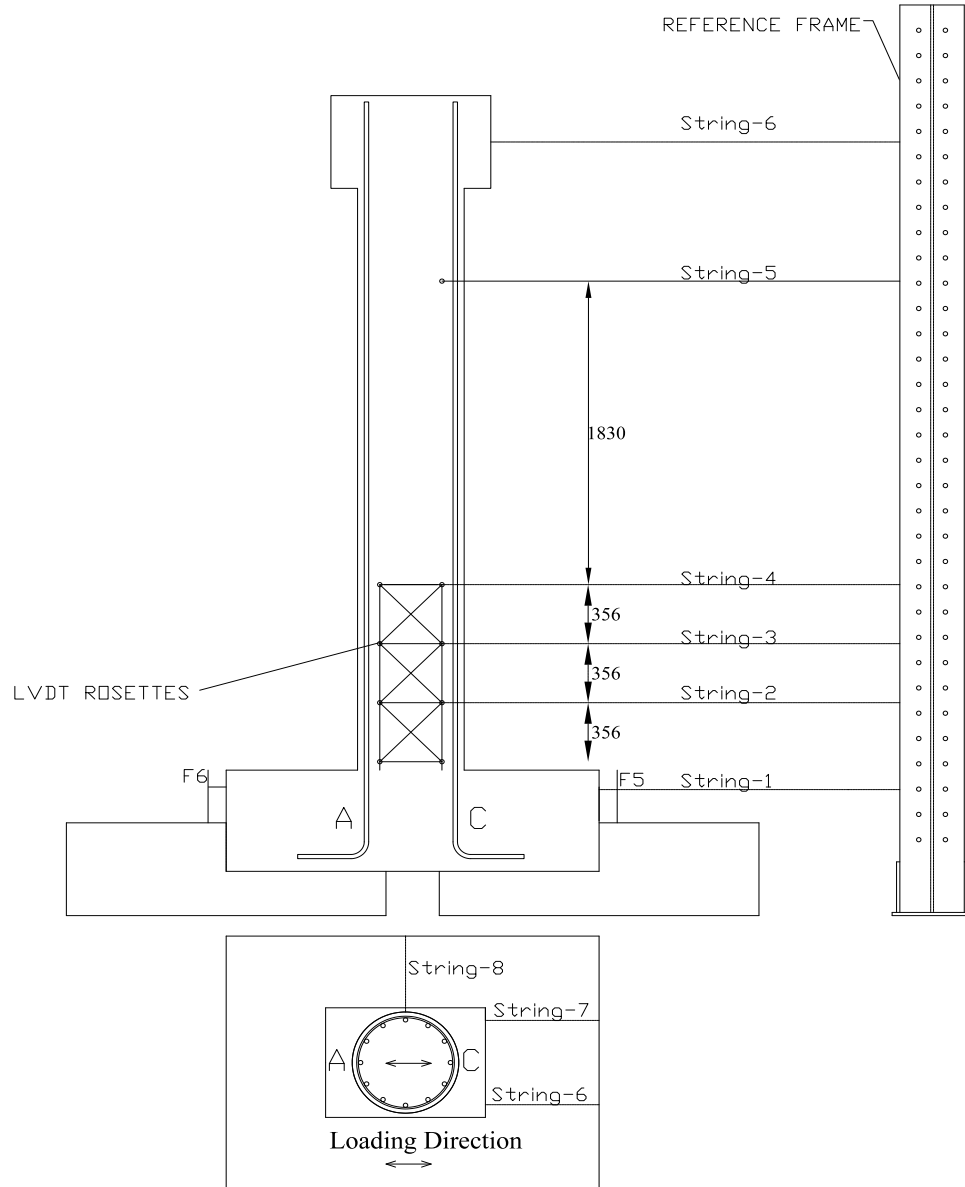
Figure 3.5 Locations of String Transducers

Displacement and twist were calculated from the string transducer displacements as follows:

$$\Delta_{avg} = \left[\frac{(\Delta_1 + \Delta_2)}{2} \right]$$

Eq. 3.6

$$\theta_{twist} = \arctan\left[\frac{\left(\Delta_1 - \Delta_2\right)}{d}\right]$$

Eq. 3.7

where Δ_1, Δ_2 are the displacements measured by the string transducers. In pure torsion, they would be nearly equal and opposite in signs. In bending and shear tests, they would be nearly equal, with the same sign.

3.5.1. Average Strain Measurement. The average strain across the cracks in the expected plastic-hinge region was measured by a system of LVDT rosettes. Each LVDT rosette was comprised of several instruments that measured the displacement across several cracks. Some of the LVDTs in the rosette could measure a displacement of up to +/- 12.7 mm; others could measure the displacements up to +/- 25.4 mm. The instruments used in this investigation were fitted to an aluminum tubing system, which was connected to two threaded bars cast into each specimen.

Three rosette systems on the western face used two pairs of instruments to measure the distributed strain in the horizontal, vertical, and diagonal directions. The instruments were connected such that they formed a square. The gauge length of the vertical and horizontal instruments is 356 mm, and the gauge length of the diagonal instrument is 503mm. Figure 3.6 shows the system of LVDT rosettes. Six distance readings were taken for this subgrid. The longitudinal strains are the average of readings 3 and 4, and the transverse strain is the average of the readings 1 and 2. One of the diagonal readings from 5 or 6 completed the Mohr's circle of strains, and other was redundant to check the consistency of measurements. The average strain measured using the rosettes were very sensitive to the number of cracks occurring over the gage length;

therefore, the values cannot be considered accurate and they are understood here to be approximate. Three LVDT rosettes were employed during testing at the expected damage locations to measure the curvature and principal strains. In each rosette, the strains ε_x (along the x-axis), ε_y (along the y-axis), ε_{45} (at axis inclined 45° to x directions) were recorded by LVDTs. Using the measured strains, the engineering shear strain, ε_{xy}, and the principal strains, ε_1 and ε_2, were calculated. The strains measured by the rosettes stretched across several cracks, therefore, the displacement measured by the rosettes divided by the gauge length was assumed to be the average strain in the concrete and reinforcement.

Typical Sub-Grid
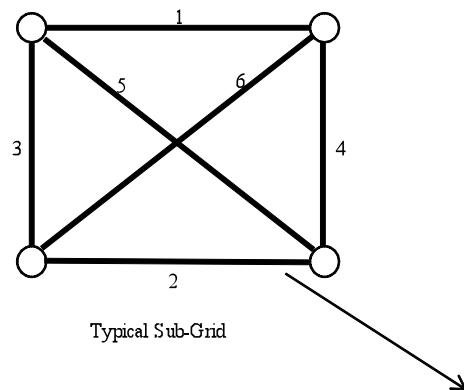
(All dimensions in millimeter)

Figure 3.6 System of LVDT Rosette

3.5.2. Reinforcement Strain. Strains in the spiral and longitudinal reinforcement were measured using electric resistance foil strain gages. The gages were made of Constantin foil with 120 ohm resistance, and had a gauge length of 6.4 mm. About 70 gages were installed on all the specimens. The strain gages applied on the longitudinal reinforcement are shown in Figure 3.7. The typical locations of strains gages on the longitudinal and transverse reinforcement are shown in Figures 3.8, 3.9 and 3.10 respectively [of flexure, pure torsion and for combined shear force, flexural and torsion specimens].
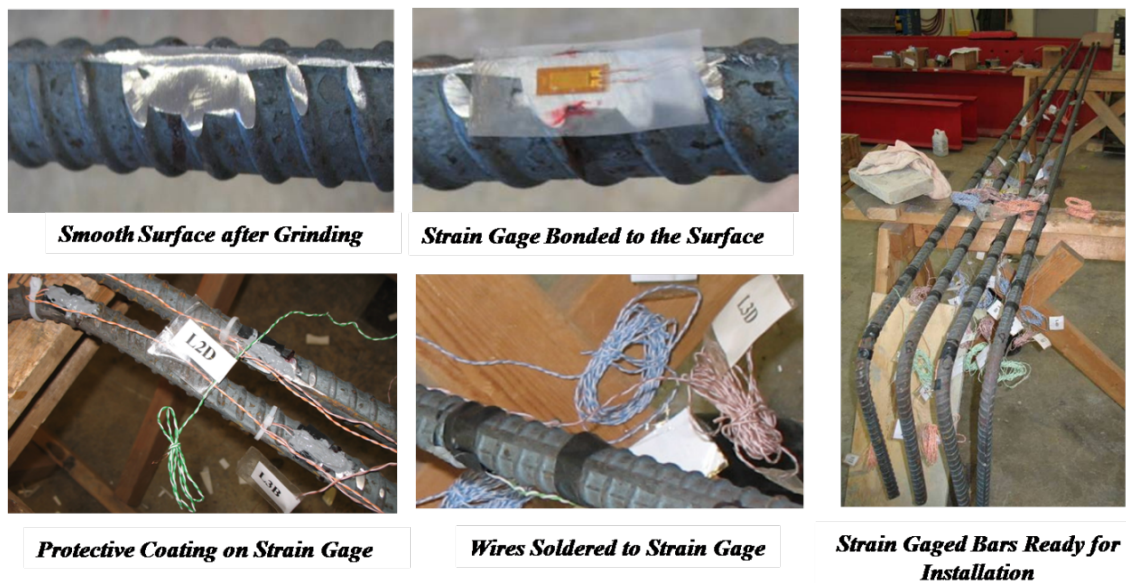
Figure 3.7 Applying Strain Gages on Longitudinal Reinforcement

Gage No.	Gage Profile			
11				
10	A		C	
9				
8	A		C	
7	A		C	
6	A		C	
5	A		C	
4	A	B	C	D
3	A	B	C	D
2	A	B	C	D
1	A		C	

24 Longitudinal Gages

Gage No.	Gage Profile			
11				
10		B		D
9		B		D
8	A	B	C	D
7	A	B	C	D
6	A	B	C	D
5	A	B	C	D
4	A	B	C	D
3	A	B	C	D
2				
1				

28 Transverse Gages
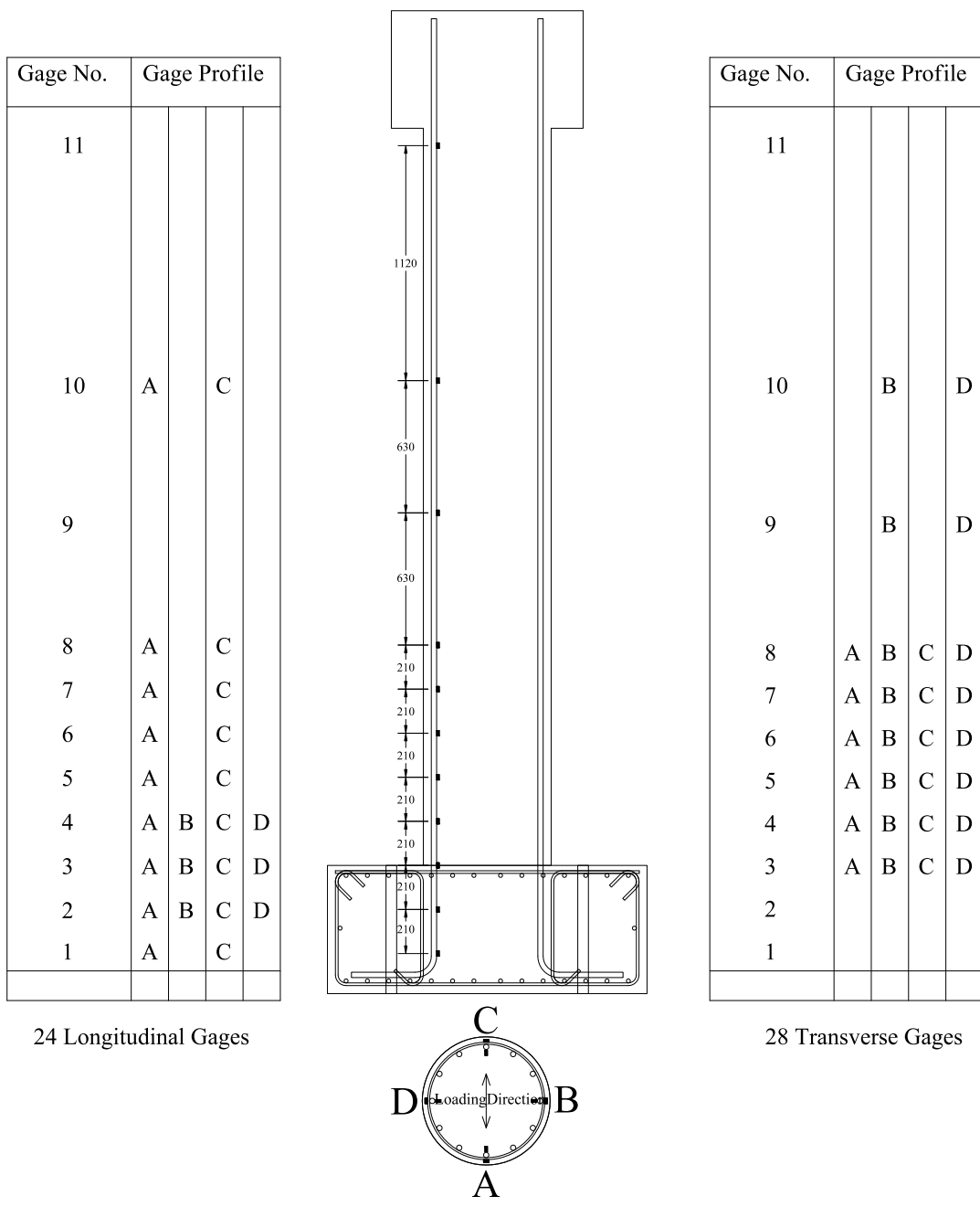
Figure 3.8 Typical Strain Gage Locations on Flexure Specimen

(All dimensions in millimeter)

Gage No.	Gage Profile			
11				
10				
9				
8	A		C	
7				
6	A		C	
5	A		C	
4				
3	A		C	
2				
1				

1120

630

630

210
210
210
210
210
210
210

8 Longitudinal Gages

Gage No.	Gage Profile			
11				
10				
9				
8	A		C	
7				
6	A		C	
5	A		C	
4				
3	A		C	
2				
1				

8 Transverse Gages

C

D — Loading Direction — B

A
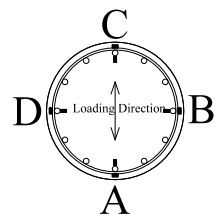
(All dimensions in millimeter)

Figure 3.9 Typical Strain Gage Locations on Pure Torsion Specimen

Gage No.	Gage Profile							
11	A		B		C			
10	A		B		C			
9	A		B		C			
8	A		B		C			
7	A		B		C			
6	A		B		C			
5	A	AB	B	BC	C	CD	D	DA
4	A		B		C		D	
3	A	AB	B	BC	C	CD	D	DA
2	A		B		C		D	
1	A				C			

40 Longitudinal Gages

Gage No.	Gage Profile			
11		B		D
10		B		D
9		B		D
8	A	B	C	D
7	A	B	C	D
6	A	B	C	D
5	A	B	C	D
4	A	B	C	D
3	A	B	C	D
2				
1				

30 Transverse Gages

(All dimensions in millimeter)
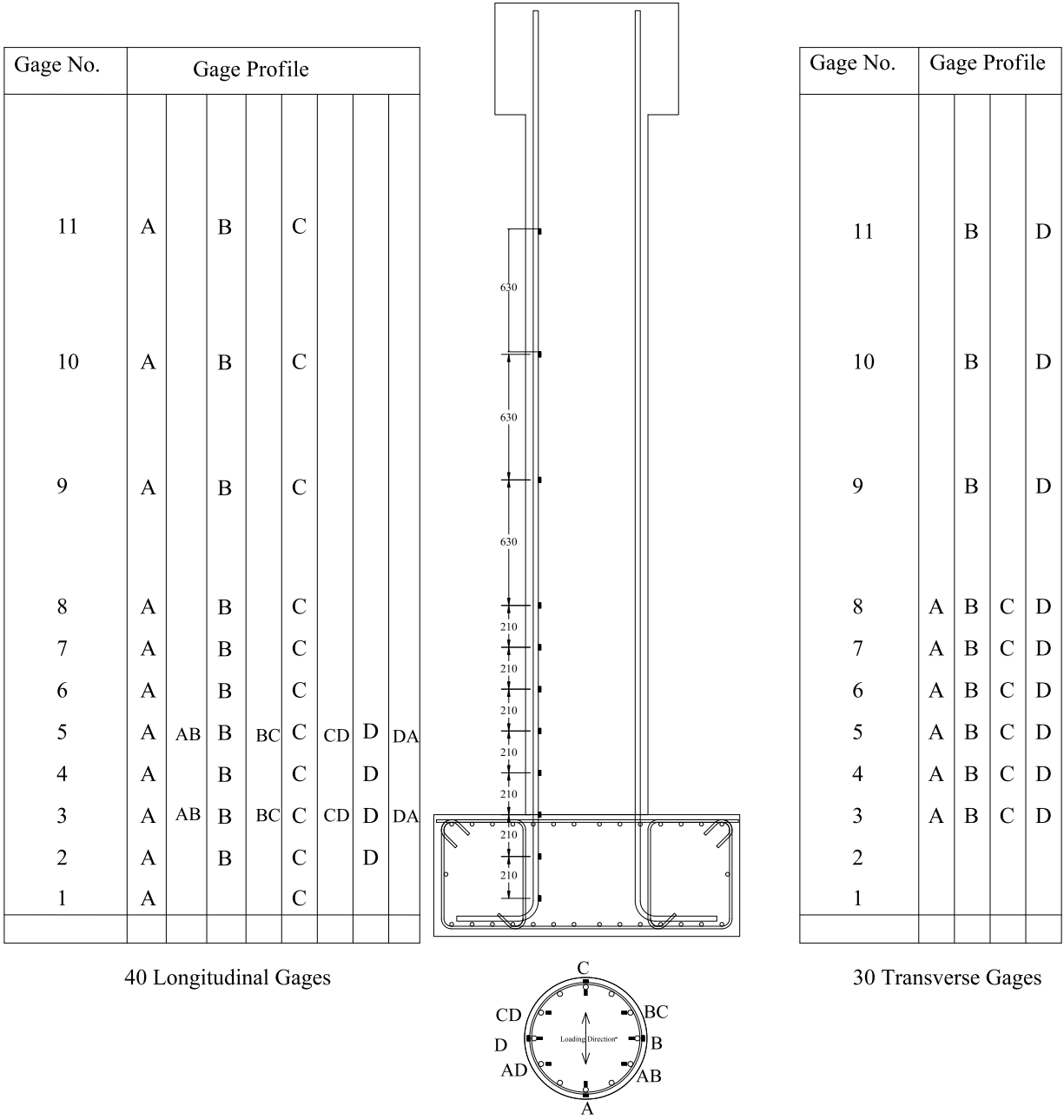
Figure 3.10 Typical Strain Gage Locations on Combined Shear Force, Flexural and Torsion Specimens

3.5.3. Load Cell. The axial load was measured by placing a tension load cell between the jack and the top chucks. The capacity of the load cell was 890 kN.

3.5.4. Data Acquisition (DAQ). The data measured by all of the electronic instruments were collected by a data acquisition (DAQ) system consisting of two conditioner cabinets A and B , each with a total of 64 channels used to condition and amplify the signals. The conditioned voltage signals then sent to DAQ, converted to a digital signal, then scaled and recorded by a personal computer. The 64 channels on the conditioner cabinets A and B were divided into channel groups for receiving the signal from load cells, alternating current (AC) devices, direct current (DC), and strain gages. Some of the LVDTs were AC devices, and the string transducers and other LVDTs were DC devices. The data recording cabinet contained analog-to-digital boards to convert the voltage into a digital signal. Once converted, the digital signal was sent to a Dell precision 340 personal computer with 1.80 GHz and 80 GB hard disk capacity. Two software programs, Measurement and Automation Explorer (MAX) and LABVIEW version 7.1, converted, scaled and recorded data. In MAX, the data signal was assigned to a scale file, which was used to convert the signal from voltage measurements into load, displacement, and strain data for the respective instruments and strain gages. The LABVIEW was used to scan and record the data. The scale files in MAX were created by calibrating the instruments and strain gages. The load cells were calibrated with a micrometer fitted on an LVDT calibration block, and the strain gages were calibrated with a strain gage calibration box.

```
                    ┌─────────────────────────────┐          ┌──────────────┐
                 ┌─►│  Combining Raw Data Files   │       ┌─►│  Comparison  │
                 │  └─────────────────────────────┘       │  │    Files     │
┌───────────┐    │  ┌─────────────────────────────┐       │  └──────────────┘
│   Data    │───►├─►│  Reducing the Combined File │       │
│ Reduction │    │  └─────────────────────────────┘       │
└───────────┘    │  ┌─────────────────────────────┐       │
                 └─►│ Zero Correction for Instruments │───┘
                    └─────────────────────────────┘
```

(a) Data Reduction

```
                          ┌──────────────┐           ┌──────────────────────┐
                       ┌─►│  Preliminary │        ┌─►│   Load/Displacement  │
                       │  │   Analysis   │        │  └──────────────────────┘
                       │  └──────────────┘        │  ┌──────────────────────┐
┌──────────┐           │                          ├─►│  Strain Gages/ LVDT  │
│ Analysis │───────────┤                          │  │      Rosettes        │
└──────────┘           │                          │  └──────────────────────┘
                       │                          │  ┌──────────────────────┐
                       │                          └─►│ Energy Dissipation and│
                       │                             │  Equivalent Damping   │
                       │                             │        ratios         │
                       │                             └──────────────────────┘
                       │  ┌──────────────┐           ┌──────────────────────┐
                       └─►│   Detailed   │        ┌─►│ Comparison of Hysteresis│
                          │   Analysis   │        │  └──────────────────────┘
                          └──────────────┘        │  ┌──────────────────────┐
                                                  ├─►│  Decoupling Strain   │
                                                  │  │ components from strain│
                                                  │  │  Gages/ LVDT Rosettes │
                                                  │  └──────────────────────┘
                                                  │  ┌──────────────────────┐
                                                  └─►│   Establishment of   │
                                                     │ Interaction equations/│
                                                     │ Design guidelines/ simple│
                                                     │        models         │
                                                     └──────────────────────┘
```

(b) Analysis Scheme

Figure 3.11 Framework for Data Analysis

Data was read from the channels every five seconds and appended to the data file. The data was recorded in a text file with each channel occupying one column. All computations were performed using Microsoft Excel. Although the data obtained was of

high quality, further correction and manipulation were needed. Correcting procedures included filtering the data to remove the noise, i.e., the excess data collected during the pauses in the testing. Each tests involved many channels to capture the complete behavior of RC columns. Data was collected at a frequency of 0.2 Hz. Column testing normally lasted a day or two. Tests results for fourteen columns involves significant amount of data. The data was reduced and analyzed by comparing results for each column based on various parameters, evaluating the existing design practice and developing new guidelines. The schematic plan for data reduction and analysis is shown in Figure 3.11.

3.6. MATERIALS

3.6.1. Concrete. The material properties specifications met the requirements for ASTM designations A 615, Grade 60, or A 706. The concrete mix was designed to model a full-scale mix to reproduce the specified compressive strength, fracture energy, and modulus of elasticity. It was supplied by Rolla Ready Mix, a local ready-mix plant. A 34 MPa design mix with a maximum aggregate size of 25 mm was requested. Table 3.2 shows the batch weights provided for each specimen. The high-range water reducer (super-plasticizer) was added to the mix at Missouri S&T, agitated according to the manufacture's requirements, then placed on the forms. The water was added only when required to improve the workability of the concrete.

Table 3.2 Concrete Material Quantities

Material	Quantity
Cement	1366 kg
Fine Aggregate	3415 kg
Coarse Aggregate	4412 kg
Water	550 L
Air entrainment	0.6 L
High-Range Water Reducer	4.3 L

The compressive strength of the concrete was obtained from concrete cylinders with 152 mm in diameter and 305 mm high; the cylinders were cast and cured with the specimens. They were capped with Rediron 9000 sulfur mortar capping compound manufactured by Global Gilson and tested to failure using a concrete cylinder testing machine with a 2700 kN capacity manufactured by Forney. Cylinders were tested on 7th day, the 28th day and the day of testing of columns. The concrete cylinder specimens were made according to Specification ASTM C 31 (2003). The cylinders were capped according to ASTM C 617 (1998), then tested according to ASTM C 39 (2005).

3.6.2 Reinforcement. The reinforcement for this investigation was supplied by Ambassador Steel Corporation, Kansas City. The steel coupons of the reinforcement were tested under uniaxial tension using a Tinius-Olsen universal testing machine to determine the modulus of elasticity; the yield stress was measured using the 0.20% offset method, and the peak stress was determined as described in ASTM A 370 (2005). Elongation over a 200 mm gage length was measured using an extensometer until the coupons exhibited strain hardening, at which point the extensometer was removed. The

measured material properties are given in Table 3.3. The stress-strain curves of the longitudinal and transverse reinforcement are shown in Figure 3.12.

Table 3.3 Reinforcement Material Properties

Measured Property	Nominal Reinforcement Size (Columns with H/D=6)			Nominal Reinforcement Size (Columns with H/D=3)		
	#3 (Spiral)	#4 (Spiral)	#8 (Longitudinal Reinforcement)	#4 (Spiral)	#6	#8 (Longitudinal Reinforcement)
Modulus of Elasticity	226 GPa	219 GPa	206 GPa	226 GPa	219 GPa	206 GPa
Yield Stress (0.20% Offset Method)	525 MPa	541 MPa	490 MPa	525 MPa	580 MPa	546 MPa
Peak Stress	675 MPa	693 MPa	702 MPa	675 MPa	590 MPa	702 MPa
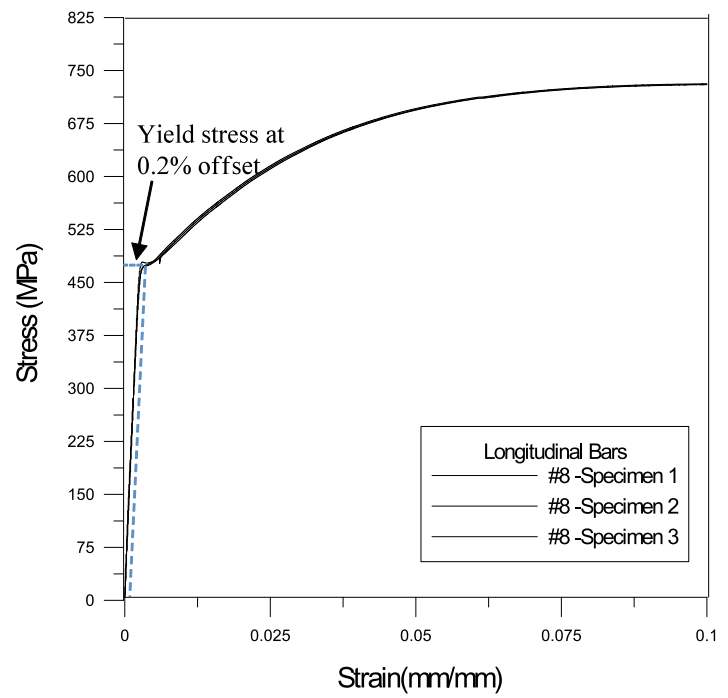
(a)
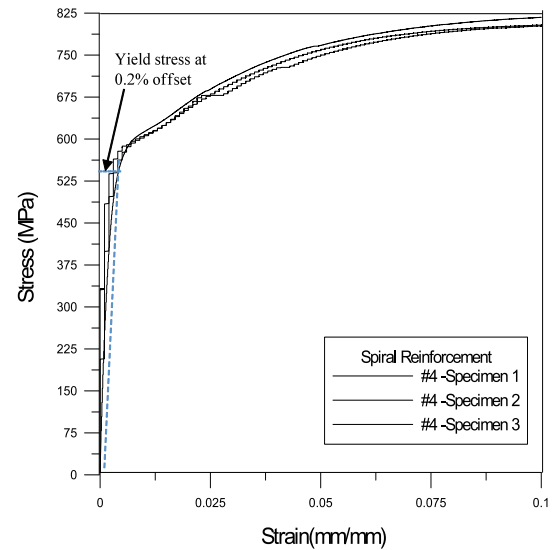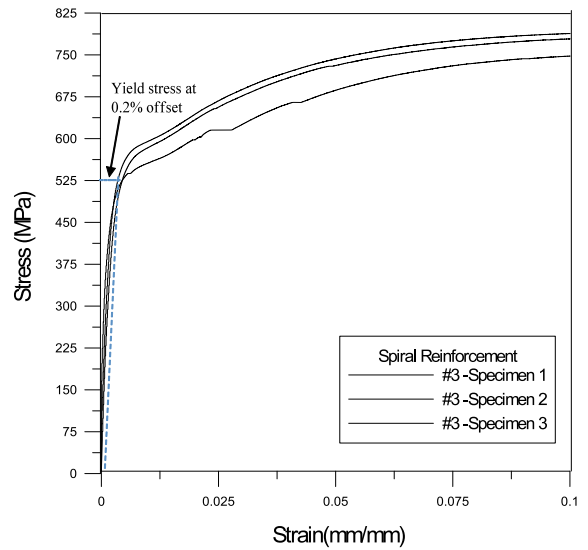
(b)

Figure 3.12 Stress Strain Curves for Steel Reinforcement

3.7. COLUMN MANUFACTURING

The column specimens were fabricated at the High Bay Structures laboratory at Missouri S&T. Figure 3.13 shows the assembly of reinforcement cages. The locations of strain gages were marked in longitudinal bars and ground before use to make a steel cage. Out of twelve longitudinal bars, eight were used to assemble the cage. Once the cage was assembled, the remaining four longitudinal bars with strain gages were installed. The assembled reinforcement cage was anchored in the foundation mat as shown in Figure 3.14. Once the reinforcement cage was anchored and centered in the bottom foundation mat of the reinforcement, the top foundation reinforcement and shear legs were installed. Figure 3.15 shows the finished foundation reinforcement. The reinforcement for the loading block was assembled with proper shear legs connecting the stirrups, as shown in Figure 3.16. The PVC tubes were also installed to connect the loading frame to the specimen and transverse guide frames for lateral prestressing. The first six columns in the test matrix were cast in two stages. First, the foundation concrete was poured. Once the concrete set, the column concrete was poured. All other columns were then poured at once. The formwork of foundation for those columns included a top cover to resist the upward pressure created when the column concrete was poured as shown in Figure 3.17, Figure 3.18. The finished column specimen is ready for installing the axial strands, as shown in Figure 3.19. Auxiliary specimens for concrete compression tests, splitting tension test and modulus of rupture tests were fabricated during the concrete pour (Figure 3.20).

Figure 3.13 Fabrication of Column Cage

Figure 3.14 Assembly of Bottom Mat of Reinforcement for Foundation

Figure 3.15 Finished Foundation Reinforcement with Column Cage

Figure 3.16 Formwork and PVC Layout on Loading Block
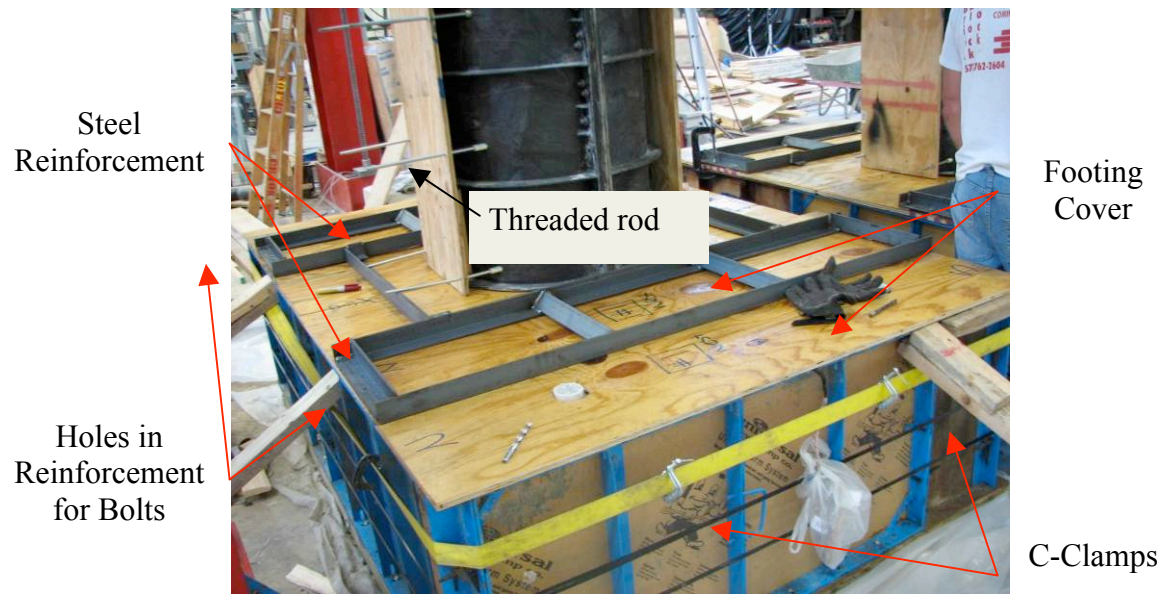
Figure 3.17 Formwork for Foundation with Top Cover

Pouring Footing and Vibrating

Placing of Footing Cover

Securing of Cover & Reinforcement

Bucket on Lift

Dumping Concrete into Column

Screening of Loading Block
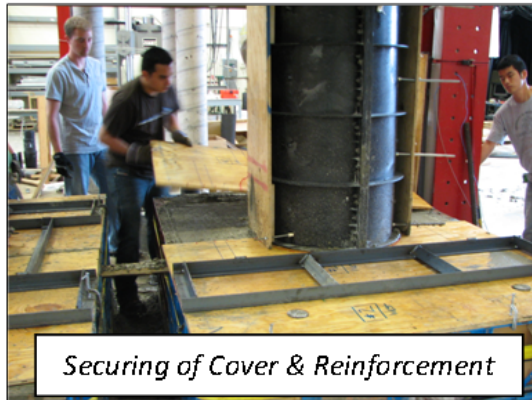
Figure 3.18 Concrete Pour for Foundation and Column

Figure 3.19 Fabricated Column at Temporary Location for Inserting Axial Tendons

Figure 3.20 Auxiliary Specimens for Concrete Material Testing

3.8. LOADING PROTOCOL

3.8.1. Columns under Flexure. Test for columns tested under flexure were conducted in load control mode until first yielding of the longitudinal bars. The load was applied in load control mode at intervals of 25%, 50%, 75%, and 100% of the predicted

yielding force, corresponding to the yielding of the first longitudinal bar (F_y). Figure 3.21 shows the loading protocol for the column under flexure. After the first yielding of the longitudinal bar, test was conduted at displacement control with three cycles of loading at each displacement ductility level (μ_Δ). Three cycles were applied to assess the stiffness and strength degradation characteristics and energy dissipation capacity. Displacement ductility (μ_Δ) is the ratio of displacement at any instant during loading to the corresponding displacement at first yielding of the longitudinal bar. Hence, the horizontal displacement corresponding to yielding of the first longitudinal reinforcement is defined as displacement ductility (μ_Δ) of one. The stroke capcity of the actuators was not adequate to complete the testing. Hence, the loads were applied only on the positive directions from dutility level of eight (Figure 3.21).
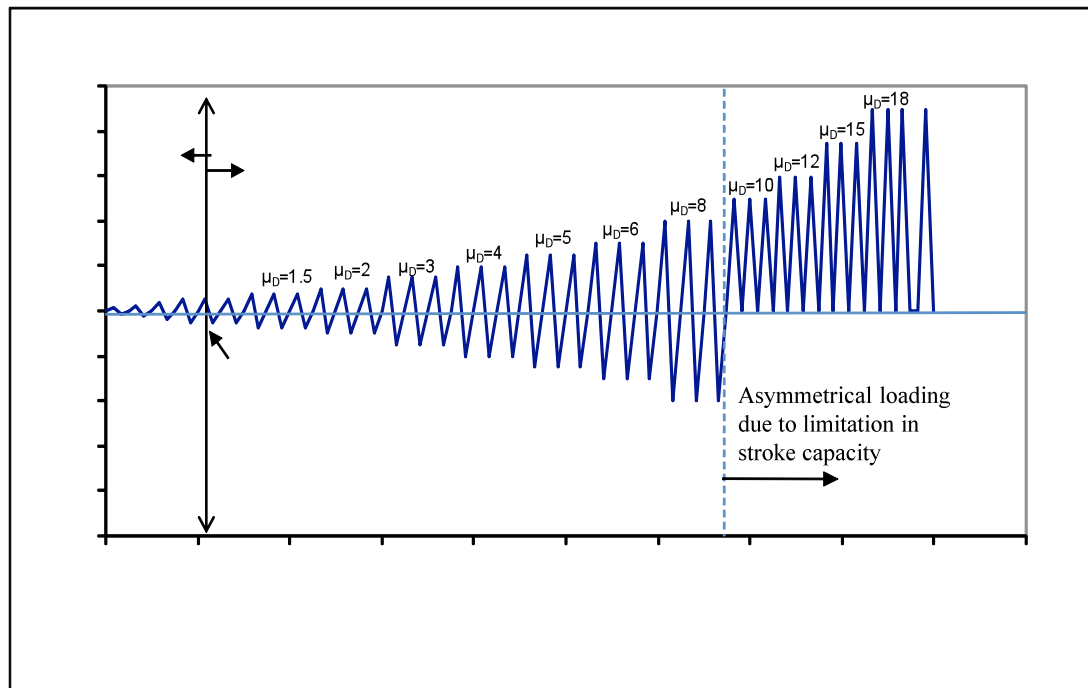
Figure 3.21 Loading Protocol for Column under Flexure

3.8.2. Columns under Pure Torsion. The column under pure torsion was loaded

under load control at intervals of 25%, 50%, 75%, and 100% of the estimated yielding of the first spiral (T_y). The loading protocol followed for the column under pure torsion is shown in Figure 3.22. After the first yielding of the spiral reinforcement, test was conduted at displacement control with three cycles of loading at each displacement ductility level (μ_Δ). Three cycles were applied to assess the stiffness and strength degradation characteristics and energy dissipation capacity. Twist ductility (μ_Δ) is the ratio of twist at any instant to the corresponding twist at first yielding of spiral reinforcement. Hence, the twist corresponded to yielding torque, which in turn corresponded to the first yielding of spiral reinforcement, is defined as a twist ductility (μ_θ) of one. The stroke capcity of the actuators was not adequate to complete the testing. Hence, the loads were applied only on the negative directions from twist dutility level of 13 (Figure 3.22).
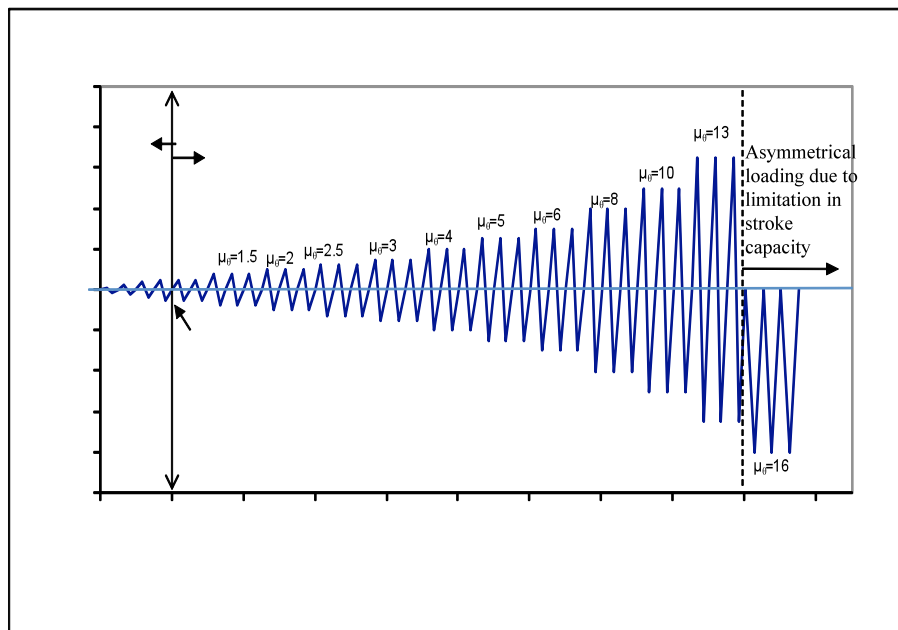
Figure 3.22 Loading Protocol for Column under Pure Torsion

3.8.3. Columns under Combined Shear Force, Bending, and Torsional

Moments. Three loading cycles were performed at each ductility level to assess the degradation of column strength and stiffness. The loadings were applied along Direction A-C following the sign convention shown in Figure 3.2. The loadings along Directions A-C and C-A were defined as positive (unlocking) and negative (locking) cycles, respectively. After the load control stage, the results were analyzed, and the yield displacement and rotation were computed. In the displacement control mode, three cycles were applied for each ductility level until the failure of the column. The three cycles were intended to calculate the flexural and torsional energy dissipation of the columns under combined bending and torsion. The T/M ratio for each cycle was maintained according to the calculated piston movements during the testing. There were some difficulties in maintaining the desired T/M ratios during loading and unloading cycles, and there was some difference in the stiffness of the actuator systems. However, the ratios were within the acceptable range. The loading protocol is shown in Figure 3.23.

```
┌─────────────┐
│    Start    │
└─────────────┘
        │
        ▼
┌───────────────────────────────────────────┐
│ Test under load control until the first    │
│ yielding of longitudinal bar (Fy) or       │
│ spiral yielding (Ty) whichever occurs first │
└───────────────────────────────────────────┘
        │
        ▼
┌───────────────────────────────┐      ┌──────────────────────┐
│ Compute displacement (Dy) and │      │ Define calculated    │
│ twist (θ) at first yielding of │─────▶│ displacement and     │
│ longitudinal bars using        │      │ twist as ductility   │
│ actuator piston movements      │      │ one (μ =1)           │
└───────────────────────────────┘      └──────────────────────┘
        │
        ▼
┌─────────────────┐      ┌──────────────────────────────┐
│ Calculate next  │      │ Calculate actuator piston    │
│ ductility level │─────▶│ movements using the          │
│ (μ)             │      │ calculated ductility (μ)     │
└─────────────────┘      │ based on the geometry of     │
                         │ actuator system              │
                         └──────────────────────────────┘
                                    │
                                    ▼
┌──────────────────────────┐   ┌──────────────────────────────┐
│ Program the calculated   │   │ Calculate piston movements to │
│ piston movements in two  │◀──│ maintain desired loading ratio│
│ steps to the MTS         │   │ by increasing or decreasing   │
│ controller software      │   │ displacement or twist by      │
└──────────────────────────┘   │ 2.5% or 5%                    │
        │                      └──────────────────────────────┘
        ▼
┌──────────────────┐      ◇─────────────◇      ┌────────────┐
│ Monitor desired  │     ╱   Within the  ╲     │ Pause the  │
│ T/M ratio at the │────▶   Acceptable    ─────▶│ cycle      │
│ end of the first │     ╲   range?      ╱     └────────────┘
│ step             │      ◇─────────────◇
└──────────────────┘             │
                                 ▼
                   ┌──────────────────────────┐
                   │ Continue cycle with next │
                   │ set of piston movements  │
                   └──────────────────────────┘
```

Figure 3.23 Loading Protocol for Columns under Combined Bending, Shear, and Torsion

3.9. CONCLUDING REMARKS

Column testing was intended to explore the interaction of combined shear force, flexural and torsional moments at constant axial compression. The columns were instrumented to measure the local and global behavior and strain distribution. Two servo-controlled hydraulic actuators were used to apply the cyclic flexural and torsional moments. A complete description of specimen fabrication, test setup, and loading protocol was provided. Test results for all columns are explained in the next Section.

4. EXPERIMENTAL RESULTS AND DISCUSSION

4.1. INTRODUCTION

This Section provides the results of experiments on the interaction of bending, shear, and torsional loads and their effects on the behavior of circular RC columns. The discussion focuses on: i) the lateral load-displacement and torsional moment-twist curves, ii) the effects of full-reversal cyclic loads on loading and unloading stiffnesses, iii) flexural and torsional energy dissipation, iv) concrete cover spalling, and v) damage progression. It examines the effects of spiral reinforcement and aspect ratio on the failure modes and energy dissipation characteristics of the columns under combined loading. It also addresses the variation in longitudinal and transverse strains, as well as strength and stiffness degradation characteristics at various T/M and M/V or H/D ratios. Finally, this section presents interaction diagrams between torsional and bending moments and discusses their significance.

4.2. OVERVIEW OF EXPERIMENTAL OBSERVATIONS

Observations of test columns indicate that the damage sequence varied from one column to another. This section provides a general description of damage progression by describing each category of damage. The sequence of damage varied slightly, however, different depending on the amount of applied torsion.

1. <u>Flexure cracking</u>: Flexural cracks formed prior to shear cracking on columns under bending and shear and combined bending, shear, and torsional loads. The spacing of

the newly formed cracks decreased at higher displacements and stabilized after yielding of longitudinal bar, leading to localized spalling.

2. Shear cracking: Shear cracks formed prior to flexural cracking under pure torsion and after flexural cracking under combined bending and torsion. The spacing of shear cracks decreased with increasing displacement/twist demands under combined bending, shear, and torsion.

3. First yielding of longitudinal reinforcement: Yielding of the extreme longitudinal bar was noticeable in the lateral displacement response under bending and shear and under combined bending, shear, and torsion loads. Yielding of longitudinal reinforcement was detected using the strain gage readings.

4. First yielding of spiral reinforcement: Yielding of the spiral reinforcement was noticeable in the torsional moment-twist response under pure torsion and combined bending, shear, and torsion. This yielding was detected by closely monitoring the strain gages on the spiral reinforcement during testing and then analyzing the data in detail.

5. Concrete cover spalling: For flexure-dominated columns, spalling started at the bottom of the column, where the bending moment was greatest above the column-footing interface. For columns under pure torsion, spalling started in the middle of the column and grew towards top and bottom surfaces with an increase in the twist and T/M levels. In general, with an increase in the T/M ratio, the spalling zone increased from the bottom portion of the column. The mechanism of concrete cover spalling was different for columns under pure flexure and for those under combined flexure and torsion.

6. <u>Complete concrete cover spalling and exposure of spiral and longitudinal steel reinforcement:</u> Complete loss of the concrete cover exposed the spirals and longitudinal steel, eliminating lateral pressure from concrete cover and facilitating the easy buckling of longitudinal steel.

7. <u>Longitudinal reinforcement buckling and spiral fracture:</u> At higher levels of displacement and twist ductility, the buckling of longitudinal bars was visually evident. In all the columns under combined bending, shear, and torsion, the longitudinal bar buckled over more than one spiral spacing.

8. <u>Spiral reinforcement fracture:</u> In flexure-dominated columns, due to longitudinal reinforcement buckling, fracturing of spiral reinforcement within the buckled length of longitudinal reinforcement was predominant. The lateral stiffness decreased as a result of spiral fracture, which permitted the other longitudinal bars to buckle over a longer length.

9. <u>Longitudinal reinforcement fracture:</u> Fracture of the longitudinal reinforcement occurred after significant buckling. Typically, fracture of one or more longitudinal reinforcement bars resulted in significant strength and stiffness degradation which in turn to overall column failure.

4.3. FLEXURAL DISPLACEMENT AND TORSIONAL TWIST DUCTILITY

Flexural and twist deformation along the length of a column under combined bending, shear, and torsion are shown in Figure 4.1. The flexural displacement distribution is essentially linear until yielding of the longitudinal bars on the tension side; thereafter, it becomes nonlinear. The yielding of longitudinal reinforcement and the

subsequent crushing of the concrete cover results in the formation of a flexural plastic-hinge. Well confined columns tested under flexure (single curvature) typically form a plastic-hinge zone in the bottom portion where the bending moment is greatest, as shown in Figure 4.1a. The twist distribution of columns tested under pure torsion is essentially linear before shear cracking, becoming nonlinear thereafter, as shown in Figure 4.1b.

Displacement Profile (Elevation View)　　　　　Twist Profile (about the longitdunal axis)

Displacement measurement (Plan View)　　　Twist measurement (Plan View)

`　　　　(a) Bending-Shear　　　　　　　　　(b) Pure Torsion
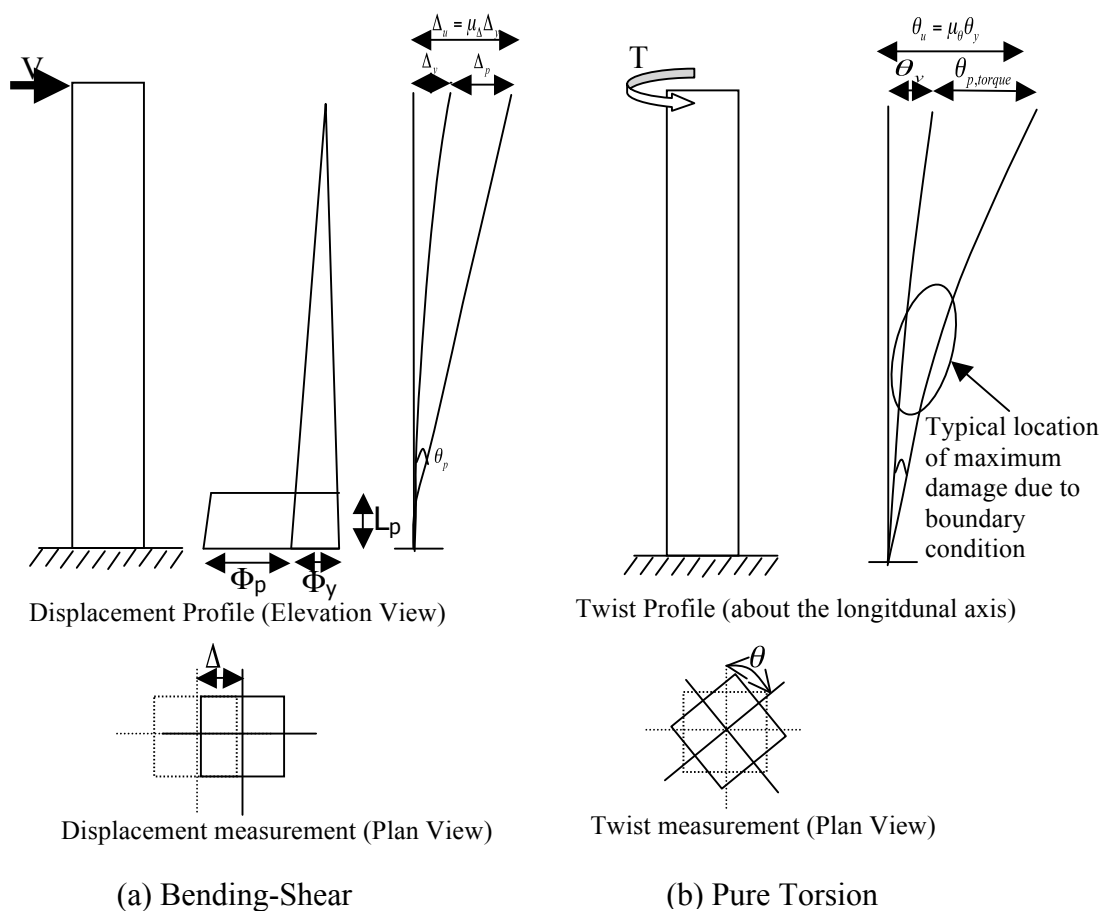
Figure 4.1 Displacements/Twist Distribution along the Length of Column

A structural system is said to be ductile if it is capable of undergoing substantial inelastic deformations without loss of strength. Under bending-shear loading, flexural displacement ductility can be derived using the moment curvature relationship and the

assumed plastic-hinge length. The total flexural displacement of the column under flexure can be expressed as the sum of yield displacement and plastic displacement:

$$\Delta_t = \Delta_y + \Delta_p = (\phi_u - \phi_y)l_p(L - 0.5l_p)$$
Eq. 4.1

where Δ_t is the total displacement, Δ_y is the yielding displacement, l_p is the length of the plastic-hinge, Φ_u is the curvature at ultimate moment, and Φ_y is the curvature at yield moment. The displacement ductility can be expressed in terms of curvature ductility:

$$\mu_\Delta = 1 + 3(\mu_\phi - 1)\frac{l_p}{L}(1 - 0.5\frac{l_p}{L})$$
Eq. 4.2

where μ_Δ is the displacement ductility and μ_Φ is the curvature ductility.

However, under combined bending, shear, and torsional loads the columns undergo not only lateral displacement but also twist. Therefore, since Equations 4.1 and 4.2 were developed based on bending-shear tests, they are not applicable to columns under combined loadings including torsion.

Similar to flexural ductility, twist ductility under torsion can be defined as the ratio of twist to the corresponding twist at the yielding of the spiral:

$$\mu_\theta = \frac{\theta}{\theta_y}$$
Eq. 4.3

where θ is the twist at the top of the column after the yielding of the spiral, θ_y is the yielding twist at the top of the column when spirals reach the yielding strain, and μ_θ is the twist ductility.

Very few studies have examined the behavior of RC columns under combined loadings, and the limited tests on combined loadings pose difficulties in establishing the relationship between curvature and twist ductility. Further, the estimation of flexural displacement using Equations 4.1 and 4.2 depends on the accuracy of the plastic-hinge length calculations. The interaction between flexural displacement and torsional twist is complex and little understood due to the paucity of test data. The damage zone on columns under combined loadings is also complex, affecting either a portion of the column or its whole length.

4.4. TEST RESULTS AND OBSERVED BEHAVIOR

The test results focuses on the overall lateral load-displacement and torsional moment-twist hysteresis and envelope curves, and damage progression of the specimens.

4.4.1. Columns under Flexure. Two specimens one with an aspect ratio of 6 and the other with 3 were tested under flexure and the results presented in the following sections.

4.4.1.1 Column H/D(6)-*T/M* (0.0)-0.73%. This column was tested under flexure with no torsion. Figure 4.2 shows the flexural hysteresis. After cyclical loading to 50% of F_y, the column tested under bending and shear exhibited flexural cracks on the bottom on sides A and C at a displacement of 7.37 mm. The cracks were observed up to a height of 457.2 mm. The crack spacing was approximately 228 mm on the face C. They were also evenly spaced on the negative cycle on the face 'A'. During the successive cycles of 0.75 F_y and 1.00 F_y, the cracks were primarily oriented in a horizontal direction. The crack width remained less than 1.5 mm up to cycle 1.00 F_y, which corresponded to

ductility level one. Narrow diagonal cracks formed at a displacement ductility level of two. The shear crack then started extended slightly. At ductility four, cracking zone extended up to a height of 2900 mm on the faces A and D. The concrete cover started spalling at a drift of about 3.2%, corresponding to a ductility level of 4.5 and displacement of 117 mm. The height of spalling also increased with an increase in the displacement ductility level after cumulative cycles of loading. At a displacement ductility level of five, the spalling began in the base of the footing. The push and pull cycles in both positive and negative directions were carried out until displacement ductility level of six due to the limitation of stroke length in one of the actuators. After that point, push and pull cycles were carried out only in positive direction until a ductility level of eight. The deformed configuration of the specimen at displacement ductility level of 12 is shown in Figure 4.3.

Failure of the specimen began with the formation of a flexural plastic-hinge at the base of the column, followed by core degradation, and finally by the buckling of longitudinal bars on the compression side at a displacement of 460 mm and a ductility level of 18. The progression of damage is shown in Figure 4.4. The flexural resistance was maintained at more or less constant levels from displacement of 110 mm to one of 460 mm, with a nearly constant bending strength of 850 kN-m. During the last cycle of loading, a longitudinal bar started buckling during unloading. The yielding zone of the longitudinal bars was about 610 mm from the base of the column. Longitudinal bars on Sides A and C both reached the yield strain at the predicted ductility level of one. The spirals remained elastic up to a ductility level of six, after which they yielded. Soon after

cracking and spalling at the location of the gages on the spiral, the gages were damaged
and data could no longer be collected.
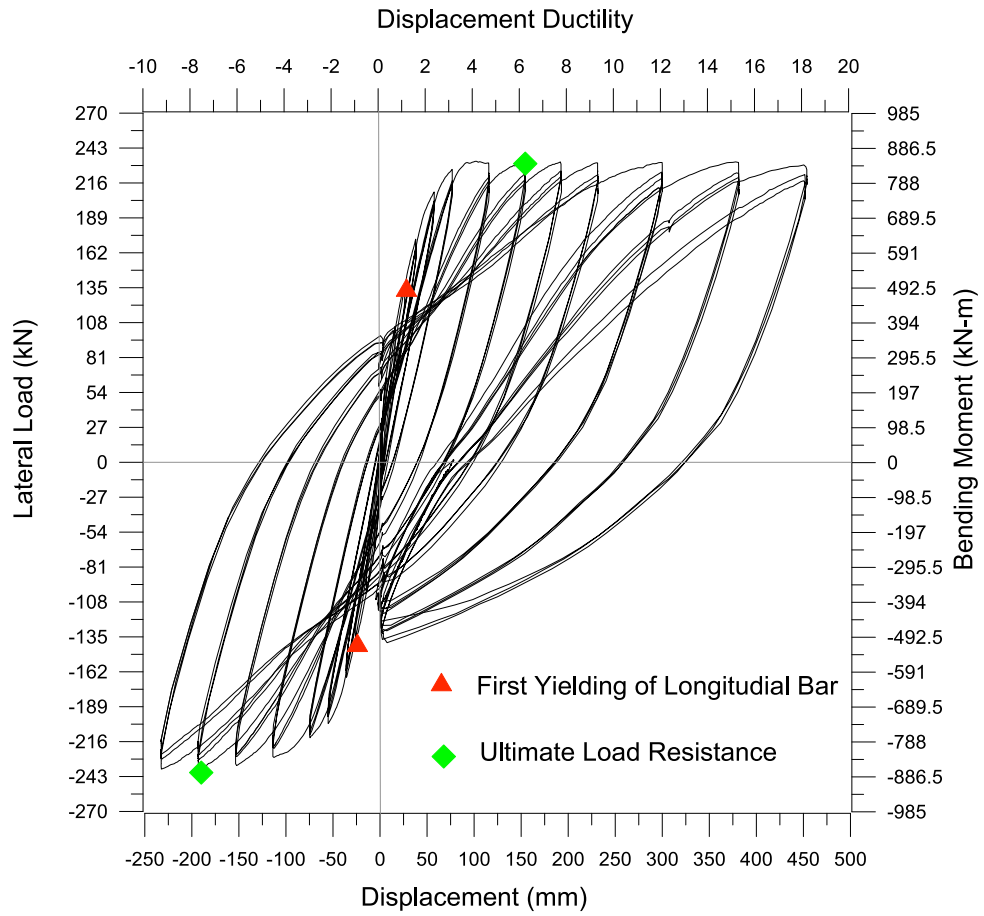
Figure 4.2 Flexural Hysteresis
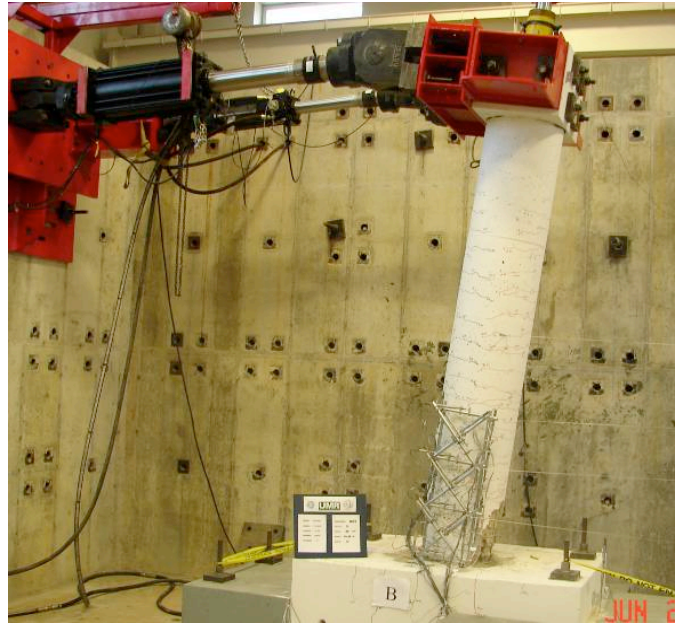
Figure 4.3 Lateral Displacement at Ductility 12

Longitudinal Yielding   Ultimate Load   Final Failure

Figure 4.4 Damage to Column H/D(6)-*T/M* (0.0)-0.73% under Flexure

4.4.1.2 Column H/D(3)-*T/M* (0.0)-1.32%.   This column was tested with a smaller H/D ratio of three. It exhibited initial flexural cracks on sides A and C at maximum moment location after cyclically loading to 50% of the force F_y corresponding

to longitudinal bar yielding. These cracks continued to grow, and new cracks appeared on both sides of the column at the higher level of ductility. The flexural resistance was constant between 1% and 4.1% drift with a flexural strength corresponding to a lateral load of 500 kN, as shown in Figure 4.5. The corresponding flexural strength was 900 kN-m indicating that due to a reduction in aspect ratio from six to three, there is a marginal increase in bending strength due to the effect of footing confinement and a subsequent increase in shear strength. The concrete cover started spalling at a drift of about 1.3% (Figure 4.5). Failure of the specimen began with the formation of a flexural plastic-hinge at the base of the column, followed by core degradation, and finally by the buckling of longitudinal bars on the compression side at a drift of about 5.1%. During the last cycle of displacement ductility 17, the longitudinal bars started buckling in the compression side. The yielding zone of the longitudinal bars was about 460 mm from the base of the column. Longitudinal reinforcement on sides A and C both reached the yield strain at the predicted ductility level of one. The spirals remained elastic throughout the loading history up to failure. As observed in the column with a H/D ratio of six, soon after cracking and spalling at the location of the spiral gages, the gages were damaged and no further data could be collected. Though the column was tested at a lower H/D ratio of 3, the failure was dominated mainly by flexure due to the relatively low longitudinal ratio of the column and increased confinement from spiral reinforcement due to a higher spiral ratio of 1.32%. Thus, the increase in spiral ratio may have helped to change the failure mode from brittle shear to ductile flexural failure as a result of the increased level of shear resulting from a reduction in the shear span ratio. The progress of the failure is shown Figure 4.6.
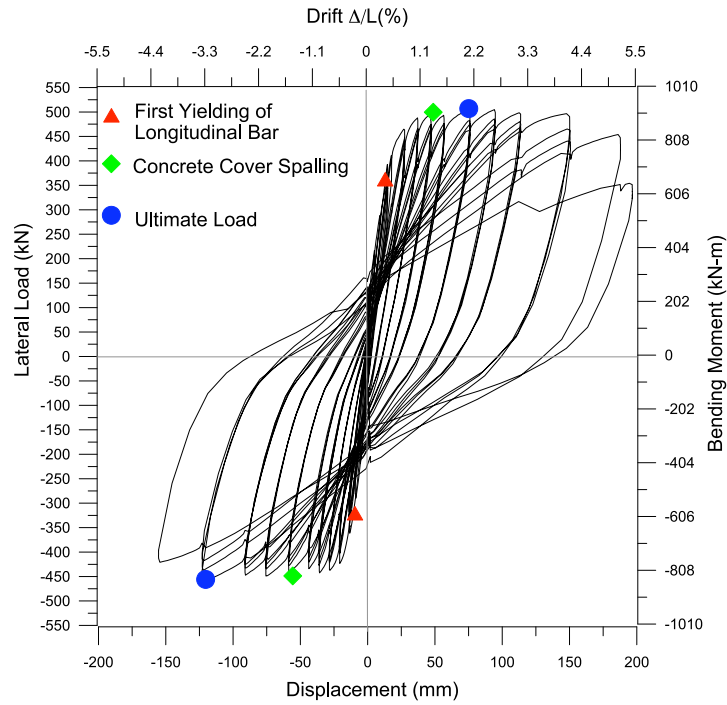
Figure 4.5 Flexural Hysteresis of Column H/D(3)-*T/M* (0.0)-1.32%

| Longitudinal Yielding | Ultimate Load | Final Failure |
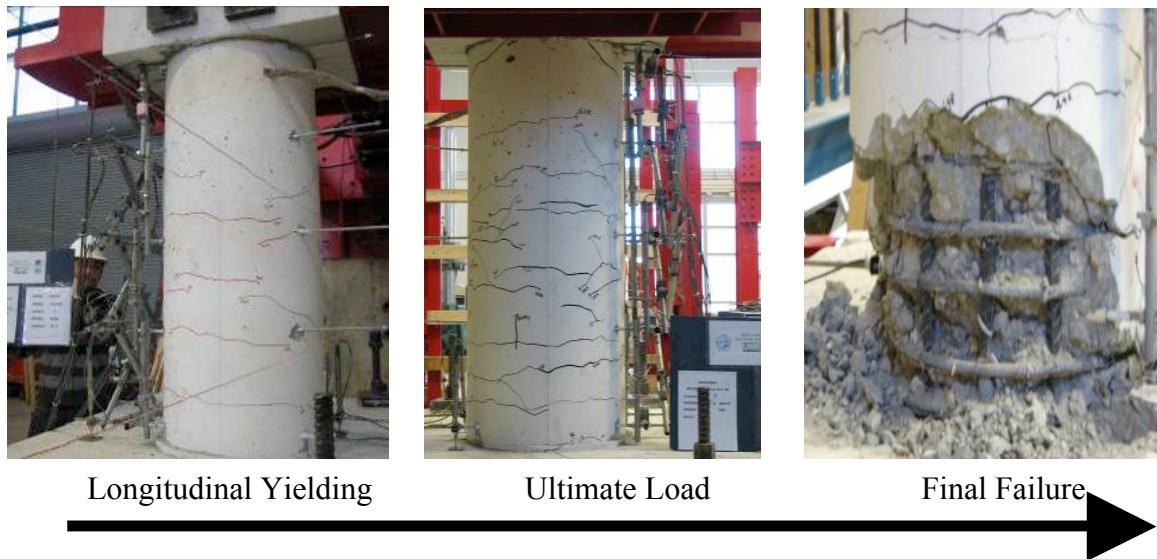
Figure 4.6 Damage of Column H/D(3)-*T/M* (0.0)-1.32% under Flexure

4.4.2. Columns under Cyclic Pure Torsion. Pure torsion is rarely present in structural members and usually occurs in combination with bending and shear. However, understanding the behavior of members subjected to pure torsion, is fundamental task for

the analysis of structural members under combined loading. Few studies have reported on the behavior of RC circular sections under pure torsion. Hindi et al. (2005) proposed the use of two cross spirals to enhance strength and ductility characteristics under pure torsion. The torsional strength of a member depends mainly on the amount of transverse and longitudinal reinforcement, the sectional dimensions, and the concrete strength. In particular, some of the columns tested in this study had been designed with a relatively low transverse reinforcement ratio (0.73%) according to CALTRANS (2002) specifications. This factor must be carefully considered when interpreting the results for columns under pure torsion.

4.4.2.1 Column H/D(6)-*T/M* (∞)-0.73% with hoop reinforcement. Columns with hoop and spiral reinforcement were tested under pure torsion to study the locking and unlocking effect of spiral reinforcement on hysteresis behavior. Figure 4.7 shows the torsional moment-twist hysteresis curves of the column with hoop reinforcement. Cracking began after cyclically loading the column to 50% of the predicted torsional yield moment, T_y. As the test progressed, these cracks lengthened as the applied torsion was increased.
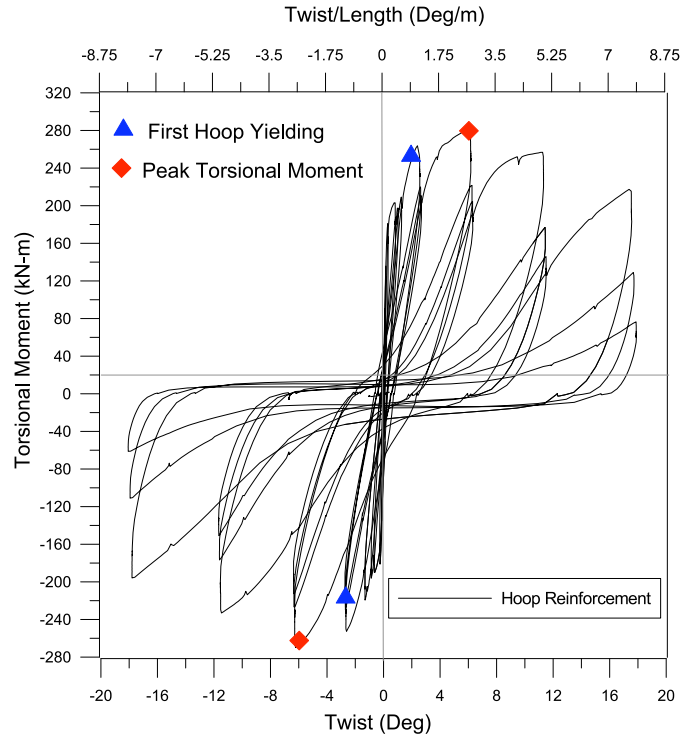
Figure 4.7 Torsional Hysteresis of H/D(6)-*T/M* (∞)-0.73% with Hoop

The first yielding of hoop reinforcement was observed at torsional moment of 275 kN-m, which was the predicted ductility level of one. The peak torsional moment was achieved in the next ductility level of three. Peak torsional moment was higher in the positive cycle than in the negative cycle because the test was started in the positive loading direction, resulting in the degradation of the column stiffness. The longitudinal bars on all sides remained elastic until a twist ductility of six. The test was stopped after torsional strength dropped significantly, corresponding to a twist of 18 degrees. Figure 4.8 shows the progression of damage. The spalling details are shown in Table 4.1.

First Cracking   Spiral Yielding   Peak Torsion   Longitudinal Bar Yielding   Final Cycle
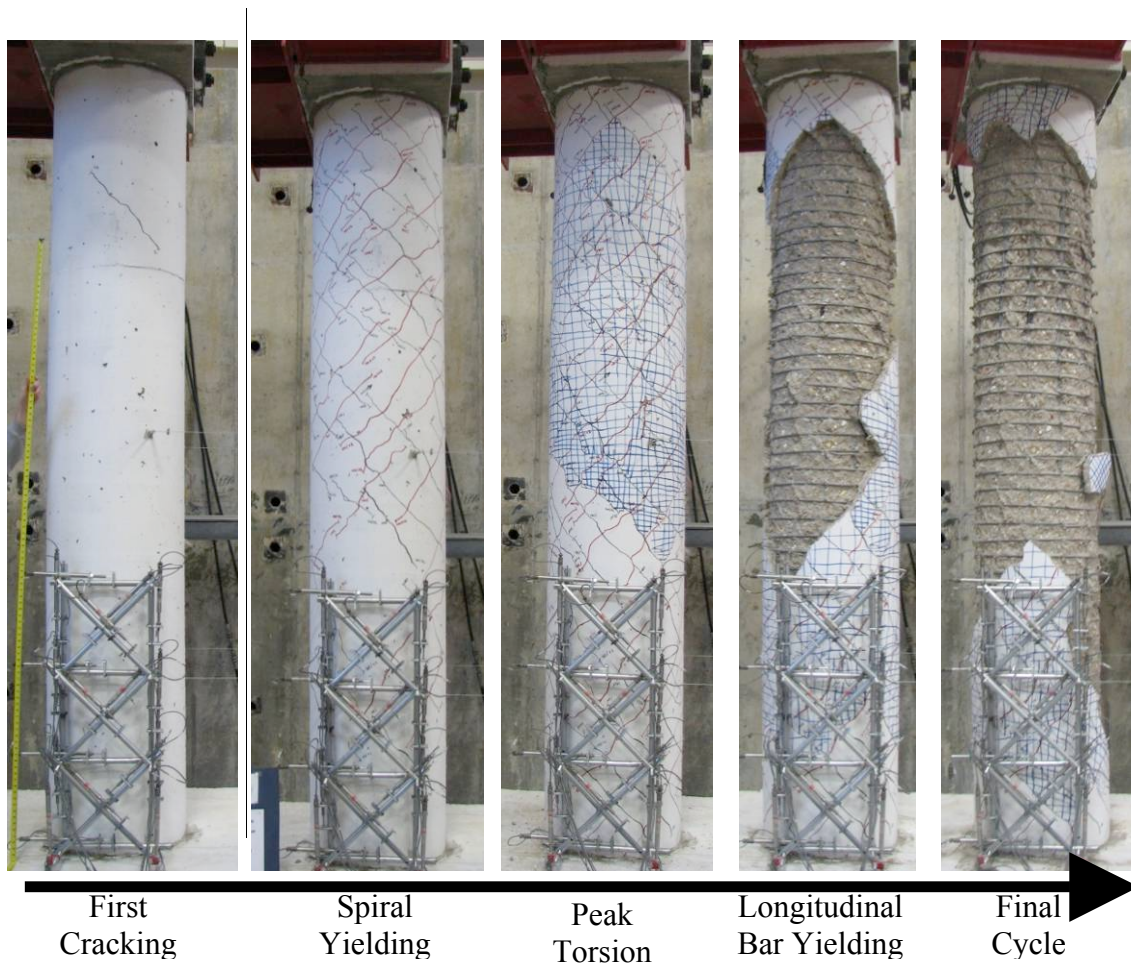
Figure 4.8 Damage Progression of H/D(6)-*T/M* (∞)-0.73% with Hoop under Pure Torsion

Table 4.1 Spalling Details of H/D(6)-*T/M* (∞)-0.73% with Hoop

Spalling State	Twist (Degrees)	Zone of Spalling (measured in 'mm' from the bottom of the column)	
		Southeast Face	Northwest Face
Initial (Twist Ductility 1.4 to 3)	2.21	1680 to 2390	1570 to 2540
Moderate (Twist Ductility 3 to 4.5)	6.31	1520 to 2740	1220 to 2950
Stable (Twist Ductility 4.5 to 13)	12.62	610 to 3200	510 to 3250

4.4.2.2 Column H/D(6)-*T/M* (∞)-0.73% with spiral reinforcement. This column was also tested under pure torsion with spiral reinforcement. Figure 4.9 shows

the torsional moment-twist hysteresis curve with spiral reinforcement ratio of 0.73%. Initial cracking was observed during the 0.75 T_y loading cycle. The rotation level corresponding to the first diagonal cracking was 33°. The diagonal crack formed at the height of 2000 mm. The crack spacing was approximately 356 mm on face C. The cracks were also evenly spaced on the negative cycle on the other face A (Figure 4.10). During the successive cycles of 0.75 T_y and 1.0 T_y, the cracks were primarily oriented diagonally. After the cycles up to T_y, the results were analyzed and the yield rotation was calculated to be 0.3154°. During the first cycle of ductility five, the cracks were formed along the full height of the column (Figure 4.10).
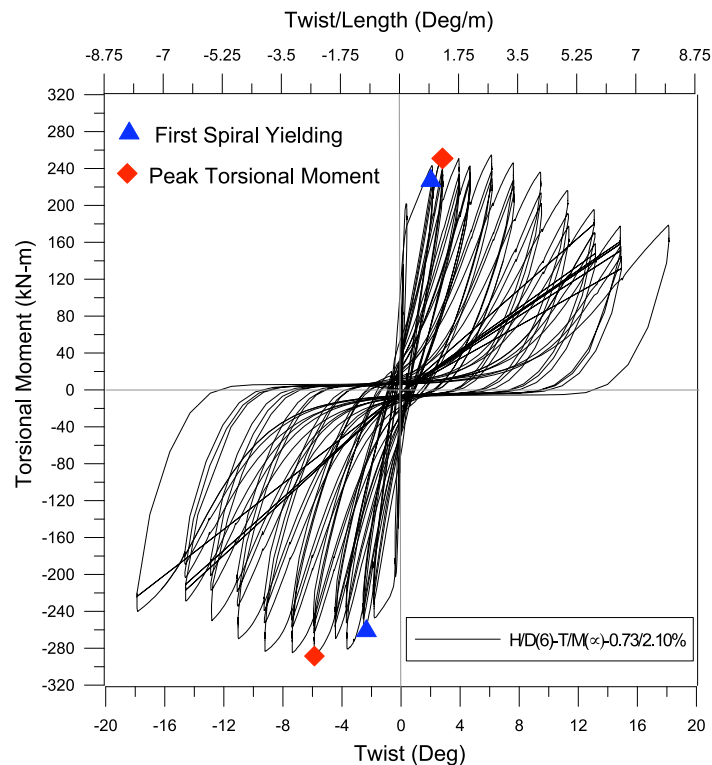
Figure 4.9 Torsional Hysteresis Behavior of H/D(6)-*T/M* (∞)-0.73%

The torsional moment-twist curves were approximately linear up to cracking and thereafter become nonlinear with a drop in the torsional stiffness. The post-cracking stiffness decreased proportionally with an increase in the cycles of loading. The behavior of columns with spiral reinforcement differed significantly from that of columns with hoop reinforcement due to the locking and unlocking effects of the spiral reinforcement. During the positive cycles of twisting, the spiral reinforcement was unlocked, which caused spalling and reduced the confinement effect on the concrete core. On the other hand, during the negative cycles of loading, the spirals were locked, and they contributed to additional confinement of the concrete core. This effect is reflected in the asymmetric nature of the observed hysteresis loop at higher levels of loading. At higher ductility levels, the load resistance on the negative cycles was higher than that on positive cycles of loading due to the added confinement generated by the locking effect of the spiral reinforcement. The longitudinal bars on sides A and C remained elastic until ductility four. The spirals, however, reached the yield strain at the predicted ductility level of one. Differences were observed in the strain levels on Sides A and C due to the effect of locking and unlocking of the spirals. Figure 4.11 compares the damage pattern in columns with hoop and spiral reinforcement. Concrete core degradation was more significant in the column with the hoop reinforcement that in that with the spiral reinforcement. This difference was mainly due to the additional confining effect of spiral in the locking direction, which helped to reduce damage in the concrete core.

| First Cracking | Spiral Yielding | Peak Torsion | Longitudinal Bar Yielding | Final Cycle |
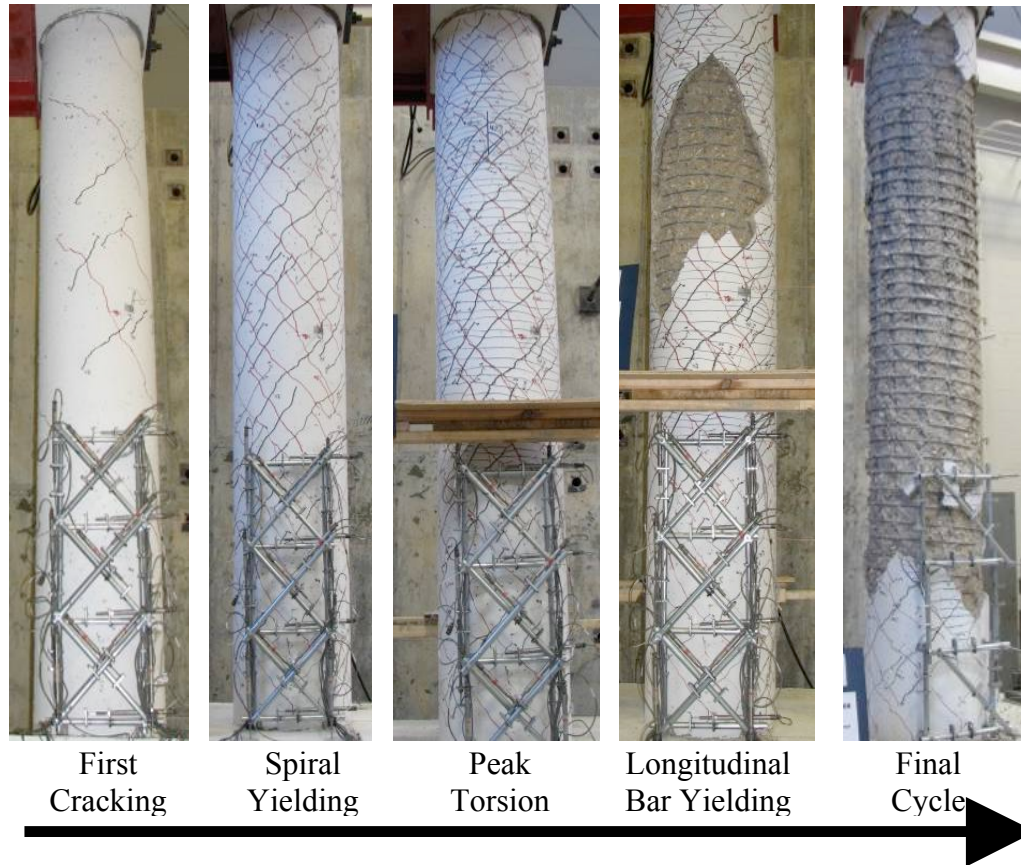
Figure 4.10 Damage of Progression of H/D(6)-*T/M* (∞)-0.73% under Pure Torsion
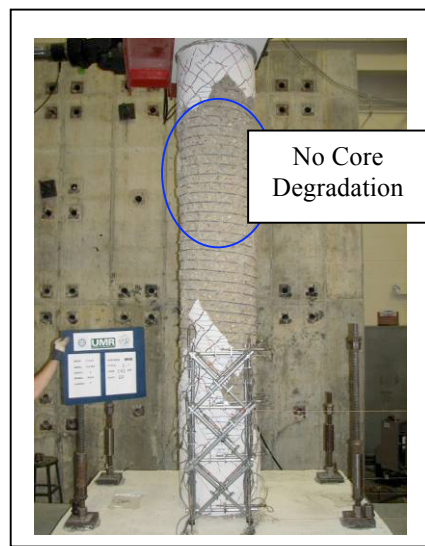
(a) Spiral
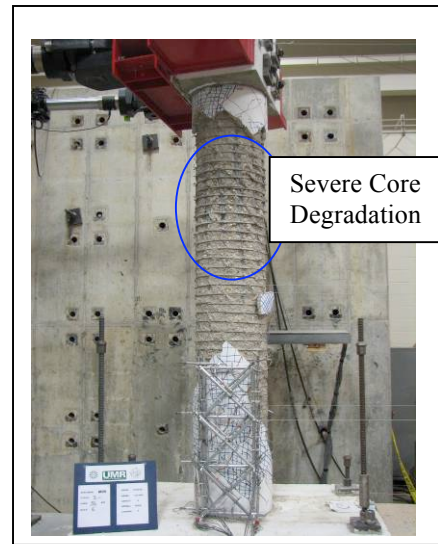
(b) Hoop

Figure 4.10 Comparison of Damage under Pure Torsion at Peak Torsional Resistance

4.4.2.3 Column H/D(3)-*T/M*(∞)-1.32% with spiral reinforcement. The torsional strength of a member depends mainly on the amount of transverse and longitudinal reinforcement as well as on the sectional dimensions and concrete strength. In the post-peak behavior, the dowel action of longitudinal bars significantly affects the load resistance at higher cycles of loading (Belarbi et al., 2008b). Figure 4.11 shows the torsional hysteresis curve of column tested under pure torsion. Under pure torsional loading and at lower ductility levels, significant diagonal cracks began to develop near mid-height on the column at lower levels of ductility. The cracks lengthened with the increase of torsional moment. Soon after the yielding of the spirals, spalling was observed. The angle of the diagonal cracks was about 40º respect to the horizontal cross section of the column. Post-cracking stiffness decreased proportionally with increase in the cycles of loading. The locking and unlocking effect of the spirals was also observed in the negative and positive loading cycles as the column with spiral reinforcement ratio of 0.73% (Figure 4.11). At higher ductility levels, the load resistance on the negative cycles was higher than that on positive cycles of loading due to the added confinement generated by the locking effect of the spirals. Spalling continued to increase along the height of the column with higher levels of ductility. The concrete cover spalled however, along the entire length of the column, and significant spalling led to the formation of a torsional plastic-hinge near the mid-height of the column. Figure 4.12 shows the progress on damage of the specimen.
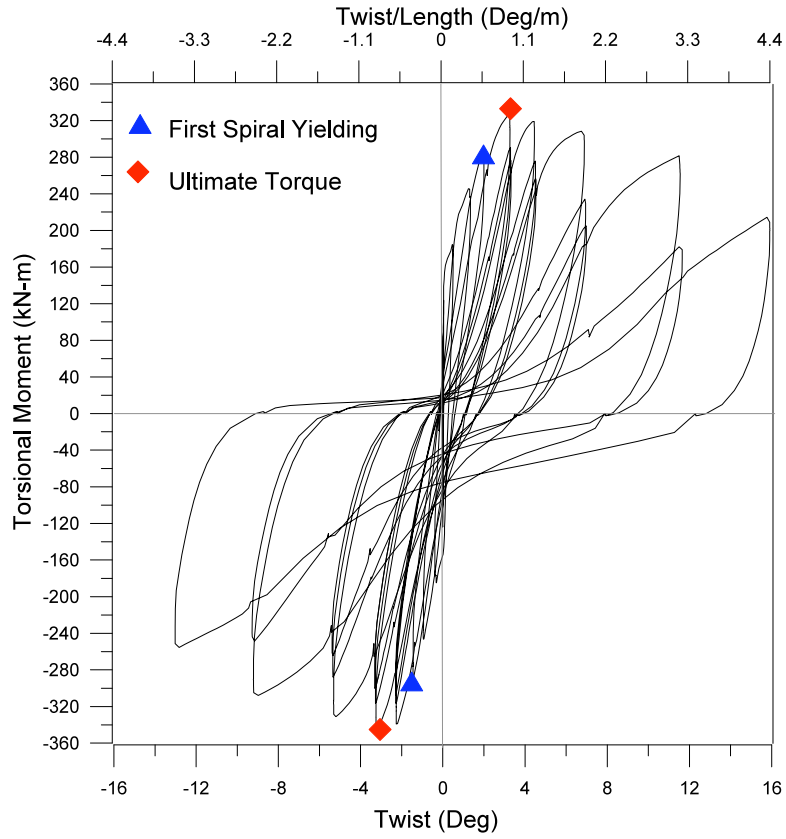
Figure 4.11 Torsional Hysteresis Behavior of H/D(3)-*T/M*(∞)-1.32%

Spiral Yielding   Peak Torsion   Final Cycle
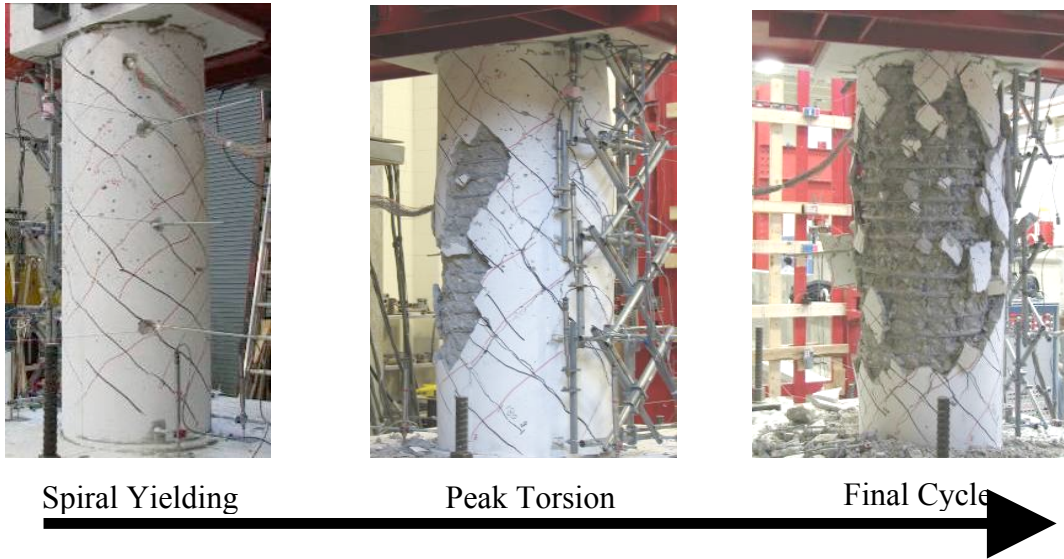
Figure 4.12 Damage to Column under Pure Torsion

The torsional strength of the specimen under pure torsion was compared with AASHTO equations in Table 4.2. Cracking strength under torsional moment is given in the metric system as:

$$T_{cr} = 0.33\sqrt{f'_c}\left(\frac{A_{cp}^2}{P_{cp}}\right)\sqrt{1 + \frac{f_{pc}}{0.33\sqrt{f'_c}}}$$

Eq. 4.4

where f'_c is the specified compressive strength of concrete at 28 days, T_{cr} is the torsional cracking moment, A_{cp} is the total area enclosed by outside perimeter of the concrete section, P_{cp} is the length of the perimeter of the concrete section, and f_{pc} is the compressive stress in the concrete after prestress losses have occurred either at the centroid of the cross-section resisting transient loads or at the junction of the web and flange where the centroid lies in the flange.

Torsional resistance was assumed to be provided only by the spiral reinforcement, as shown in metric system. Based on the thin tube analogy, torsional resistance is given by

$$T_n = \frac{2A_o A_t f_y}{s}\cot\theta$$

Eq. 4.5

where A_t is the area of one leg of closed torsion reinforcement within a spacing s, A_o is the area enclosed by the shear flow path (taken as $0.85A_{oh}$), A_{oh} is the area enclosed by the centerline of the outermost closed transverse torsion reinforcement, and θ is the angle of diagonal compressive stress. The value of θ depends on the level of strain in the section ε_x

and the level of applied shear stress v/f_c'. The cracking strength and ultimate strength of columns with hoop and spiral reinforcement are compared with AASHTO equations, as shown in Table 4.2. These equations are conservative compared with experimental values.

Table 4.2 Comparison of Results with AASHTO Equations for Pure Torsion

Parameter	AASHTO	Column with Hoop Reinforcement ($\rho_t = 0.73\%$)	Column with Spiral Reinforcement ($\rho_t = 0.73\%$)
Cracking strength	175.4	181.3	202.5
Ultimate strength	220.0	269.9	245.6

4.4.3. Columns under Cyclic Combined Bending, Shear, and Torsion. In general, three failure modes can be observed on RC members under combined bending, shear, and torsion with respect to the longitudinal and transverse reinforcement ratio: under-reinforced (longitudinal and transverse steel yield before concrete crushes), partially over-reinforced (only longitudinal steel yields or only transverse reinforcement yields), and over-reinforced (concrete crushing occurs before any of the longitudinal or transverse steel yields). The behavior of columns with different spiral ratios of 0.73% and 1.32% and aspect ratios of six and three are explained in the following sections.

4.4.3.1 Columns with a spiral ratio of 0.73% and H/D ratio of 6. Three columns with a spiral ratio of 0.73% were tested under combined bending and torsional moments by maintaining *T/M* ratios of 0.1, 0.2, and 0.4, respectively (Table 3.1). One

column was tested at a *T/M* ratio of 0.1 to validate the consideration of minimum torsional moment from a design point of view. The ACI and AASHTO codes suggest disregarding the presence of torsional moment if it is less than 25% of cracking torque (T_{cr}). This level of cracking torque (T_{cr}) in a column with spiral reinforcement of 0.73% is calculated to be about 50 kN-m. According to ACI code calculations, the theoretical flexural strength is 786 kN-m, resulting in a T_{cr}/M_u ratio of about 0.065. Hence, the column was tested at a *T/M* ratio of 0.1 to determine the effect of the simultaneous application of a relatively small torsional moment along with bending and shear from a design point of view. The results of tests on columns under flexure and pure torsion provided a basis for analysis of the behavior of other specimens tested under combined shear, bending, and torsional moments.

One column was tested at a *T/M* ratio of 0.4 to establish the balance point in the interaction diagram by reaching the yield strain of longitudinal reinforcement and spiral reinforcement simultaneously. The bending moment M_y= 497.9kN-m corresponding to first yielding of the longitudinal bar under bending-shear was calculated theoretically based on flexure. The torsional moment T_n = 220 kN-m corresponding to yielding of the spiral reinforcement was calculated using the AASHTO equation. The ratio of M_y/T_n was calculated to be 0.44. Hence, test was conducted at a ratio of 0.4 to investigate the sequence of longitudinal bar yielding and spiral yielding. The other column was tested at an intermediate *T/M* ratio of 0.2 to determine the strength and stiffness degradation for *T/M* ratios between 0.1 and 0.4. Based on seismic analysis of bridges, previous studies have found the maximum *T/M* ratio to be up to 0.5 (Belarbi et al., 2008).

Figure 4.13 shows the interaction of bending and torsional moment loading curves for all the columns at peak levels of cycles. The columns at a T/M ratio of 0.1 reached the bending strength before reaching the torsional strength. However, the columns tested at T/M ratios of 0.2 and 0.4 reached torsional strength before they reached bending strength. Ratios cannot be maintained at the desired values once bending or torsional strength is reached. After the columns reached the ultimate state, the displacement and twist were increased at increments to complete the test. In all the columns under combined bending and torsional moments, the actuator with lower force had displacement in the same direction as the other actuator with a higher force. Under pure torsion, the direction of displacement in the actuators was opposite. The pressure force calibration of the actuators was checked and found to be consistent with behavior observed during the testing.
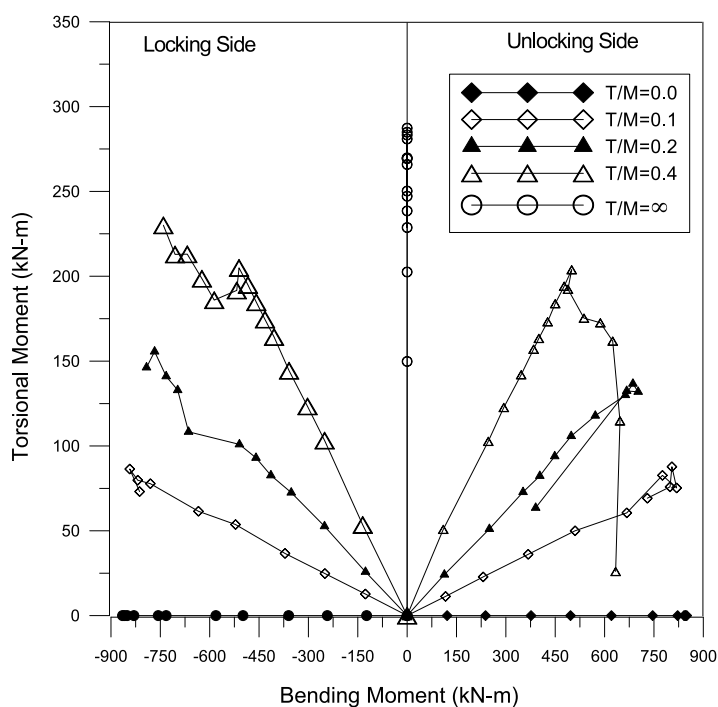
Figure 4.13 Interaction of Torsion and Bending Moment Loading Curves

4.4.3.1.1 Column H/D(6)-*T/M*(0.1)-0.73% . In all the columns tested under combined bending and torsion, flexural cracks first appeared near the bottom of the column. The angle of the cracks became more inclined at increasing heights above the top of the foundation with increasing cycles of loading and depending on the *T/M* ratio. Figure 4.14 shows the flexural and torsional hysteresis. It demonstrates that the specimen was dominated by flexure due to the application of low torsional moment. The specimen failed at low twist ductility, mainly due to the application of very low torsional moment at a *T/M* ratio of 0.1, and it could not resist the applied torsional moment at a displacement ductility level of 9.0. The corresponding torsional ductility at failure was 1.25, indicating that torsional moment occurred simultaneously corresponding to spiral yielding and peak torque. Figure 4.16 shows the progression of damage.
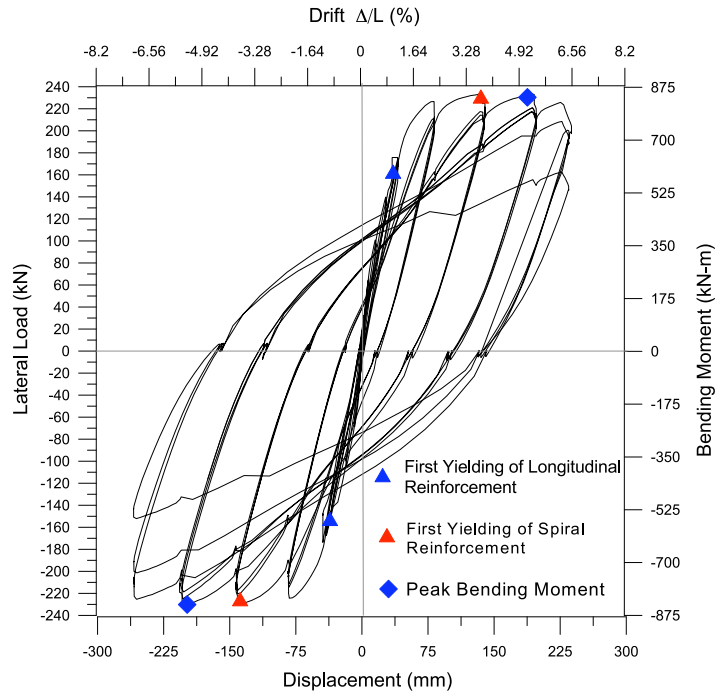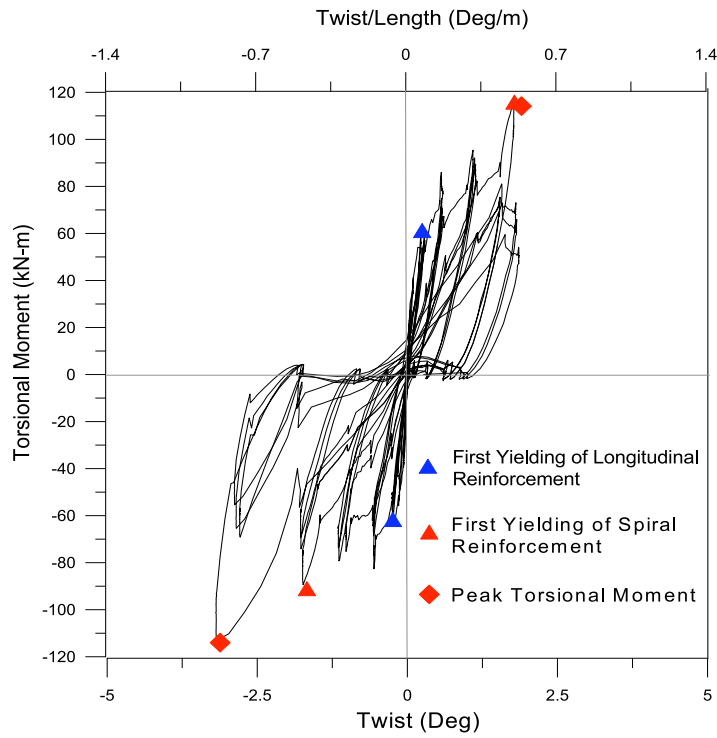
(a) Flexural

(b) Torsional

Figure 4.14 Hysteresis Behavior of H/D(6)-*T/M*(0.1)-0.73%
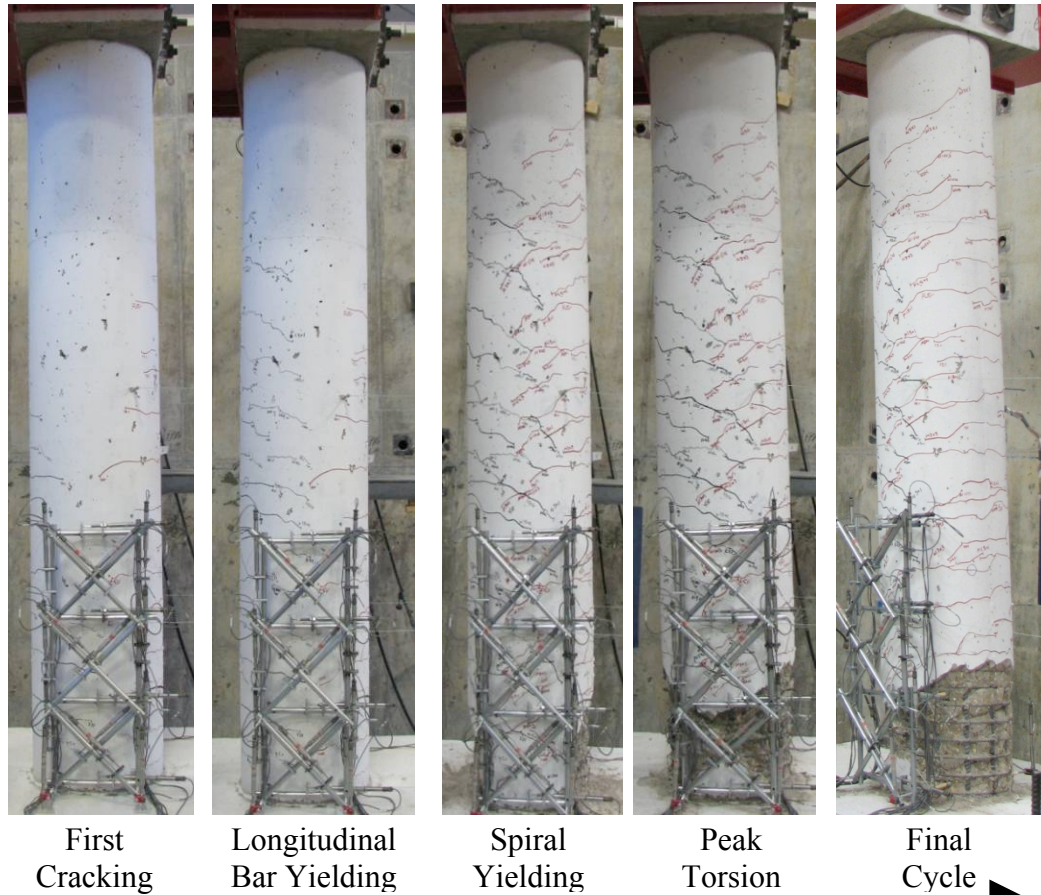
Figure 4.15 Damage to Column H/D(6)-*T/M*(0.1)-0.73% on the West Face

4.4.3.1.2 Column H/D(6)-*T/M*(0.2)-0.73%. Figure 4.17 shows the flexural hysteresis and torsional hysteresis of the column tested at a *T/M* ratio of 0.2. The specimen was dominated by both flexure and torsion. That is, the column failed as a result of both torsional and flexural damage. The specimen reached peak shear at a drift of 3.5% with a displacement ductility of 7.0, and finally failed at a drift of 6.5% and a displacement ductility of 9.5. The corresponding torsional twist ductility was 1.76; however, the peak torsional moment was reached at a twist ductility of one. The locking and unlocking effect of the spiral reinforcement was clearly reflected in the torsional hysteresis. Figure 4.18 shows the progression of damage.
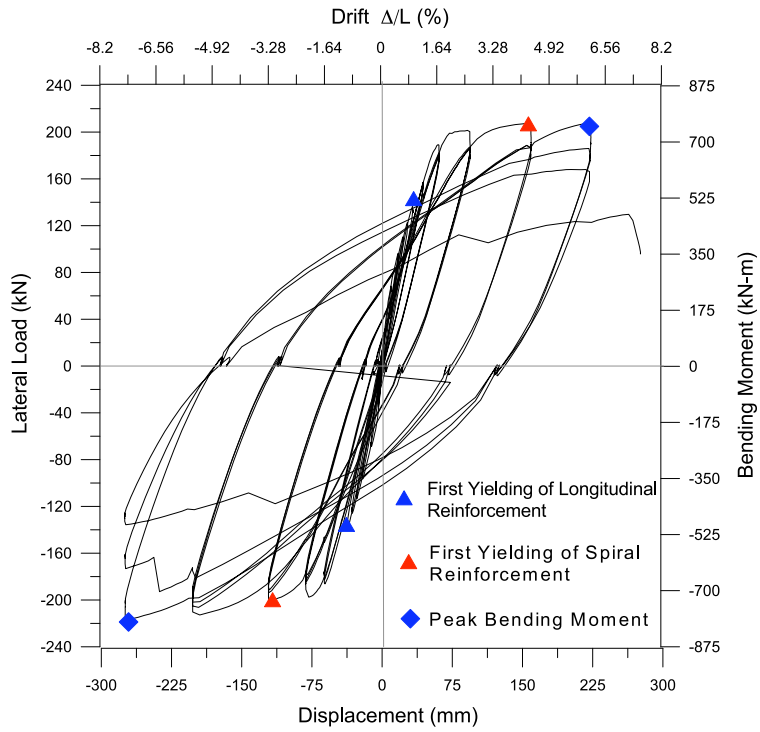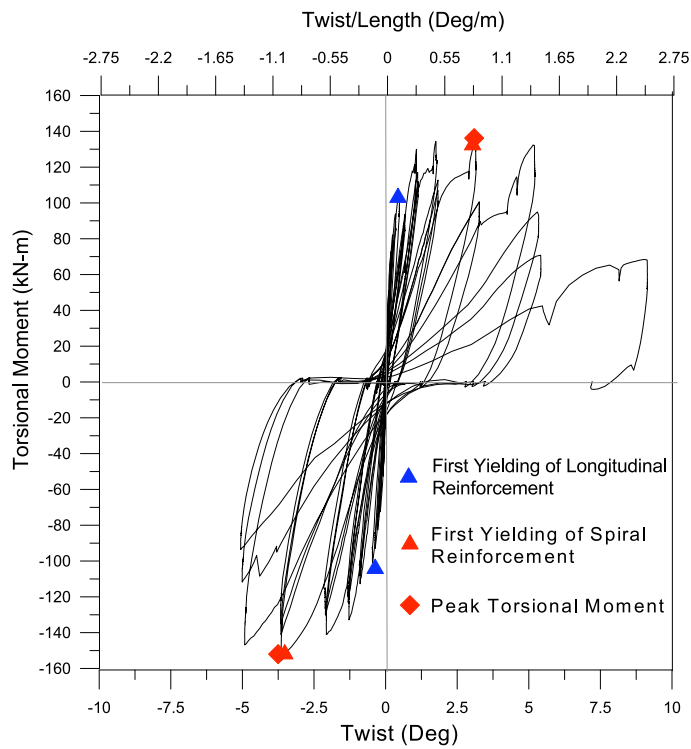
(a) Flexural

(b) Torsional

Figure 4.16 Hysteresis Behavior of H/D(6)-*T/M*(0.2)-0.73%

| First Cracking | Longitudinal Bar Yielding | Spiral Yielding | Peak Torsion | Peak Shear |
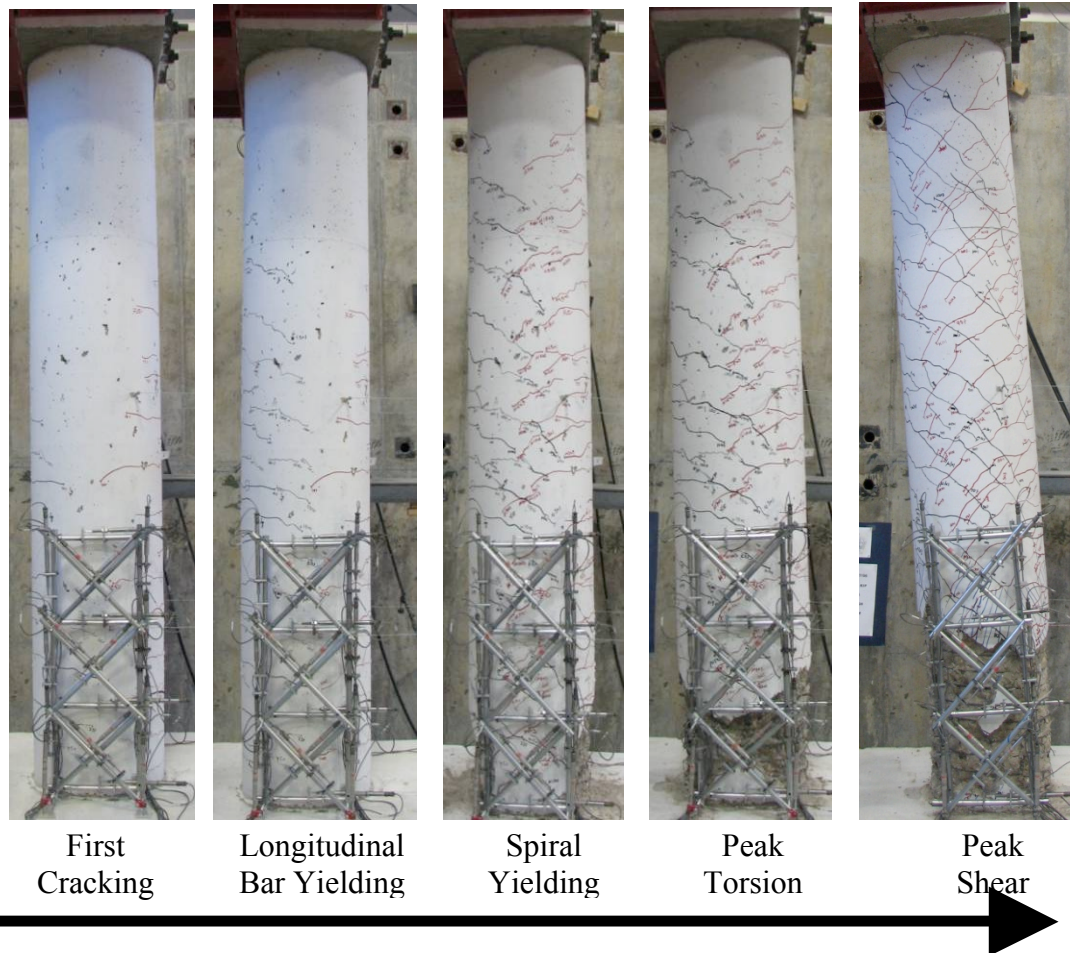
Figure 4.17 Damage of Progression of Column H/D(6)-*T/M*(0.2)-0.73%

4.4.3.1.3 Column H/D(6)-T/M(0.4)-0.73%. Figure 4.18 shows the flexural hysteresis and torsional hysteresis of the column tested at a *T/M* ratio of 0.4. The column reached its torsion strength prior to reaching its bending strength. The damage was initiated by spiral reinforcement yielding and cover spalling. This resulted in more energy dissipation under torsion than under flexure; thus, the behavior of the specimen was dominated by torsion. A significant difference due to the locking and unlocking effect of spiral reinforcement is also apparent in the asymmetric behavior of the hysteresis curve under both flexure and torsion (Figure 4.18). Yielding of longitudinal and spiral

reinforcements occurred relatively close to each other for the column tested at a *T/M* ratio of 0.4. The specimen reached the peak shear at a displacement ductility of 4.5 and failed soon after. The corresponding torsional ductility at failure was 4.0; however, the peak torsional moment was reached at a twist ductility of 1.0. Control of the *T/M* ratio was lost soon after the column reached its torsional strength. Spalling and core degradation were observed up to a maximum height of 910 mm from the base of column for a *T/M* ratio of 0.4, demonstrating that the torsional damage location changed due to the effect of bending. The specific location of the damage zone, however, depended on the applied *T/M* ratio. Figure 4.20 shows damage progression in a T/M ratio of 0.4. In all columns under combined bending and torsion, failure began due to combinations of severe shear and flexural cracks leading to progressive spalling of cover concrete. The columns under combined loading finally failed due to severe core degradation followed by buckling of the longitudinal bars on side C.
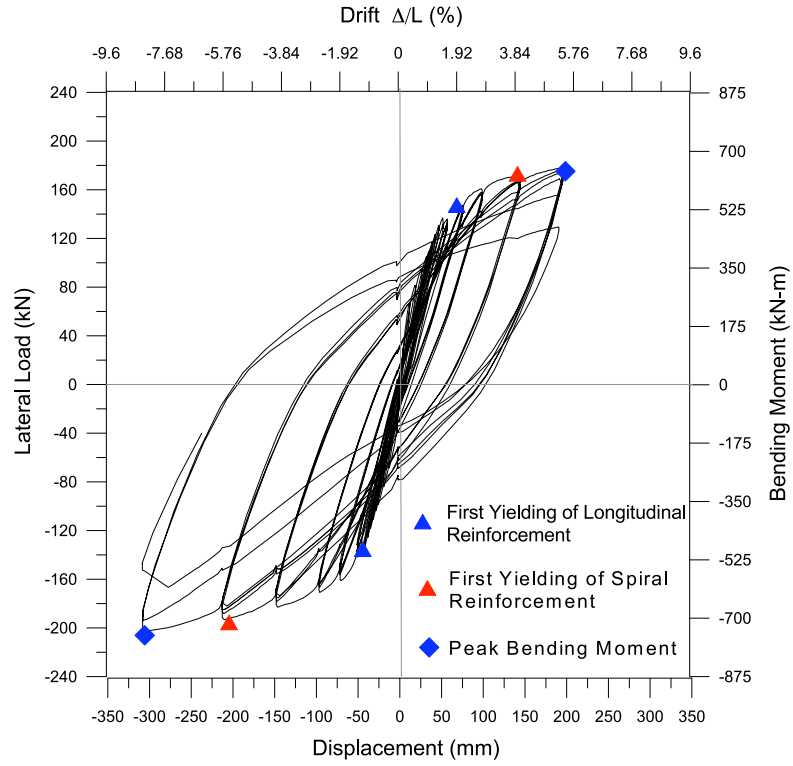
(a) Flexural
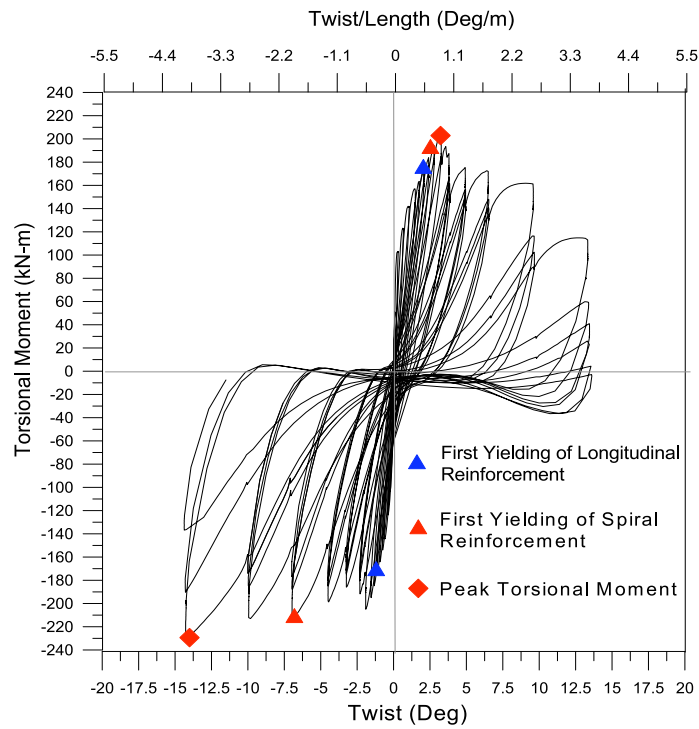
(b) Torsional

Figure 4.18 Hysteresis Behavior of H/D(6)-*T/M*(0.4)-0.73%

| First
Cracking | Longitudinal
Bar Yielding | Spiral
Yielding | Peak
Torsion | Peak
Shear |
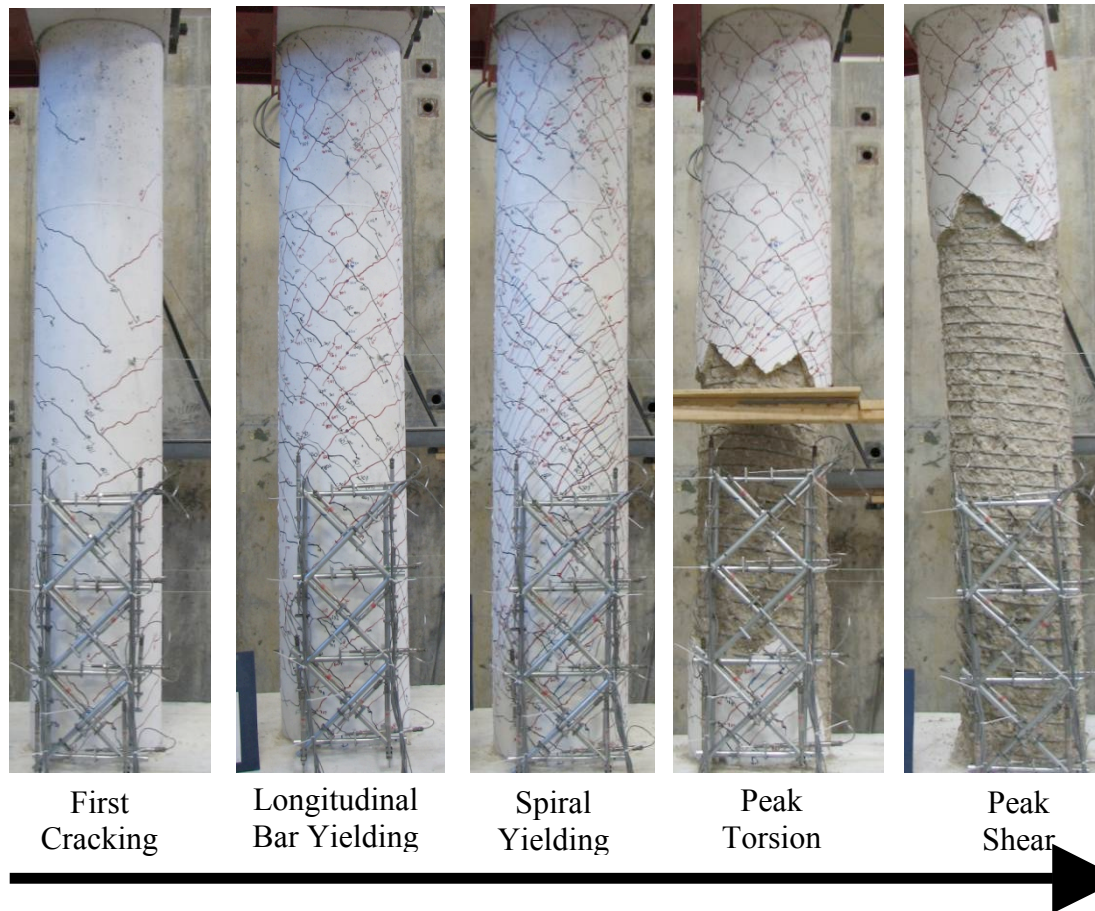
Figure 4.19 Damage Progression of H/D(6)-*T/M*(0.4)-0.73%

4.4.3.2 Columns with spiral ratio of 1.32% and H/D ratio of 6. Figure 4.20 shows the interaction of torsion and bending moment loading curves for the columns tested under combined bending and torsion with varying spiral reinforcement ratios. The curves indicate that all specimens reached their torsional strength prior to reaching their flexural strength. However, the longitudinal reinforcement yielded before the spiral reinforcement. Hence, the failure sequence in all specimens started by flexural cracking followed by diagonal cracking, longitudinal reinforcement yielding, spalling of concrete cover, spiral reinforcement yielding, and then final failure by buckling of the longitudinal reinforcement. Spiral and longitudinal reinforcement yielding occurred in quick

succession for the specimen with a spiral ratio of 0.73%. An increase in spiral ratio significantly improved torsional and bending strength. More importantly, significant twist ductility could also be achieved in torsional behavior. To study the effectiveness of increasing the spiral reinforcement ratio, columns under combined loading were tested under *T/M* ratios of 0.2 and 0.4, with spiral reinforcement ratios of 0.73 and 1.32%, respectively.
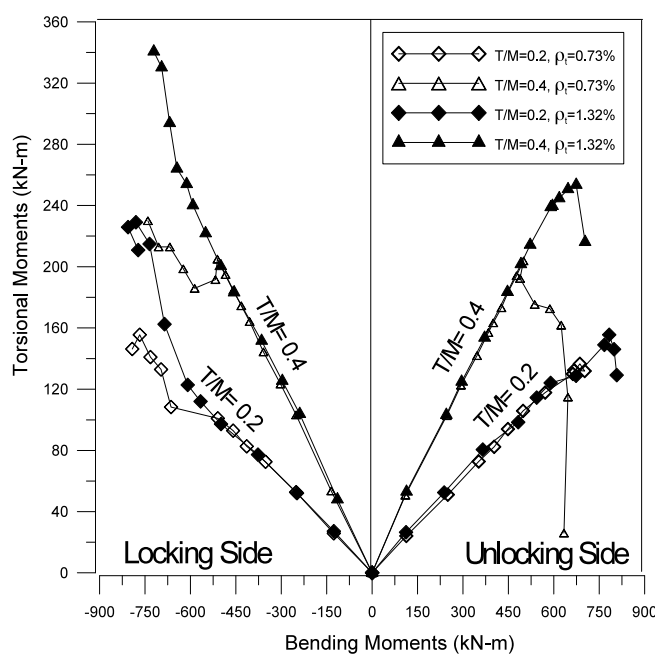
Figure 4.20 Interaction of Torsion-Bending Moment Loading Curves at Peak of Cycle for Various Combined Loading

4.4.3.2.1 Column   H/D(6)-*T/M*(0.2)-1.32% Figure 4.22 shows the flexural hysteresis and torsional hysteresis of the column with a spiral reinforcement ratio of 1.32% and tested at a *T/M* ratio of 0.2. The behavior of the specimen was dominated by both flexure and torsion. The specimen reached peak shear at a displacement ductility of 7.0 and finally failed at a displacement ductility level of 9.5. The corresponding twist ductility at failure was 1.76; however, the peak torsional moment was reached at a twist

ductility level of 1.0. The locking and unlocking effect of spiral reinforcement was clearly reflected in the torsional hysteresis as in the pure torsion (Figure 4.22b). The progression of damage is shown in Figure 4.23.
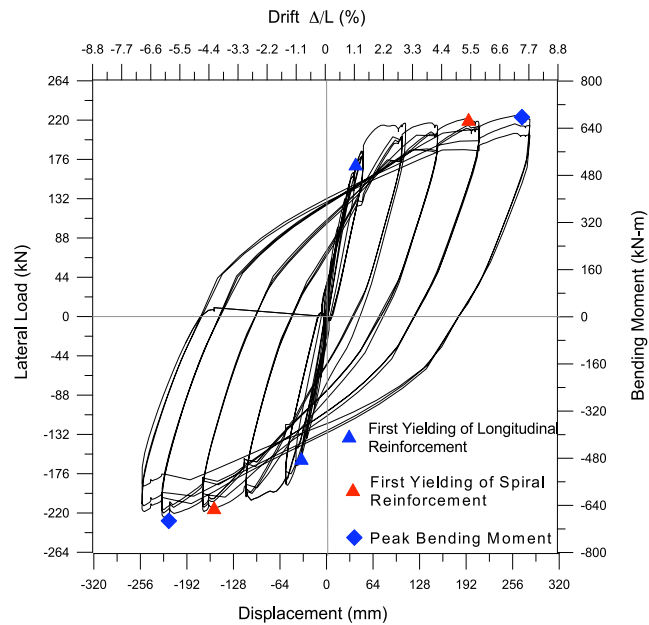
(a) Flexural
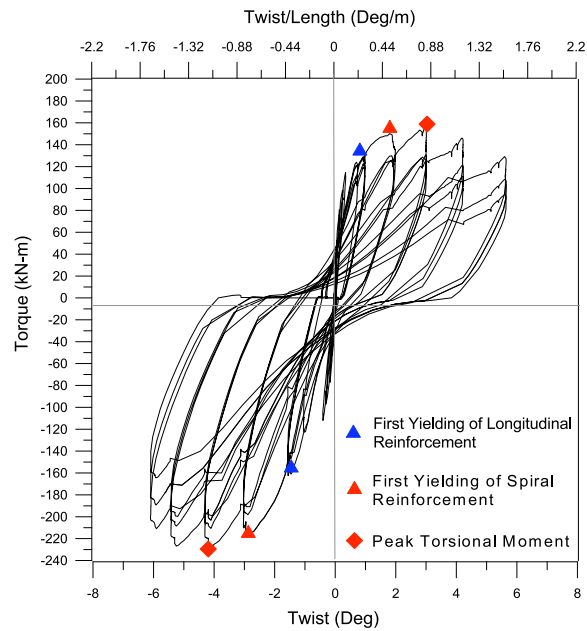
(b) Torsional

Figure 4.21 Hysteresis Behavior of H/D(6)-*T/M*(0.2)-1.32%

| First | Longitudinal | Spiral | Peak | Peak |
| Cracking | Bar Yielding | Yielding | Torsion | Shear |
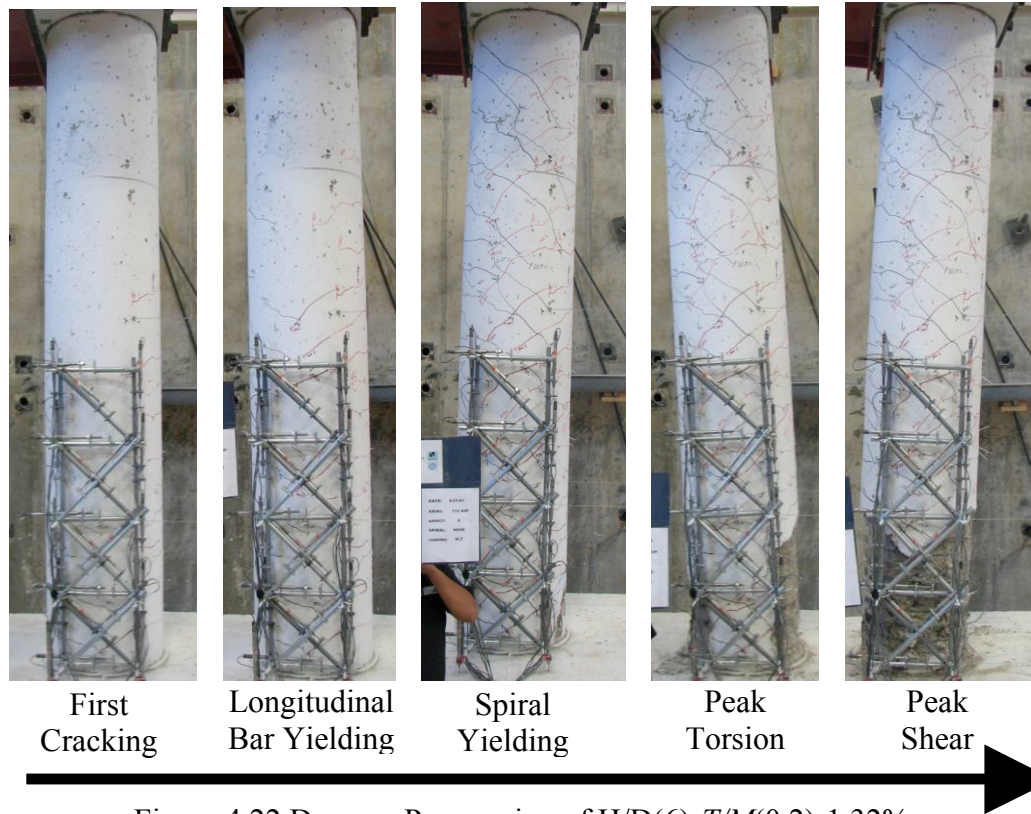
Figure 4.22 Damage Progression of H/D(6)-*T/M*(0.2)-1.32%

4.4.3.2.2 Column H/D(6)-*T/M*(0.4)-1.32%. Figure 4.23 shows the flexural hysteresis and torsional hysteresis of the column with a spiral reinforcement ratio of 1.32%, which was tested at a *T/M* ratio of 0.4. The energy dissipation under torsion was increasing due to damage from shear cracking and spiral yielding. Thus, the behavior of the specimen was dominated by torsion. The asymmetric behavior of the hysteresis curve under both flexure and torsion revealed a significant difference due to the locking and unlocking (Figure 4.23b). The specimen reached the peak shear at a displacement ductility level of 4.5 and failed soon after. The corresponding twist ductility at failure was 4.0; however, the peak torsional moment was reached at a twist ductility of 1.0. Control of the *T/M* ratio could not be maintained after the column reached its torsional strength.
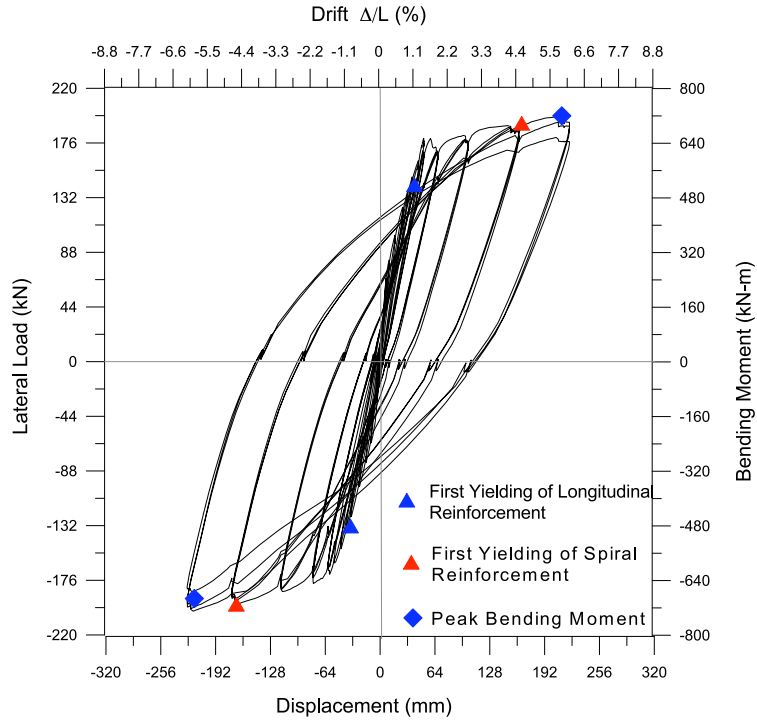
(a) Flexural
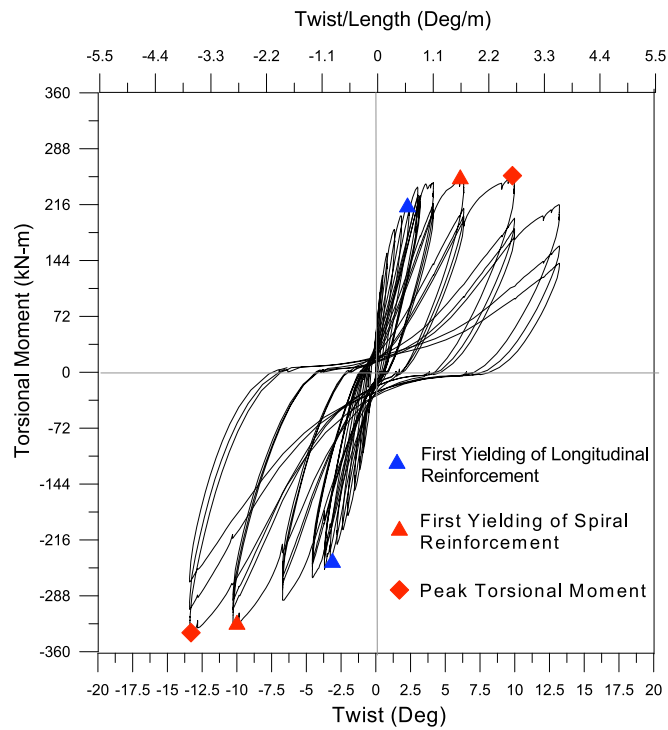
(b) Torsional

Figure 4.23 Hysteresis Behavior of H/D(6)-*T/M*(0.4)-1.32%

Spalling of concrete cover and core degradation occurred up to a maximum height of 910 mm from the base of column for a *T/M* ratio of 0.4, indicating that the torsional damage location changed due to the effect of bending. The specific location of the damage zone, however, depends on the applied *T/M* ratio. In all columns under combined bending and torsion, failure began due to severe combinations of severe shear and flexural cracks, leading to progressive spalling of the concrete cover. The columns under combined loading finally failed due to severe core degradation followed by buckling of the longitudinal bars on side C. Figure 4.24 shows the progression of damage.

| First Cracking | Longitudinal Bar Yielding | Spiral Yielding | Peak Torsion | Peak Shear |

Figure 4.24 Damage Progression of H/D(6)-*T/M*(0.4)-1.32%
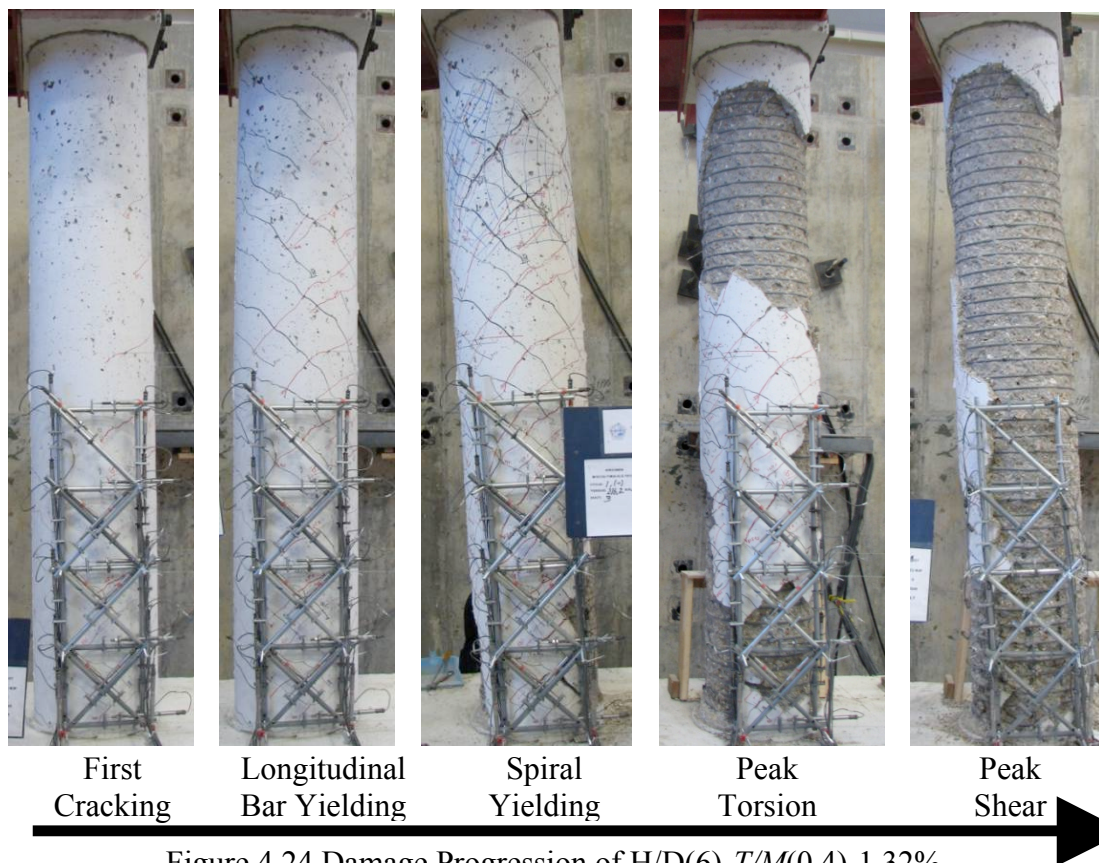
4.4.3.3 Columns with spiral ratio of 1.32% and H/D ratio of 3. Two columns with an aspect ratio of three were tested under combined bending and torsional moments by maintaining *T/M* ratios of 0.2, and 0.4, respectively. One column was tested at a T/M ratio of 0.6; however, it had a low spiral ratio of 1.03%. The other column was tested at a T/M ratio of 0.2 but with a higher axial load of 200 kip to study the effect of axial compression. Figure 4.25 shows the interaction of torsional and bending moment loading curves at peak cycles of testing.
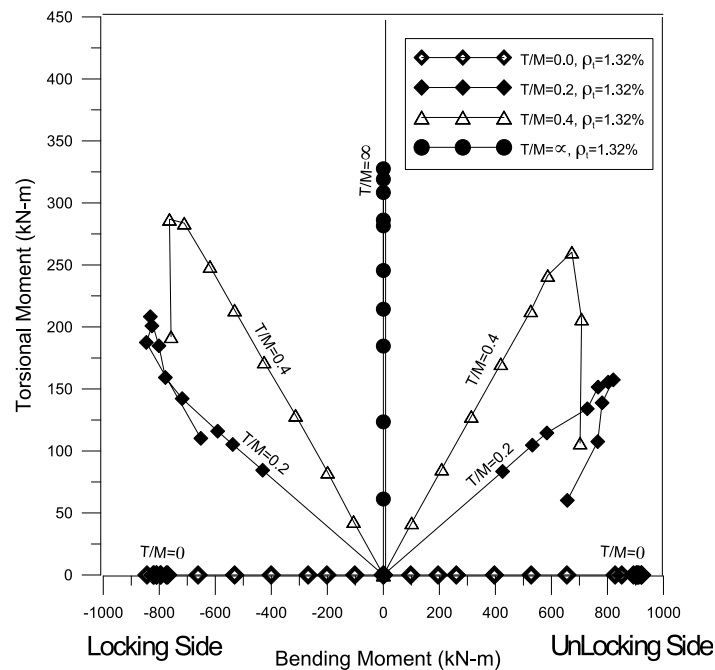
Figure 4.25 Interaction of Torsion and Bending Moment Loading Curves

4.4.3.3.1 <u>Column H/D(3)-*T/M*(0.2)-1.32%</u>   Figure 4.26 shows the flexural hysteresis and torsional hysteresis of the column with a spiral reinforcement ratio of 1.32% and tested at a *T/M* ratio of 0.2.
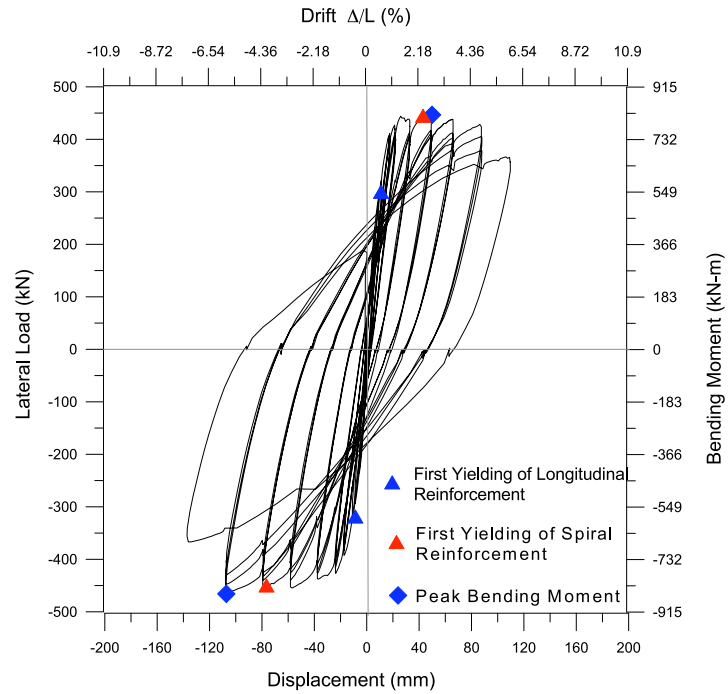
(a) Flexural
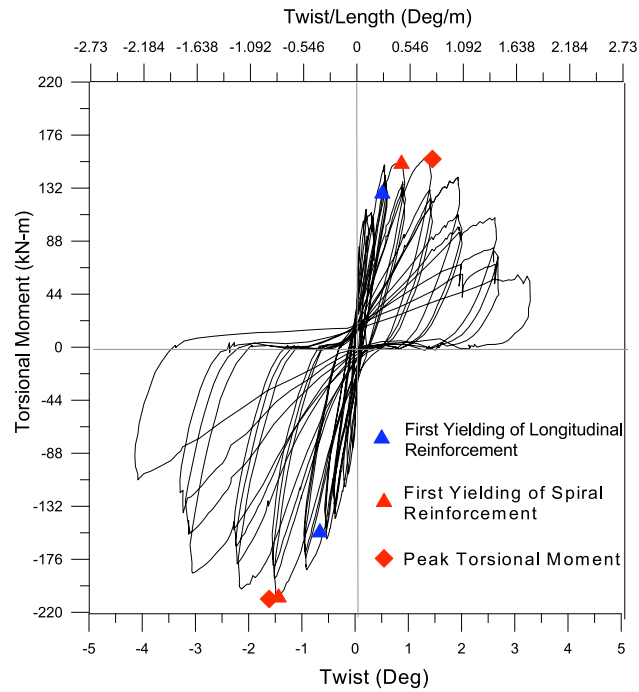
(b) Torsional

Figure 4.26 Hysteresis Behavior of H/D(3)-*T/M*(0.2)-1.32%

The behavior of the specimen was dominated by both flexure and torsion. The specimen reached the peak shear at a displacement ductility level of 7.0 and finally failed at a displacement ductility level of 9.5. The corresponding twist ductility at failure was 1.76; however, the peak torsional moment was reached at a twist ductility of 1.0. The locking and unlocking effect of spiral reinforcement was clearly reflected in the torsional hysteresis, as it was in the pure torsion specimen (Figure 4.26b). The progression of damage is shown in Figure 4.27.

| First Cracking | Longitudinal Bar Yielding | Spiral Yielding | Peak Torsion/Shear | Final Cycle |
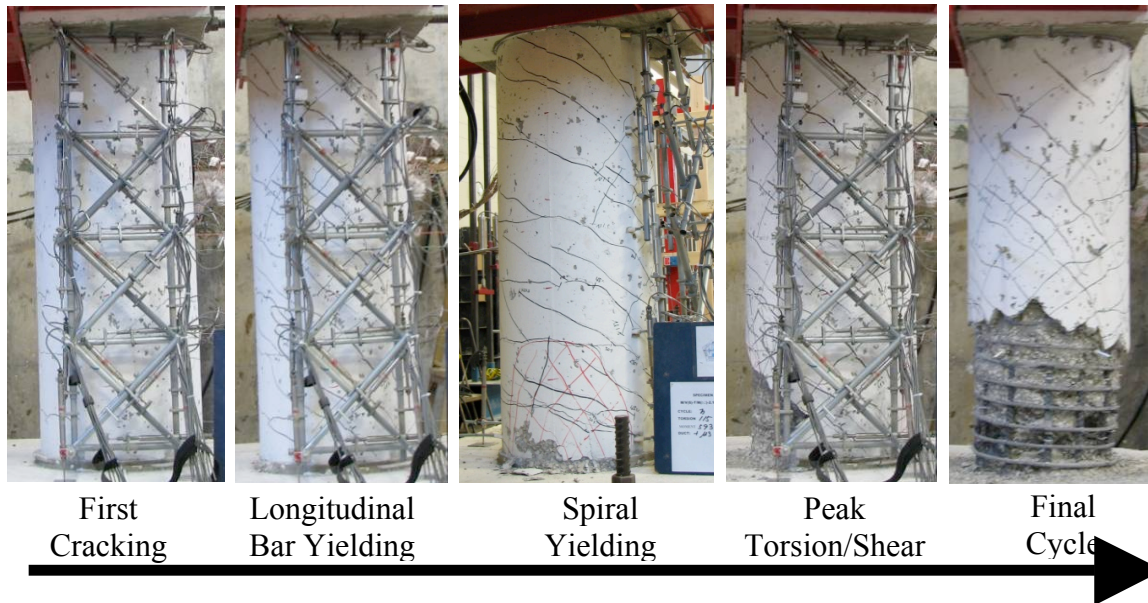
Figure 4.27 Damage Progression of H/D(3)-*T/M*(0.2)-1.32%

4.4.3.3.2 Column H/D (3)-*T/M* (0.2)-1.32%/ with axial load of 200 kip. Figure 4.29 shows the flexural and torsional hysteresis of the column with a spiral reinforcement ratio of 1.32% and tested at a *T/M* ratio of 0.2. The behavior of the specimen was dominated by both flexure and torsion.
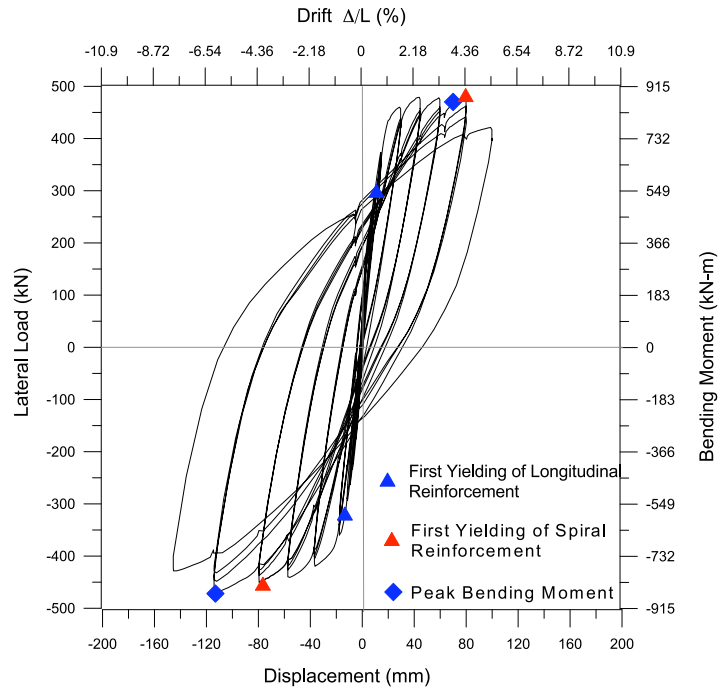
(a) Flexural
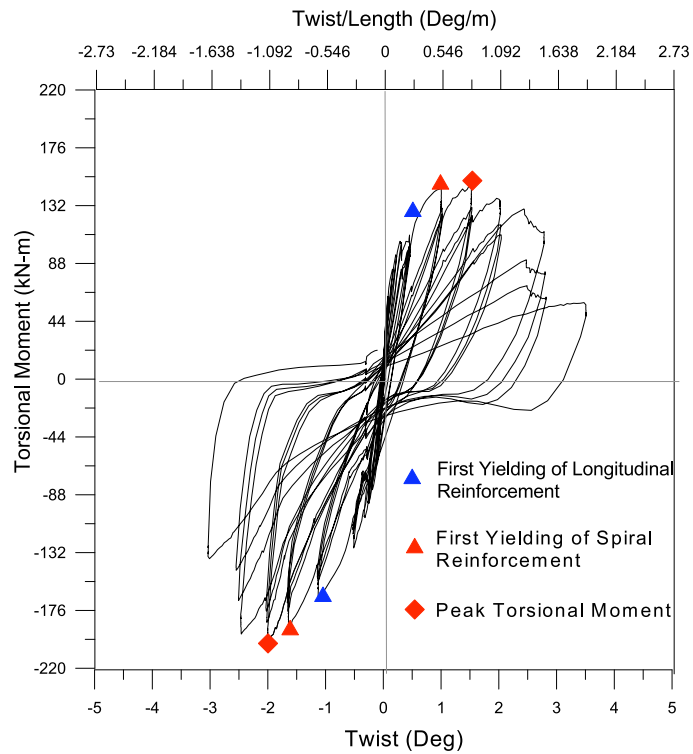
(b) Torsional

Figure 4.28 Hysteresis Behavior of H/D(3)-*T/M* (0.2)-1.32%

The specimen reached peak shear at a displacement ductility of 7.0 and finally failed at a displacement ductility level of 9.5. The corresponding twist ductility at failure was 1.76; however, the peak torsional moment was reached at a twist ductility of 1.0. The locking and unlocking effect of spiral reinforcement was clearly reflected in the torsional hysteresis, as it was in the pure torsion specimen (Figure 4.29b). The progression of damage is shown in Figure 4.29.

| First Cracking | Longitudinal Bar Yielding | Spiral Yielding | Peak Torsion | Peak Shear |
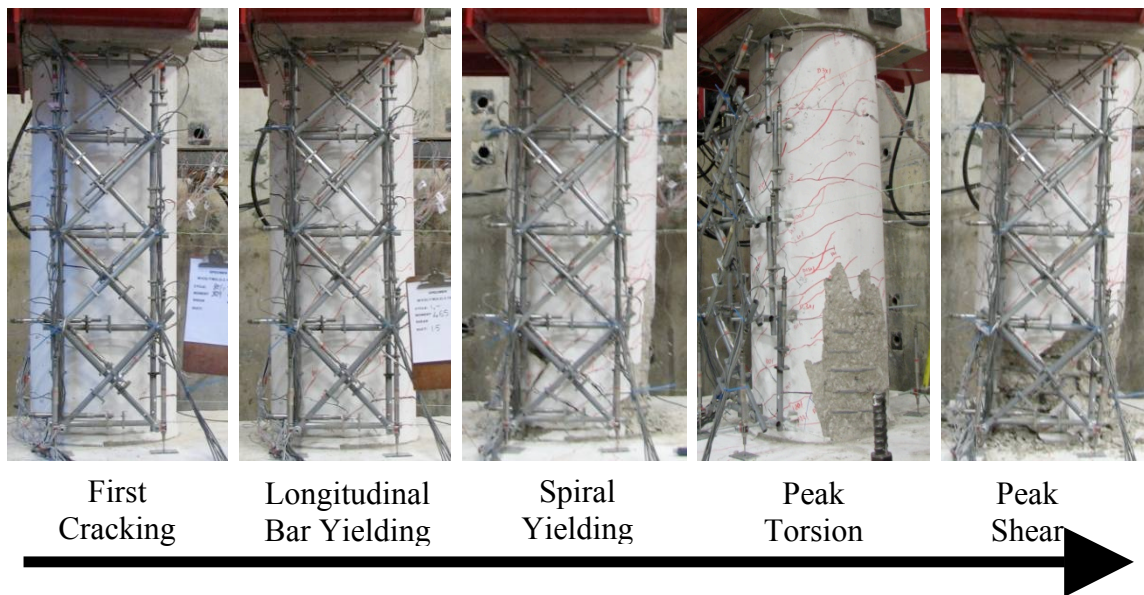
Figure 4.29 Damage Progression of H/D(3)-*T/M*(0.2)-1.32%

4.4.3.3.3 Column H/D(3)-*T/M*(0.4)-1.32%. Figure 4.31 shows the flexural and torsional hysteresis of the column with a spiral reinforcement ratio of 1.32% and tested at a *T/M* ratio of 0.4. The behavior of the specimen was dominated by both flexure and torsion. The specimen reached peak shear at a drift level of 4.4% and failed. The corresponding twist ductility at failure was 1.1; however, the peak torsional moment was reached at a twist ductility of 1.0. The locking and unlocking effect of spiral reinforcement was clearly reflected in the torsional hysteresis as in the pure torsion specimen (Figure 4.31b). The damage progression is shown in Figure 4.32.
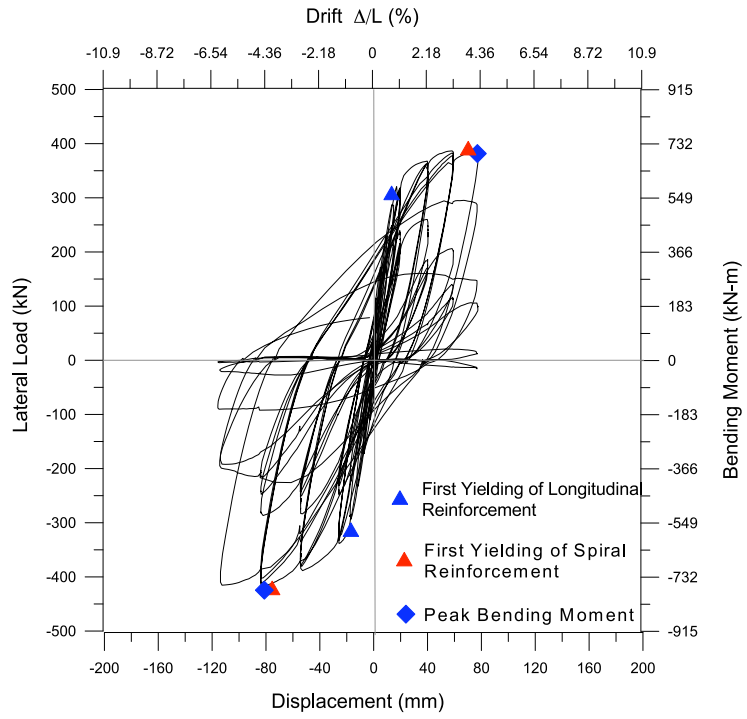
(a) Flexural
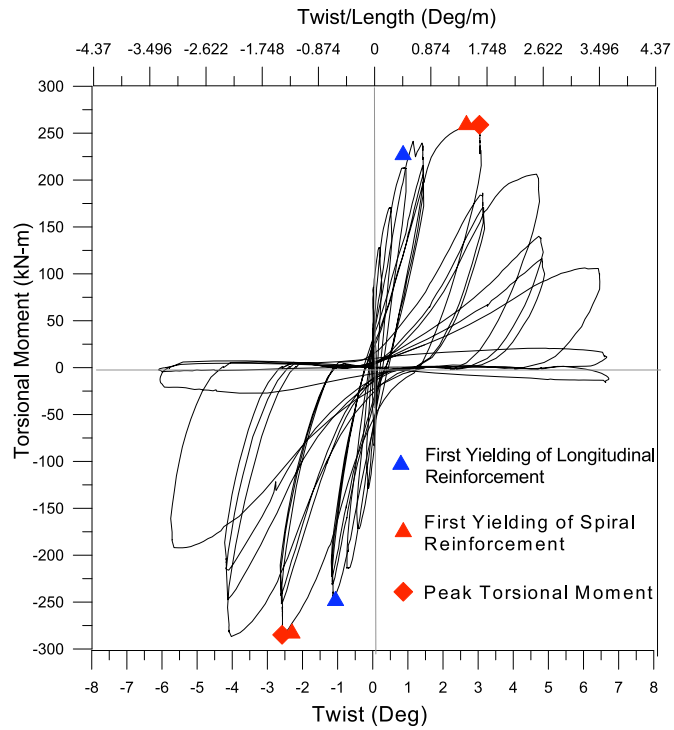
(b) Torsional

Figure 4.30 Hysteresis Behavior of H/D(3)-*T/M*(0.4)-1.32%
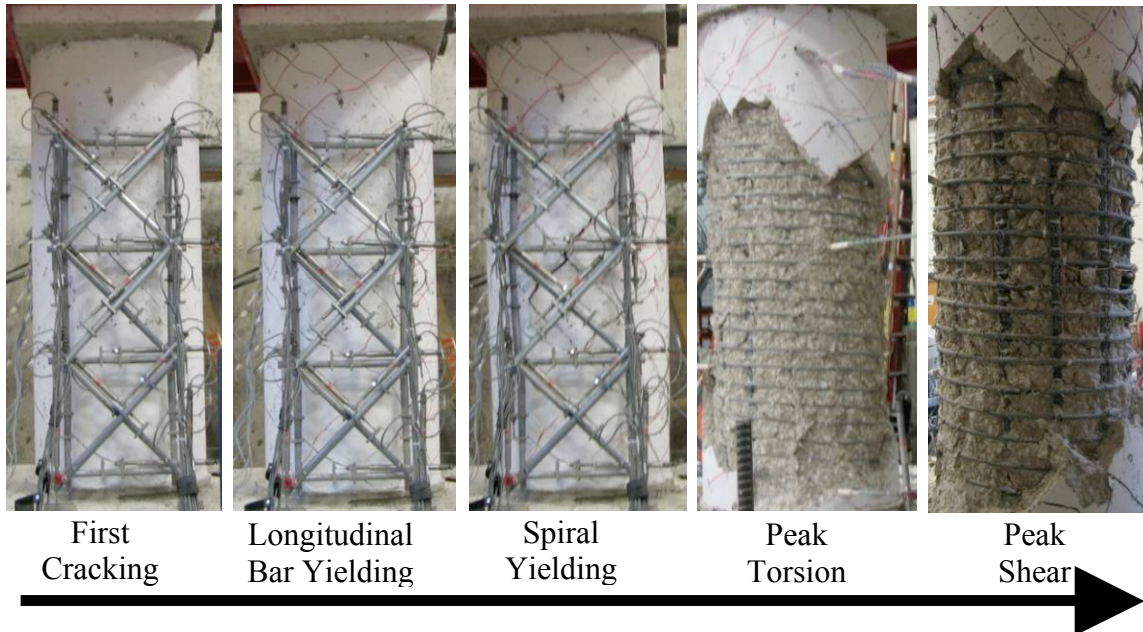
Figure 4.31 Damage Progression of H/D(3)-*T/M*(0.4)-1.32%

4.4.3.3.4 Column H/D(3)-*T/M*(0.6)-1.01%. Figure 4.32 shows the flexural hysteresis and torsional hysteresis of the column with a spiral reinforcement ratio of 1.32% and tested at a *T/M* ratio of 0.6. The behavior of the specimen was dominated by torsion due to application of higher T/M ratio of 0.6. The specimen reached the peak shear at a drift of 2.1% and finally failed at a drift level of 4.4. The corresponding twist ductility at failure was 1.2; however, the peak torsional moment was reached at a twist ductility of 1.0. The locking and unlocking effect of spiral reinforcement was clearly reflected in the torsional hysteresis as in the pure torsion specimen (Figure 4.32b). Figure 4.33 shows the damage progression of the column.
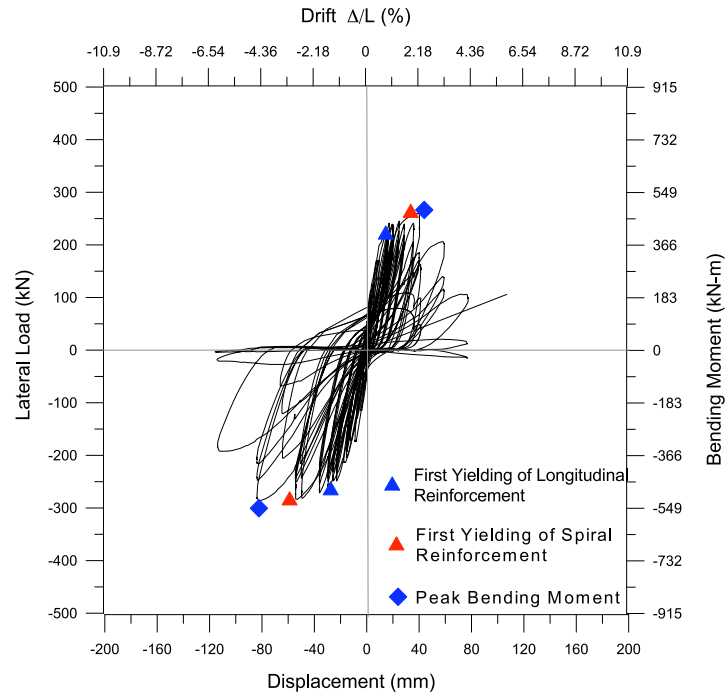
(a) Flexural
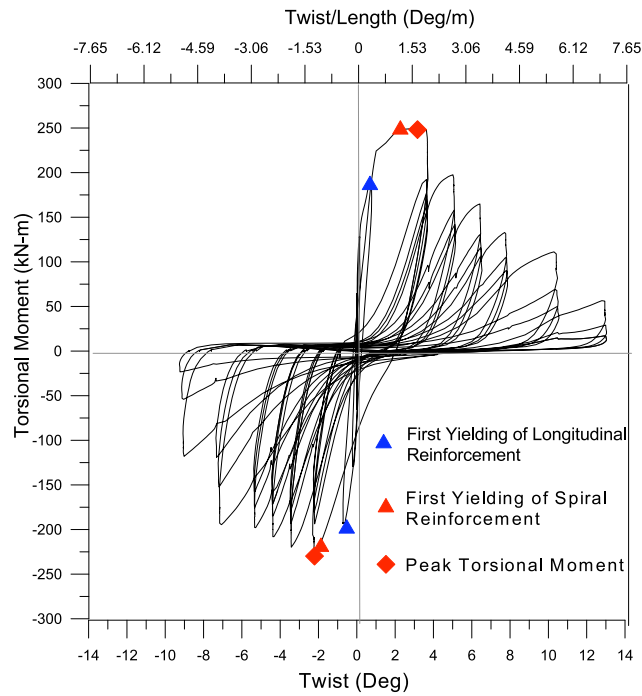
(b) Torsional

Figure 4.32 Hysteresis Behavior of H/D(3)-*T/M*(0.6)-1.01%

| First Cracking | Longitudinal Bar Yielding | Spiral Yielding | Peak Torsion | Peak Shear |
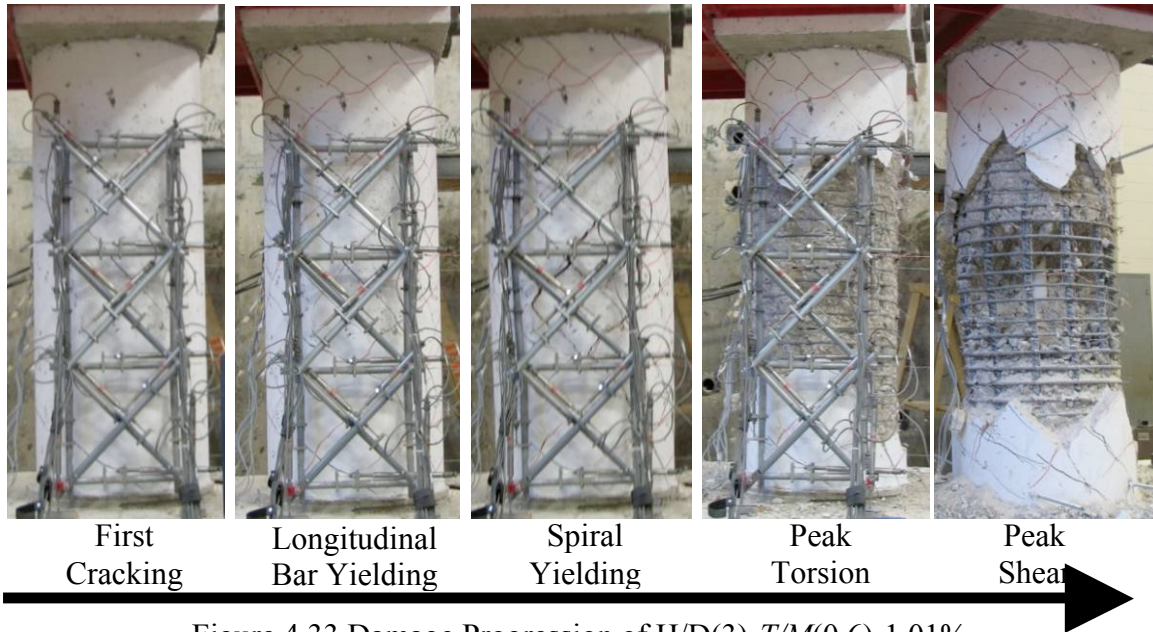
Figure 4.33 Damage Progression of H/D(3)-*T/M*(0.6)-1.01%

4.5. DISCUSSION OF RESULTS

The performance of specimens with respect to hysteresis behavior, load-displacement and torsional moment-twist envelopes are compared with respect to several test parameters in the following sections.

4.5.1. Flexural and Torsional Hysteresis Behavior. The hysteresis behavior of columns with low shear and low spiral ratio, low shear and high spiral ratio and high shear and high spiral ratio are compared in the following sections.

4.5.1.1 Columns with low shear and a low spiral ratio. Figure 4.34 shows the hysteretic load-displacement and torsional moment-twist curves of the columns tested at low shear (H/D=6) with low spiral ratio of 0.73% at various T/M ratios. The strength and stiffness degradation was clearly reflected both in the flexural and torsional hysteresis. It was more significant in the torsional hysteresis with increase in T/M ratio. The combination of bending and torsional moments reduced the torsional moment required to

cause yielding of the transverse reinforcement and the peak torsional component. Similarly, the combination of bending and torsional moment reduced the bending moment required to cause yielding of the longitudinal reinforcement and the peak component of bending moment. The ultimate displacement reduced with reduction in flexural energy dissipation capacity with increase in T/M ratio. Similarly, the ultimate twist reduced with torsional energy dissipation with decreasing T/M ratio. Due to the effect of combined loading, the energy dissipation reduced with increasing T/M ratios in the flexural hysteresis (Figure 4.34a) and with decrease in T/M ratios in torsional hysteresis (Figure 4.34b).

(a) Flexural   (b) Torsional

Figure 4.34 Hysteresis Behavior of Columns with Low Shear and Low Spiral Ratio

4.5.1.2 Columns with low shear and a high spiral ratio. Figures 4.36 and 4.37 compares the hysteretic load-displacement and torsional moment-twist curves of the columns at low shear with spiral ratios of 0.73% and 1.32% at T/M ratios of 0.2 and 0.4.

(a) Flexural　　　　　　　　　(b) Torsional
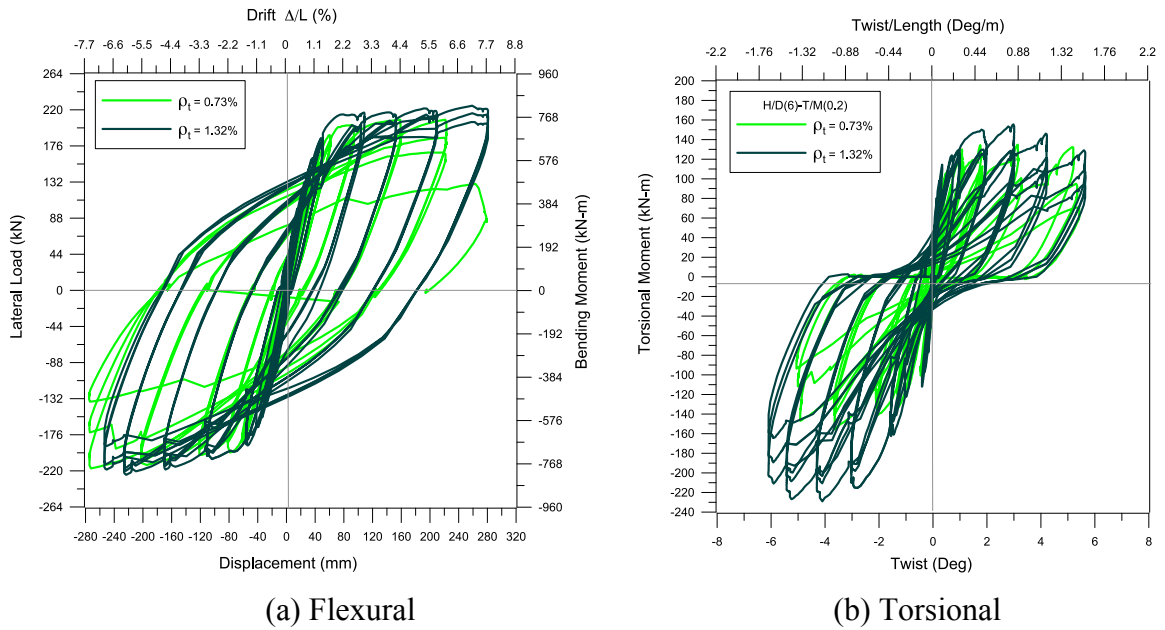
Figure 4.35 Hysteresis Behavior of Columns with Low Shear and High Spiral Ratio
at T/M (0.2)

(a) Flexural　　　　　　　　　(b) Torsional
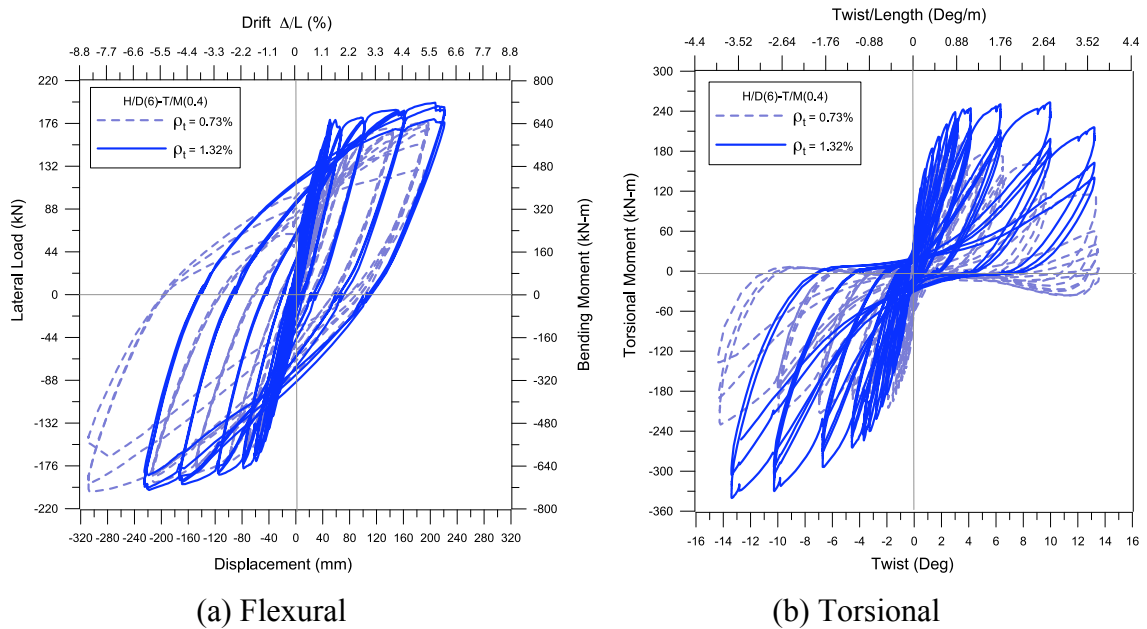
Figure 4.36 Hysteresis Behavior of Columns with Low Shear and High Spiral Ratio
at T/M (0.4)

Strength and stiffness increased both in the flexural and torsional hysteresis with an increase in the spiral reinforcement ratio. Due to increase in spiral ratio, the torsional strength and stiffness increased significantly due to its improved contribution to the resistance of shear and torsional loads. Figure 4.36 compares the flexural and torsional hysteresis curves for the column with a spiral reinforcement ratio of 0.73% and 1.32% subject to a T/M ratio of 0.2. The specimen failed as a result of both flexural and torsional strength and stiffness degradation. Damage contribution due to yielding of spiral and longitudinal reinforcement occurred at the same rate. Thus, the failure of the specimen was by both constant rate of flexural and torsional stiffness and strength degradation. Figure 4.37 shows the flexural and torsional hysteresis curves of the column with a spiral reinforcement ratio of 0.73% and 1.32% subjected to a T/M ratio of 0.4. The behavior of the specimen was dominated by torsion. The flexural strength and stiffness of the specimen did not degrade before its failure by torsion. The asymmetric behavior of the hysteresis curve under both flexure and torsion revealed a significant difference due to the locking and unlocking effect. Due to the effect of combined loading, the post-cracking torsional stiffness degraded faster than that observed under pure torsion. Torsional strength, bending strength, and deformational capacity also improved significantly with an increase in the spiral reinforcement ratio. Due to the effect of combined loading, the energy dissipation also increased with increasing spiral in the flexural hysteresis curves and in torsional hysteresis curves.

Figure 4.38 shows hysteretic load-displacement and torsional moment-twist curves respectively, of the columns tested at moderate shear (H/D=3) with spiral ratio of 1.32%. Both the flexural and torsional hysteresis clearly reflected the strength and

stiffness degradation. The strength and stiffness degradation was more evident in the torsional hysteresis as observed; in the columns tested at low shear. Due to the effect of combined loading, the energy dissipation also decreased as the T/M ratio increased in the flexural hysteresis (Figure 4.38a) and it decreased in torsional hysteresis (Figure 4.38b).

(a) Flexural   (b) Torsional
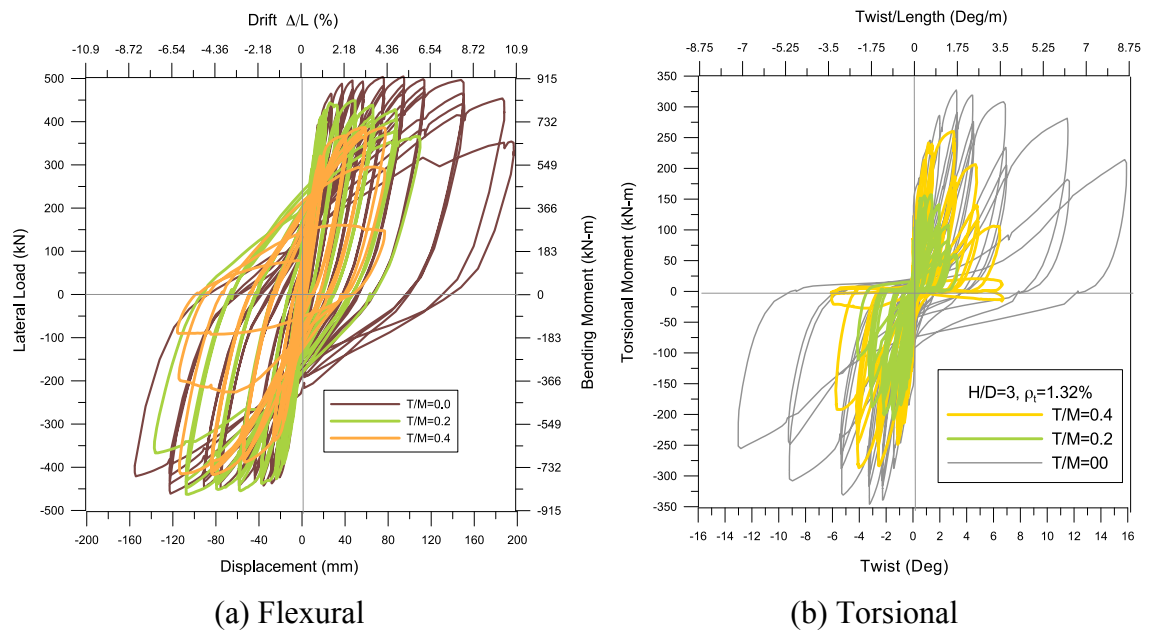
Figure 4.37 Hysteresis Behavior of Columns with Moderate Shear and High Spiral Ratio

4.5.2. Lateral Load-Displacement Envelopes. The lateral load-displacement curves of columns with low shear and low spiral ratio, low shear and high spiral ratio and high shear and high spiral ratio are compared in the following sections.

4.5.2.1 Columns with low shear and a low spiral ratio. Figure 4.38 compares the lateral load-displacement envelope curves of the columns tested at low shear with low spiral ratio of 0.73% under combined loading. Due to the effect of combined loading, torsional and bending strengths dropped considerably according to the applied *T/M* ratio. Marginal strength and stiffness degradation was observed for the column tested at a *T/M*

ratio of 0.1. For the other columns tested at higher *T/M* ratios of 0.2 and 0.4, strength and stiffness degraded significantly with an increase in the loading cycles at each ductility level. With an increase in the *T/M* ratio, the yielding displacement increased, and the lateral load corresponding to the first yielding of longitudinal reinforcement decreased.
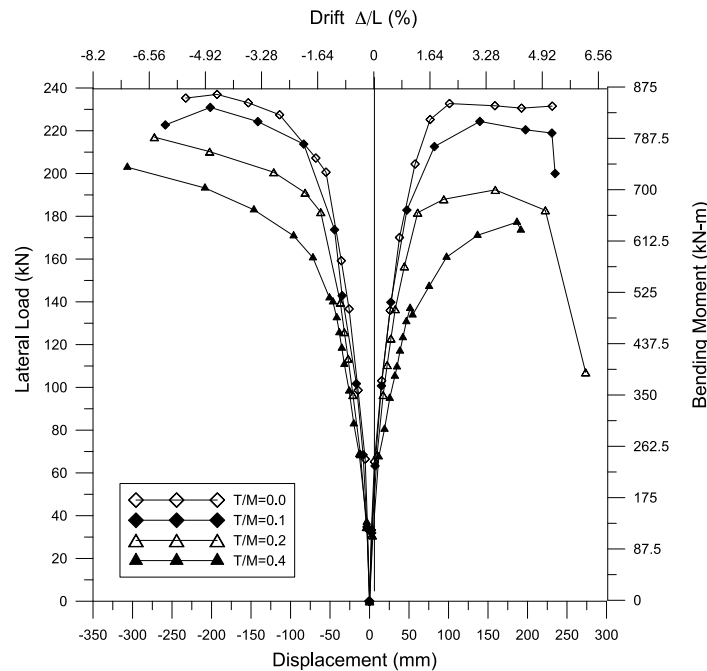
Figure 4.38 Comparison of Lateral Load-Displacement Envelopes of Columns with Low Shear and Low Spiral Ratio
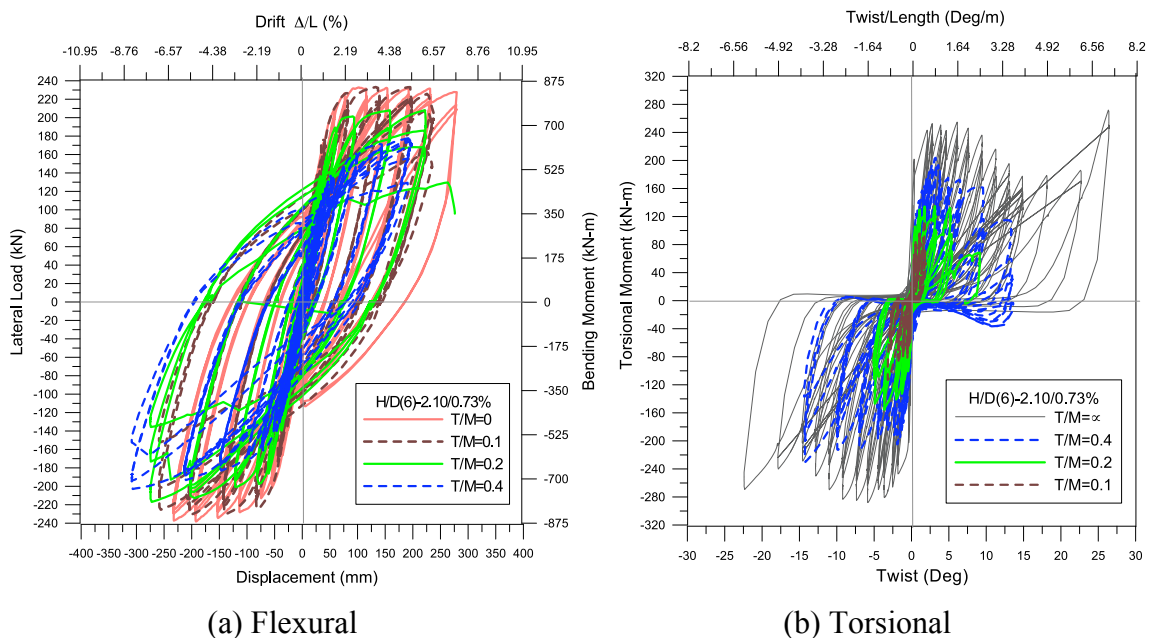
4.5.2.2 Columns with low shear and a high spiral ratio. Figure 4.39 compares the load-displacement curves. It clearly shows that due to the effect of combined loading, bending strength decreases considerably according to the applied T/M ratio as observed in the columns with a low spiral ratio. Strength and stiffness degraded with increases in the loading cycles at each ductility level. Torsional strength, bending strength, and deformational capacity improved significantly with an increase in the spiral reinforcement ratio. The components of shear stresses from bending and torsion are

additive, resulting in more damage and less load resistance. Thus, the asymmetric nature

of the flexural envelopes under combined bending and torsion occurred because one face

was subject to higher shearing stresses.
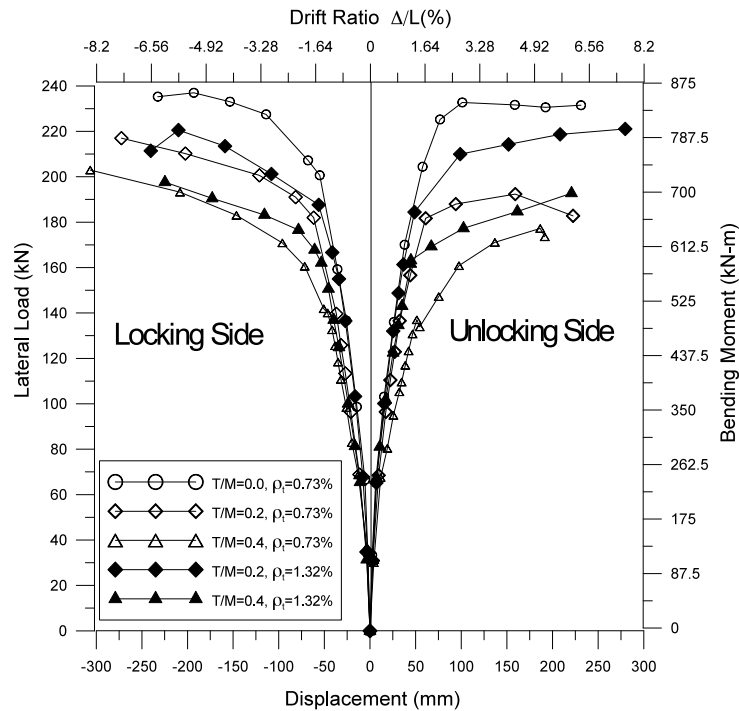
Figure 4.39 Comparison of Lateral Load-Displacement Envelopes of Columns with Low
Shear and High Spiral Ratio

4.5.2.3 Columns with moderate shear and a high spiral ratio. Figure 4.40

compares the lateral load-displacement envelope curves under combined loading for the

columns tested at moderate shear (H/D=3). Due to the effect of combined loading,

torsional and bending strengths dropped considerably according to the applied *T/M* ratio,

as observed in the columns with low shear and a low spiral ratio. For the columns tested

at higher *T/M* ratios of 0.2 and 0.4, strength and stiffness degraded significantly with an

increase in the loading cycles at each ductility level. With an increase in the *T/M* ratio,

the yielding displacement increased, and the lateral load corresponding to the first yielding of longitudinal reinforcement decreased.
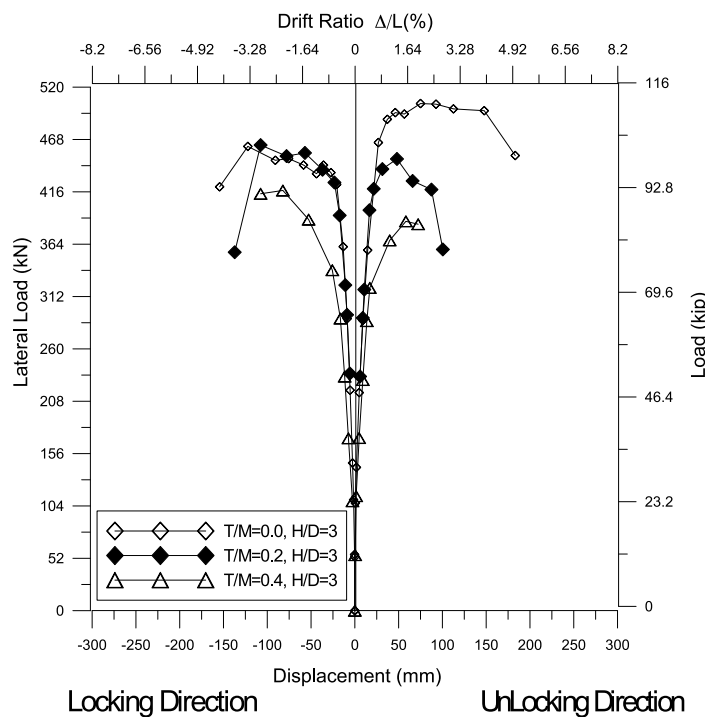
Figure 4.40 Comparison of Lateral Load-Displacement Envelopes of Columns with Moderate Shear and High Spiral Ratio

4.5.3. Torsional Moment-Twist Envelopes. The lateral load-displacement curves of columns with low shear and low spiral ratio, low shear and high spiral ratio and high shear and high spiral ratio are compared in the following sections.

4.5.3.1 Columns with low shear and a low spiral ratio. Figure 4.41 compares the torsional moment-twist curves for columns with a low spiral ratio of 0.73% and low shear (H/D=6). Due to the effect of combined loading, these curves demonstrate that torsional strengths decreased considerably according to the applied T/M ratio. The asymmetric nature of the torsional envelopes was due to the locking and unlocking effect of the spiral reinforcement, as explained in the behavior of columns under pure torsion.
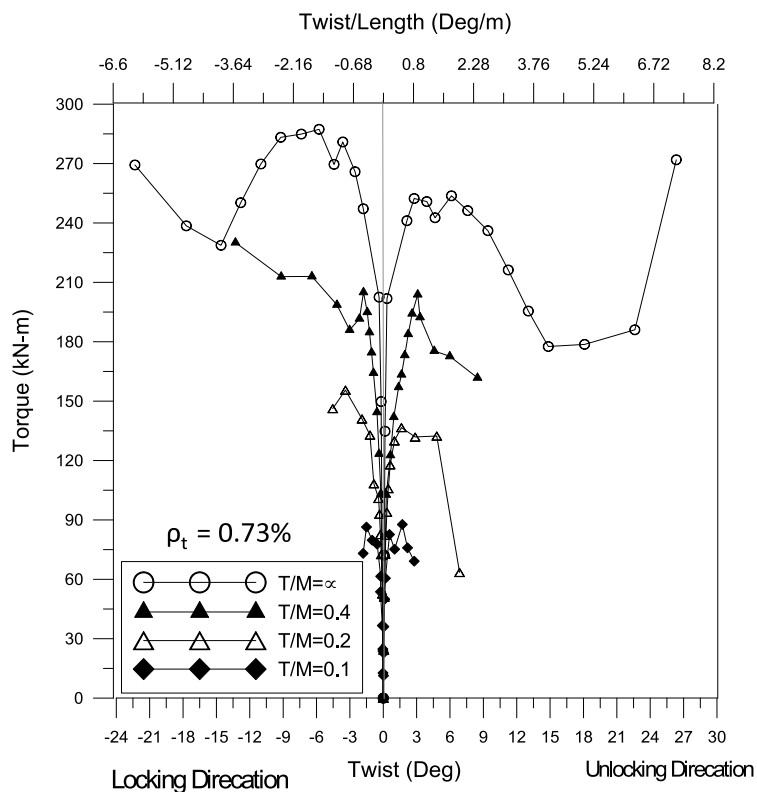
Figure 4.41 Comparison of Torsional Moment-Twist Envelopes for Columns with Low Shear and Low Spiral Ratio

4.5.3.2 Columns with low shear and a high spiral ratio. Figure 4.42 compares the torsional moment-twist curves for the columns with a spiral ratio of 0.73% and 1.32% tested at low shear (H/D=6). Torsional strength improved significantly, and the twist capacity increased with increase in spiral ratio. The locking effect of spiral ratio was more pronounced at a higher spiral ratio and T/M ratio.
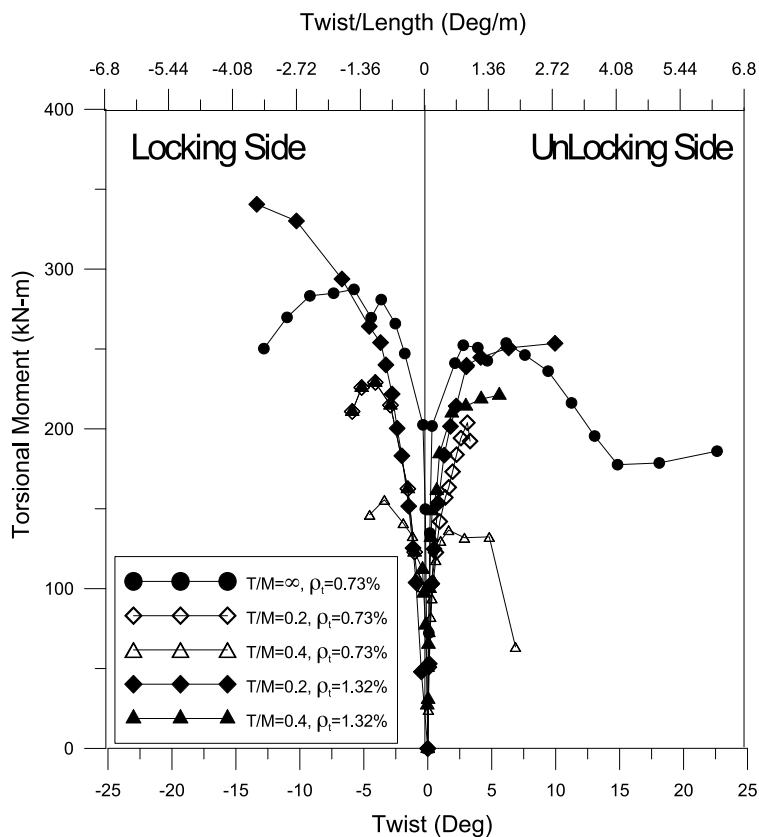
Figure 4.42 Comparison of Torsional Moment-Twist Envelopes for Columns with Low Shear and High Spiral Ratio

4.5.3.3 Columns with moderate shear and a high spiral ratio. Figure 4.43 compared the torsional moment-twist envelopes of columns tested at moderate shear with a high spiral ratio. Strength and stiffness degraded significantly with an increase in the loading cycles at each ductility level for all the columns. The asymmetric nature of the torsional envelopes was again due to the locking and unlocking effect of the spiral reinforcement as observed in the columns tested at low shear with low spiral ratio. Due to the combination of bending and torsional moments, the post-yield torsional stiffness degraded faster than under pure torsion.
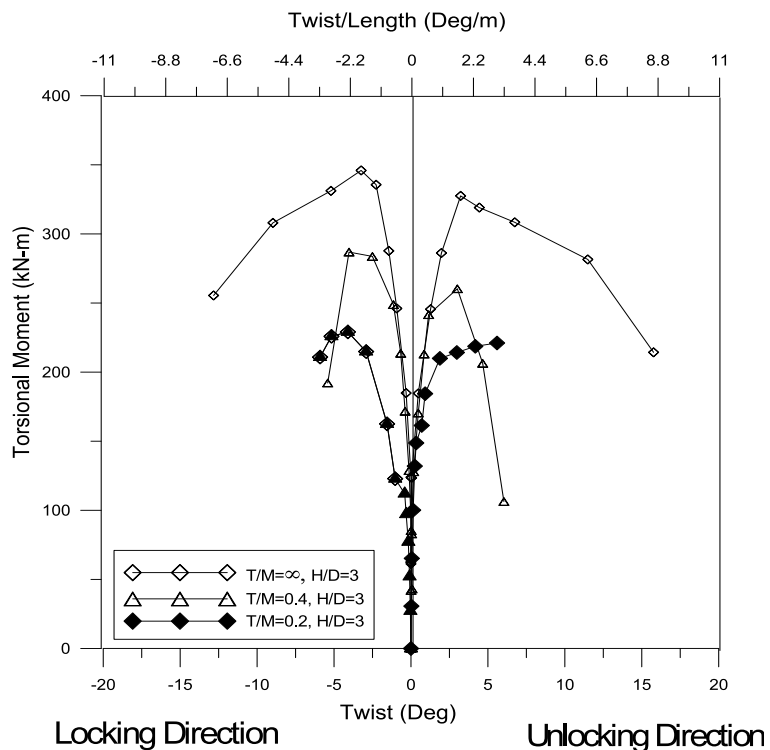
Figure 4.43 Comparison of Torsional Moment-Twist Envelopes of Columns with
Moderate Shear and High Spiral Ratio

4.5.4. Comparison of Principal Tensile and Shear Strains. Three layers of
linear variable displacement transformer (LVDT) rosettes were employed to measure the
curvature and principal strains at the expected damage locations as explained in Section
3.5.1. Figure 4.44 shows the variation in shear strains with respect to lateral load and
torsional moment for the columns tested under combined loading. Measured average
strains were very sensitive to the number of cracks occurring over the gage length.
Accordingly, the values cannot be considered accurate, but approximate. Though, these
values are approximate the variation in shear strain was clearly observed. The shear
strains increased with an increase in the T/M ratio for any given bending moment (Figure
4.44a) and decreased with an increase in the T/M ratio for any given torsional moment
(Figure 4.44b).
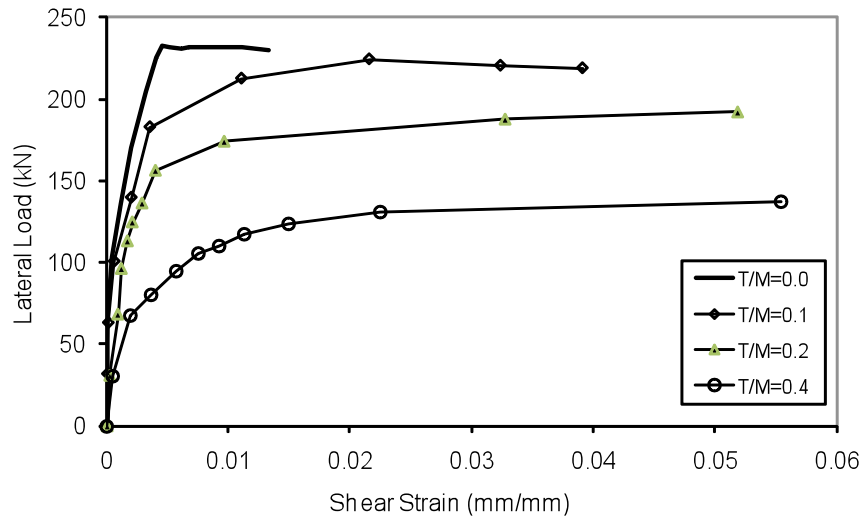
(a) Flexure
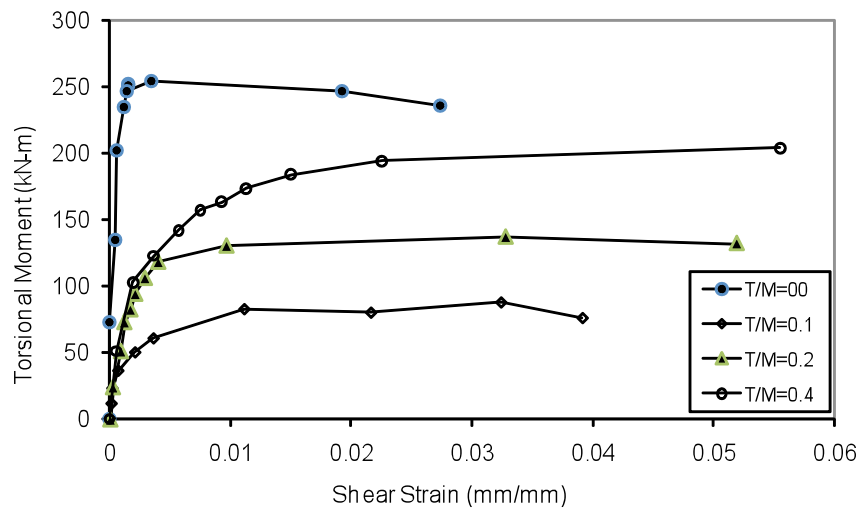
(b) Torsion

Figure 4.44 Variation in Shear Strain from Rosette at 600 mm from Base

Figure 4.45 shows the variation in principal tensile strain with respect to the applied bending moment and torsional moment. It also shows that the principal tensile strain increased with an increase in the T/M ratio.
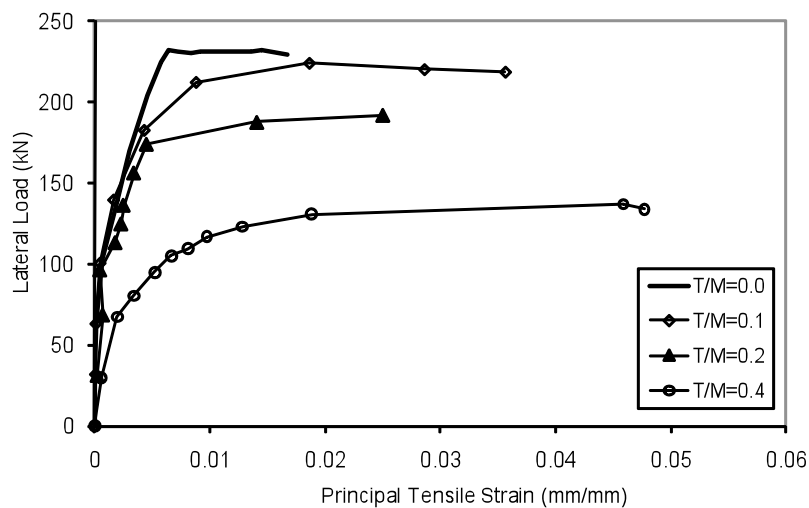
(a) Flexure
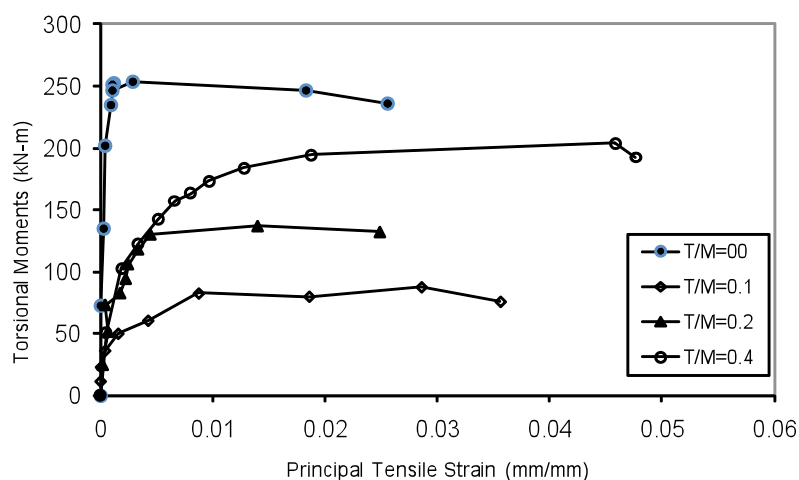
(b) Torsion

Figure 4.45 Variation in Principal Tensile Strains from Rosette at 600mm from Base

4.5.5. Comparison of Displacement and Twist Profiles along the Height.

Figure 4.46 shows the displacement distribution along the height of the columns under combined bending and torsion. It clearly reflects the stiffness degradation due to the addition of torsional moments at the yield as well as at ultimate state. However, this degradation was more evident at the ultimate state.
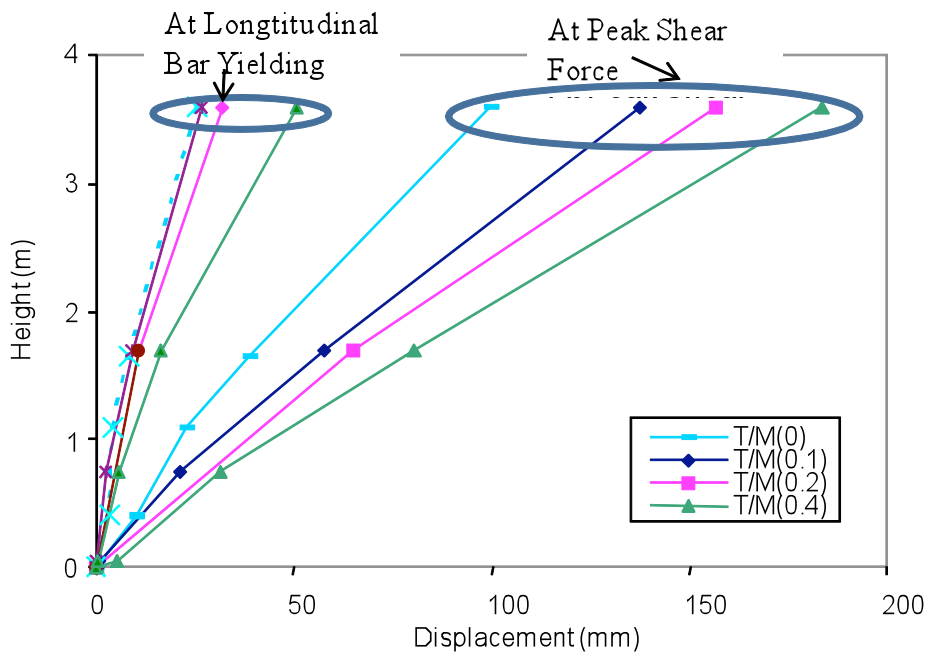
(a) Flexure
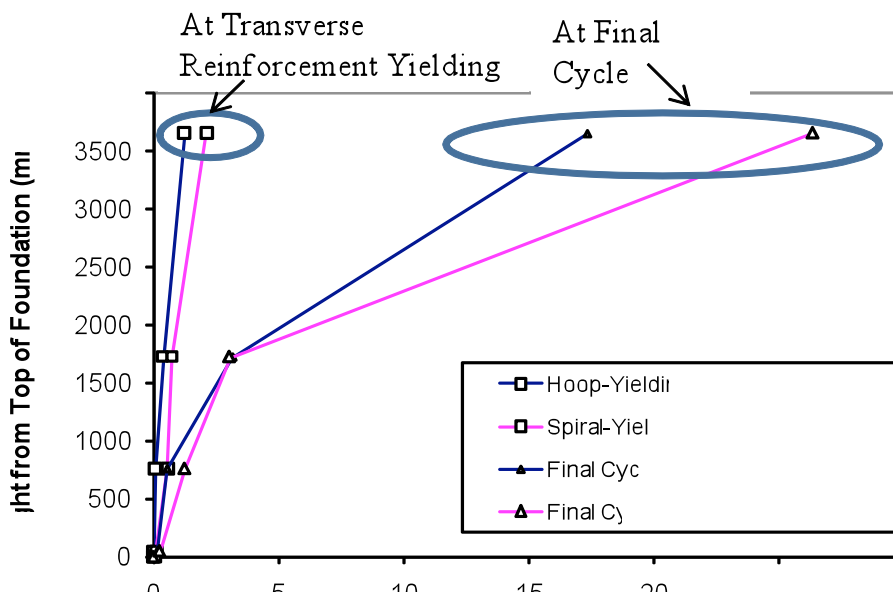
(b) Torsion

Figure 4.46 Displacement Profiles along the Height of the Column

The twist distribution along the height of the columns is shown in Figure 4.46b. Torsional stiffness did not show significant degradation until the yield of transverse reinforcement (both spiral and hoop). The twist distribution, however, clearly shows that stiffness degradation (in the damage zone) was more prominent at the middle height of the column under pure torsion after the yielding of transverse reinforcement. Lesser degradation in torsional strength was observed at the top and bottom due to the influence of boundary conditions from the loading block and foundation.

4.5.6. Bending Moment-Curvature Behavior. Moment-curvature analyses are widely used as a basis for assessing the nonlinear force displacement response of an RC member subjected to inelastic deformation demands under seismic loads. For this work, the curvature was calculated at 240 mm from the top of foundation. The yield curvature increased with respect to increases in the applied T/M ratio. Although flexural strength was attained earlier for the column with a T/M ratio of 0.4, there was a reduction in flexural stiffness, which in turn resulted in more curvature due to the simultaneous application of a higher level of torsion (Figure 4.47). Also, torsion changes the damage location in a column, which changes the behavior under combined loading. Methods for estimation of plastic-hinge lengths proposed by Priestley et al. (1996) are not applicable in the presence of torsional loadings because they do not yield practical results. Also, the yield moment increased and yield curvature dropped considerably with increase in the spiral reinforcement ratio (Figure 4.47b).
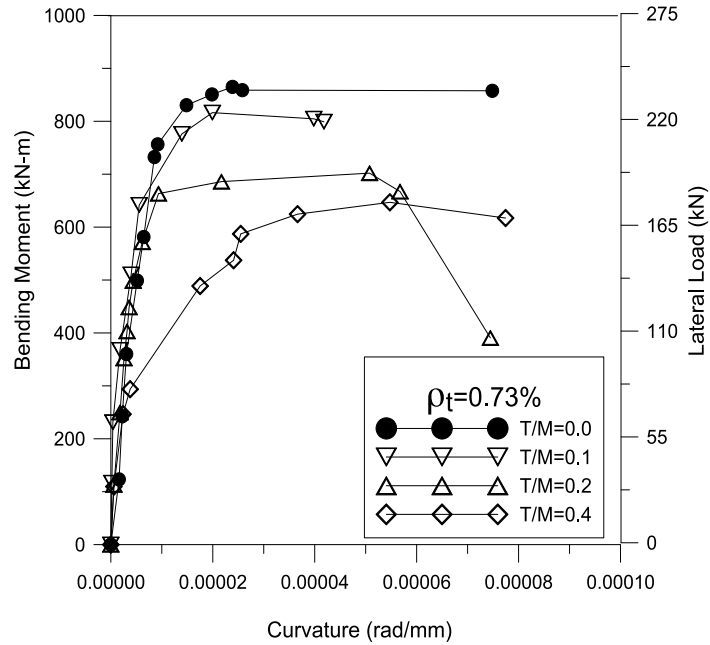
(a) Spiral Ratio of 0.73%
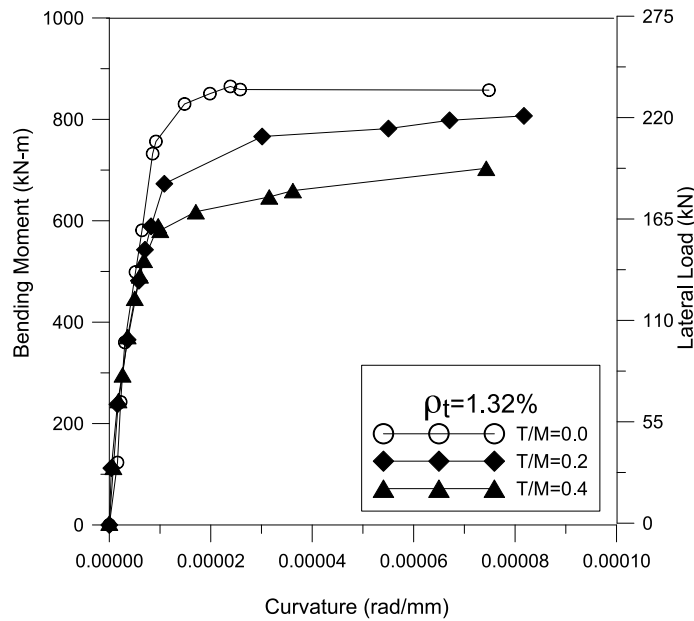
(b) Spiral Ratio of 1.32%

Figure 4.47 Bending Moment-Curvature Behavior under Combined Loading

4.5.7. Cracking and Spalling Distribution. Under combined shear force, bending, and torsional moments, the strain distribution in longitudinal and spiral reinforcement vary across the depth of the cross section and along the height of the

column. The inclination of principal compressive stress or the crack angle also varies along the length of the column and across the cross section. Figure 4.48 shows that with an increase in the *T/M* ratio, the angle of diagonal compression measured with respect to longitudinal axis increases. Test results show that these values varied from 134º under pure torsion to 90º for the column tested under flexure only, indicating that spirals will be highly strained with an increase in the applied *T/M* ratio, and longitudinal reinforcement will be highly strained with a reduction in applied *T/M* ratios.
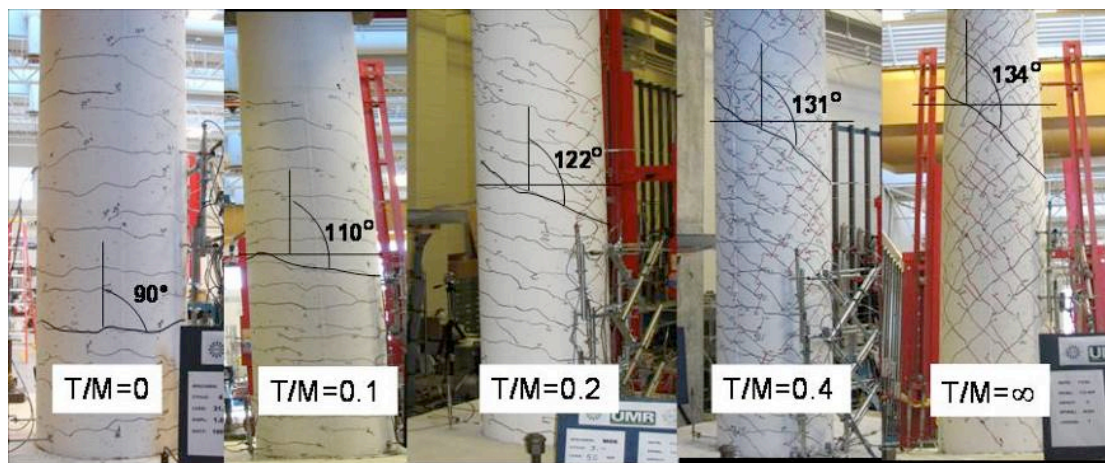
Figure 4.48 Effect of Combined Torsional and Bending Moments on the
Crack Distribution

Spalling of the concrete cover has been shown to be of concern for columns subjected to high axial loads or combined loading. Spalling of concrete cover starts at a load lower than the theoretical flexural strength. In the presence of torsional loads, the capacity of the column is limited to that of the spalling load. Two processes are prerequisites for the spalling of concrete cover away from the concrete core. The first involves interface cracking between the concrete cover and the core; the second requires a driving mechanism to push the concrete cover away from the section. Although ultimate strength may or may not be affected by spalling, it definitely affects the

serviceability requirements. A minimum thickness of concrete cover is recommended by various design codes to protect the reinforcement from severe environmental conditions which cause carrion or to satisfy design requirements for fire. This minimum thickness of concrete cover depends on the type and exposure of the member and the fire rating. Greater cover thickness, however, can also have adverse effects if the member is subjected to shear or combined shear and torsion. If the principal tensile stress due to shearing stresses from torsional moment and shear force exceeds the tensile strength of the concrete, spalling of concrete cover occurs along the plane of weakness formed by the transverse reinforcement. A thick concrete cover increases the possibility of spalling and leads to larger crack width and spacing (Rahal and Collins, 1995).

Figure 4.49 shows the spalling distribution along the height of the column. Under flexural loading, the spalling is influenced by the cover-to-lateral dimension ratio, the amount of transverse reinforcement, the axial load ratio, and the aspect ratio. Under torsional loadings, the concrete cover is assumed to spall off before the ultimate torsional capacity is reached; the shear flow path is related to the dimension of the stirrups. The timing of spalling is important from a design point of view. Whether it occurs before or after a column reaches the peak torsional load determines the effective cross-sectional dimensions to be used in the design calculations. If spalling occurs before a column reaches peak load, only core section excluding the concrete cover should be considered in the calculation of ultimate capacity of RC members. Researchers have modeled spalling in several ways for RC rectangular and box sections. Hsu and Mo (1985a) have suggested a simple model based on cover thickness and shear flow thickness to determine the whether spalling would occur or not. In a study by Rahal and Collins (1995) of

members under combined shear force and torsional moment, the potential for spalling was assumed to be proportional to the compressive force in the concrete cover, the cover thickness, and the area of the splitting plane occupied by the reinforcement; it was assumed to be inversely proportional to the concrete tensile strength and the size of the section. Spalling, however, depends on a number of factors, such as reinforcement ratio, clear cover, and type of section (square, rectangular, or circular), none of which have been adequately investigated.
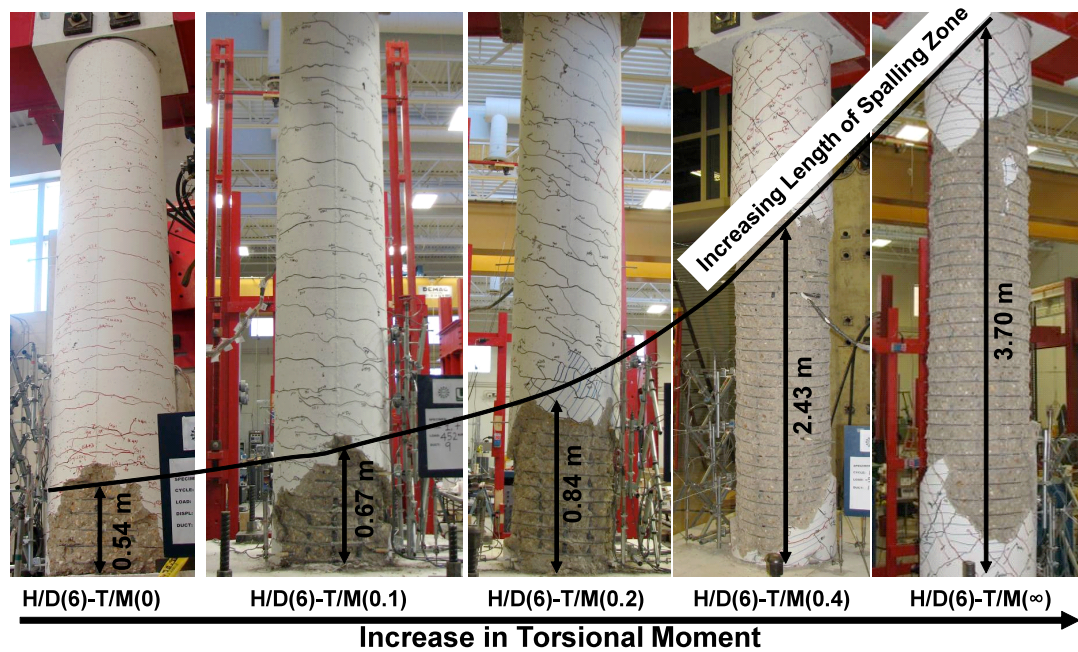
Figure 4.49 Effect of Combined Loading including Torsion on Spalling Distribution

4.5.8. Ductility and Energy Dissipation Characteristics. From a performance-based design point of view, designers are interested in strength, stiffness, deformation, and the energy dissipation capacity of members under combined loading [Lehman et al., 1998]. Energy dissipation capacity is an important parameter in assessing the seismic

performance of a structure. Reinforced concrete members dissipate energy through crack formation, internal friction resulting from plastic deformation of the reinforcement, and friction due to sliding of the concrete struts. The strength and stability of bridge columns and their superstructures depend on the capacity of the columns to sustain numerous inelastic deformation reversals without significant strength decay. Table 4.3 defines the parameters needed to define the energy dissipation and equivalent damping ratios of the RC columns with respect to flexural and torsional behavior. The energy dissipated in one cycle is the area under that cycle of loading in bending and torsion, as shown in Figure 4.50.

Table 4.3 Parameters for Energy Dissipation and Equivalent Damping Ratio

Parameters	Torsional Hysteresis		Bending Hysteresis	
Energy Dissipation	$E_{D,torsion} = A_{hyst,torsion}$	Eq. 4.6	$E_{D,flexure} = A_{hyst,flexure}$	Eq. 4.7
Average Peak Moment/Force	$T_m = \frac{1}{2}(T_{max} - T_{min})$	Eq. 4.8	$F_m = \frac{1}{2}(F_{max} - F_{min})$	Eq. 4.9
Average Peak Twist/ Displacement	$\theta_m = \frac{1}{2}(\theta_{max} - \theta_{min})$	Eq. 4.10	$\Delta_m = \frac{1}{2}(\Delta_{max} - \Delta_{min})$	Eq. 4.11
Effective Stiffness	$k_{eff,\,torsion} = \frac{T_m}{\theta_m}$	Eq. 4.12	$k_{eff,\,flexure} = \frac{F_m}{\Delta_m}$	Eq. 4.13
Strain Energy in Equivalent System	$A_{e,torsion} = \frac{k_{eff,\,torsion}}{2}(\theta_m)^2$	Eq. 4.14	$A_{e,flexure} = \frac{k_{eff,\,flexure}}{2}(\Delta_m)^2$	Eq. 4.15
Equivalent Damping System	$\xi_{eq,torsion} = \frac{A_{hyst,torsion}}{4\pi A_{e,torsion}}$	Eq. 4.16	$\xi_{eq,flexure} = \frac{A_{hyst,flexure}}{4\pi A_{e,flexure}}$	Eq. 4.17

(a) Bending hysteresis   **(b) Torsional hysteresis**
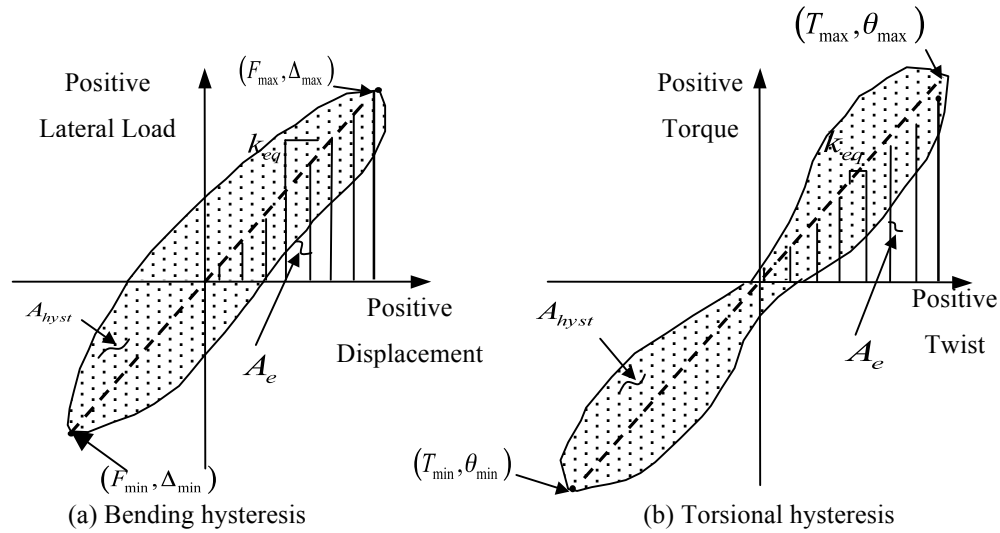
Figure 4.50 Energy Dissipation and Equivalent Definition of Parameters

Figure 4.51a and Figure 4.51b compare energy dissipated by the columns in the form of bending ($E_{D,bending}$) and torsion ($E_{D,torsion}$) respectively, for columns with a transverse spiral reinforcement ratio of 0.73% and an aspect ratio of 6. Bending energy dissipation decreases significantly with as the T/M ratio increases. Also, the torsional energy dissipation capacity decreases as the T/M ratio decreases (Figure 4.51). Similarly, Figure 4.53 shows variation in the equivalent damping ratio with respect to an increase in T/M ratios. The equivalent damping ratio is significantly lower for torsional hysteresis than for bending hysteresis.
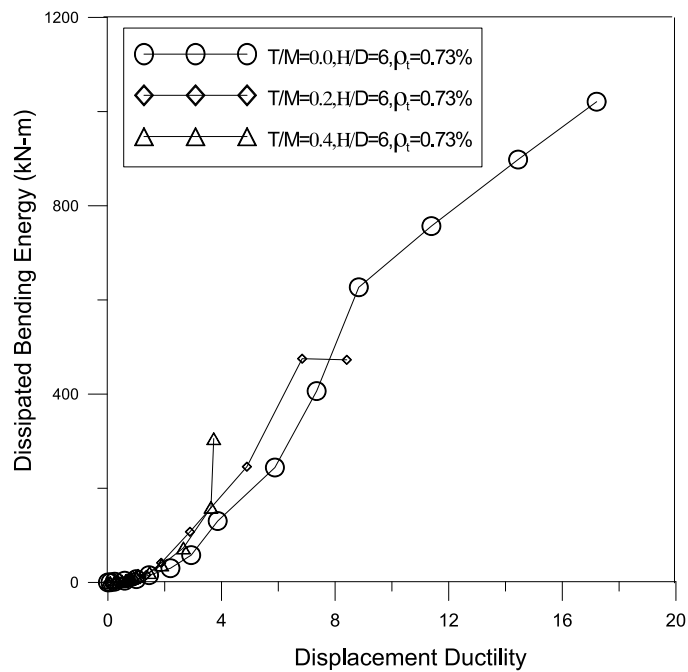
(a) Bending Hysteresis
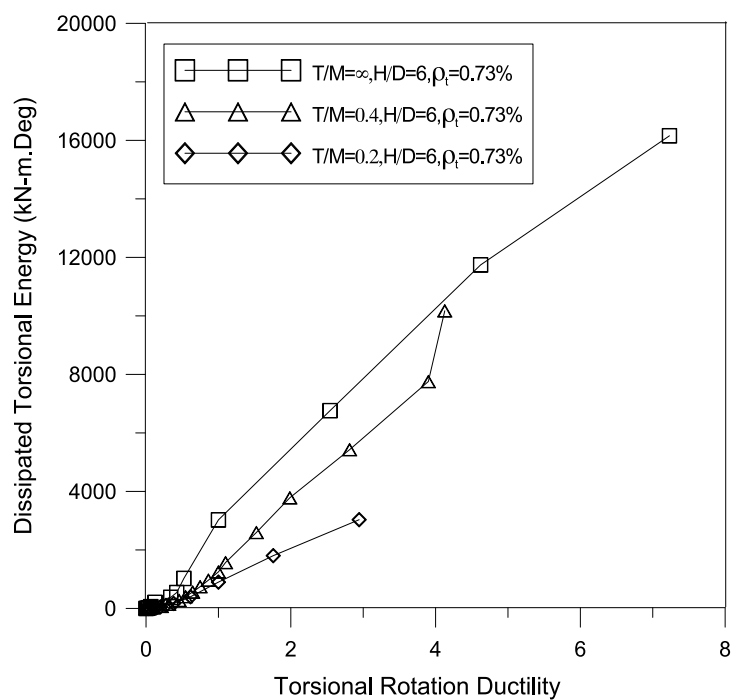
(b) Torsional Hysteresis

Figure 4.51 Cumulative Energy Dissipation
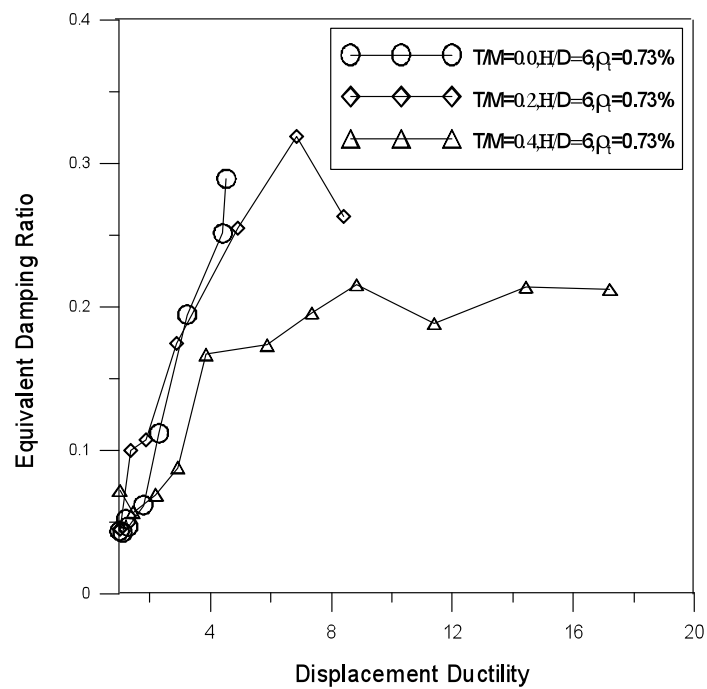
(a) Bending Hysteresis
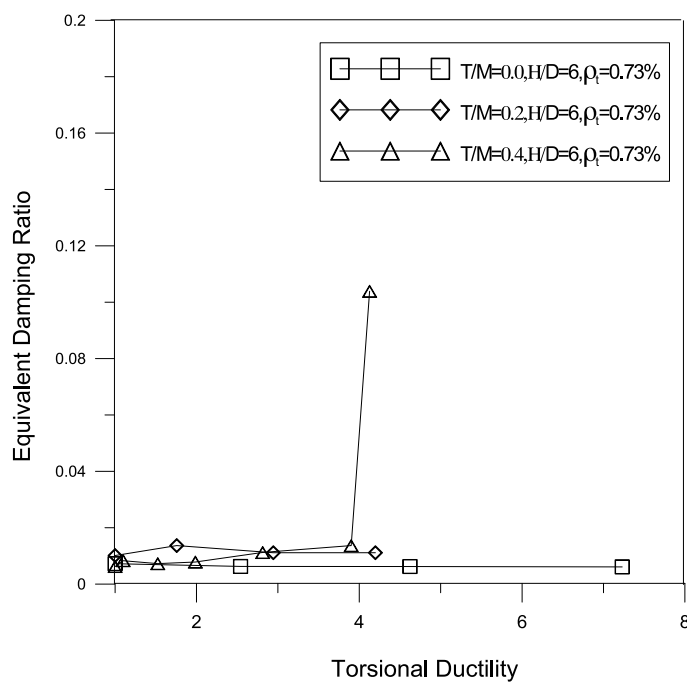
(b) Torsional Hysteresis

Figure 4.52 Effect of Torsion on Equivalent Damping Ratio

4.6. TORSION AND BENDING MOMENT INTERACTION DIAGRAMS

Test results were used to create the interaction diagrams (Figure 4.53) between torsion and bending moment. All the specimens subjected to combined loading reached their torsional capacity before reaching their flexural capacity. The longitudinal reinforcement, however, yielded before the spiral reinforcement. Yielding of longitudinal and spiral reinforcements occurred in quick succession for the columns reinforced with a spiral ratio of 0.73%. An increased spiral reinforcement ratio significantly improved the torsional and bending strengths. Interaction diagrams between torsion and bending moments were determined at the peak torsional moment (Figure 4.53a) and peak shear (Figure 4.53b) for all the columns tested. The *T/M* ratio was maintained close to the desired loading ratio in all the columns until peak torsional moment was attained in the unlocking direction. Soon after the columns reached peak torsional strength, the desired loading ratio could no longer be maintained because the torsional stiffness was degrading much faster in both the unlocking and locking directions. The bending strength, however, started degrading faster than the torsional strength in the locking direction for the columns with a spiral reinforcement ratio of 1.32%; hence, the load ratio could not be maintained to complete the test. As expected, the columns with a lower aspect ratio (H/D=3) had more shear capacity (i.e., approximately about twice that of the columns with a higher aspect ratio (H/D=6)). However, there was no appreciable change in the torsional moment and bending moment capacity due to change in aspect ratio.
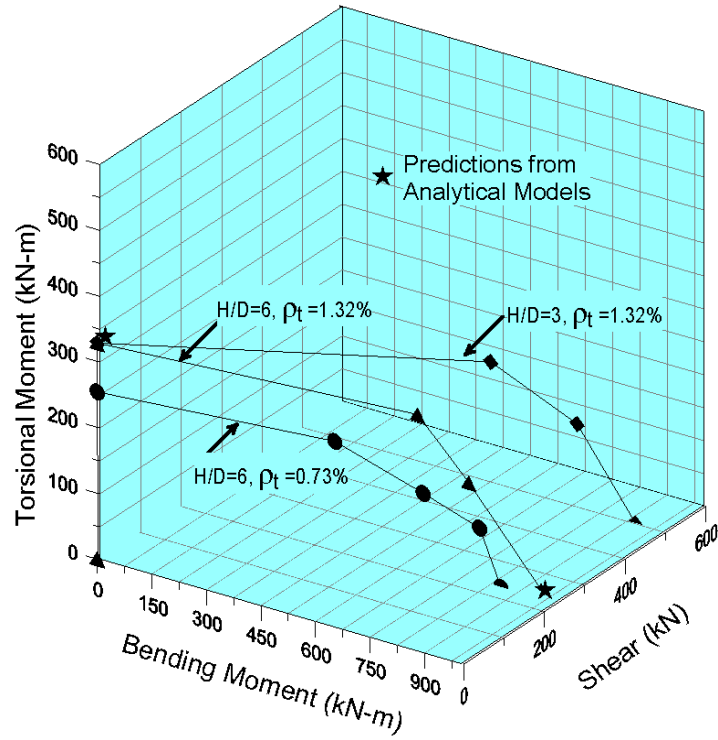
(a) Peak Torque
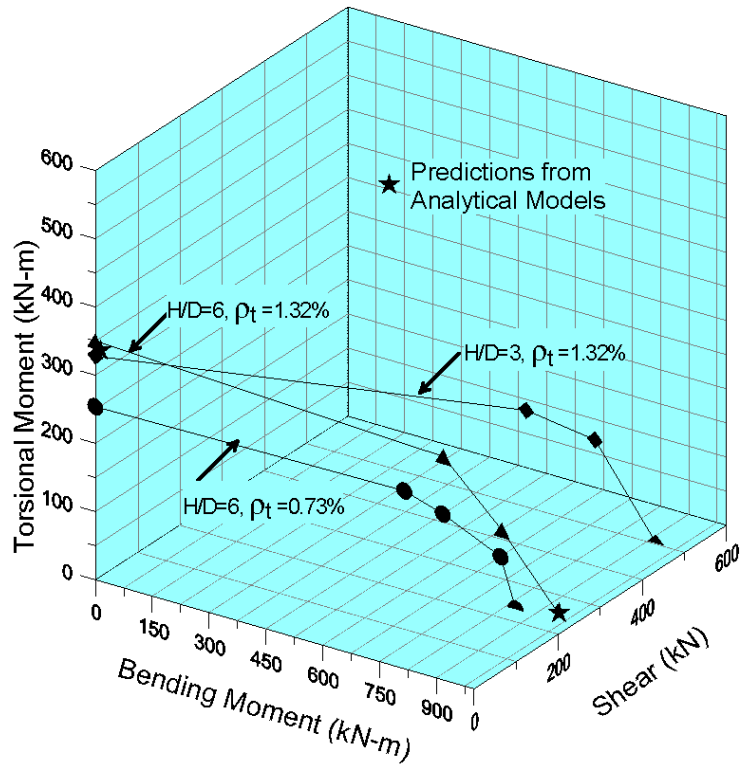
(b) Peak Shear

Figure 4.53 Bending-Shear-Torsion Interaction Diagrams

Interaction between bending and torsional moment depended on a number of factors, such as the amount of transverse and longitudinal reinforcements, the aspect ratio of the section, and concrete strength. The effect of combined loading on flexural cracking and longitudinal yielding was not significant until the *T/M* ratio reached 0.2. Combined loading, however, had a pronounced effect on spiral yielding and ultimate torsional strength. Torsional moment corresponding to yielding of the spiral reinforcement and the ultimate torsional strength followed in quick succession in all the tested columns. This indicates that a transverse reinforcement ratio which is adequate from a confinement design point of view may not satisfy design performance standards in the presence of torsional loadings.

4.7. EFFECT OF SHEAR SPAN

The behavior of RC columns can be classified as flexure- or shear-dominated or with significant flexure-shear interaction. The aspect ratio of a column determines the level of interaction between flexure and shear. Few studies have addressed flexure and shear interaction; therefore, the phenomenon is not well understood (Ang et al., 1989; and Kowalsky and Priestley, 2000). To adopt plastic analysis methods in the design of RC members by assigning plastic-hinges at the weak regions, inelastic response at the plastic zone must be assessed in the presence of combined loadings including torsion with various levels of shear. Specifically, designers must quantify flexural response so that the dependability of flexural plastic-hinges can be assessed under dominant shear/torsional loads.

The results of tests on six columns supported an investigation of the effect of shear span under combined loading including torsion. One column was tested under cyclic flexure (H/D=3), (ii) one under cyclic pure torsion (H/D=3), and (iii) four under combined cyclic bending and torsion with varying ratios of T/M (such as 0.2 and 0.4) and different shear spans (H/D=6 and 3). Analytical models were used to predict the behavior of columns with an aspect ratio of 6 under flexure and of others under pure torsion. All the columns had a spiral reinforcement ratio of 1.32%. Figure 4.54 shows the interaction of torsion and bending moment loading curves for the columns under combined loading with two different aspect ratios. These curves indicate that the columns with low and high aspect ratios reached their torsional and bending moment capacity almost simultaneously in the unlocking direction. Their behavior in the locking direction, however, was somewhat different. After yielding of the spiral and longitudinal reinforcement, the bending and torsional strength increased in a nonlinear fashion due to the locking effect of the spiral, which resulted in better confinement of the concrete core. Hence, the ratios were not closely maintained in the locking direction. Torsional and bending strength did not change significantly with a change in the aspect ratio, mainly due to the flexural failure mode observed in the columns with high and low aspect ratios. However, the effect of aspect ratio would have been more pronounced if the columns had failed in shear.
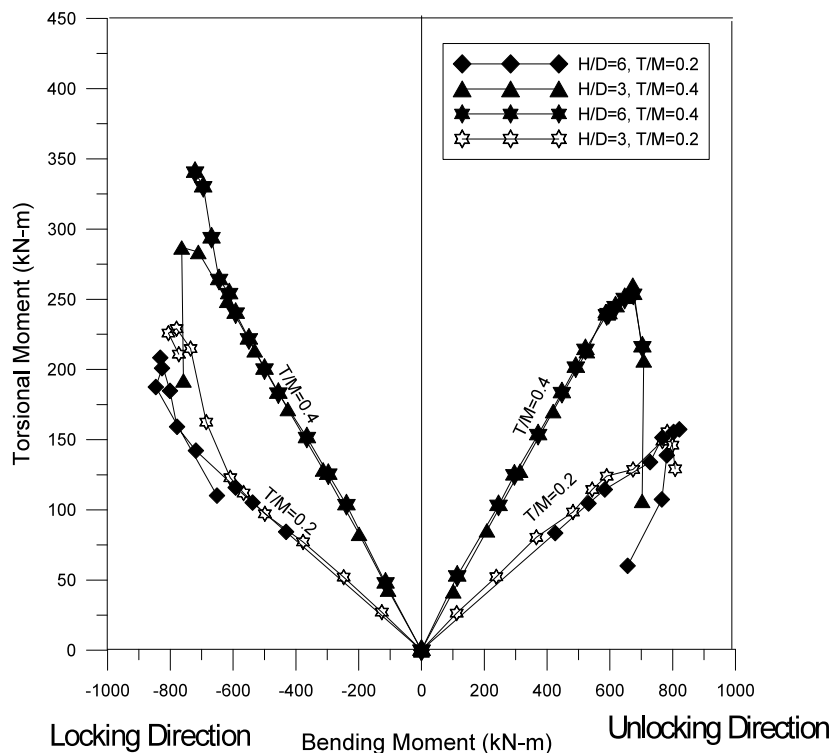
Figure 4.54 Interaction of Torsion-Bending Moment Loading Curves for
Aspect Ratios of 6 and 3

Figure 4.55 shows the lateral load-displacement and torsional moment-twist curves for specimens under combined loading. As expected, the columns with a lower aspect ratio had more shear capacity (i.e., about twice that of the columns with a higher aspect ratio). However, there was no appreciable increase in the torsional moment capacity. The displacement and twist capacity decreased considerably with a reduction in aspect ratio. Interaction diagrams between torsion and bending moments were determined at peak torsional moment (Figure 4.56a) and peak shear (Figure 4.56b) for the columns tested. The T/M ratio was not maintained close to the desired loading ratio in the locking direction due to the locking effects of the spiral reinforcement. This variation in T/M ratio resulted in nonlinear variation in bending and torsional stiffness after the spiral and longitudinal reinforcement yielded.

(a) Lateral Load-Displacement Curves

(b) Torsional Moment-Twist Curves
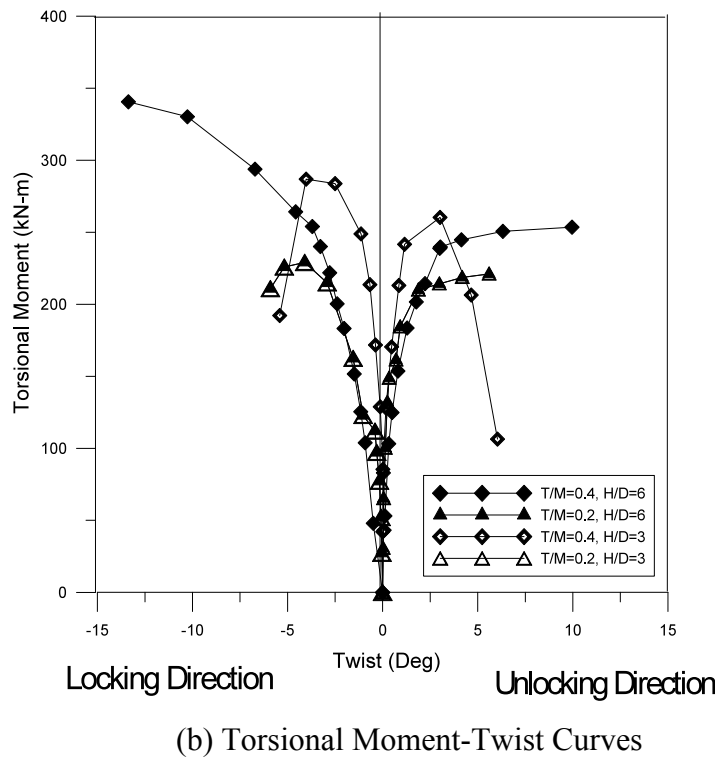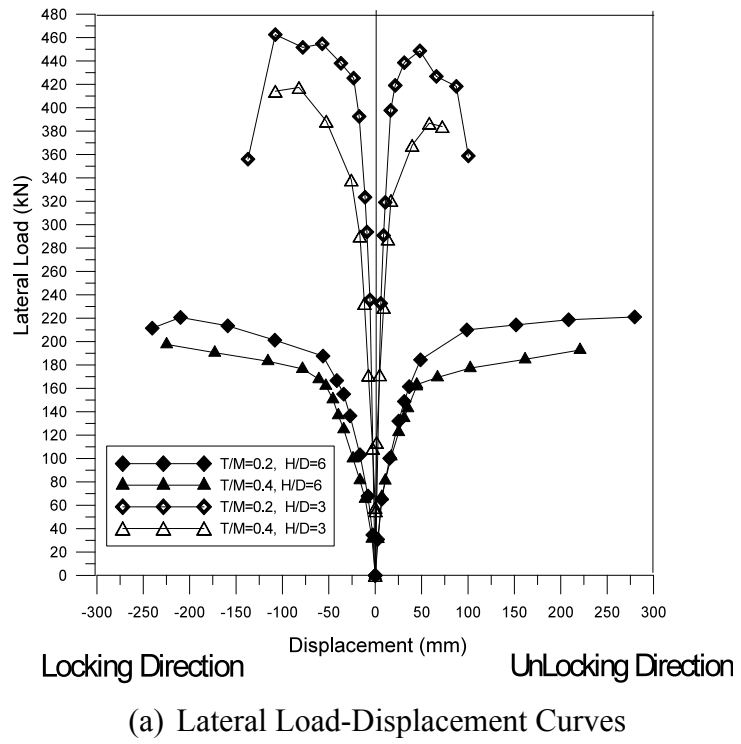
Figure 4.55 Comparison of Behavior for H/D=6 and H/D=3

(a) Peak Torsional Moment

(b) Peak Shear Force
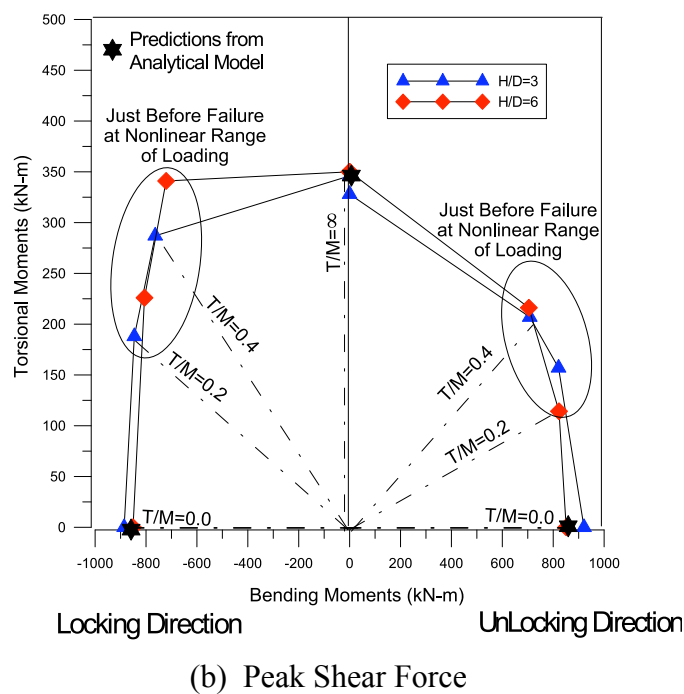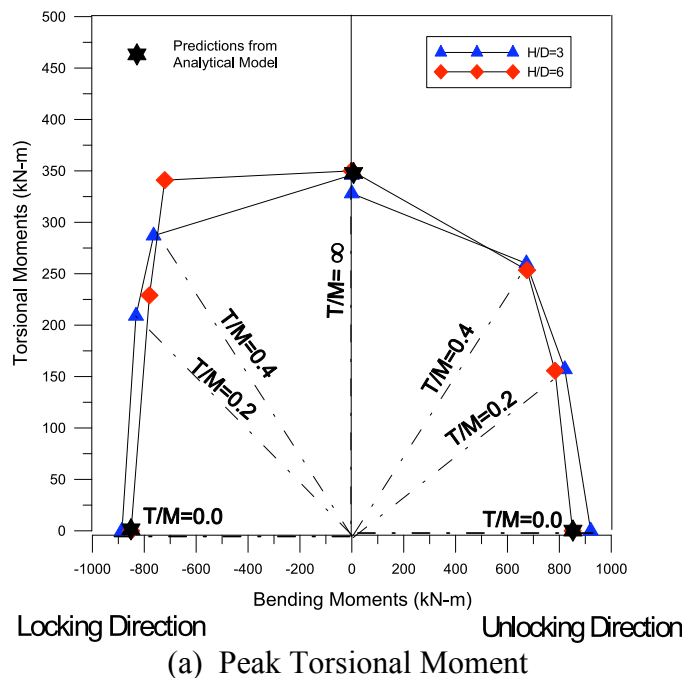
Figure 4.56 Torsion-Bending Moments Interaction Diagrams

The presence of shear stresses due to torsional moment and shear force induced strains not only in the transverse reinforcement but also in the longitudinal reinforcement. The effect of shear span on strain distribution is shown in Figure 4.58 and 4.59 for the

specimens tested under T/M ratios of 0.2 and 0.4. Both longitudinal and transverse strain increased due to the increased level of shear force applied on the columns with moderate shear.
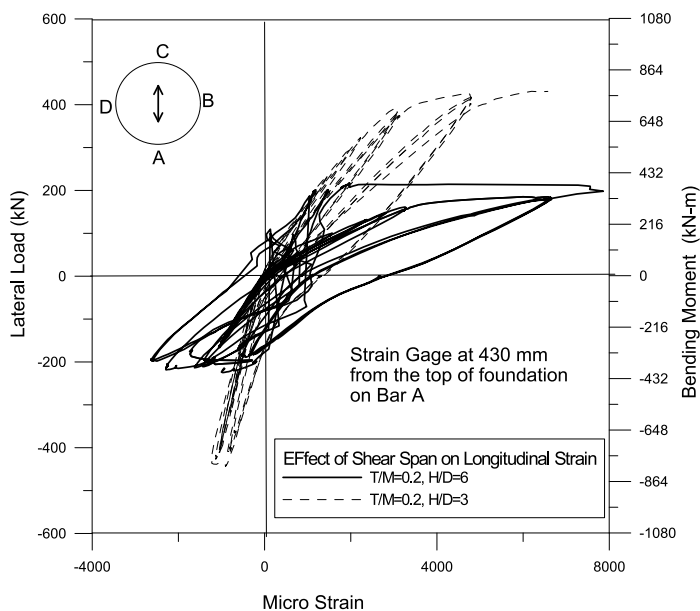
(a) Longitudinal Strain
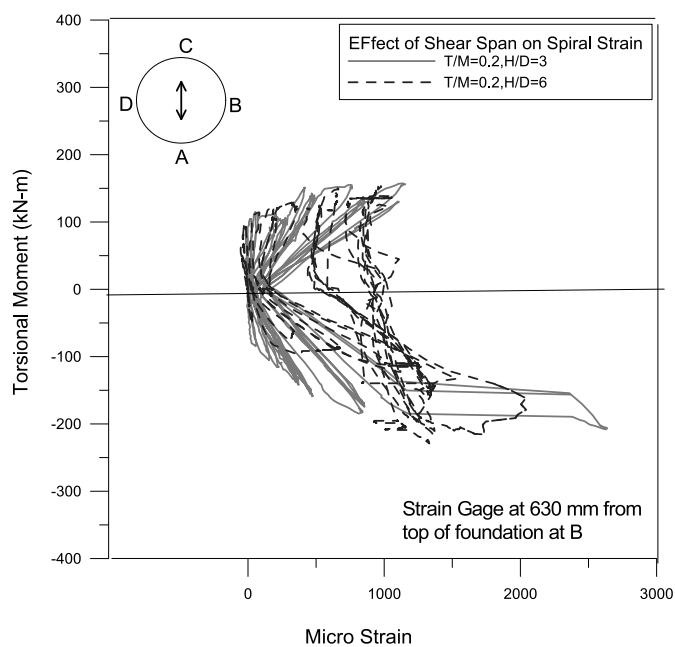
(b) Spiral Strain

Figure 4.57 Effect of Shear Span on Strain Distribution under Combined Bending and Torsion moments at T/M (0.2)
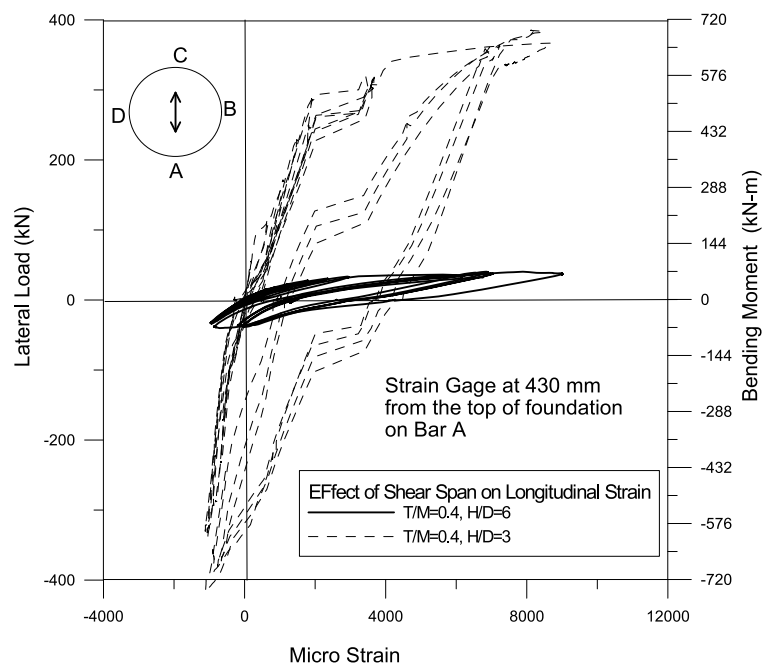
(a) Longitudinal Strain
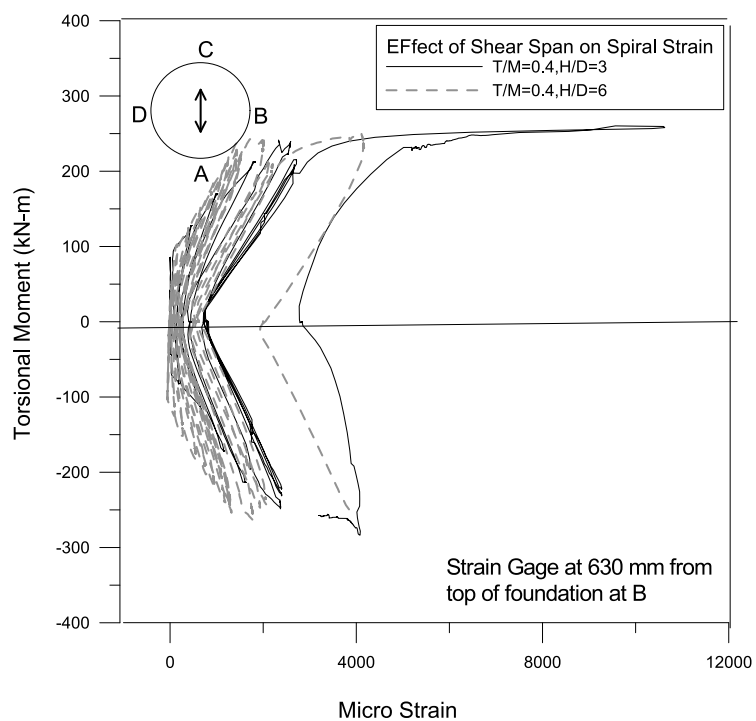
(b) Spiral Strain

Figure 4.58 Effect of Shear Span on Strain Distribution under Combined Bending and Torsion Moments at T/M (0.4)

Figure 4.59 compares damage distribution in columns with various aspect ratios. For the lower T/M ratio of 0.2, the damage distribution in the column with a high aspect ratio (H/D=6) was localized to 26% of the total height of the column, whereas it was 40% for the column with a lower aspect ratio (H/D=3). For a higher T/M ratio of 0.4, the damage distribution was nearly the same in columns with high and low aspect ratios (H/D=6, H/D=3) i.e., about 75% of the height of the column. These results show that for flexure dominant behavior, damage distribution was more localized for columns with a high aspect ratio. Finite element analysis of the columns with different aspect ratio under combined loading also illustrated the similar behavior (Prakash et al., 2009).
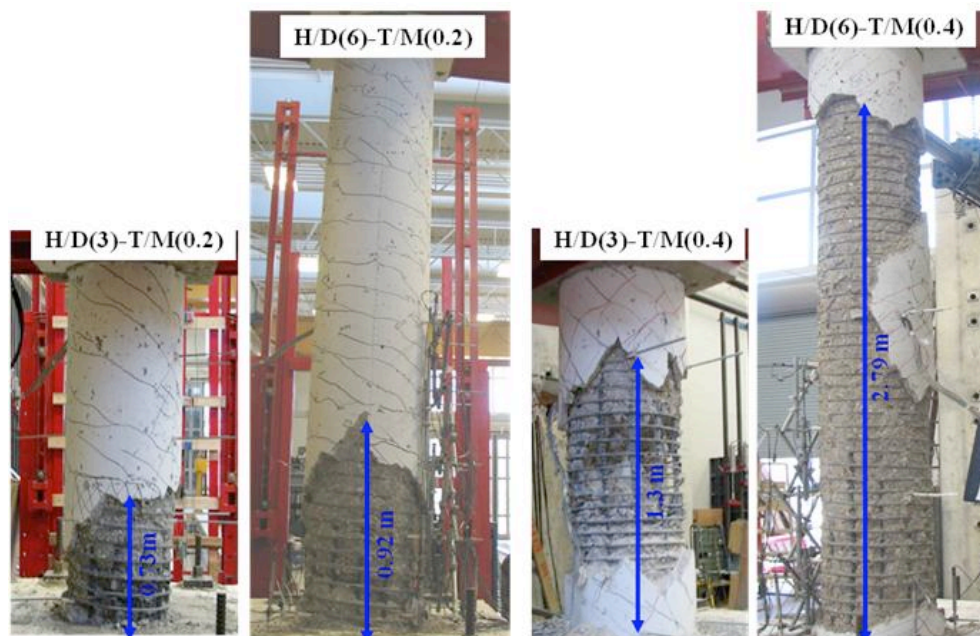
Figure 4.59 Effect of Shear Span on Damage Distribution under Combined Bending and Torsional Moments

Columns with a lower aspect ratio of three or shear-dominated columns had less energy dissipation capacity in both bending and torsion than did columns with an aspect ratio of six (Figure 4.60). The lower aspect ratio reduced torsional twist and displacement

ductility. Further, the equivalent damping ratio decreased with a reduction in the aspect

ratio or with decrease in the moment-to-shear ratio (Figure 4.61).

(a) Bending Energy

(b) Torsional Energy

Figure 4.60 Effect of Shear Span on Energy Dissipation
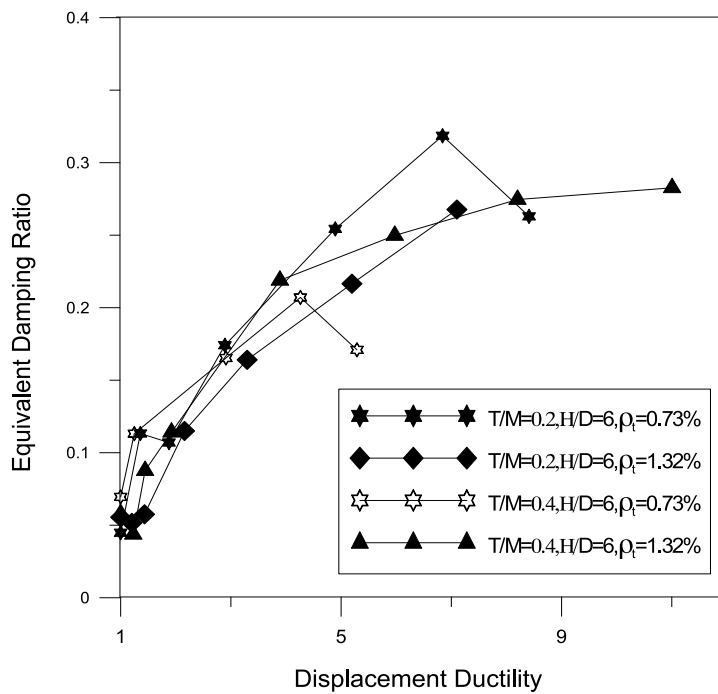
(a) Bending Hysteresis
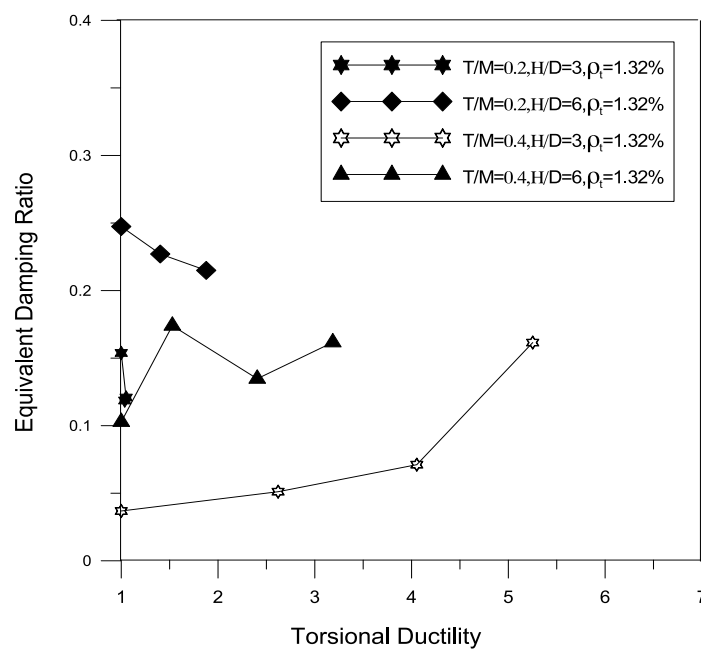
(b) Torsional Hysteresis

Figure 4.61 Effect of Shear Span on Equivalent Damping Ratio

4.8. EFFECT OF SPIRAL REINFORCEMENT RATIO

Figure 4.62 compares the torsional moment-twist hysteresis curves of columns with spiral reinforcement ratios of 0.73% and 1.32% under pure torsion. These curves are approximately linear up to the point of cracking; thereafter, they become nonlinear with a reduction in torsional stiffness. Post-cracking stiffness decreased proportionally with an increase in the cycles of loading until the effect of dowel action became apparent with a spiral reinforcement ratio of 0.73%. The column with a spiral reinforcement ratio of 1.32% had greater post-cracking stiffness and strength. The yielding strength increased up to 20% and the ultimate strength up to 30% due to an increase in the spiral reinforcement ratio from 0.73% to 1.32%. The locking and unlocking effect of the spirals was also apparent in both negative and positive loading cycles. During the positive cycles of twisting, the spirals were unlocked, which contributed to significant spalling and reduced the confinement effect on the concrete core. On the other hand, during the negative cycles of loading, the spirals were locked and contributed more to the confinement of concrete core. This effect was reflected in the asymmetry of the hysteresis loop at higher levels of loading. At higher cycles of loading, the load resistance in the negative cycles was higher than that in the positive cycles of loading due to the added confinement generated by the locking effect of the spiral reinforcement. The column with a spiral reinforcement ratio of 1.32% had higher post-cracking stiffness and strength. The yielding strength increased up to 20% and the ultimate strength up to 30% due to an increase in the spiral reinforcement ratio from 0.73% to 1.32%. More importantly, twist ductility increased significantly.
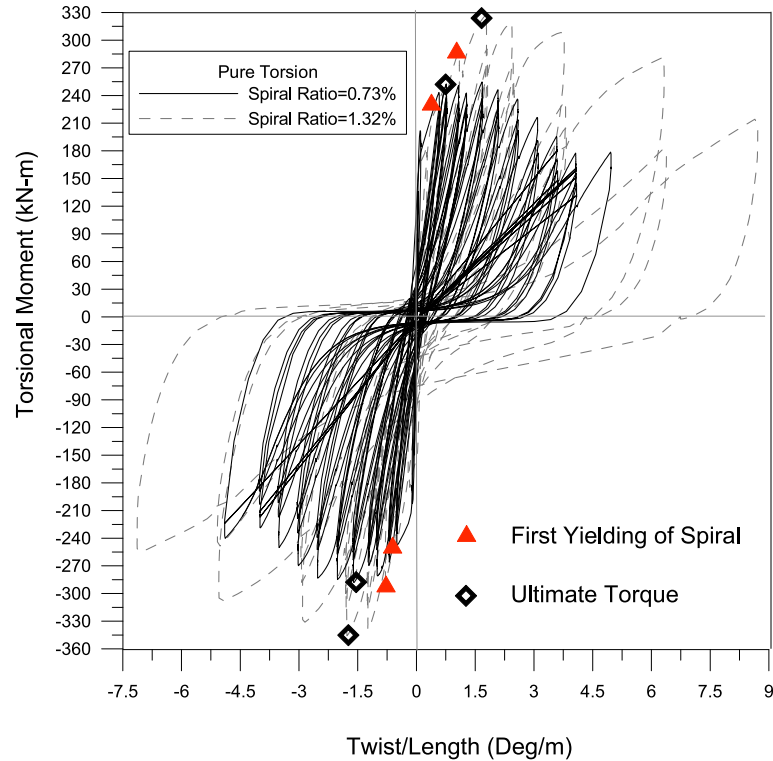
Figure 4.62 Torsional Hysteresis under Pure Torsion with Various Spiral Reinforcement Ratios

Four columns were tested under combined bending and torsional moments by maintaining T/M ratios of 0.2 and 0.4 at two different spiral reinforcement ratios of 0.73% and 1.32%, as shown in Table 3.1. In all the columns tested under combined flexural and torsional moments, flexural cracks first appeared near the bottom of the column. With increasing cycles of loading and higher T/M ratios, the angle of the cracks became more inclined at greater heights above the top of the footing. In all columns, side A exhibited less damage than side C, (Figure 3.3) largely because that side A always experienced more shear stresses. These additional stresses were due to the additive components of stresses caused by shear and torsion, and they were greater than stresses in side C where torsional shear stresses were subtracted from shear stresses.

Figure 4.63 compares the flexural hysteresis and torsional hysteresis of the column with a spiral reinforcement ratio of 0.73% and 1.32%, tested at a T/M ratio of 0.2. The behavior of the specimen was dominated by both flexure and torsion. The failure of the specimen was by both flexural and torsional stiffness and strength degradation.

(a) Flexure   (b) Torsion
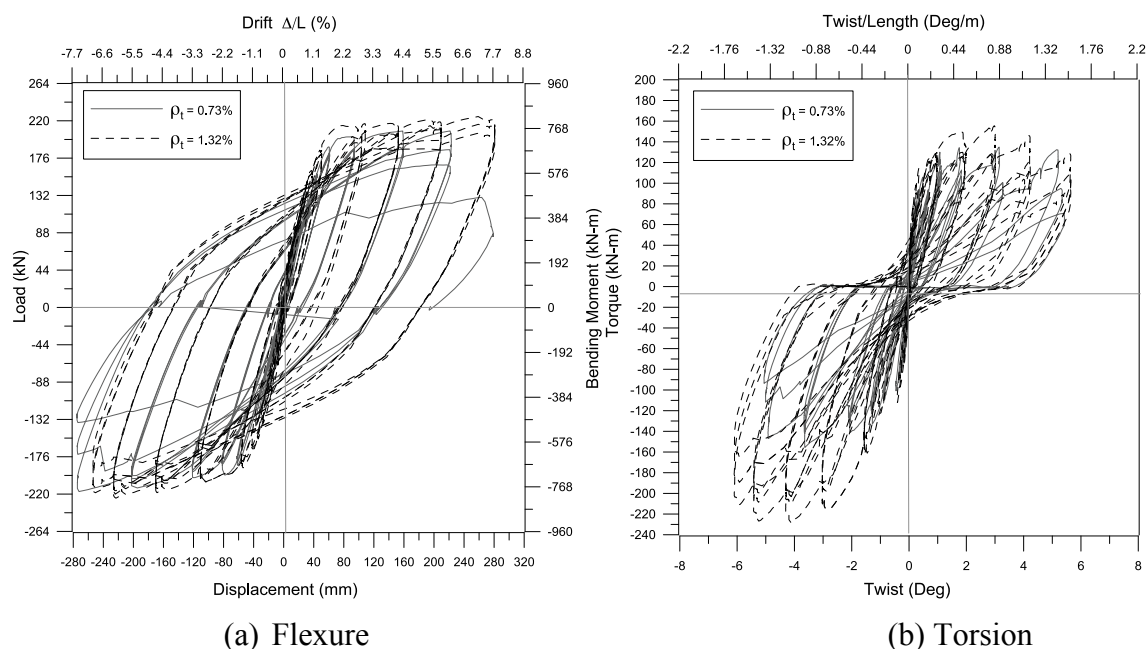
Figure 4.63 Comparison of Hysteresis Behavior of T/M (0.2)-H/D(6) with Spiral Ratios of 0.73% and 1.32%

Figure 4.64 shows the flexural hysteresis and torsional hysteresis of the column with a spiral reinforcement ratio of 0.73% and 1.32%, tested at a T/M ratio of 0.4. The behavior of the specimen was dominated by torsion due to damage initiation from spiral yielding and concrete cover spalling under high torsional moment. The flexural strength and stiffness of the specimen did not degrade before the failure by torsion. The asymmetric behavior of the hysteresis curve under both flexure and torsion revealed the significant effects of the locking and unlocking.

(a) Flexure (b) Torsion
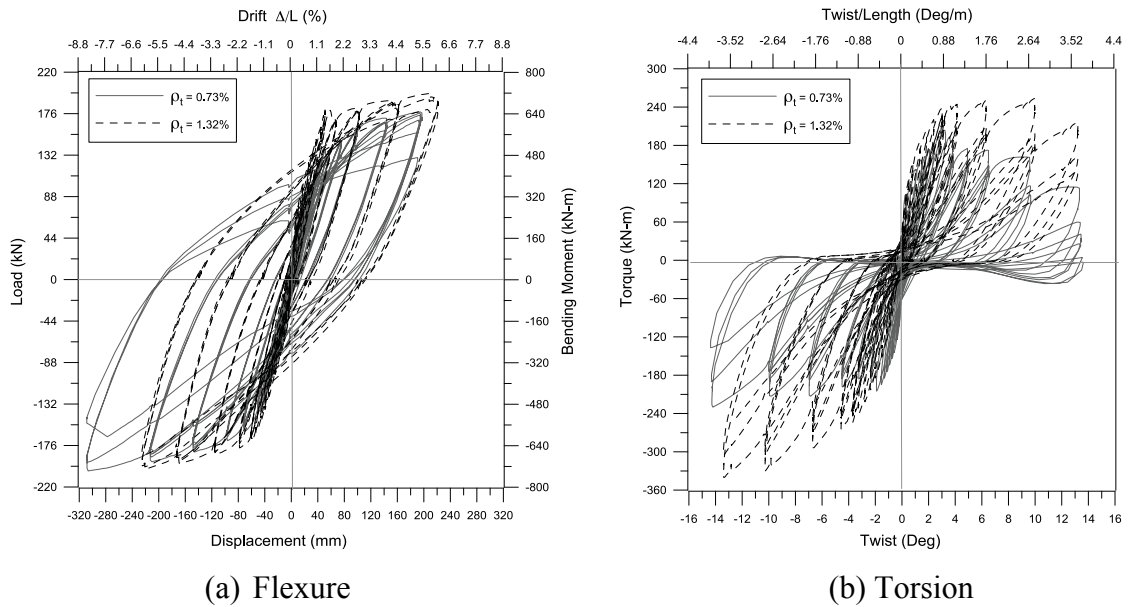
Figure 4.64 Comparison of Hysteresis Behavior of T/M (0.4)-H/D(6) with Spiral Ratios of 0.73% and 1.32%

Figure 4.65 compares the lateral load-displacement and the torsional moment-twist curves. These curves are due to the effect of combined loading, and they indicated that the torsional strength decreased with a decrease in T/M ratio, and bending strength decreased with an increased in T/M ratio. The asymmetric nature of the torsional envelopes was due to the locking and unlocking effect of the spirals. Due to combined loading, the post-cracking torsional stiffness degraded faster than that observed under pure torsion. Torsional strength, bending strength, and deformational capacity are also improved significantly with an increase in the spiral reinforcement ratio. The components of shear stresses from bending and torsion were additive, resulting in more damage and less load resistance. Thus, the asymmetric nature of the flexural envelopes under combined bending and torsion was due to the fact that one face was subject to higher shearing stresses than the other.
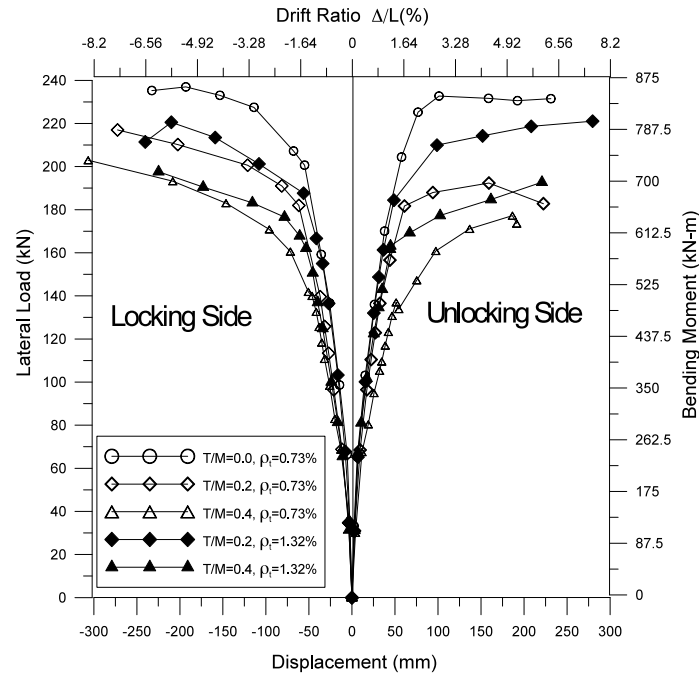
(a) Lateral Load-Displacement Curves
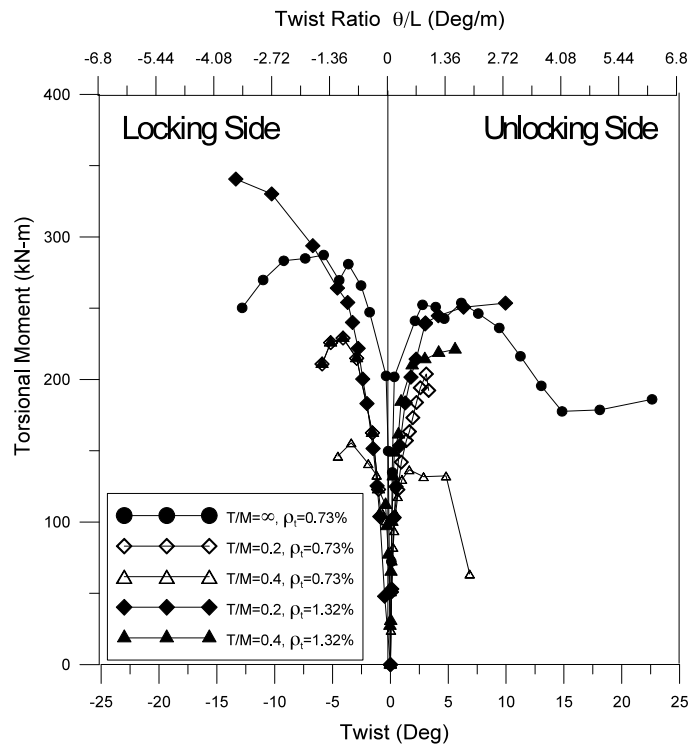
(b) Torsional Moment-Twist Curves

Figure 4.65 Comparison of Behavior for Spiral Ratios of 0.73% and 1.32%

Figure 4.66 shows the effect of an increasing spiral reinforcement ratio on the progression of failure under combined loading. This increase reduced the damage level at spiral yielding and at ultimate torsional moment compared to the column with a lower spiral reinforcement ratio.

Spiral Ratio 0.73%   Spiral Ratio 1.32%

(a) First Yielding of Spiral

Spiral Ratio 0.73%   Spiral Ratio 1.32%

(b) Peak Torsional Moment

Spiral Ratio 0.73%   Spiral Ratio 1.32%

(c) Overall Failure
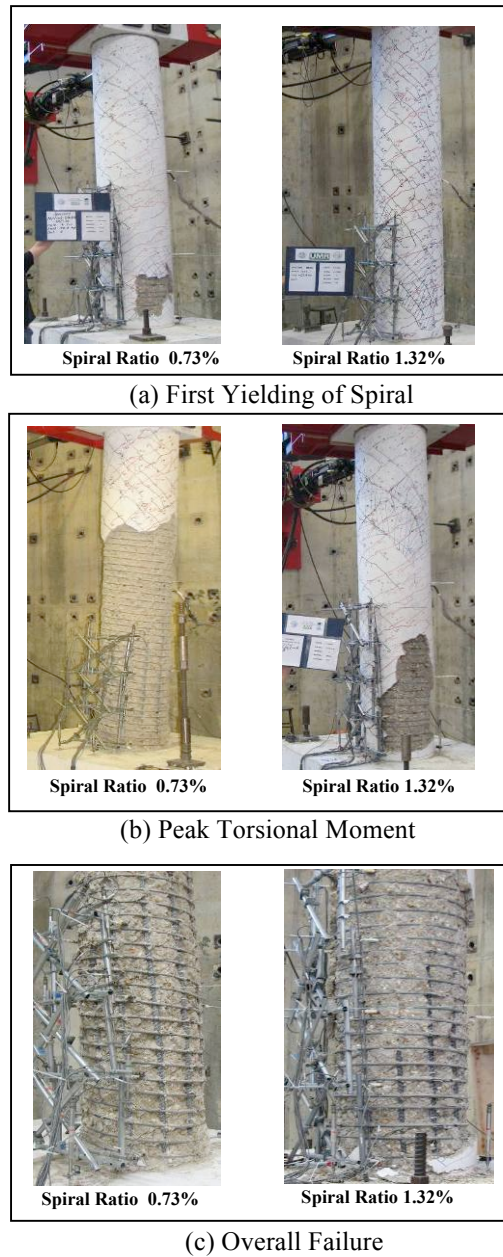
Figure 4.66 Effect of Spiral Reinforcement Ratio on Failure Modes under Combined Bending and Torsion at T/M=0.4

Figure 4.67 and Figure 4.68 show the effect of an increased spiral reinforcement ratio on longitudinal and spiral strain distribution for test columns with a T/M ratio of 0.2. Figure 4.69 and Figure 4.70 show the same effect on the test column with a T/M ratio of 0.4. Although an increase in the spiral reinforcement ratio reduced longitudinal strain only marginally, spiral strains decreased considerably in test columns with T/M ratios of 0.2 and 0.4 at the same load level. This reduction shows that an increase in the spiral reinforcement ratio limited the torsional damage by increasing the torsional strength and stiffness under combined bending and torsional moments. Finite element analysis of the columns with different spiral ratio under combined loading also illustrated the similar behavior (Belarbi et al., 2009).
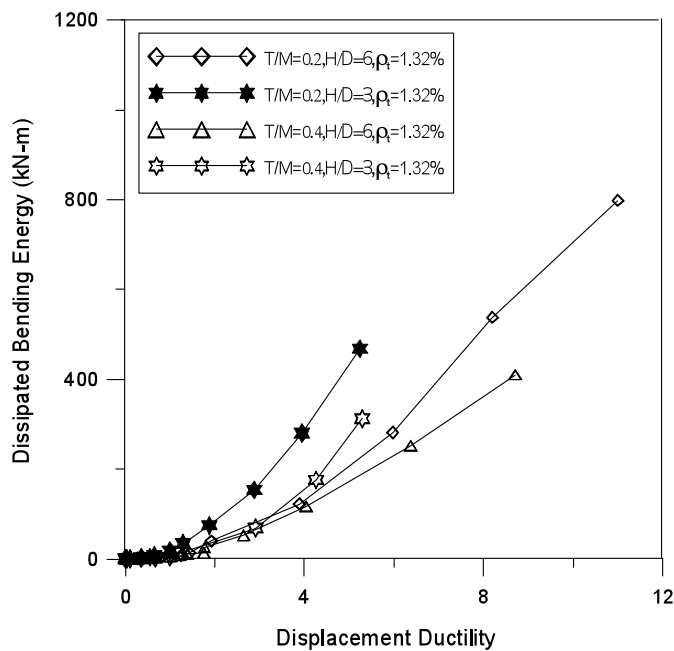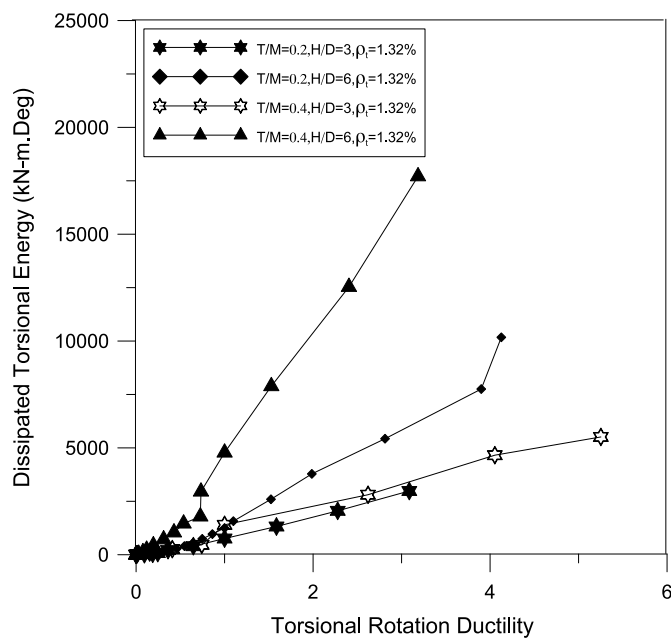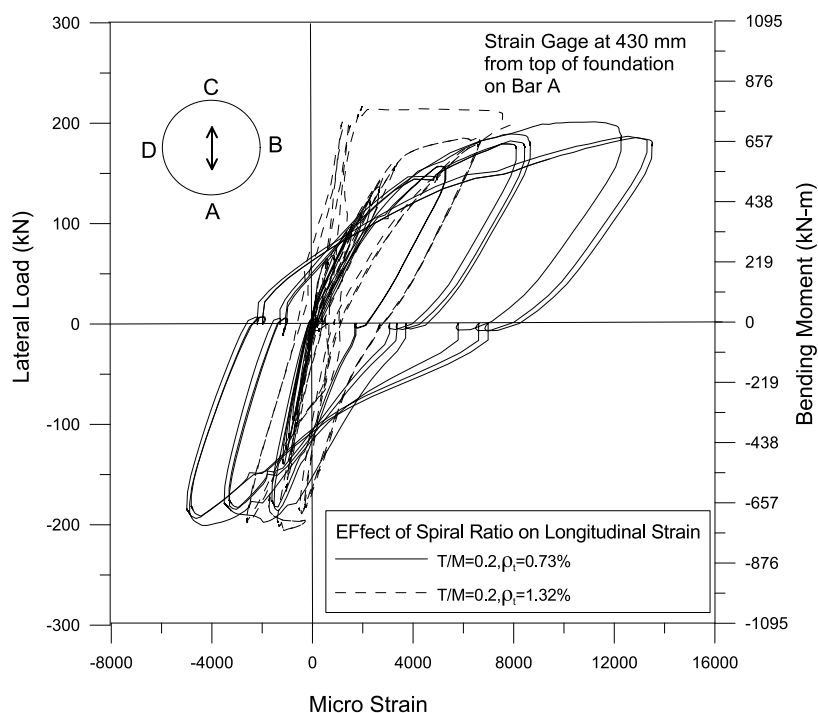

Figure 4.67 Effect of Spiral Reinforcement Ratio on Longitudinal Strain Distribution under Combined Bending and Torsion Moments at T/M=0.2
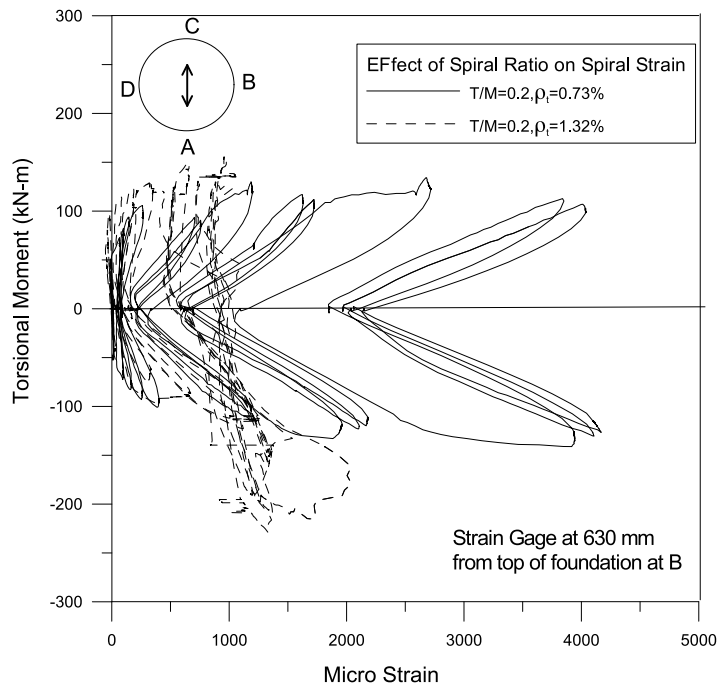
Figure 4.68 Effect of Spiral Reinforcement Ratio on Spiral Strain Distribution under Combined Bending and Torsion Moments at T/M=0.2
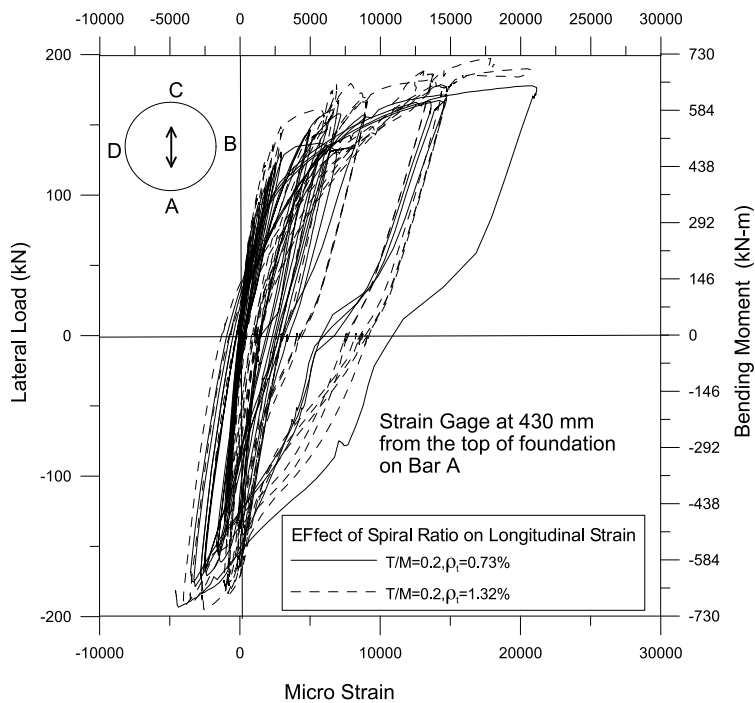
Figure 4.69 Effect of Spiral Reinforcement Ratio on Longitudinal Strain Distribution under Combined Bending and Torsion Moments at T/M=0.4
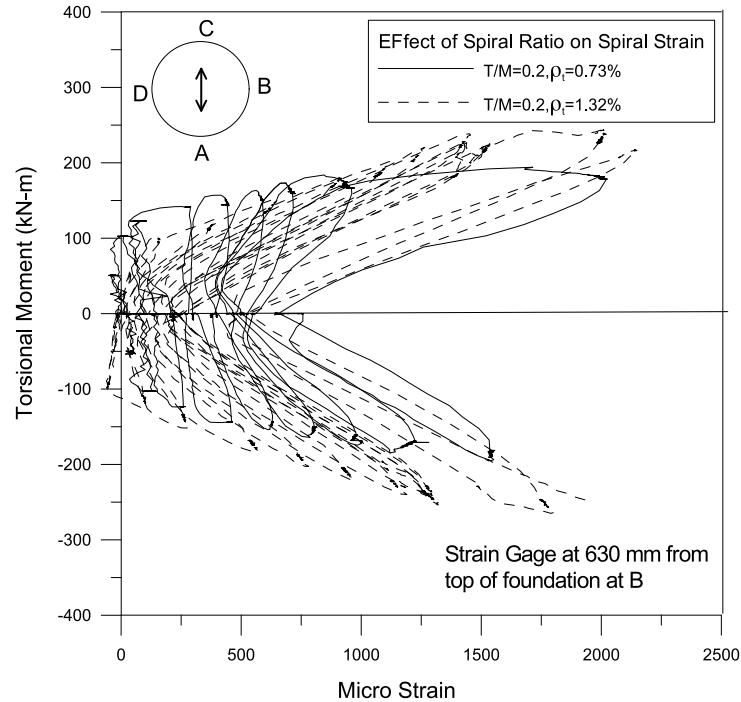
Figure 4.70 Effect of Spiral Reinforcement Ratio on Spiral Strain Distribution under Combined Bending and Torsion Moments at T/M=0.4

Figure 4.71 shows the effect of increasing the transverse spiral reinforcement ratio on energy dissipation capacity and ductility. It indicates that increasing the transverse spiral reinforcement ratio significantly increased the energy dissipation capacity and ductility under combined bending and torsion. Similarly, Figure 4.72 shows the effect of increasing the transverse spiral reinforcement ratio on the equivalent damping ratio. For both bending and torsional hysteresis in the transverse spiral reinforcement ratio significantly increased energy dissipation and improved the equivalent damping ratio (Figure 4.71, Figure 4.72).
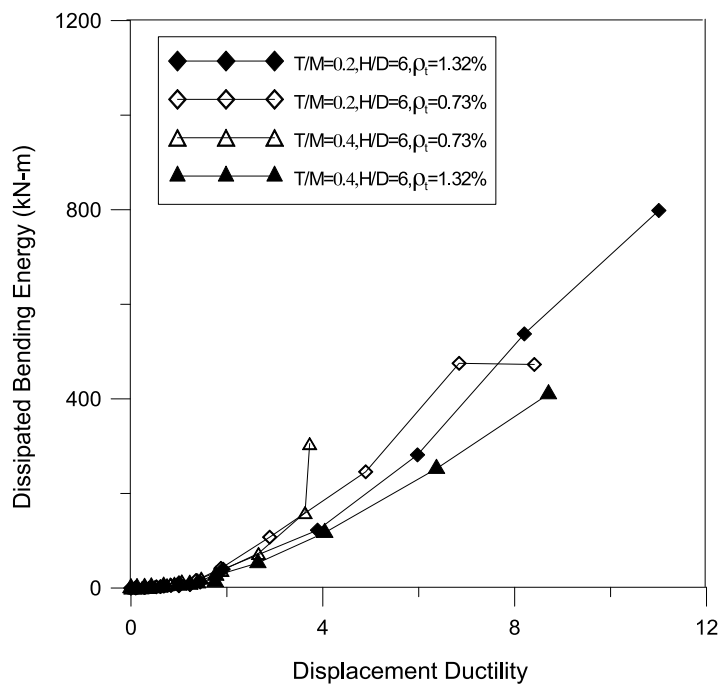
(a) Bending Energy
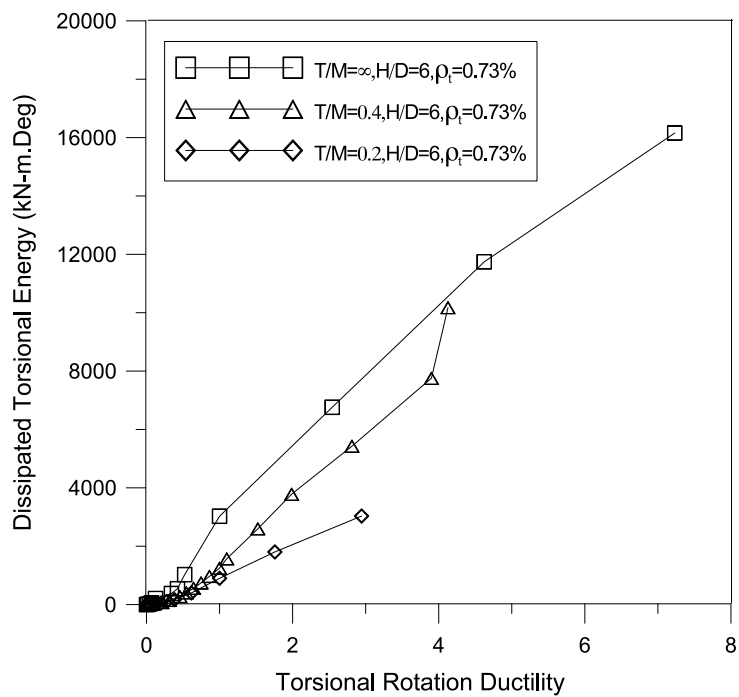
(b) Torsional Energy

Figure 4.71 Effect of Transverse Spiral Reinforcement Ratio on Energy Dissipation
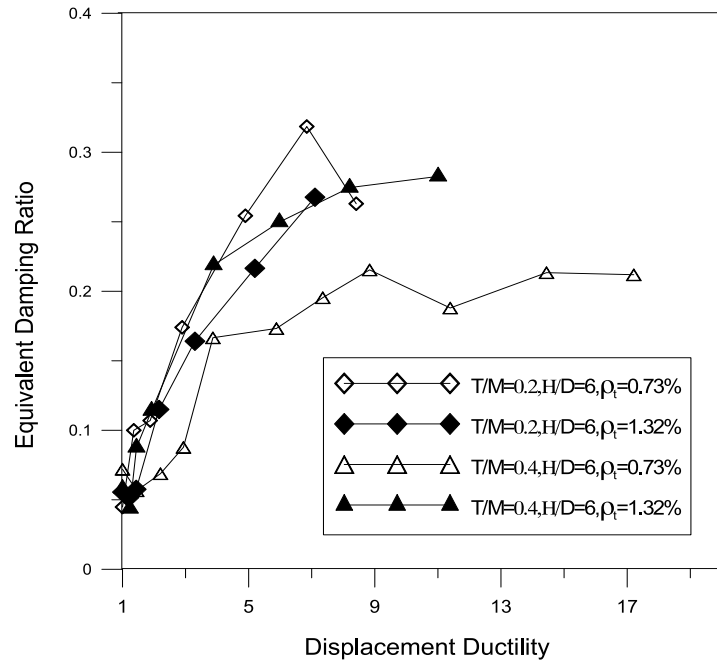
(a) Bending Hysteresis
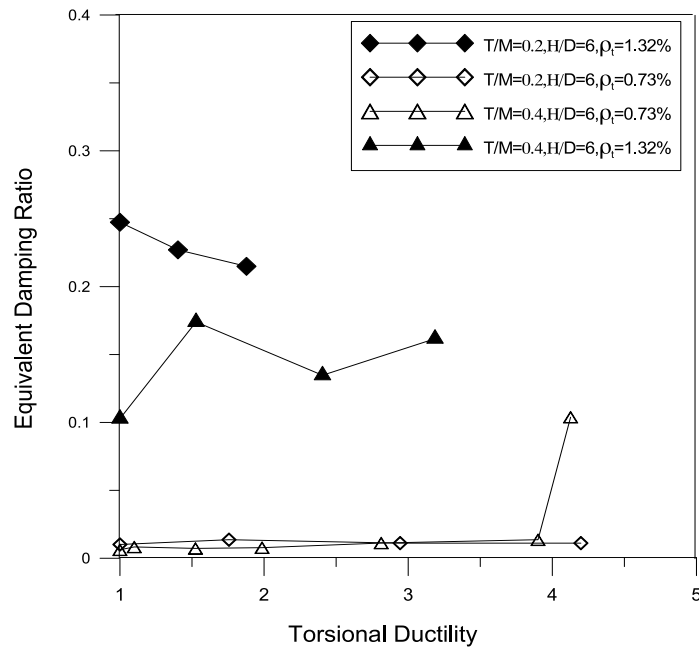
(b) Torsional Hysteresis

Figure 4.72 Effect of Transverse Spiral Reinforcement Ratio on Equivalent Damping
Ratios

Figure 4.73 shows the interaction of torsion and bending moment loading curves for the columns tested under combined bending and torsional moments at the peak of each ductility level. These curves indicate that The T/M ratio was maintained close to the desired loading ratio in all columns until peak torsional moment in the unlocking direction. Soon after peak torsional strength, the desired loading ratio could not be maintained because torsional stiffness degraded much faster in both the unlocking and locking directions. However, bending strength degraded faster than torsional strength in the locking direction for the columns with a spiral reinforcement ratio of 1.32%; hence, the load ratio could not be maintained to complete the test. The longitudinal reinforcement yielded before the spiral reinforcement yielded in all the test columns. Hence, the failure sequence in all test columns was flexural cracking, followed by shear cracking, longitudinal reinforcement yielding, spalling, and spiral yielding. Overall failure occurred finally with buckling of the longitudinal bars immediately after significant core degradation, as observed in the columns with varying shear span. Yielding of longitudinal and spiral reinforcement occurred at roughly same time for the test column with a spiral reinforcement ratio of 0.73%. With an increase in the spiral reinforcement ratio, torsional and bending strengths improved significantly. More importantly, significant twist ductility was achieved in torsional moment-twist behavior.
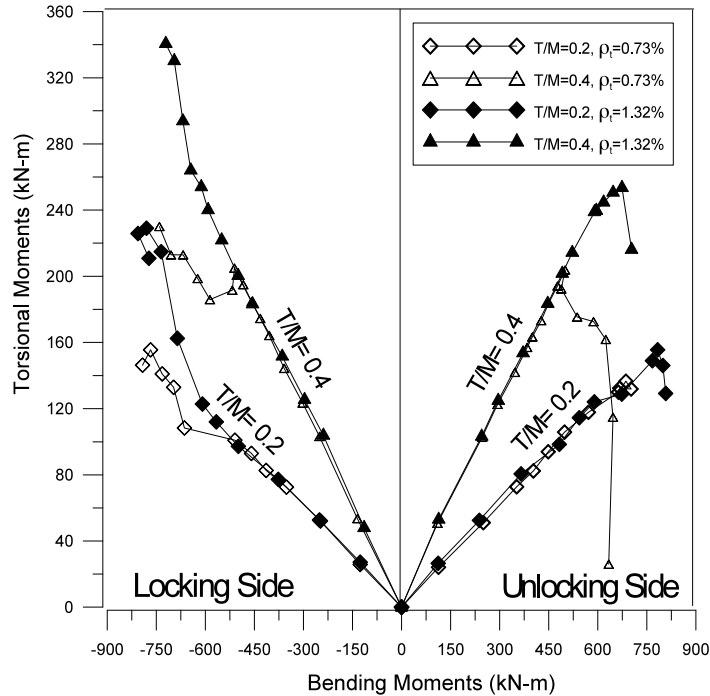
Figure 4.73 Interaction of Torsion and Bending Moments Loading Curves for Various Spiral Ratios

For all the test columns, torsion-bending moment interaction diagrams were created at peak torsional moment (Figure 4.74) and peak shear force (Figure 4.75). Significant improvement in strength was obtained with increased in spiral reinforcement ratio. The effect of spiral reinforcement ratio in increasing the torsional strength was more effective than in flexural strength. The locking effect of spiral was more effective with increase in spiral ratio. This is reflected in asymmetric nature of interaction diagrams. More importantly, increase in spiral ratio changed the failure mode from torsional dominant to flexural dominant. These results indicate that design detailing (particularly the transverse reinforcement configuration and its spacing) must change in columns when torsional moments are anticipated.
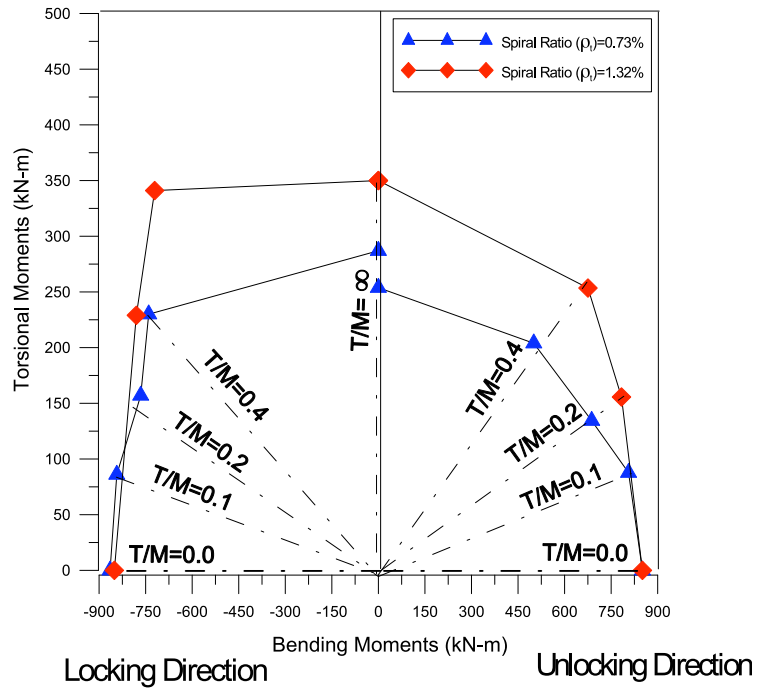
Figure 4.74 Torsion-Bending Moment Interaction Diagram at Peak Torque
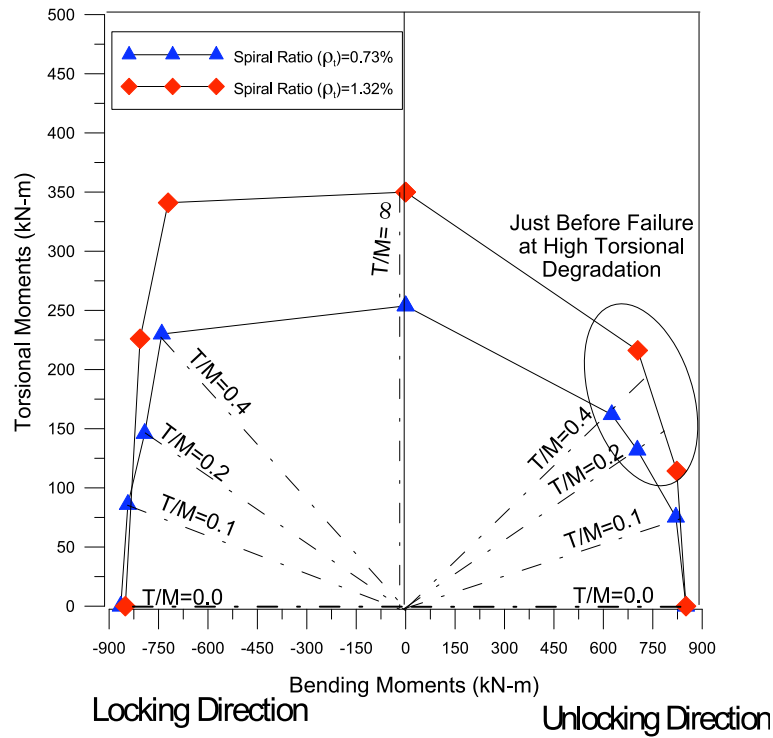
Figure 4.75 Torsion-Bending Moment Interaction Diagram at Peak Shear

4.9. CONCLUDING REMARKS

This Section presented the test results for columns under flexure, pure torsion, and shear force combined with flexural and torsional moments. The test results provide significant information that will improve the understanding of the behavior of circular RC columns under combined loading including torsion. The objective of the program was to quantify the influence of three factors on the behavior of circular RC columns: the T/M ratio, an increase in the spiral reinforcement ratio, and a reduction in aspect ratio. The test results support the following conclusions:

4.9.1. General Conclusions.

• Degradation in the strength of columns with aspect ratios of six and three under flexure occurs by formation of a flexural plastic-hinge at the base of the column, followed by core degradation, and finally by the buckling of longitudinal bars on the compression side.

• Columns subject to pure torsion was induced fail by severe diagonal cracking, leading to the formation of a torsional plastic-hinge near the mid-height of the column.

• Columns under combined shear force, flexural, and torsional moments fail due to severe core degradation followed by the buckling of the longitudinal bars. However, the location of the plastic zone shifts up from the base of the column according to the applied T/M ratio.

4.9.2. Effect of Torsion-to-Bending Moment Ratio.

• The location and length of the plastic-hinge changes with specific combinations of bending and torsion, i.e., with changes in the torsion-to-bending ratio.

• A combination of flexural and torsional moments reduces the torsional moments required to cause yielding of the transverse reinforcement and the peak torsional strength.

• Similarly, a combination of flexural and torsional moment reduces the bending moment required to cause yielding of the longitudinal reinforcement and the peak flexural strength.

• Under combined torsion and bending, torsional stiffness degrades more rapidly than bending stiffness with the increments of displacement/twist for the columns reinforced with both 0.73% and 1.32% transverse reinforcement.

• The ultimate displacement decreases with a reduction in the flexural energy dissipation capacity accompanied by an increase in the T/M ratio. Similarly, ultimate twist decreases with a reduction in the torsional energy dissipation capacity accompanied by a reduction in the T/M ratio.

4.9.3. Effect of Spiral Reinforcement Ratio.

• Degradation in the strength of a column under pure torsion is contained by increasing the spiral reinforcement ratio. Such an increase improves torsional strength and twist ductility by increasing deformational capacity after spiral reinforcement yielding.

• An increase in the spiral reinforcement ratio provides more confinement and thus reduces the degradation of bending and torsional strength under combined flexural and torsional moments.

• An increase in the spiral reinforcement ratio limits the damage corresponding to spiral yielding and peak torsional moment of a column under combined flexural and torsional moment when compared to the one with a lower spiral reinforcement ratio.

4.9.4. Effect of Aspect Ratio.

• The shear capacity of columns under flexure increases with a reduction in aspect ratio. However, displacement and twist at ultimate shear and ultimate torque of columns under combined loadings decreases significantly.

• Localized core degradation of concrete occurs at mid-height of columns with a high aspect ratio of six under pure torsion due to stress concentration in this region. However, the stress distribution is more uniform in columns with a low aspect ratio of three, resulting in no localized failure.

• No appreciable reduction in bending and torsional strength occurs with a reduction in aspect ratio. This is mainly due to the predominant of the flexural failure mode, which was due to low longitudinal reinforcement ratio considered in this study. However, energy dissipation under bending and torsional moments decreases considerably with reduction in shear span ratio.

5. ANALYTICAL STUDIES USING MECHANICAL MODELS FOR FLEXURE, SHEAR, TORSION AND INTERACTION DIAGRAMS

5.1. INTRODUCTION

Reinforced concrete members can be subjected to torsional moments in addition to flexural moment, axial load, and shear forces during earthquake excitations. In the 3-dimensional case, a beam or a column element can be subjected to six internal forces (Figure 5.1): three normal (axial force and two bending moments) forces and three tangential (torsion and two shear forces) forces. For most design situations, flexural moment and shear forces are considered primary effects, whereas torsion is regarded as secondary. In this study, an attempt is made to investigate and improve the existing analytical models for flexure, pure torsion and combined loading.

The objectives of the analytical investigation are to (i) modify and extend the existing models for circular sections under flexure by incorporating the changes in confinement models, (ii) develop the existing softened truss model for circular section under pure torsion by eliminating the warping considerations, and (iii) to validate the torsion, bending and shear force interaction diagrams of experimental results by using semi-empirical formulations. The failure interaction curves under combined flexure, shear force, and torsional moments are calculated using a semi-empirical relationship proposed by Elfgren (1972) based on the results of flexure, pure shear, and pure torsion.

Under flexure, plastic-hinge-based models incorporating the moment curvature analysis were used to predict the load-displacement behavior. Modified compression field theory was used to predict the behavior under pure shear. The softened truss model developed for circular section was used to study (i) the interaction of axial compression

and torsional moment and (ii) the effect of spiral reinforcement ratio. The predictions from analytical models were compared with experimental results and the findings are discussed.
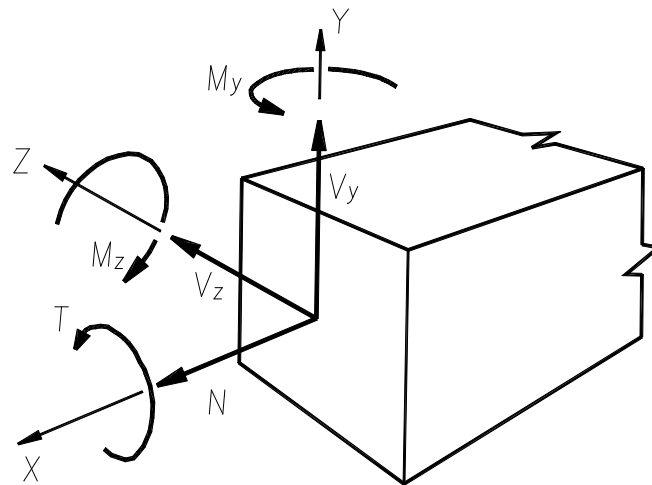
Figure 5.1 General Case of Loading on an RC Member

5.2. PLASTIC-HINGE-BASED MODEL FOR FLEXURE

The design of RC columns requires analytical models that can accurately predict the load-displacement behavior under flexure. Plastic-hinge-based models have been widely adopted for predicting the behavior of RC columns under flexure dominated behavior. Moment-curvature analysis forms the basis of plastic-hinge-based models, it is discussed in the following section.

5.2.1. Moment-Curvature Analysis. Conventional layer-by-layer approach is applied for the moment-curvature analysis which is performed by iterating the extreme compressive fiber strain (ε_c) from the initial increment value to the ultimate strain capability of the concrete (Figure 5.2). For each iteration, the neutral axis is found by

iterating through the section depth until the axial force is balanced, that is, to satisfy the compatibility and equilibrium conditions. The concrete sections are broken up into layers and integrated through their depth. The force at each layer is determined by calculating the stress from the strain at each location as shown in Figure 5.2. The approach used here was similar to that adopted by Priestley et al. (1996), with some modifications to the confinement models as described below.
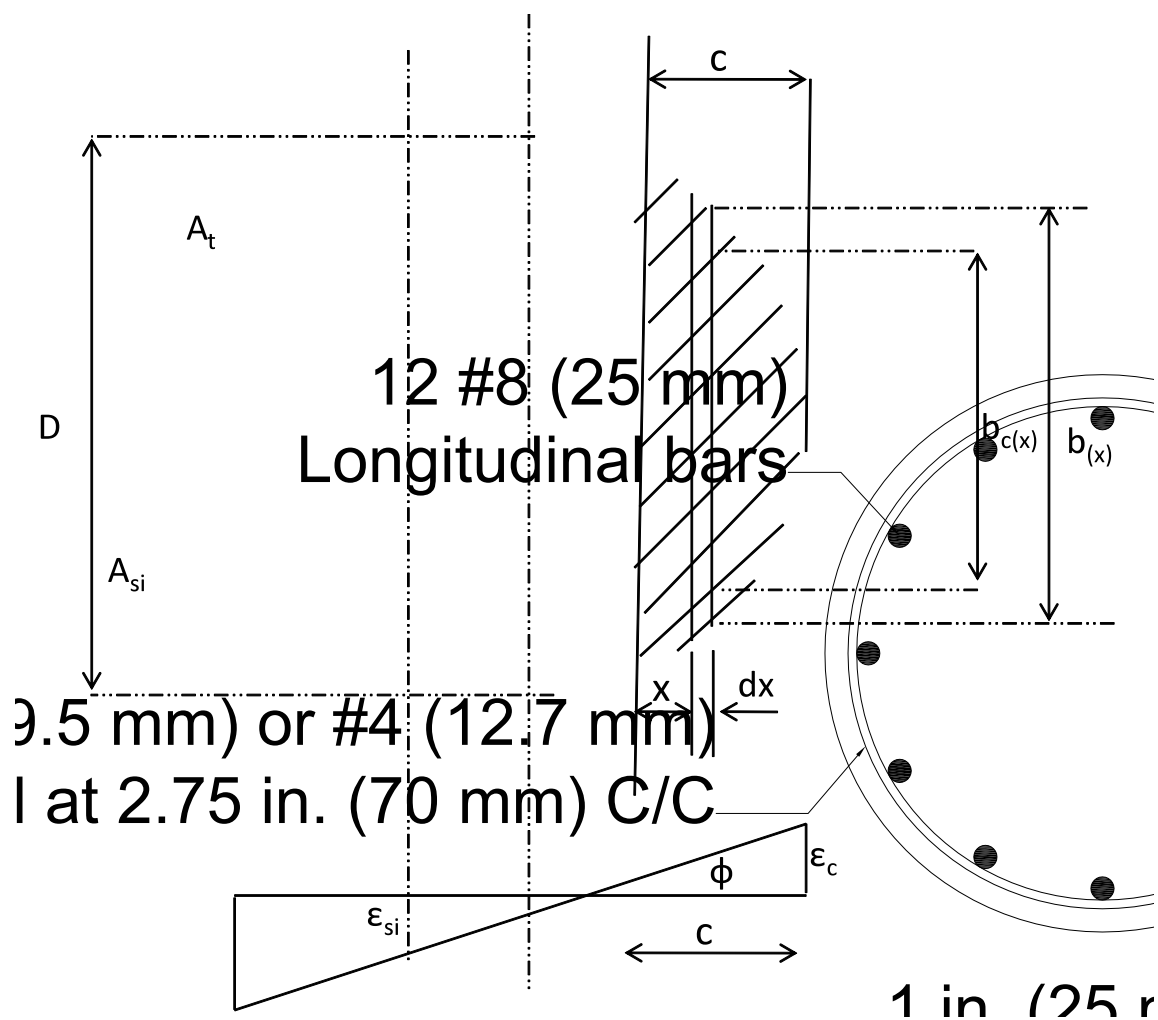
Figure 5.2 Strain Profile Across the Circular Cross Section

5.2.2. Concrete Stress-Strain Behavior. For concrete cover, an unconfined parabolic stress-strain curve is assumed in the moment-curvature analysis as shown in Figure 5.3. This region follows Mander's model for unconfined concrete until the strain reaches the spalling strain. At that point, the stress drops to zero. Mander's stress-strain model is also used for confined concrete which also accounts for spalling outside the confinement area.
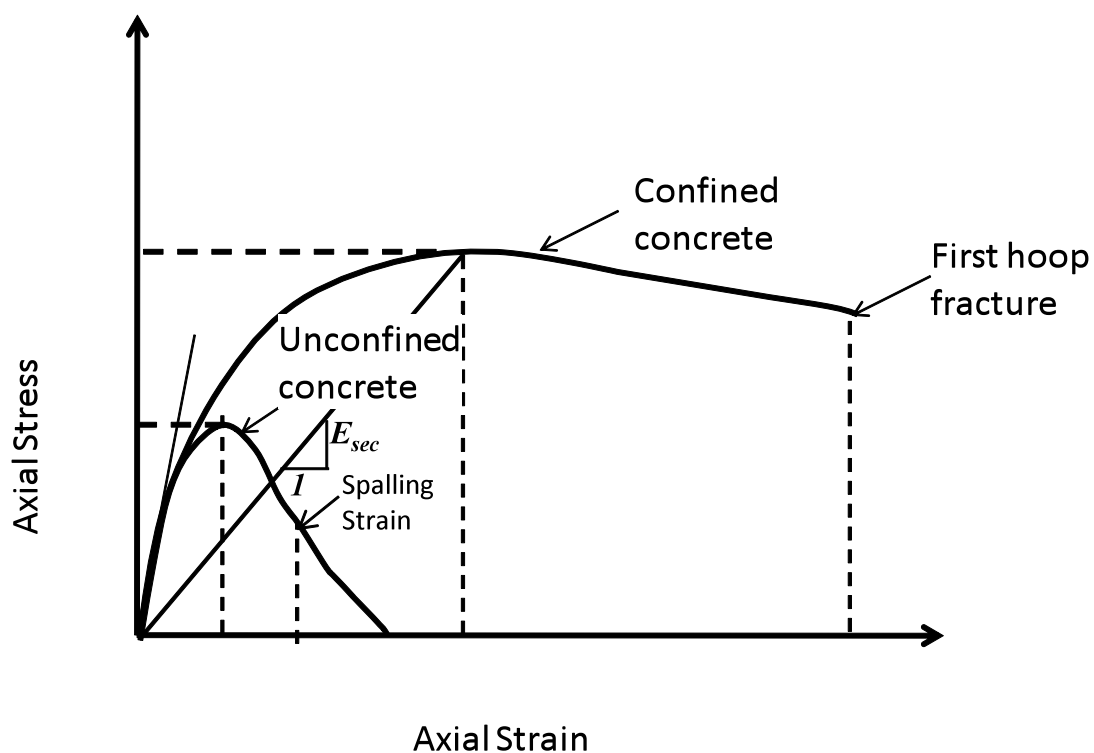
Figure 5.3 Stress-Strain Model for Concrete in Compression

The confinement stress-strain formula for columns with spiral reinforcement is shown in Eq. 5.8, and the relevant parameters that are used in the equation are shown below. The area of concrete core is calculated by Eq. 5.1. The transverse reinforcement

ratio is defined by Eq. 5.13. The confinement efficiency factor k_e is given by Eq. 5.5. The

effective lateral confining stress is given by Eq. 5.7.

$$A_{core} = 3.14 * \frac{D_c^{\ 2}}{4}$$

Eq. 5.1

$$A_{cc} = A_{core} - A_{reinf}$$

Eq. 5.2

$$d_e = D_c - (s - d_s)/2$$

Eq. 5.3

$$A_e = 3.14 \times d_e \times \frac{D_c}{4}$$

Eq. 5.4

$$k_e = \frac{A_e}{A_{cc}}$$

Eq. 5.5

$$\rho_s = 3.14 * d_s^{\ 2} / (D_c \times s)$$

Eq. 5.6

$$f_{lp} = k_e * \rho_s * f_{yh} / 2$$

Eq. 5.7

$$f_c = \frac{f_{cc}' x r}{r - 1 + x^r}$$

Eq. 5.8

$$f_c = f_c' \, [2.254\sqrt{1 + \frac{7.94 f_l'}{f_c'}} - \frac{2 f_l'}{f_c'} - 1.254] \qquad \text{Eq. 5.9}$$

$$x = \frac{\varepsilon_c}{\varepsilon_{cc}} \qquad \text{Eq. 5.10}$$

$$\varepsilon_c' = 0.002 \left[1 + 5 \left(\frac{f_{cc}'}{f_c'} - 1 \right) \right] \qquad \text{Eq. 5.11}$$

$$r = \frac{E_c}{E_c - E_{sec}} \qquad \text{Eq. 5.12}$$

$$E_c = 5000\sqrt{f_c'} \qquad \text{Eq. 5.13}$$

$$E_{sec} = \frac{f_{cc}'}{\varepsilon_{cc}'} \qquad \text{Eq. 5.14}$$

where f_l' represents confining pressure; ε_{cc} is maximum confined strain; and E_c is the Concrete compressive modulus. The ultimate strain formula [Eq. 5.15] is used rather than a computation of the complicated strain energy balance for the confinement reinforcing (Priestley et al., 1996).

$$\varepsilon_{cu} = 0.004 + 1.4 \rho_s \times f_{yh} \times \frac{\varepsilon_{sf}}{f_{cc}} \qquad \text{Eq. 5.15}$$

These equations and stress-strain formulations simplify the computations and provide a slightly more conservative result.

5.2.3. Stress-Strain Relationship for Reinforcement. The stress-strain relationship of reinforcement shown in Figure 5.4 is used in the plastic-hinge model. The stress-strain relationship given by Eq. 5.16 was assumed for both the transverse and longitudinal reinforcement (Priestely et al., 1996).

$$f_s = f_{ye} \left[1.5 - 0.5 \left(\frac{0.12 - \varepsilon_s}{0.112} \right)^2 \right] \qquad \text{Eq. 5.16}$$

where E_s is the modulus of elasticity, and f_s and ε_s are the stress and strain in the reinforcement, respectively. In this stress-strain relationship, ε_{sh} is taken as 0.008 and ε_{su} is taken as 0.12.
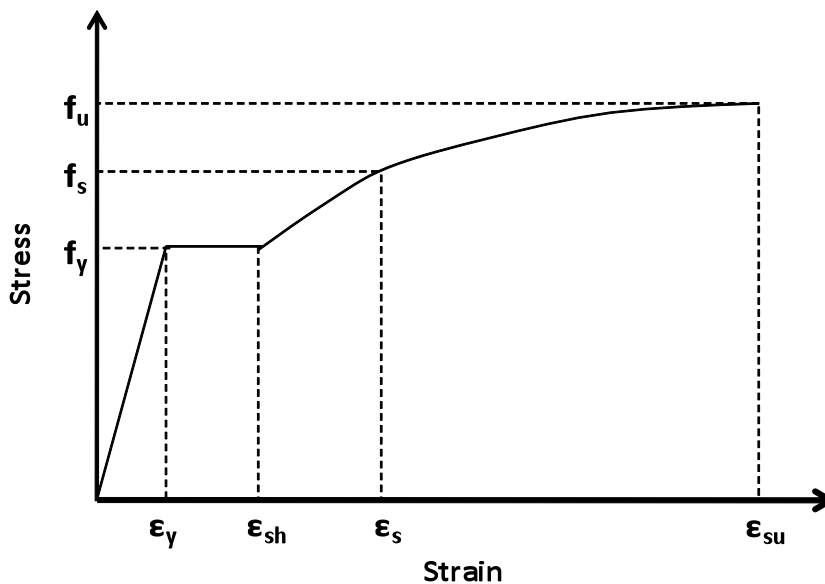
Figure 5.4 Material Models for Reinforcement for Monotonic Loading of Grade 60

5.2.4. Axial and Moment Equilibrium Equations. The axial equilibrium of forces is calculated as:

$$P = \int\limits_{x=(D/2)-c}^{D/2} \left[b_{c(x)} f_c(\varepsilon_x) + \left((b_{(x)} - b_{c(x)}) f_{cu}(\varepsilon_x) \right) \right] dx + \sum_{i=1}^{n} A_{si} f_s(\varepsilon_{xi})$$

Eq. 5.17

where

$$\varepsilon_x = \frac{\varepsilon_c}{c}(x - 0.5D + c)$$

Eq. 5.18

The moment equilibrium is given by

$$M = \int\limits_{x=(D/2)-c}^{D/2} \left[b_{c(x)} f_c(\varepsilon_x) + \left((b_{(x)} - b_{c(x)}) f_{cu}(\varepsilon_x) \right) \right] x \, dx + \sum_{i=1}^{n} A_{si} f_s(\varepsilon_{xi}) x_i$$

Eq. 5.19

where $f_c(\varepsilon)$, $f_{cu}(\varepsilon)$, and $f_s(\varepsilon)$ are the stress strain relationship for the confined concrete, unconfined concrete, and reinforcing steel, respectively, and A_{si} is the area of reinforcing bar with distance x_i from the centroidal axis.

The curvature is given by

$$\phi = \frac{\varepsilon_c}{c}$$

Eq. 5.20

5.2.5. Solution Procedure for Moment Curvature Prediction. The entire response from zero shear force to the peak shear force can be calculated by varying ε_c from near zero to a limiting value. The value of ε_c should be limited to 0.0035 mm/mm for unconfined concrete or the ultimate compression strain for the confined core concrete as defined in Eq. 5.15. The following information must be given: cross section dimensions, D; quantity and spacing of reinforcement and prestressing, A_L, A_T, and s;

reinforcement material properties, f_{Ly}, f_{Ty}, E_s; and concrete material property, f_c'.

The following procedure was used to solve the plastic-hinge-based model.

1. Select a value of ε_c.

2. Assume a value for the depth of neutral axis c

3. Calculate the corresponding concrete stress in concrete cover and core for each value of the depth of neutral axis at a particular increment.

4. Calculate the steel strain distribution according to the assumed value of ε_c and c

5. Using the steel strain distribution, calculate the stress according to Eq. 5.16.

6. Check for the axial and moment equilibrium as per Eq. 5.17 and   Eq. 5.19.

7. If the equilibrium equations are not satisfied, change the depth of the neutral axis and solve for the value by satisfying axial and moment equilibrium.

This process resulted in specified value of moment and the corresponding curvature for the assumed concrete strain. Similarly, concrete strains were incremented and the whole curve of moment-curvature was predicted. Using the calculated moment-curvature relationships, force-displacement envelopes can be calculated using plastic-hinge models.

5.3. FORCE-DISPLACEMENT BEHAVIOR USING PLASTIC-HINGE MODEL

The plastic-hinge model used in this study assumes that the curvature between the section of first yield and the critical section is linearly distributed. The first yield moment corresponds to the first yielding of the longitudinal bar on the tension side of the section. The distance from the section where the first yielding occurs to the critical section (bottom-most section in a cantilever column) is treated as the length on which the

transition occurs and is referred to here as l_p. As the lateral force increases, and while the moment at the critical section is less than the yield moment for the given combined axial load and bending moment, the entire length is in a linear elastic state and there is no l_p. As the moment at the critical section reaches the yield moment, the l_p starts to increase, reaching its maximum when the critical section experiences the maximum moment as expressed in Eq. 5.21.

$$l_p = l.(1 - \frac{M_y}{M_u})$$

Eq. 5.21

where l is the total length, M_y is the yield moment under combined axial load and bending moment, and M_u is the moment at the critical section. Let the maximum value of plastic-hinge length be $l_{p\text{-}max}$. Therefore, l_p is always either growing or it remains constant at its maximum achieved value so far. When the curvature is less than that corresponding to the maximum moment (for the existing force at the step), the curvature at the top of the plastic-hinge is equal to the actual analytical value corresponding to the moment situation. Analytically, it is equal to the yield curvature Φ_y and its corresponding moment is M_y, which is also equal to:

$$M_y = (\frac{l - l_p}{l}) M_u$$

Eq. 5.22

When the curvature on the critical section exceeds the curvature corresponding to the maximum moment, the curvature at the top of this l_p drops linearly with the part

above it that has been within the elastic-linear range so far. If the moment at this instance is M_u and the yield curvature and moment corresponding to the existing situation are M_y and Φ_y, respectively, then the curvature at the top of l_p is equal to:

$$\phi_{lp} = \phi_y \left(\frac{M_{lp}}{M_y}\right)$$

Eq. 5.23

where Φ_{lp} is the curvature at the top of the plastic-hinge and Φ_y is the first yield curvature. The term M_{lp} is the moment at the top of the plastic-hinge; it is calculated as:

$$\phi_{lp} = \phi_y \left(\frac{M_u}{M_y}\right)\left(\frac{l - l_p}{l}\right)$$

Eq. 5.24

The displacement at the tip of the column D is then

$$\Delta = \Delta_e + \Delta_p$$

Eq. 5.25

where D_p is the plastic flexural deflection. This deflection is calculated as

$$\Delta_p = \int_0^{l_p} \left[\phi_{lp} + \frac{\phi_u - \phi_{lp}}{l_p} x\right](l - l_p + x)dx$$

Eq. 5.26

Here, D_e is the elastic deflection, calculated as

$$\Delta_e = \int_0^{l - l_p} \frac{\phi_{lp}}{(l - l_p)} x\, dx$$

Eq. 5.27

The accuracy of the analyses is summarized for the columns tested in flexure in this study in Table 5.1. The analytical predictions and experimental data are compared in Figure 5.5. The measured flexural strength varied from 95% to 98% of the calculated flexural strength. The measured stiffness (calculated at first yield of the reinforcement or at a strain of 0.002, whichever came first) varied from 81% to 98% of the calculated effective stiffness. Deflection at the tip of the column, where the horizontal force was applied during the test, was considered a combination of the elastic deflection associated with the elastic portion of the column and the plastic deflection associated with deformation within the plastic-hinge region. Shear deformation and bond slip are not considered in the modeling; therefore, the displacements at ultimate load are approximate.

Table 5.1 Comparison of Results with Plastic-Hinge Model for Flexure

Parameter	Spiral Ratio of 0.73%		Spiral Ratio of 1.32%	
	Model	Experiment	Model	Experiment
Flexural Moment at First Yielding M_y (kN-m)	520	502	524	542
Ultimate Flexural Moment M_0 (kN-m)	805	850	860	854
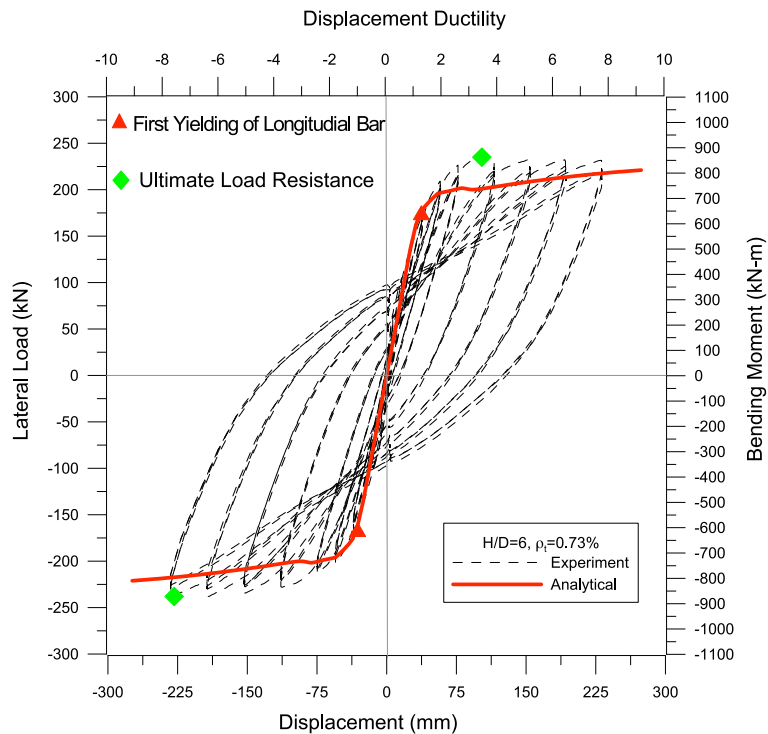
(a) H/D=6, Spiral Ratio=0.73%
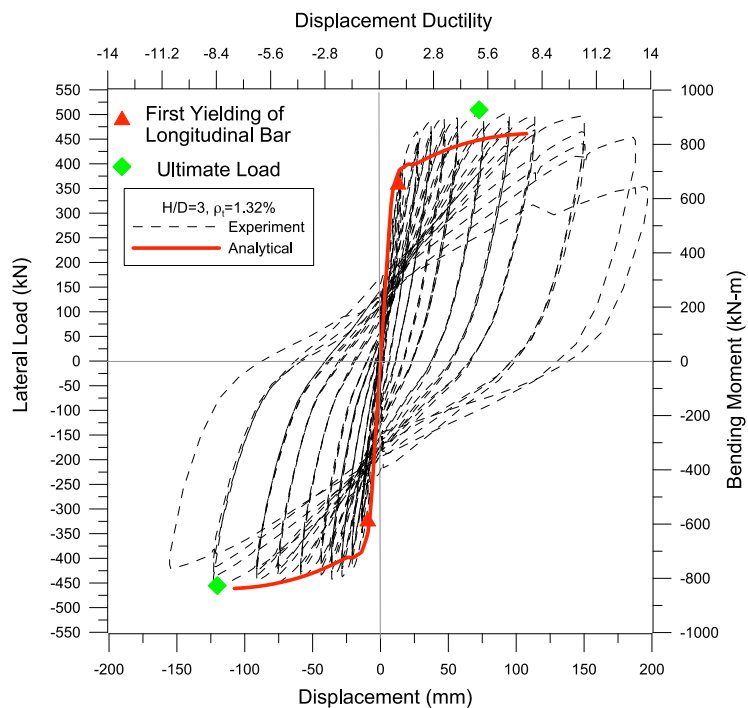
(b) H/D=3, Spiral Ratio=1.32%

Figure 5.5 Comparison of Experimental and Analytical Results under Flexure

5.4. MCFT MODEL FOR SHEAR CAPACITY

Previous work has established a reliable means to predict pure shear capacity for membrane elements (Vecchio and Collins, 1988, Belarbi and Hsu 1993; Pang and Hsu, 1994) and prismatic members. However, very few experimental and analytical works studied the shear capacity of circular RC members [Kowalsky and Priestley, 2000]. Among well-established analytical models, the MCFT offers good predictions for circular sections (Collins et al., 2002). Hence, it is used in this study to predict the behavior of circular RC members considered in the experimental program. Figure 5.6 summarizes the equilibrium, compatibility and stress-strain relationships used by the MCFT. In the relationships, θ is the angle between the x-axis, and the direction of the principal compressive average strain. These average strains were measured over base lengths greater than the crack spacing. For specified applied loads, the angle, θ, the average stresses and the average strains can be calculated from the given equilibrium equations in terms of average stresses, the given compatibility equations in terms of average strains, and the given average stress-strain relationships. A detailed description of MCFT is provided by Vecchio and Collins, 1988 and Collins and Mitchell, 1993.

Equilibrium:

Average Stresses:

$$\rho_x f_{xx} = f_x + \upsilon \cot\theta - f_1$$

$$\rho_y f_{yy} = f_y + \upsilon \tan\theta - f_1$$

$$f_2 = \upsilon(\tan\theta + \cot\theta) - f_1$$

Stresses at Cracks:

$$\rho_x f_{xx} cr = f_x + \upsilon \cot\theta + \upsilon_{ci} \cot\theta$$

$$\rho_y f_{yy} cr = f_y + \upsilon \cot\theta + \upsilon_{ci} \tan\theta$$

Geometric Conditions:

Average Strains:

$$\varepsilon_x = (\varepsilon_1 \tan^2\theta + \varepsilon_2)/(1 + \tan^2\theta)$$

$$\varepsilon_y = (\varepsilon_1 + \varepsilon_2 \tan^2\theta)/(1 + \tan^2\theta)$$

$$\gamma_{xy} = 2(\varepsilon_x - \varepsilon_2)/\tan\theta$$

$$\gamma_{xy} = 2(\varepsilon_x - \varepsilon_2)/(\varepsilon_y - \varepsilon_2)$$

Crack Widths:

$$w = s_\theta \varepsilon_1 \qquad \text{where}$$

$$s_\theta = 1/\left(\frac{\sin\theta}{s_x} + \frac{\cos\theta}{s_y}\right)$$

Average Stress-Average Strain Relationships:

Reinforcement:

$$f_{xx} = E_s \varepsilon_x \leq f_{xyield}$$

$$f_{yy} = E_s \varepsilon_y \leq f_{yyield}$$

Concrete:

$$f_2 = \frac{f_c'}{0.8 + 170\varepsilon_1}\left[2\frac{\varepsilon_2}{\varepsilon_c'} - (\frac{\varepsilon_2}{\varepsilon_c'})^2\right]$$

$$f_1 = \frac{f_{cr}}{1 + \sqrt{500\varepsilon_1}}$$

Allowable Shear stress on Crack

$$\upsilon_{ci} \leq \frac{0.18\sqrt{f_c'}}{0.31 + \frac{24w}{a + 16}}$$

Figure 5.6 MCFT for Shear Behavior (Concepts from Collins and Mitchell, 1993)

This study relied on the computer program Response 2000 based on MCFT; to predict the behavior of circular RC columns. Evan Bentz (2000) developed this program at the University of Toronto as a part of his doctoral dissertation work, supervised by Professor Michael P. Collins. This two-dimensional sectional analysis program for beams and columns calculates the strength and ductility of a RC cross-section subjected to shear, moment, and axial loads. All three loads can be considered simultaneously to find the full load-deformation response. Response 2000 calculates the shear strength of beams and columns with rectangular sections as well as others. Shear strength of circular columns containing various transverse reinforcements can be predicted with ease using Response 2000. This program treats each cross-section as a stack of biaxial element. Evan Bentz

(2000) assumed that "plane sections remain plane, and that there is no transverse clamping stress across the depth of the beam". For sections of a beam or column a reasonable distance away from a support or point load, these assumptions usually results in accurate predictions. The predictions of pure shear capacity using Response 2000 are shown in Table 5.2.

Table 5.2 Predictions of Shear Capacity using Response 2000

Parameter	Spiral Ratio 0.73%	Spiral Ratio 1.32%
Pure Shear Capacity V_0 (kN)	271	373

5.5. STM FOR CIRCULAR SECTION UNDER PURE TORSION

This section describes the development of a model for predicting the torsional moment-twist behavior of a circular RC member based on the original STM including the effect of concrete tension stiffening for continuous prediction. The inclusion of tension stiffening in the model is very important because it improves the prediction of RC members in the cracking state as well as a reduces the overestimation of the ultimate torsional moment. In order to account for the concrete acting in tension, a stress-strain relationship for concrete in tension was used (Greene, 2006). Greene (2006) validated the tension-stiffening model for RC members and pure torsion using the test data available in the literature. The proposed C-TS-STM adopts the equilibrium and compatibility equations developed for an RC panel under a membrane stress field.

5.5.1. Thickness of Shear Flow Zone. An important issue in extending the behavior of the membrane elements to a three-dimensional member under pure torsion and combined loading is in the accurate estimation of the thickness of shear flow zone, t_d. The estimation of t_d better established for rectangular sections than for circular sections. When an RC member twists, the walls are warped; causing flexural stresses in the concrete struts. Thus, there is a compatibility relationship between twisting and curvature. However, the concrete struts in a torsional circular member are dominated by the in-plane principal compression and tension stresses due to the circulatory shear stresses without warping. In the original STM, the thickness of shear flow zone is assumed to extend into the member from the outer surface to the neutral axis. The concrete inside the neutral axis acts in tension and considered ineffective. Such a member is assumed to be fully cracked as the concrete and reinforcement acting as a truss. Although research has shown this to be an effective model of a fully cracked RC member (Mitchell and Collins 1974; and Hsu and Mo 1985a), it cannot be used to predict the behavior of an uncracked member. According to St.Venant's elastic theory, shear stress and shear strain increases linearly from zero at the center of the section to a maximum at the midpoint of the longest side in a rectangular section and to a larger value at the outer surface of a circular section. As such there is no clear transition of an existing model from a uncracked behavior to cracked behavior. Greene (2006) tried to resolve this problem and it had its own limitations. In the analytical model proposed in this study, the cracking torsional moment and twist are calculated according to the expressions given by Collins and Mitchell (1993). The expression for t_{d0} is given by Eq. 5.28 (ACI 318 2005)

and represents the effective thickness of a thin tube at cracking. In Eq. 5.28, p_c is the perimeter of the section and A_{cp} is the area of concrete bounded by p_c.

$$t_{d0} = \frac{3}{4}\frac{A_{cp}}{p_c}$$
<div align="right">Eq. 5.28</div>

The thickness of shear flow zone increases after cracking according to the increase in torsional moment upto the peak point.

5.5.2. Constitutive Relationships for C-TS-STM. Figure 5.7 shows stress conditions in reinforced concrete membrane element subjected to in-plane stress which made a foundation of basic governing equations for shear. The directions of the longitudinal and transverse steel bars are designated as the l and t-axes, respectively, constituting the l-t coordinate system. Accordingly, the normal stresses are σ_l and σ_t and the shear stress is τ_{lt}. After the development of diagonal cracks, the concrete struts are subjected to compression and the steel bars act as tension links, thus forming a truss action. The compression struts are oriented in the d-axis, which is inclined at an angle α to the longitudinal steel bars. This direction is also assumed to be the direction of the principal compressive stress and strain. Taking the direction perpendicular to the d-axis as the r-axis, we have a d-r coordinate system in the direction of the principal stresses and strains. The normal principal stresses in the d and r directions are σ_d and σ_r, respectively.

(a) Definitions of Stresses and Coordinate System

(b) Superposition of Concrete Stresses and Steel Stresses
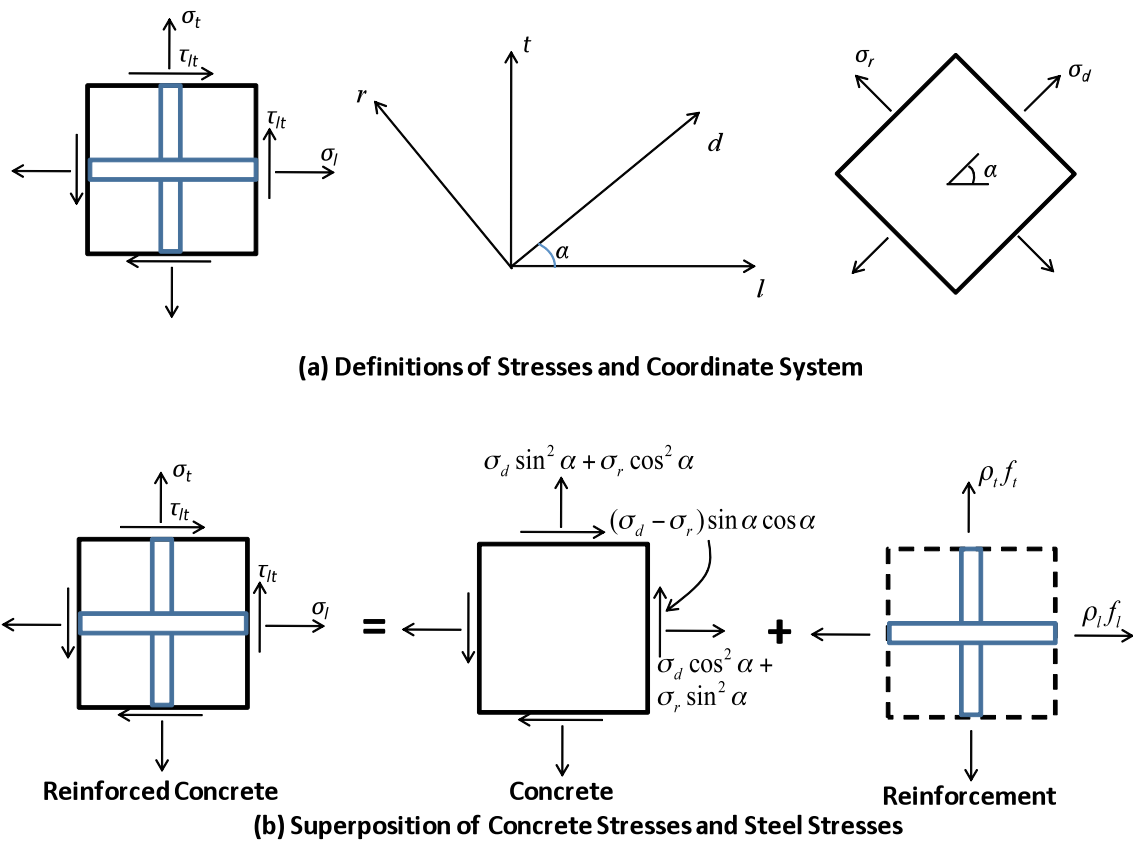
Figure 5.7 Reinforced Concrete Membrane Elements Subjected to In-Plane Stresses

5.5.2.1 Concrete stress-strain curves under compression. The uniaxial compression constitutive relationship of the concrete is assumed to be a parabolic model. Eq. 5.29 and Eq. 5.30 give the ascending and descending portions of the stress-strain relationship. In addition, Eq. 5.31 gives the softening coefficient used in the compressive stress-strain relationship.

$$\sigma_d = \zeta f_c' \left[2\left(\frac{\varepsilon_d}{\zeta \varepsilon_0} \right) - \left(\frac{\varepsilon_d}{\zeta \varepsilon_0} \right)^2 \right] \qquad \left(\frac{\varepsilon_d}{\zeta \varepsilon_0} \right) \le 1 \qquad \text{Eq. 5.29}$$

$$\sigma_d = \zeta f_c ' \left[1 - \left(\frac{\varepsilon_d / \zeta \varepsilon_0 - 1}{4 / \zeta - 1} \right)^2 \right] \qquad \left(\frac{\varepsilon_d}{\zeta \varepsilon_0} \right) \geq 1 \qquad \text{Eq. 5.30}$$

$$\zeta = \frac{5.8}{\sqrt{f_c '(Mpa)}} \frac{1}{\sqrt{1 + 400 \varepsilon_r}} \leq 0.9 \qquad \text{Eq. 5.31}$$

5.5.2.2 Concrete stress-strain curves under tension. The original STM for rectangular members (Hsu, 1993) disregarded the effect of tensile capacity of concrete resulting in unreasonable prediction of full torsional moment-twist response. This tension-stiffened response is related to the tensile stress-strain response of concrete. To model the full response of a circular RC member accurately, the effect of tensile capacity of concrete should be included in the C-TS-STM. To take into account the tension stiffening effect, an average tensile stress-strain relationship of concrete proposed by Greene (2006) was chosen as given by Eq. 5.32 and Eq. 5.33 (Figure 5.8). Greene (2006) effectively showed that the difference between the experimental and analytical torsional moment-twist curve was entirely due to tension stiffening effect. Figure 5.8 shows the calculated stress strain data of concrete under tension.

Tensile stress-strain relationships of concrete under tension are expressed as.

$$\sigma_r = E_c \varepsilon_r \qquad \varepsilon_r \leq \varepsilon_{cr} \qquad \text{Eq. 5.32}$$

$$\sigma_r = f_{cr} e^{-379.6(\varepsilon_r - \varepsilon_{cr})} \qquad \varepsilon_r > \varepsilon_{cr} \qquad \text{Eq. 5.33}$$
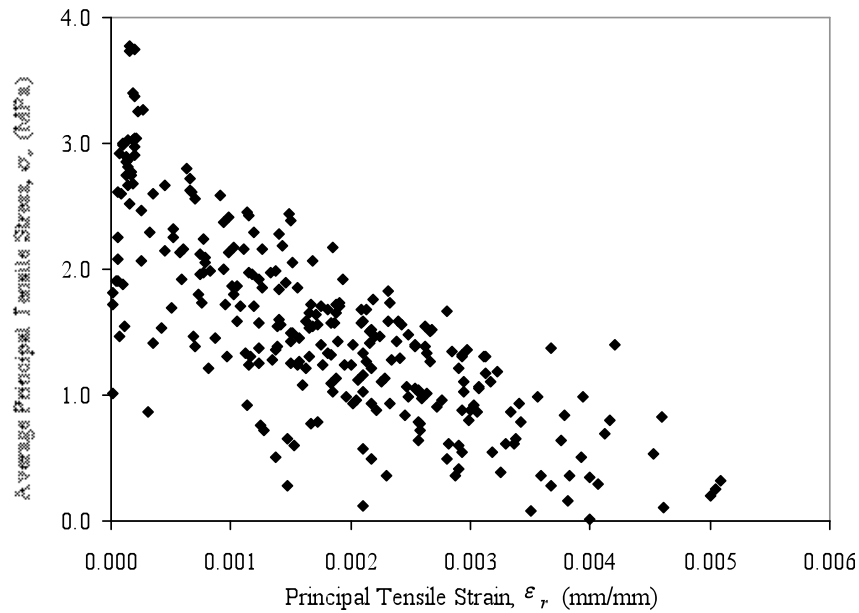
Figure 5.8 Calculated Tensile Stress-Strain Data (adapted from Greene, 2006)

5.5.2.3 Stress-strain curves for steel. The relationship of f_s and ε_s is expressed by a bilinear model. In Eqs. 5.34 and 5.35, l replaces s in the subscripts of the symbols for longitudinal steel, and t replaces s in the subscripts of the symbols for transverse steel. The stress-strain relationship for the longitudinal and transverse reinforcement can be expressed as in Eq. 5.36 and Eq. 5.37.

$$f_s = E_s \varepsilon_s \qquad \varepsilon_s \leq \varepsilon_n \qquad \text{Eq. 5.34}$$

and $\quad f_s = f_y[(0.91 - 2B) + (0.02 + 0.25B)\dfrac{\varepsilon_s}{\varepsilon_y}] \qquad \varepsilon_s > \varepsilon_n \qquad \text{Eq. 5.35}$

where

$$\varepsilon_n = \varepsilon_y(0.93 - 2B), \quad B = \frac{1}{\rho}\left(\frac{f_{cr}}{f_y}\right)^{1.5}$$

$$f_l = f(\varepsilon_l) \qquad \text{Eq. 5.36}$$

$$f_t = f(\varepsilon_t) \qquad \text{Eq. 5.37}$$

5.5.3. Governing Equations for C-TS-STM. For an RC member subjected to a torsional moment, STM solves number of equations by satisfying Navier's principle. They comprise of three equilibrium equations, seven compatibility equations, and five constitutive laws for concrete and steel. The above equations are described in the following sections.

5.5.3.1 Equilibrium equations. The two-dimensional equilibrium condition relates the average internal stresses in the concrete (σ_d and σ_r) and in the reinforcement (f_l and f_t) to the average applied stresses (σ_l, σ_t and τ_{lt}) with respect to the angle of inclination of the d-axis for the *l*-axis (α) as shown in Eqs. 5.38, 5.39 and 5.40. The torsional moment induced by internal shear stress can be expressed as Eq. 5.41.

$$\sigma_l = \sigma_d \cos^2\alpha + \sigma_r \sin^2\alpha + \rho_l f_l \qquad \text{Eq. 5.38}$$

$$\sigma_t = \sigma_d \sin^2\alpha + \sigma_r \cos^2\alpha + \rho_t f_t \qquad \text{Eq. 5.39}$$

$$\tau_{lt} = (-\sigma_d + \sigma_r)\sin\alpha\cos\alpha \qquad \text{Eq. 5.40}$$

$$T = \tau_{lt}(2A_0 t_d) \qquad \text{Eq. 5.41}$$

5.5.3.2 Compatibility equations. The two-dimensional compatibility condition expresses the relationship between the average strains in different coordinate systems. The transformation of average strains along the l, t-coordinate system ($\varepsilon_l, \varepsilon_t$ and γ_{lt}) into the d, r principal axes ($\varepsilon_d, \varepsilon_r$) is possible based on the membrane element behavior (Eqs. 5.42, 5.43, 5.44).

$$\varepsilon_l = \varepsilon_d \cos^2\alpha + \varepsilon_r \sin^2\alpha \qquad\qquad \text{Eq. 5.42}$$

$$\varepsilon_t = \varepsilon_d \sin^2\alpha + \varepsilon_r \cos^2\alpha \qquad\qquad \text{Eq. 5.43}$$

$$\frac{\gamma_{lt}}{2} = (-\varepsilon_d + \varepsilon_r)\sin\alpha\cos\alpha \qquad\qquad \text{Eq. 5.44}$$

Additional equations are used to solve the torsional problem accounting for the strain and stress distributions in concrete struts. The angle of twist (θ), the thickness of shear flow zone (t_d) and the shear strain are related as shown in Eq. 5.45.

$$\theta = \frac{p_0}{2A_0}\gamma_{lt} \qquad\qquad \text{Eq. 5.45}$$

5.5.4. Variables and Equations. All the variables and equations related to the out-of-plane warping effect that causes bending in concrete struts are eliminated in the STM. The elimination of variables and equations makes the number of differences between variables and equations zero as shown in Table 5.3. Thus, the terms related to concrete properties in tension are included in the proposed method not only to resolve the unbalance between the number of equations and variables but also to improve the accuracy of the predictions. In the original STM method, these discrepancies between

unknown variables and equations were iteratively resolved by assuming two constant values, σ_l = applied axial stress and σ_t = 0. A value is selected for ε_d, ε_r and t_d are iterated by a trial and error process till a proper solution is reached. The difference between number of variables and equations in the proposed method and original method is shown in Table 5.4. The variables eliminated in the proposed are shown with shaded color. The stresses σ_l, σ_t are related to σ_d, σ_r as in the following equations.

$$\sigma_L = \sigma_d \left(\frac{\varepsilon_r - \varepsilon_L}{\varepsilon_r - \varepsilon_d} \right) + \sigma_r \left(\frac{\varepsilon_L - \varepsilon_d}{\varepsilon_r - \varepsilon_d} \right) + f_L \left(\frac{A_L}{t_d p_0} \right) \qquad \text{Eq. 5.46}$$

$$\sigma_T = \sigma_d \left(\frac{\varepsilon_r - \varepsilon_T}{\varepsilon_r - \varepsilon_d} \right) + \sigma_r \left(\frac{\varepsilon_T - \varepsilon_d}{\varepsilon_r - \varepsilon_d} \right) + f_T \left(\frac{A_T}{t_d s} \right) \qquad \text{Eq. 5.47}$$

The angle of inclination of the diagonal cracks to the member's longitudinal axis, α, is related to the strains ε_d, ε_T and ε_L as follows:

$$\alpha = \arctan \sqrt{\frac{(\varepsilon_L - \varepsilon_d)}{(\varepsilon_T - \varepsilon_d)}} \qquad \text{Eq. 5.48}$$

The strains ε_d, ε_L, ε_T and ε_r are related by a compatibility condition as follows:

$$\varepsilon_d = \varepsilon_L + \varepsilon_T - \varepsilon_r \qquad \text{Eq. 5.49}$$

Unless explicitly stated in the study, E_s was assumed to be 200 GPa (ACI 318 2008). Also, ε_0 was assumed to be -0.002 mm/mm (Vecchio and Collins 1986) and an average strain value of 0.00010 mm/mm was taken for ε_{cr} (Belarbi and Hsu 1994; Gopalaratnam and Shah 1985).

Table 5.3 Equations and Variables in the Proposed Method

Category	Variables			Equations		
	Stresses or Forces	Strains or Geometry	Material	Equilibrium	Compatibility	Material (Constitutive)
For Shear	σ_l	ε_l	ζ	Eq. 5.38	Eq. 5.42	
	σ_t	ε_t		Eq. 5.39	Eq. 5.43	
	τ_{lt}	γ_{lt}		Eq. 5.40	Eq. 5.44	
	σ_d	ε_d				Eq. 5.29
	σ_r	ε_r				Eq. 5.30
	f_l	α				Eq. 5.36
	f_t					Eq. 5.37
Additional For torsion	T	θ	(k_1)	Eq. 5.41	Eq. 5.45	
		(ψ)				
		t_d				
		(ε_{ds})				
Number	7(7)	8(10)	1(2)	4(4)	4(7)	4(5)
Total	16(19)			12(16)		

Table 5.4 Comparison of Original STM and the Proposed Method

Model	No. of Variables	No. of Equations	Differences	Given	Solving Method
Original STM	19	16	3	$\sigma_t = \sigma_l = 0$ (or σ_l =constant) ε_d = variable	Iterative
Proposed Method	16	12	4	σ_l =constant, $\sigma_t = 0$ ε_r = variable, t_d=variable	Iterative

5.5.5. Method of Solution. The proposed C-TS-STM follows the basic equilibrium and compatibility equations used in the original STM. In addition, the material relationships for concrete compression and tension have been updated as described here. This section gives the additional equations needed for calculations and provides an efficient solution procedure to solve the system of equations.

Given the dimensions of the cross section, the transverse and longitudinal reinforcement, and the material properties, a "displacement-controlled" solution to the

equations can be calculated by first selecting ε_d, ε_r, then assuming trial values for t_d. Next, an iterative procedure is used to assign the variable values that solve the equilibrium equations, compatibility equations, and stress-strain relationships. This procedure finds a single point on a torsional moment-twist curve. Additional points are found by varying the selected values of ε_d from a near zero value (0.0001) to a maximum value that causes the peak torsional moment. The angle of inclination of the diagonal cracks to the member's longitudinal axis, α, is included a lot in the equilibrium and compatibility equations. To simplify the calculation algorithm, this value is expressed in terms of strains. Eq. 5.46 and Eq. 5.47 were derived to eliminate α from the equilibrium equations for σ_L and σ_T. Accordingly, the entire response from zero torsional moment to its peak can be calculated by varying ε_d. In the calculation procedure, the value of ε_d was limited to certain values causing the peak torsional moment or when the strains start reducing which is physically not possible.

The following information is required: cross-section dimensions, D; and concrete cover thickness, quantity, and spacing of the reinforcement, A_L, A_T, and s; reinforcement material properties, f_{Ly}, f_{Ty}, E_s, ; and concrete material property, f_c'.

5.5.5.1 Initial calculations. The following initial calculations were made for variables that are constant during the solution process. Calculations of A_{cp}, A_g, p_c, t_{d0}, ε_{Ly}, ε_{Ty}, f_{cr}, and E_c were done from the respective equations.

5.5.5.2 Solution algorithm. The following procedure was used to solve the proposed STM and is summarized as a flow chart in Figure 5.9.

1. Select a value of ε_d.

2. Assume a value of ε_r.

3. Assume a value of t_d.

4. Calculate ζ, σ_d, A_0, and p_0 from the corresponding equations. Before cracking, calculate σ_r using Eq. 5.32. After cracking, use the tension stiffening model to calculate σ_r using Eq. 5.33.

5. Calculate ε_L.

6. Calculate ε_T.

7. Calculate ε_r from Eq. 5.49. If the difference between the assumed and calculated value of ε_d is not within a tolerable limit, then repeat Steps 2 to 6 until the convergence is achieved by assuming different values of t_d and ε_r.

8. Calculate α, τ_{LT}, T, γ_{LT}, and θ corresponding to one value of ε_d.

9. Repeat the process for various values of ε_d

10. Stop the procedure when the strains begin to decrease in the longitudinal and transverse reinforcement.
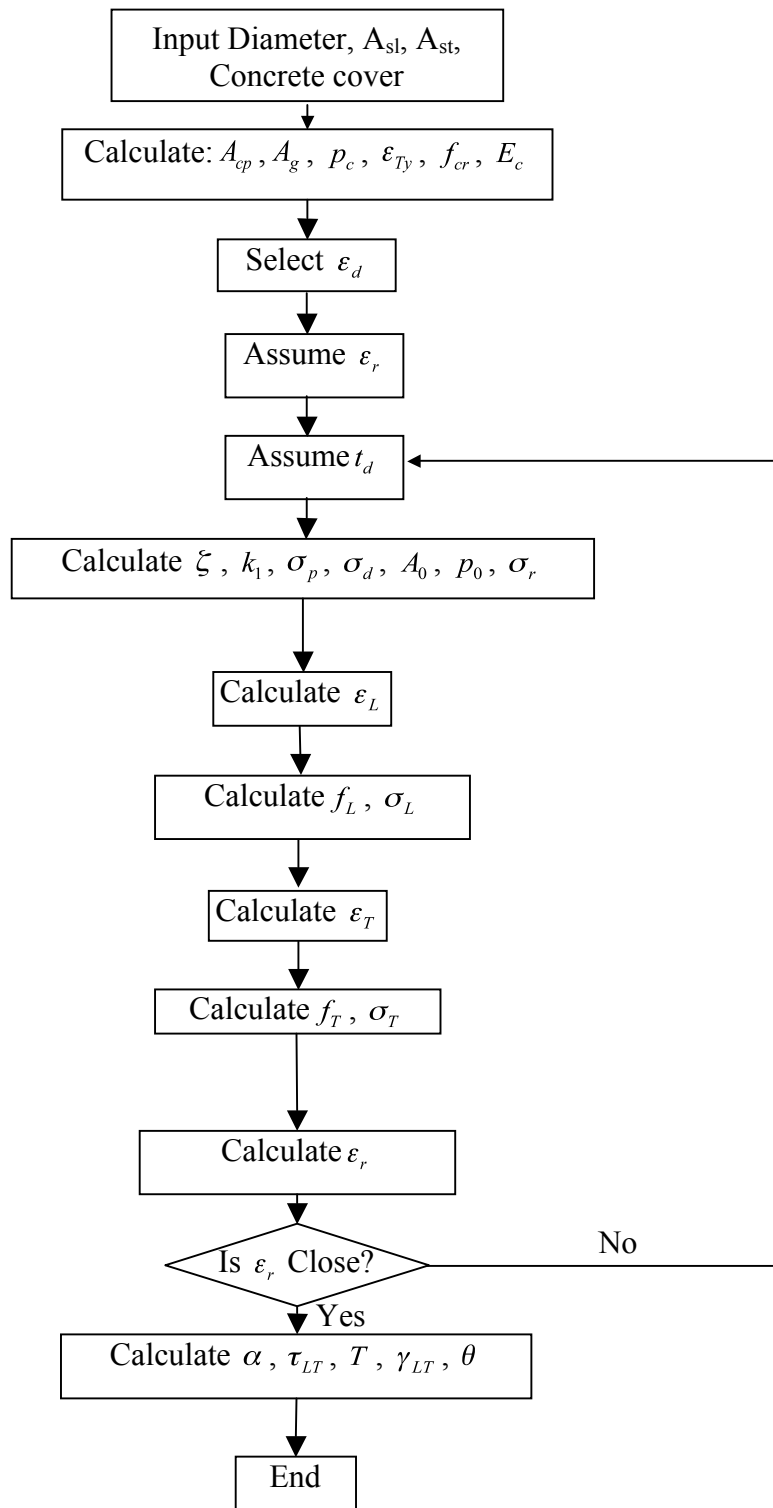
Figure 5.9 Solution Procedure for Circular TS-STM

5.5.6. Calculated Results and Validation with Test Data. The predictions of the proposed model for columns with spiral ratios of 0.73% and 1.32% are compared with test results in Table 5.5. Also, the predictions of the C-TS-STM for three different levels of compression capacity of the columns (0%, 7%, and 20% of $f'_c A_g$) are shown in Figure 5.10. The predictions of the model agree closely to the experimental one. Although the prediction of ultimate torsional capacity proved accurate, those for the post cracking stiffness and post yield behavior were approximate. However, the trend in variation of longitudinal and transverse strain distribution was close to experimental one. The predictions also indicated that with an increase in axial compression, the cracking torsional moment increases significantly and ultimate torsional moment would increase marginally for spiral ratios of 0.73% and 1.32%. Figure 5.11 shows the variation of longitudinal and transverse reinforcement strain. For spiral ratios of 0.73% and 1.32%, the model predicted that the transverse reinforcement would yield before the longitudinal reinforcement; as observed in the experiments. At failure, the longitudinal strain reduced after diagonal compression failure which is physically impossible. This is due to the discrepancy between concrete and steel constitutive laws after the peak point. This discrepancy arises because of disregarding the Poisson Effect. Figure 5.12 shows the variation of diagonal compression stress-strain.

Table 5.5 Comparison of Results with C-TS-STM Model for Pure Torsion

Parameter	Spiral Ratio of 0.73%		Spiral Ratio of 1.32%	
	Model	Experiment	Model	Experiment
Yielding Torsional Moment T_y (kN-m)	204	181.3	278	270
Ultimate Torsional Moment T_0 (kN-m)	253	269.9	304	330
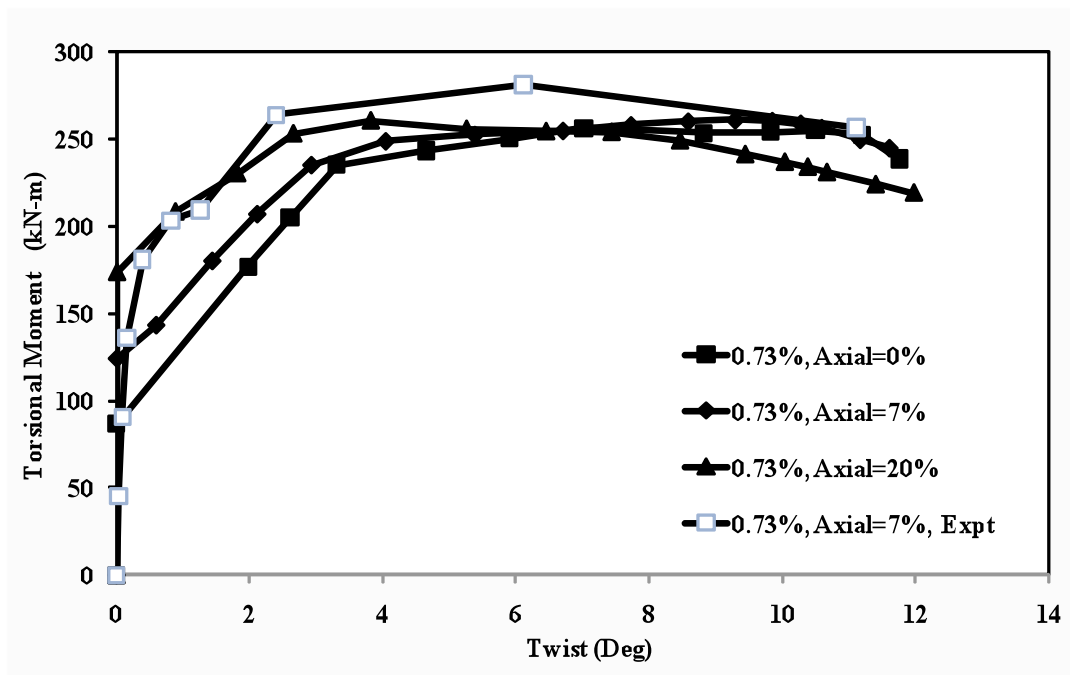
(a) Spiral Ratio of 0.73%
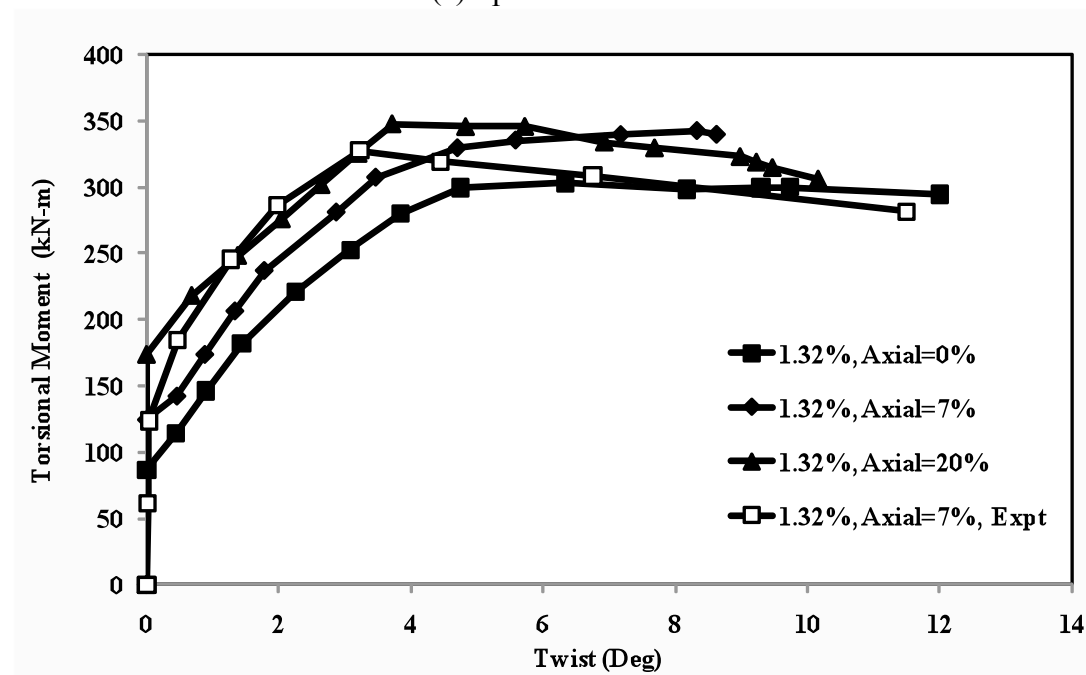
(b) Spiral Ratio of 1.32%

Figure 5.10 Comparison with Experimental and STM Results
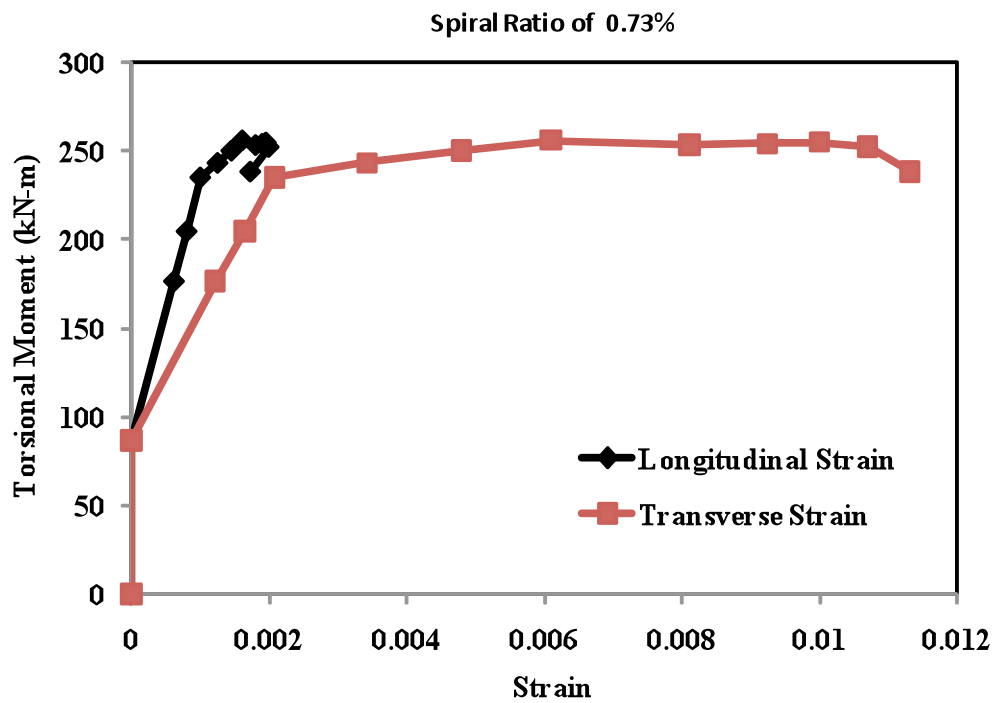
(a)
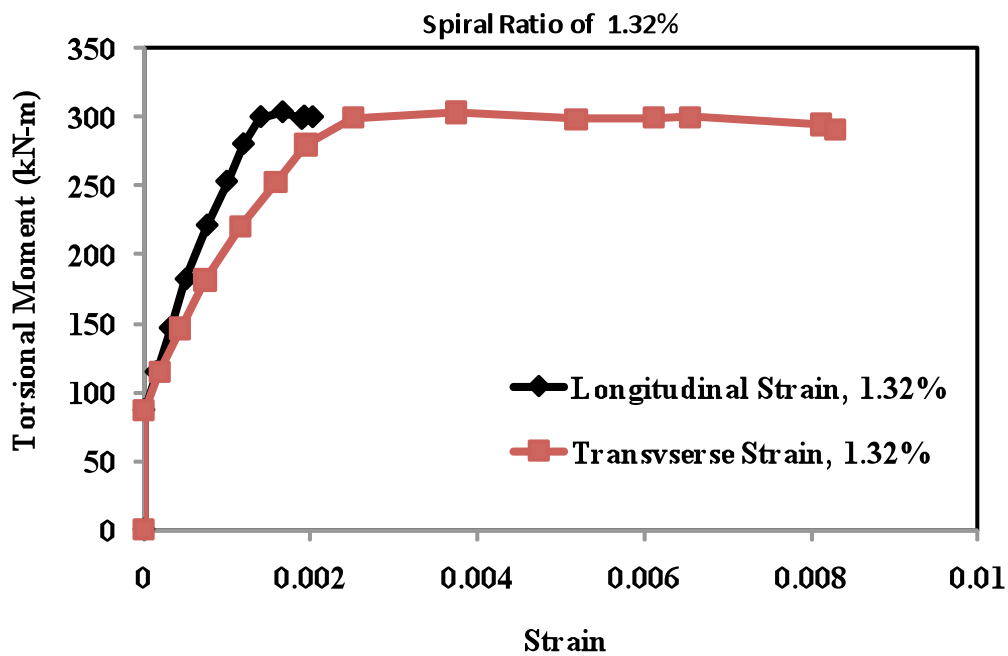
(b)

Figure 5.11 Variation in Longitudinal and Transverse Strain in the Absence of Axial Compression or Different Transverse Reinforcement Ratios
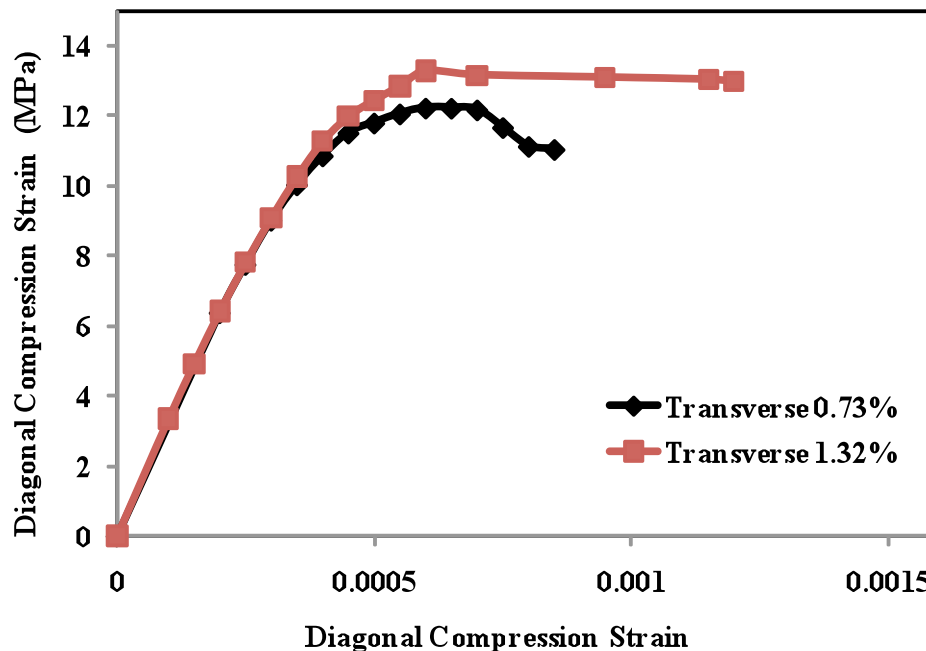
Figure 5.12 Variation in Diagonal Compression Stress-Strain Curves for Different Transverse Reinforcement Ratios

5.5.7. Effect of Axial Compression. Failure under combined torsion and axial compression is not common because this load combination rarely occurs without flexure. This study considers a simple case of circular sections with uniformly distributed longitudinal bars subject to uniform longitudinal strains under pure torsion and axial compression. Asymmetrical reinforced sections develop curvature of the longitudinal axis, and the response of such sections under torsion and axial compression is similar to that for combined bending and torsion.

Pure torsional moment causes cracks spiraling around the column. This results in concrete compression field in the form of diagonal struts that induces uniform longitudinal and transverse strains. If axial compression is applied together with torsional moment, and assuming that the circular column section is cracked due to torsion, the

tension in the longitudinal steel induced by torsion is reduced by the axial compression. Thus, the axial compression loading produces the similar effect of increasing the longitudinal steel content when resisting applied torsion. It results in increased torsion capacity of the section. This increase reaches a maximum value at the level of axial compression that totally restrains column elongation due to torsion; that is, it results in zero elongation under the combined axial compression and torsional moment. Greater axial compression inhibits diagonal cracking due to torsional moment and, as axial compression comes to dominate, failure occurs in the form of sudden explosive crushing of concrete. The effect of axial compression on a circular cross section considered in this experimental study was predicted using the proposed C-TS-STM (Figure 5.13). This model indicated that The increase in axial compression significantly would increase the cracking strength and slightly increase the ultimate strength. In most cases, it predicted due to diagonal crushing of the concrete strut. Thus, it showed that the effect of axial compression would be limited due to the sectional parameters considered in the study. More test results from future research work should clarify this phenomenon.
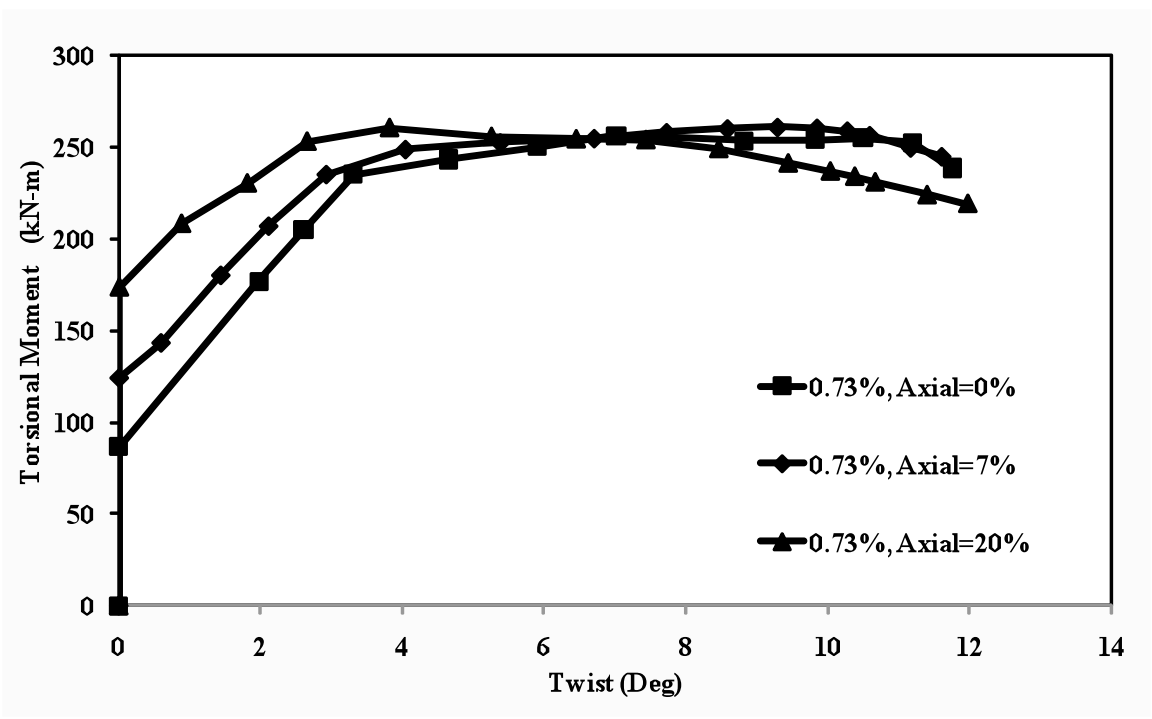
(a) 0.73%
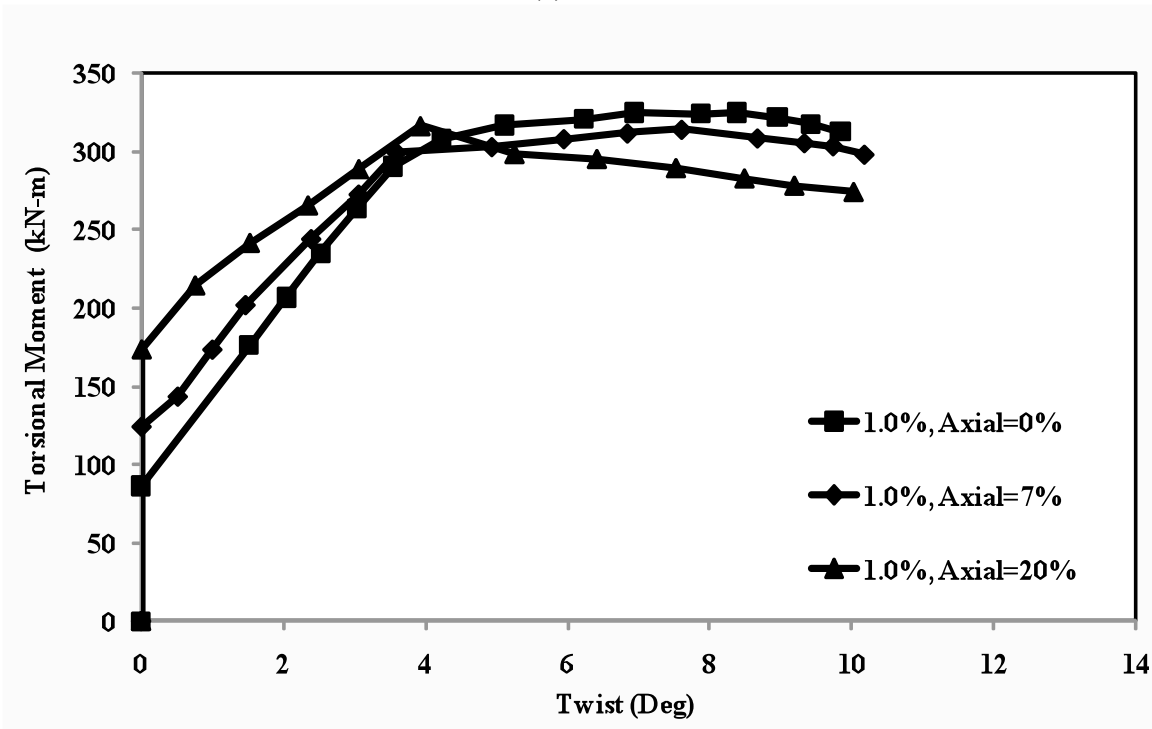
(b) 1.00%

Figure 5.13 Effect of Axial Compression on Torsional Strength for Different Spiral
Reinforcement Ratios

(c) 1.32%
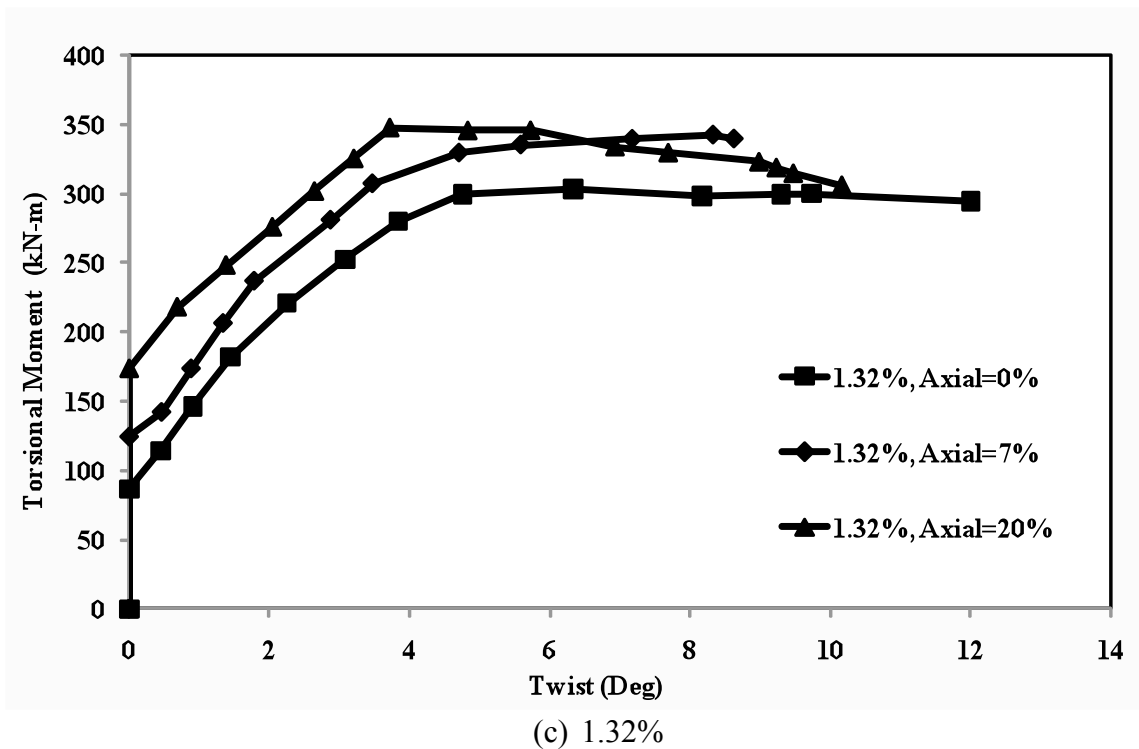
Figure 5.13 (Continued)

5.5.8. Effect of Transverse Reinforcement Ratio. This work investigated the effect of transverse reinforcement on the torsional moment-twist response curve. The increase in transverse reinforcement ratio increased the peak torsional strength (Figure 5.14). However, it also reduced the twist component at the ultimate torsional moment. This effect was due to the change in failure mode from less ductile to brittle diagonal compressive strut failure. Figure 5.15 compares the variation in longitudinal and transverse strain for transverse reinforcement ratios of 0.73% and 1.32%. It shows that an increase in the reinforcement ratio limits the strain levels in both longitudinal and transverse reinforcement, indicating that an increase in the transverse reinforcement ratio limits the damage in columns under pure torsion.
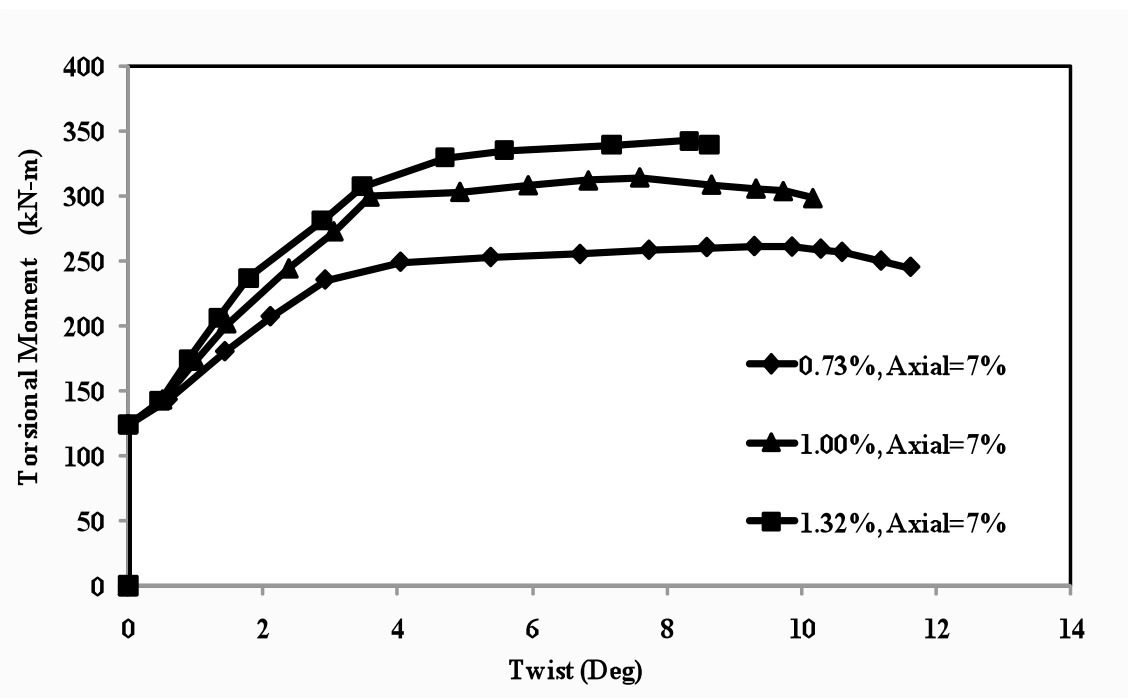
Figure 5.14 Effect of Transverse Reinforcement Ratios on Torsional Strength
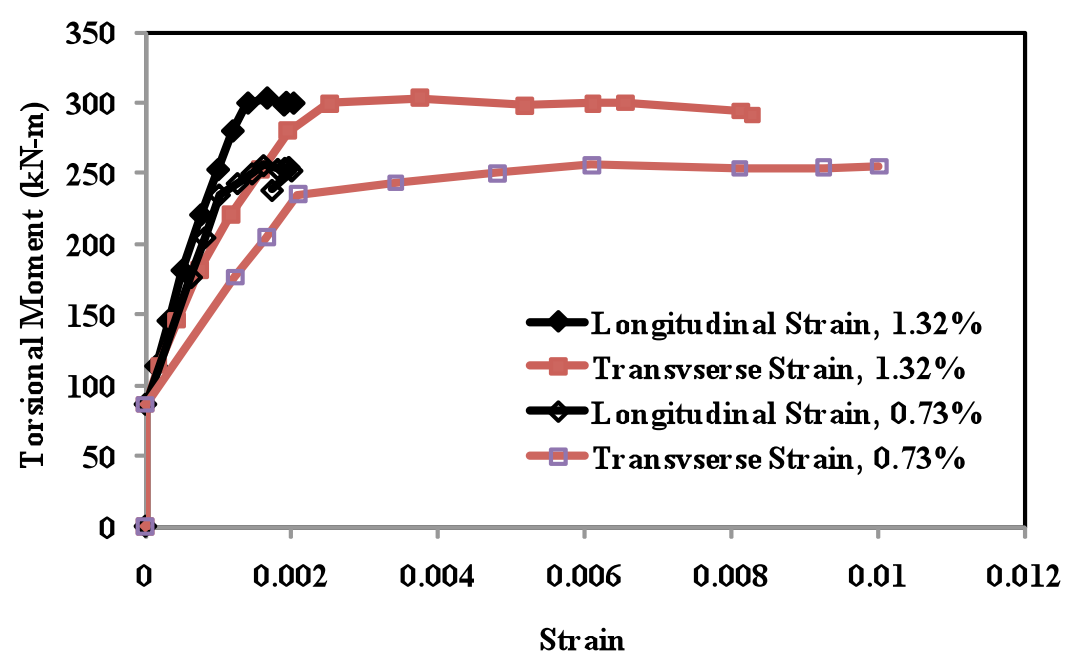
Figure 5.15 Effect of Transverse Reinforcement Ratios on Longitudinal and Transverse Strain Variation

5.5.9. Torsion-Axial Load Interaction Diagram. The failure interaction curve between axial compression and torsional moment is shown in Figure 5.16. The response curve for the case of pure torsion (T_0) to the point of zero elongation is predicted using the C-TS-STM corresponding to the case where the strain is found to be zero in longitudinal bars. A linear response is assumed between the points zero elongation and that representing pure axial compression. To predict the interaction response using the C-TS-STM, the concrete compressive strain on the effective surface was assumed to be at the crushing strain taken to be at a ε_{co}. The longitudinal strains and hoop strains were assumed to be uniform. At low levels of axial compression, the torsional capacity of a section is enhanced as in the case of axial compression and bending interaction. Unfortunately, there was not enough test data on circular columns with various amounts of axial compression to validate the predictions. To establish clearly the point of zero elongation, future testing should focus on application of axial compression greater than that required to restrain elongation due to torsion. In addition, the failure modes under diagonal concrete compression would limit the enhancement of torsional strength with an increase in axial compression. The influence of longitudinal and transverse reinforcement ratio is also important and demands further investigation.
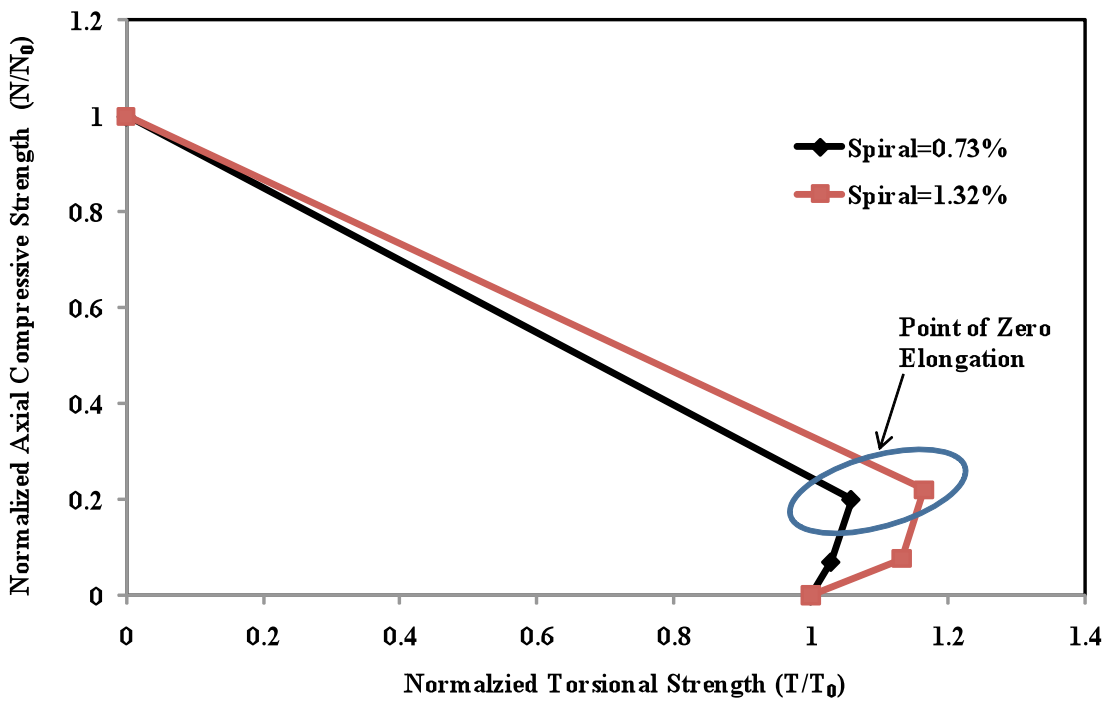
Figure 5.16 Axial Compression-Torsional Moment Interaction Diagram

5.6. TORSION-BENDING-SHEAR INTERACTION CURVES FROM FLEXURE AND PURE TORSION ANALYSIS

The interaction of shear, torsion and bending capacities can be calculated using the semi-empirical equations suggested by Elfgren (1972). The pure flexural capacity, pure shear capacity and pure torsion capacity are calculated using the models described in the previous Sections 5.3, 5.4 and 5.5. To get the same dimensions on all axes of the interaction curves, the shear capacity can be multiplied by the diameter of the column section:

$$\left(\frac{M}{M_0}\right)^2 + \left(\frac{T}{T_0}\right)^2 r + \left(\frac{V}{V_0}\right)^2 r = 1 \qquad \text{Eq. 5.50}$$

where

M_0 = Pure ultimate flexural capacity with no consideration of interaction with torsional moment into consideration (From section 5.2)

M = Flexural moment capacity with full interaction found from the loading conditions.

T_0 = Pure torsional moment capacity without taking any interaction as per section 6.3.2.

T = Torsional capacity with full interaction found from the loading conditions.

V_0 = Pure shear capacity without taking any interaction as per the MCFT model.

V = Shear capacity with full interaction found from the loading conditions.

r = Ratio of transverse reinforcement to longitudinal reinforcement; defined as $\dfrac{\rho_t}{\rho_l}$

Figure 5.17 shows the behavior of columns reinforced with spiral ratio of 0.73%. It also shows the corresponding test specimens with torsion-to-bending moment (T/M) ratios of 0, 0.1, 0.2, 0.4 and ∞. The strengths of all specimens was close to the outer interaction surface, indicating that the predictions were in reasonable agreement with the test results. Although all specimens had a low spiral ratio of 0.73%; the longitudinal reinforcement yielded before the spiral reinforcement under flexure and combined loading. Hence, the equation suggested by Elfgren (1972) for the failure mode-1 is a good way to predict the interaction diagrams of columns used in this study.
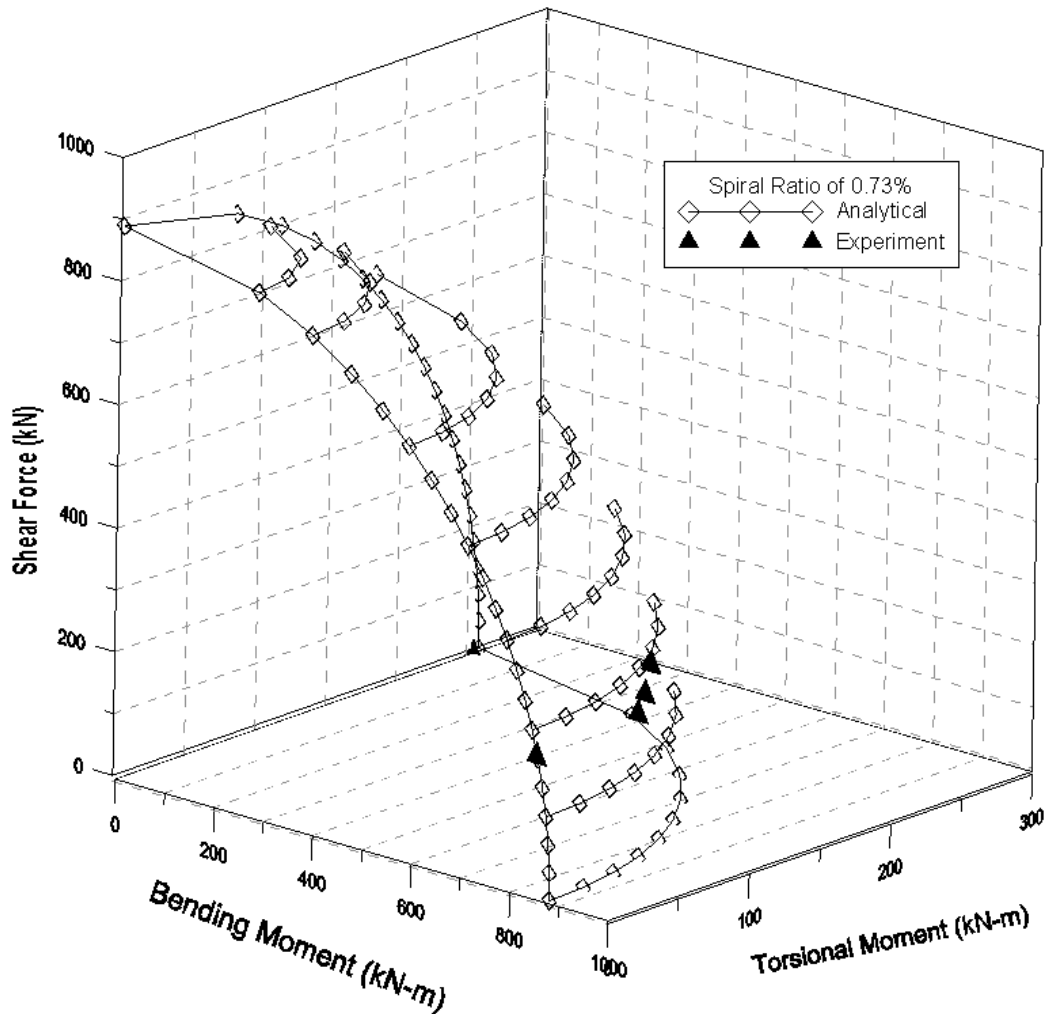
Figure 5.17 Torsion-Bending-Shear Interaction Diagrams for Columns with Spiral Ratio of 0.73%

Similarly, Figure 5.18 shows the behavior of columns reinforced with spiral ratio of 1.32%. It also shows the corresponding test specimens with T/M ratios of 0.2, 0.4, and ∞. The strengths of all specimens was at or close to the outer interaction surface. The projections of analytical predictions on Torsion and bending moment interaction surface is compared with test results in Figure 5.19. These predictions are also in reasonable agreement with the test results. Then behavior of columns with spiral ratio of 1.32% but

with different aspect ratio of 6 and 3 are compared along with the predictions in Figure

5.20. In addition, the normalized predictions are represented in Figure 5.21.
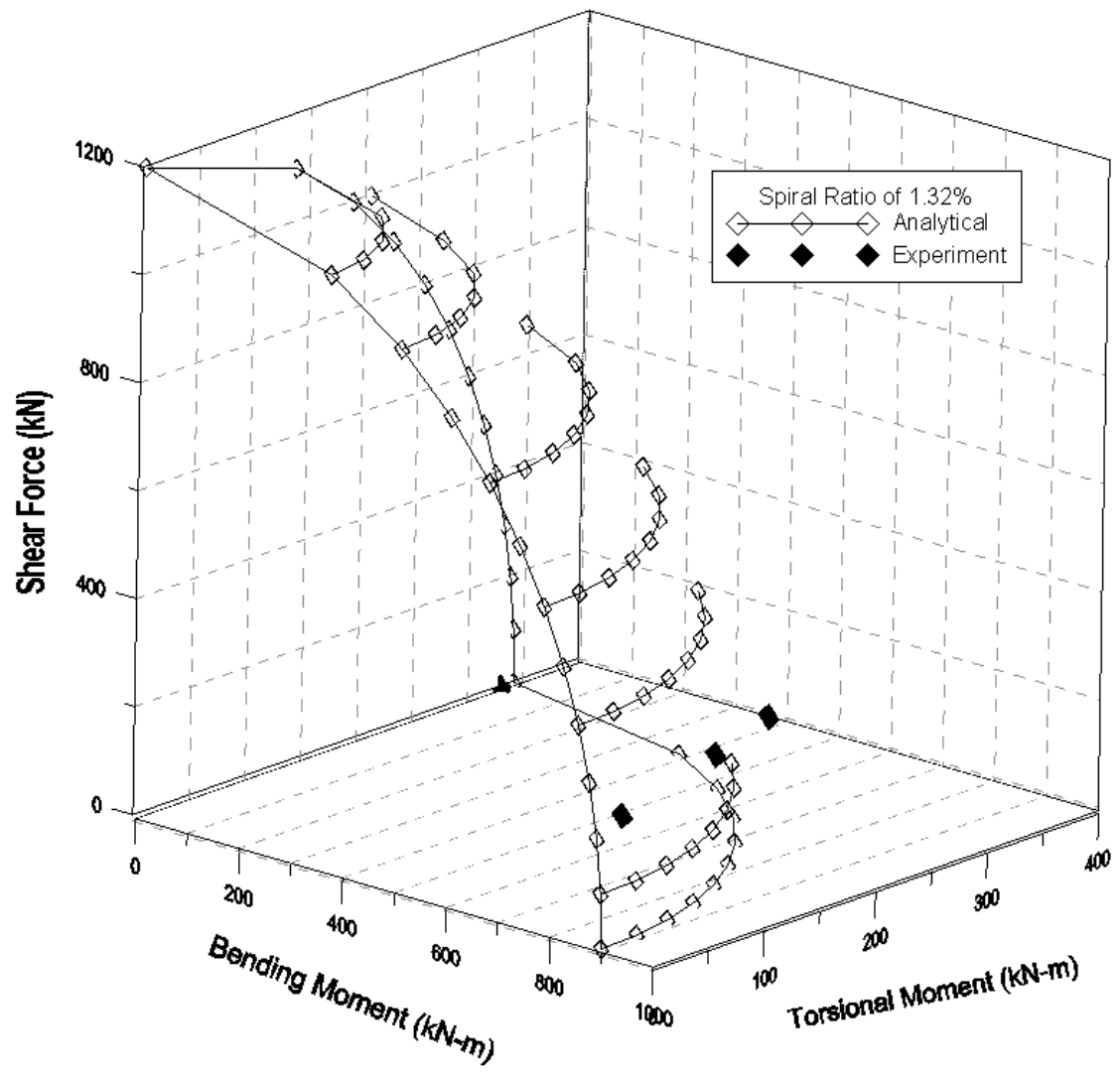
Figure 5.18 Torsion-Bending-Shear Interaction Diagrams for Columns with Spiral Ratio
of 1.32%
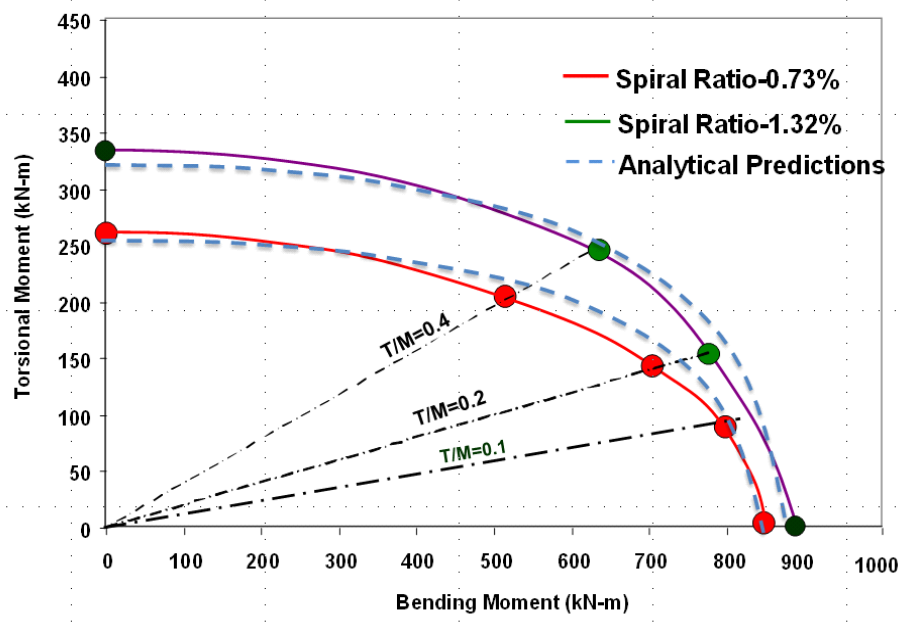
Figure 5.19 Comparison of Analytical Predictions with Test Results
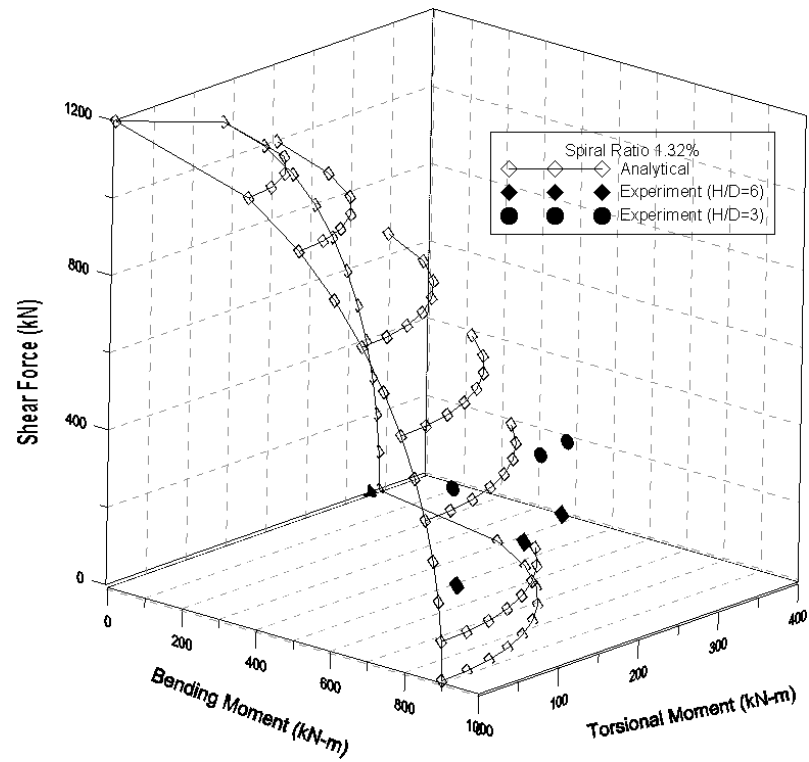
Figure 5.20 Torsion-Bending-Shear Interaction Diagrams for Columns with Spiral Ratio
of 1.32%
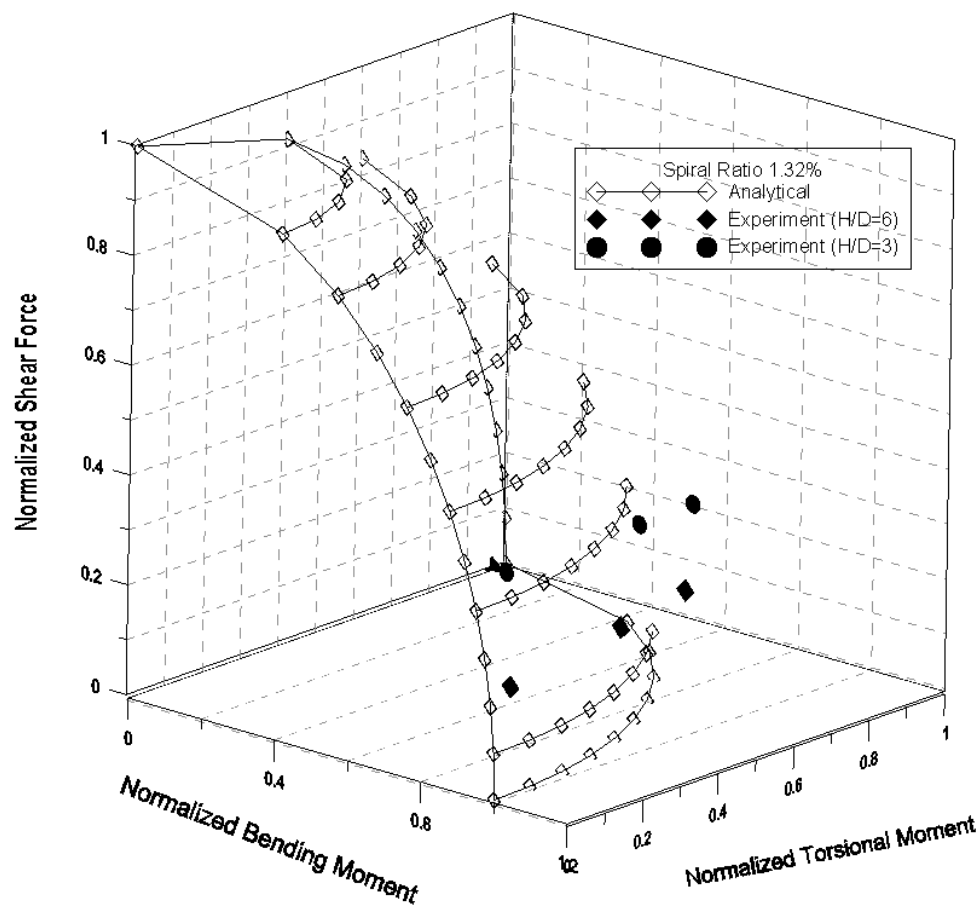
Figure 5.21 Torsion-Bending-Shear Interaction Diagrams for Columns with
Spiral Ratio of 1.32%

5.7. CONCLUDING REMARKS

This work developed analytical model for well-confined columns under flexure using the existing plastic-hinge-based models with some modifications. It extended the softened truss model to circular sections incorporating the tension-stiffening effect. It used the Response 2000 based on MCFT model to predict the shear capacity of circular columns. Interaction curves were established using analytical results from flexural, shear and pure torsion results as benchmark. The predictions agree closely with the experimental results; however, a significant improvements are required to develop a

unified model for combined loading including shear force and bending and torsional moments.

- Existing plastic-hinge-based model was used to predict the behavior of circular RC columns under flexure. The predictions agreed closely with experimental results. The model developed in this study can be extended to predict the behavior of columns under combined loading by adjusting the constitutive models for concrete to include the confinement and softening effect.

- Original Softened Truss Model was modified to circular sections by removing the variables related to warping and by including a tension-stiffening effect. The predictions under pure torsion were in good agreement with experimental data. However, the model could better predict the post-peak behavior if it were to include the Poisson effect.

- The predictions of the interaction diagrams agreed substantially with the experimental results.

6. DAMAGE-BASED DESIGN APPROACH FOR COMBINED LOADING INCLUDING TORSION

6.1. INTRODUCTION

The main objective of a performance-based or damage-based design is to consider the complex relationships between the severity of an earthquake and the desired performance of structural components. Since current seismic design codes focus mainly on the strength and serviceability requirements of members, they do not meet this performance objective. They are limited because they address the design of structures to meet particular seismic load levels but not necessarily to achieve specific performance objectives that incorporate damage prevention. Such objectives, however, including prescribed damage limit states can be incorporated in a performance-based design approach [Ghobarah, 2001; Floren and Mohammadi, 2001]. To implement a performance or damage-based design approach for a given earthquake level, design engineers require analytical models to define the damage in terms of engineering criteria such as strain and ductility levels. To facilitate repair and retrofit decisions, they must also quantify the damage in simple terms under various loading conditions, creating damage indices that take into account various design parameters. This section presents a damage-based design approach developed for combined loading including torsion. It also presents a detailed description of damage index models for combined loading.

6.2. BACKGROUND ON DAMAGE INDICES

This study extends the existing damage indices for flexural failure mode to combined loading. Development of damage-based design approach has three objectives: First, decoupled damage index models for combined loading must be developed to

identify the implications of combined loading from the perspective of performance-based seismic design. Second, experimental data must be used to examine the trends in the progression of damage with respect to increase in the T/M ratio, an increase in the transverse spiral reinforcement ratio, and a reduction in shear span needs to be explored using the experimental data. Finally, from a design perspective, damage index limits must be determined for various performance levels under combined loading. To achieve these objectives, this work validated the proposed damage index models based on test results, and key results are presented here.

Using predicted hysteresis curves, the damage indices can evaluate the performance of structural components during earthquakes of varying magnitudes. A proper damage index should include the parameters that describe the hysteretic behavior under combined loading including shear forces, flexural and torsional moment, and axial loads during earthquakes. Several studies have proposed damage indices based on flexural behavior [Williams and Sexsmith, 1995; Williams et al., 1997; Chung and Meyer, 2000; Hindi and Sexsmith, 2001; Khashaee, 2005]. However, none of these indices predict the progression of damage under combined loading. Jeong and Elnashai (2000) were the first to develop a three dimensional damage index for RC buildings with planar irregularities taking into account the bidirectional and torsional response. The authors decomposed the three dimensional structure into planar frames and incorporated the sensitivity of the local damage indices into the out-of-plane response. They also suggested a method to combine the local damage indices, and they verified their results with conventional damage indices. However, no damage index models have been developed explicitly to study the interaction effects of flexural and torsional damage

indices. The present study, therefore, is the first to define damage indices at various damage limit states for combined loadings. Under-reinforced circular columns tested under pure torsion have shown the damage was distributed along the whole length of columns before the ultimate stage after then severe core damage was observed around the middle height of the columns in the final stage. When flexural and torsional moments are applied to a column simultaneously, the distribution of damage increases depending on the applied T/M ratio as shown in Figure 6.1. This effect was also illustrated in the experimental results presented in Section 4.
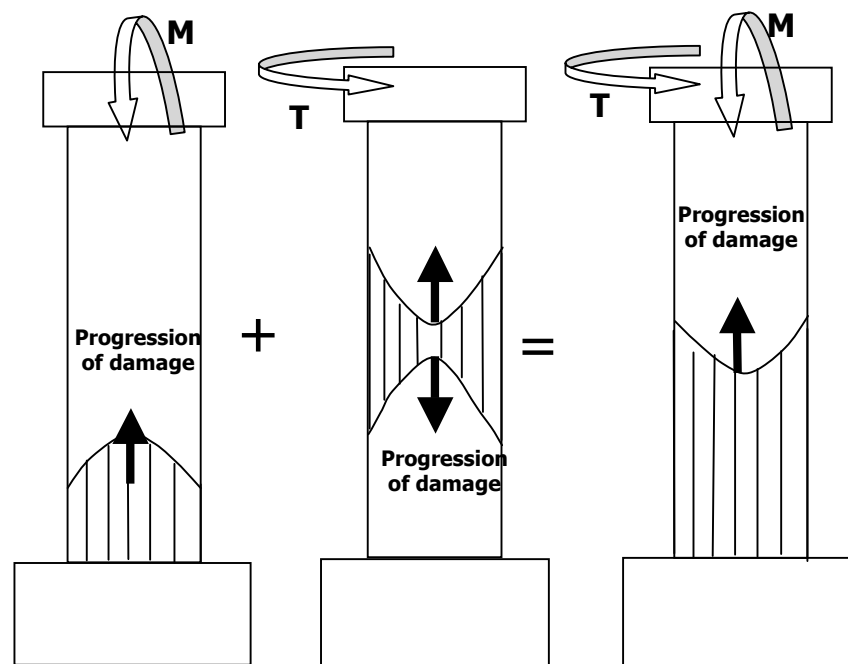
Figure 6.1 Possible Failure Sequences under Combined Loading

6.2.1. Previous Research on Damage Index Models. Damage indices provide a means to quantify the damage sustained by concrete structures during earthquakes. Damage indices may be defined locally at the cross section or at a member level either

for an individual element or for an entire structure. The earliest and simplest measures of damage were based on ductility and inter-storey drift. These simple damage indicators, however, consider neither degradation in the stiffness of the member or structure, nor energy dissipation under cyclic loadings. Current local damage indices are cumulative, and depend on damage and the amplitude and number of cycles of loading [Williams and Sexsmith, 1995; Hindi and Sexsmith, 2001]. Damage indices can inform retrofit decisions disaster planning, and post-earthquake assessment. They are dimensionless parameters; the lowest value of which indicates an undamaged structure. The highest value indicates a structure near or at collapse, and intermediate values estimating the degree of damage. Since these indices are based on flexural behavior, they cannot be used to correlate the limit states corresponding to flexure, shear, and torsion.

6.2.1.1 Non-cumulative damage indices. Banon et al. (1981) developed a damage index based on the ratio of initial stiffness to secant stiffness corresponding to the maximum displacement in a given cycle. The authors called their damage index as a flexural damage ratio. Later, Roufaiel and Meyer (1987) defined damage in terms of flexibility and modified the flexural damage ratio to develop the following formulation.

$$D_{RM} = \frac{f_m - f_0}{f_u - f_0} \qquad \text{Eq. 6.1}$$

where D_{RM} is the damage index of Raufaiel and Meyer, f_0 represents the pre-yield flexibility, f_m represents the secant flexibility at a given load, and f_u is the secant flexibility at ultimate load. However, this formulation does not reliably indicate failure since it does not include the effect of cyclic loading.

6.2.1.2 Energy-based cumulative damage indices. The damage indices proposed by Park and Ang and Hwang and Scribener are widely used in damage analysis and discussed in the following sections.

6.2.1.2.1 <u>Park and Ang damage index.</u> Park and Ang (1985) proposed a linear combination of non-cumulative and cumulative damage indices. Their model is defined by Eq. 6.2, in which the first term accounts for ductility in the system and the second presents the normalized cumulative energy absorbed by the member:

$$D_{PA} = \frac{u_m}{u_u} + \beta \frac{E_{hm}}{Q_y u_u} = \frac{\mu}{\mu_u} + \beta \frac{E_{hm}}{Q_y u_y \mu_u} \qquad \text{Eq. 6.2}$$

where u_u represents the ultimate displacement under static load, u_y is the yield displacement, μ is displacement ductility, μ_u is the displacement ductility at ultimate, β is a constant accounting for the effect of cyclic load and structural properties, E_{hm} represents the maximum hysteretic energy demand, Q_y is the yield strength of the structure. The levels D_{PA} are interpreted as follows:

$D_{PA} < 0.1$	No damage, or localized minor cracking
$0.1 \le D_{PA} < 0.25$	Minor damage: light cracking throughout
$0.25 \le D_{PA} < 0.40$	Moderate damage: severe cracking, localized spalling
$0.4 \le D_{PA} < 1.00$	Severe damage: concrete crushing, reinforcement exposed
$D_{PA} \ge 1.0$	Collapse

The parameters used in this model are shown in Figure 6.2. The β factor, which accounts for the effect of cyclic earthquake load, ranges from 0.05 to 0.15. It shows that more weight is given to the displacement ductility term than to the energy dissipation term. The accuracy of the prediction depends mainly on the definition of ultimate parameters from the predicted monotonic curve. Taylor and Stone (1993) have found that the damage index goes slightly higher than the damage index value of 1. The main advantage of Park and Ang damage index is that it is simple and physically intuitive since it ranges from '0', representing no damage to '1', representing near collapse. Kunnath et al. (1997) analyzed this model with a number of experimental data and concluded that the model is most appropriate for column failure resulting from large plastic displacement demands.

(a) Flexural Hysteresis   (b) Torsional Hysteresis
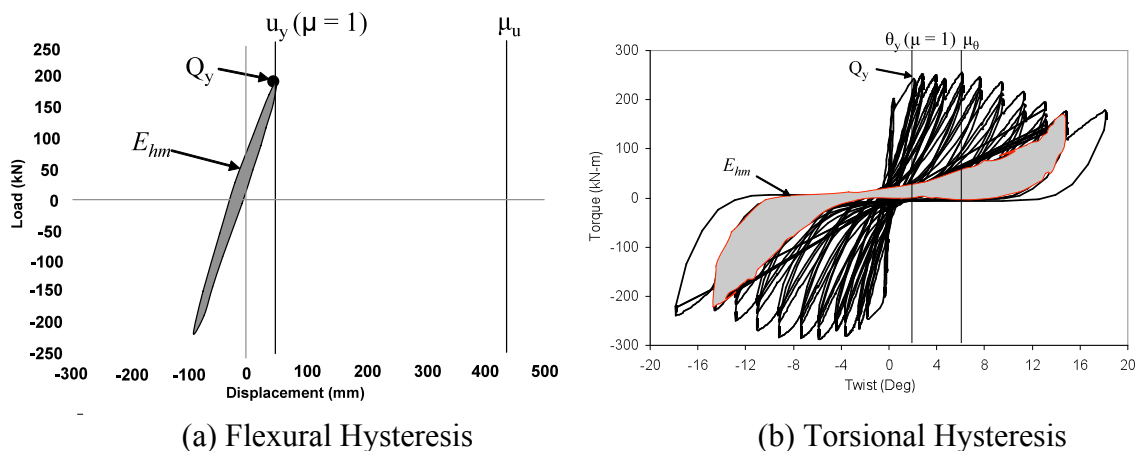
Figure 6.2 Definition of Parameters for Park and Ang Model

6.2.1.2.2 <u>Zahrah and Hall damage index.</u> The index developed by Zahrah and Hall (1984) represents the level of damage in the member by the number of equivalent yield excursions. This index includes the maximum hysteretic energy demand,

displacement ductility, and yield strength of the member:

$$N_{eq} = \frac{E_{hm}}{Q_y u_y (\mu - 1)}$$ Eq. 6. 3

where u_y is the yield displacement, μ is displacement ductility, E_{hm} is the maximum

hysteretic energy demand, Q_y is the yield strength of the structure, and N_{eq} is the number of

equivalent yield excursions.

        6.2.1.2.3 <u>Hwang and Scribner damage index.</u> This model includes stiffness and

energy dissipation along with displacements in a given cycle. Figure 6.3 defines

parameters for this index. The formula for the calculation of the damage index is

$$D_{HS} = \sum_{i=1}^{M} \Delta E_{hi} \frac{K_{mi}}{K_o} \frac{u_{mi}^2}{u_y^2}$$ Eq. 6. 4

where D_{HS} represents the damage index by Hwang and Scribner, i is the cycle number, M

is the total number of yield cycles, K_o is the pre-yield stiffness, ΔE_{hi} is the hysteretic

energy dissipated in the ith cycle, u_{mi} is the maximum displacement in the ith cycle, K_{mi} is

the secant stiffness corresponding to u_{mi}, and u_y is the yield displacement. This damage

index assigns equal importance to all parameters (Hwang and Scribner, 1984). The

authors called it a work index since it includes force and displacement. The main

disadvantage of this index is that its range is not unity like that that of the index proposed

by Park and Ang. Further, it depends heavily on the cross sectional property of the

member and the loading history. This dependence makes it difficult to quantify the

damage limit states based on performance for members with different cross sectional details.
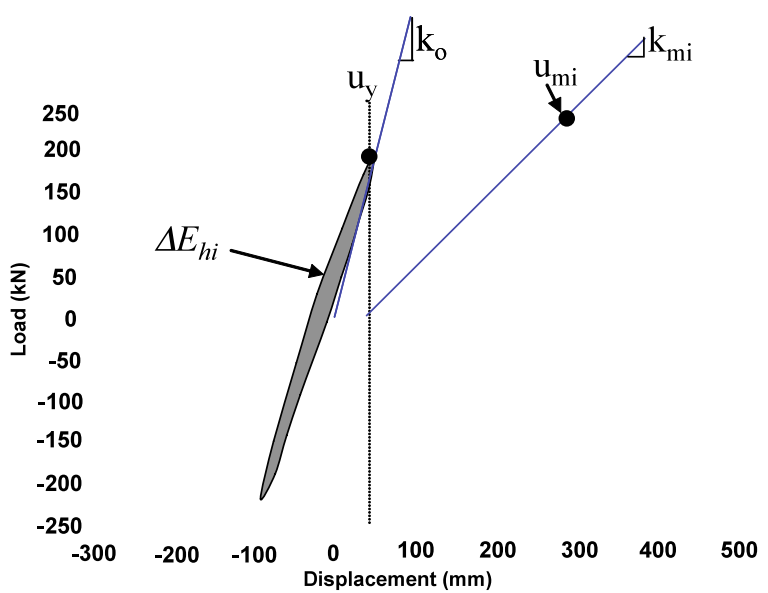
(a) Flexural Hysteresis
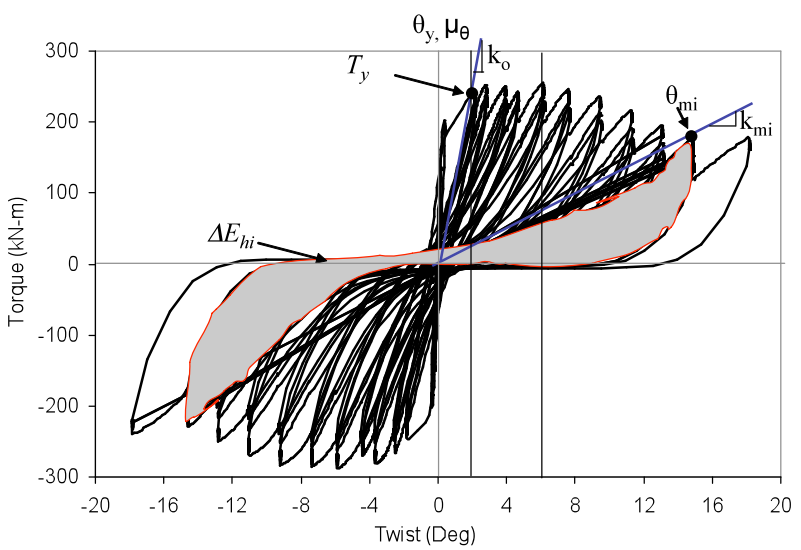
(b) Torsional Hysteresis

Figure 6.3 Definition of Parameters for Modified Hwang and Scribner Model

Only limited calibration of these indices has been performed against observed damage in laboratory tests or post-earthquake investigations. The physical meaning of

these indices categorized into the numerical values will remain unclear until they are validated with experimental results under various types of loading. In addition, these indices are based primarily on flexural failure mode: however, the experience of recent earthquakes suggests that even structures designed according to very recent codes often fail in shear or in combined shear and flexure modes. The ability of the indices to describe the damage levels with respect to failure mechanisms other than flexural yielding is largely untested. A proper understanding of damage states under combined loadings is thus necessary to develop damage index models for combined loadings.

6.3. CATEGORIZATION OF DAMAGE STATES UNDER COMBINED LOADING

In general, parameters such as member geometry, sectional details, material properties, and loading combinations are used to characterize the behavior of RC columns under combined loading. Due to the influence of multiple parameters, the failure modes of columns under combined loadings are very complex. However, damage under combined bending, shear, and torsion loadings can be broadly categorized as explained in the sections below.

6.3.1. Flexural and Shear Cracking. Cracking will occur when the principal tensile stresses reach the cracking strength of concrete. For RC sections under pure flexure, cracks will form perpendicular to the longitudinal axis of the member. For columns under combined bending, shear, and torsion, the cracking directions are inclined to the longitudinal axis of the member depending on the level of applied shear forces and torsion. Under the combined actions of torsion, bending, and shear, the inclination of principal compressive stresses (i.e., the direction of crack angles) and the strain

distribution in longitudinal reinforcement and spiral reinforcement vary across the depth of the cross section and along the length of the member. With an increase in T/M ratio, the angle of diagonal compression increases. For the columns tested in this study, the angle of diagonal compression with respect to longitudinal axis varied from 134° under pure torsion to 90° under flexure [Belarbi et al., 2008]. These results show that spirals will be highly strained with an increase in the applied torsion-to-bending moment ratios, and longitudinal reinforcement will be highly strained with a reduction in applied T/M ratios.

6.3.2. Longitudinal Reinforcement Yielding. Yielding of the longitudinal reinforcement marks the onset of permanent structural distress and represents an important damage limit state. Under combined bending and torsion, the yielding mechanism of longitudinal reinforcement is complex. Torsional loads induce uniform tensile strain in the longitudinal bars. Under bending, however strains vary from compression on one side to tension on the other side. Due to geometry, yielding in a circular section is more progressive than in other cross sectional shapes under bending. Yielding of longitudinal reinforcement starts on the tension side and gradually spreads to adjacent bars around the column. In the test specimens used here, the first yielding of longitudinal reinforcement was measured using strain gages.

6.3.3. Initial Cover Spalling. The onset of spalling of the cover concrete depends on a number of factors such as the longitudinal reinforcement ratio, clear cover, type of section (i.e., square/rectangular/circular), and types of stress (i.e., shear or flexure). Spalling of the concrete cover is significantly different under compression from under bending-shear, and it is different still under combined bending, shear, and torsion.

A mesh of closely spaced longitudinal and transverse reinforcement produces an interfacial failure between the concrete cover and core. The separation of this plane is triggered by a change in the direction of compressive stresses in the concrete cover and by the differences in the mechanical behavior of the concrete core and cover.

Under bending and shear, spalling typically occurs when the concrete at the cover approaches the crushing strain. Spalling of concrete cover in the plastic-hinge region will generally occur following extensive yielding of longitudinal reinforcement and prior to reaching the ultimate flexural load. Thereafter, stiffness begin to degrade. The extent of spalling along the column height is also important since it determines the minimum length over which confinement by transverse spiral reinforcement is required from a flexural design point of view. Under combined bending, shear, and torsion loadings, spalling of concrete cover occurs due to shear flow characteristics and changes in the shear flow direction. The potential for spalling under torsional loadings is proportional to the compressive stresses in concrete cover, the cover thickness, and the area of the splitting plane occupied by the reinforcement and inversely proportional to the concrete tensile strength and size of the section. In general, the spalling of concrete cover represents moderate damage that can be repaired without much difficulty.

6.3.4. Crushing of the Diagonal Compression Strut. After cracking of concrete, the applied torsional loadings are resisted by the diagonal concrete compression struts as a compressive element and by steel reinforcements as a tension element similar to a truss mechanism. Like the compression block under bending loads, there is a depth of compression zone under torsion called a thickness of shear flow zone. Once the concrete reaches it's the compressive strength, then crushing starts in the diagonal strut.

However, due to softening effect, the diagonal compressive strength is much lower than the normal compressive strength under combined loadings. This crushing of the diagonal strut is a very important damage limit state as it represents the failure of the RC member under combined bending, shear, and torsion loadings.

6.3.5. Yielding of the Transverse Reinforcement. Under torsional loadings, yielding of transverse reinforcement is an important damage limit state from a torsional ductility point of view. This yielding of transverse reinforcement can result from significant shear forces and or torsion. Torsional resistance increases only slightly after yielding of transverse reinforcement. Test results have also shown that columns adequately designed in flexure often reach the yielding of transverse reinforcement much faster under the presence of even small amounts of torsion [Prakash and Belarbi, 2009]. In addition, the post-yield plateau is much smaller under combined bending, shear, and torsion, which leads to much smaller increase in torsional resistance.

6.3.6. Longitudinal bar buckling, spiral fracture, and longitudinal bar fracture. After severe spalling of concrete cover and significant degradation of the concrete core, the spiral and longitudinal reinforcement are exposed. The longitudinal bars then begin to buckle due to the nature of cyclic loadings during an earthquake. Typically, in all test specimens used in this study, the buckling of longitudinal bars was typically observed in the flexural plastic-hinge zone. However, the length of the buckled longitudinal bar increased with the level of applied torsion. This buckling is a final damage limit state because it represents the collapse of the structure.

6.4. FAILURE DEFINITIONS UNDER COMBINED LOADING

The force-displacement and torsional moment-twist hysteresis curves under combined loading are shown in Figure 6.4. This study assumed that failure is reached when a reduction in strength of at-least 10% is achieved and stiffness begins to degrade. In some of the specimens the reduction in strength was less than 10% until the rupture of longitudinal bars was observed. The test was stopped after rupture of longitudinal bars due to safety reasons. In such specimens, the failure was taken at the cycle of the rupture of longitudinal bars. Under combined loading, failure in flexure and torsion may or may not happen simultaneously in the same cycle. In such cases, interaction diagrams of the index for damage under flexure and torsion would be useful; the following sections offer such diagrams.
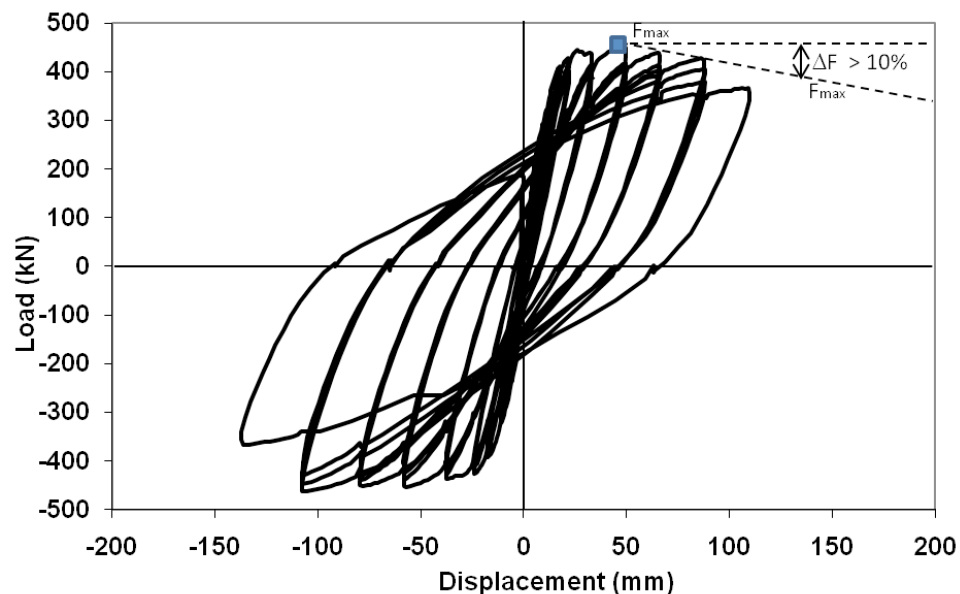
(a) Flexural Hysteresis

Figure 6.4 Definition of Failure Cycles
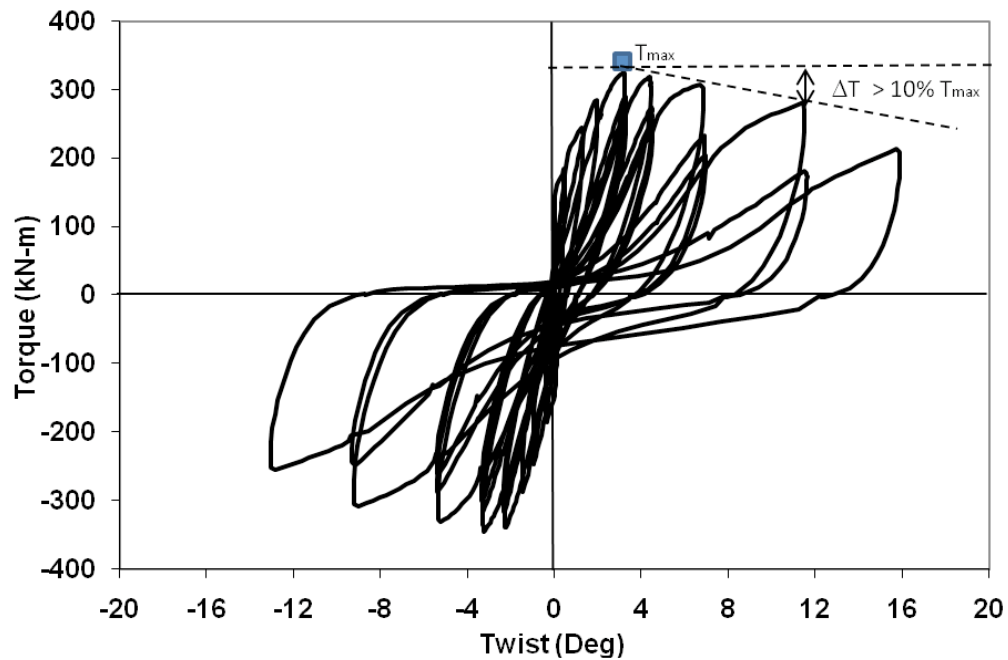
(b) Torsional Hysteresis

Figure 6.4 (Continued)

6.5. PROPOSED DAMAGE INDEX FOR COMBINED LOADING

Schematic framework for the design of RC columns under combined loadings using damage index models is shown in the Figure 6.5. There are two principal steps required to develop a damage index for seismic structural assessment under combined loading. First, nonlinear flexural and torsional response of a column subject to an earthquake must be obtained from either an analytical or an experimental study. Since the indices in this study are computed directly from the experimental hysteresis data, no analytical hysteresis data are required. This study investigates whether damage indices can provide reliable information on the extent of structural damage, based on the hysteresis data under combined loading. The Park and Ang damage index and the modified Hwang and Scribner damage index were used to predict damage under flexure.

Based on this approach, damage index models were developed for pure torsional loading. The models used for combined shear forces, flexural and torsional moment were decoupled to distinguish the effect of flexural and torsional behavior from the combined loading state. The accuracy of the predictions depends on the accuracy of the flexural and torsional hysteresis used for the evaluation. Models are available to predict the hysteretic behavior of RC circular columns under flexure (Priestley et al., 1996) and their static behavior under pure torsion (Hsu, 1993). However, no analytical models have yet been developed to predict the hysteresis behavior of RC circular columns under combined loading. The second step in developing a damage index for combined loading is to accommodate the study of damage progression. This step involves i) determination of the force at longitudinal yielding and the corresponding displacement, ii) torsional moment at spiral yielding and corresponding twist from the predicted hysteresis curves.
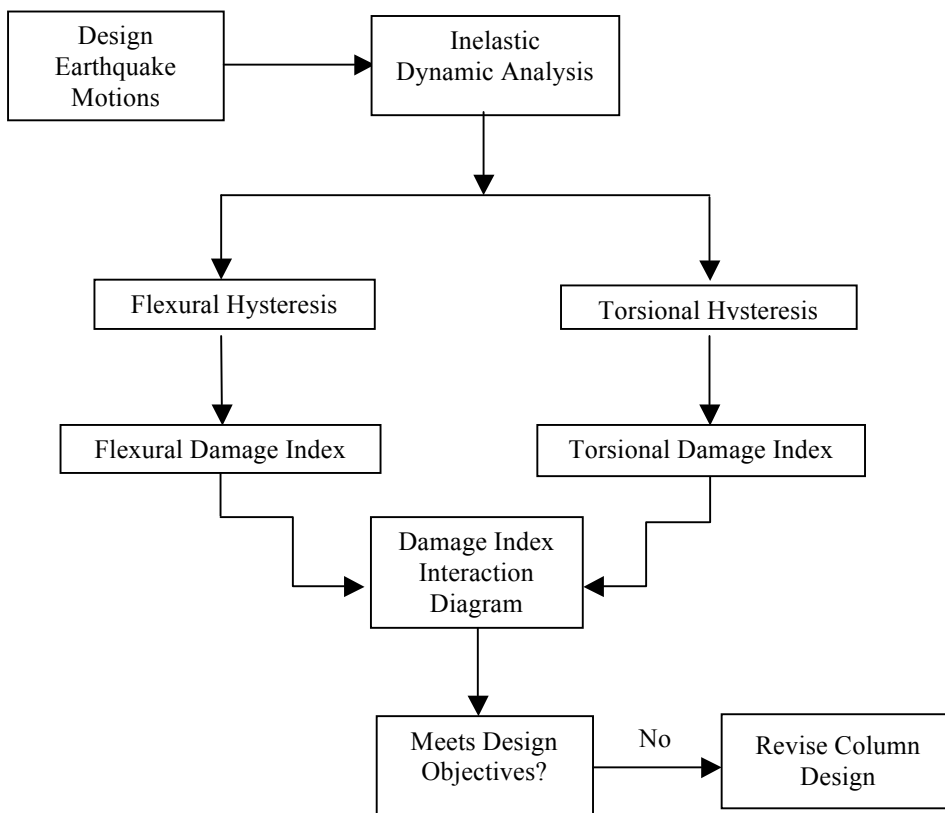
Figure 6.5 Design Framework for RC Columns under Combined Loading Using Damage Index Models

6.5.1. Damage Index Model using Park and Ang Approach. A cumulative damage index model proposed by Park and Ang (1985) was modified here for torsional loading. The flexural and torsional hysteresis was used to calculate the damage index for flexure and torsion respectively, under combined loading. The existing equations for a flexural and torsional damage index under combined loading are

$$DI_{Flexural, Combined} = \frac{u_m}{u_u} + \beta \frac{E_{hm}}{Q_y u_u}$$

Eq. 6.5

and

$$DI_{Torsional,Combined} = \frac{\theta_m}{\theta_u} + \beta \frac{E_{hm}}{T_y \theta_u}$$

Eq. 6.6

The parameters needed to calculate the damage index under torsion are; i) the maximum twist in a cycle, ii) yielding torsional moment, iii) ultimate twist corresponding to ultimate torsional moment. These parameters are derived from analytical prediction or experimental data and the energy dissipated in the given cycle, as shown in Eq. 6.6 and Figure 6.2b.

6.5.2. Damage Index Model using the Hwang and Scribner Approach. The damage index model proposed by Hwang and Scribner was modified here for flexural hysteresis by normalization with respect to energy dissipated under flexure. The approach adopted to predict damage under flexure was modified for torsional loading using the energy dissipation, stiffness, and twist components from torsional hysteresis. Again, the proposed index for torsion was normalized with the energy dissipation under torsional hysteresis to make it a dimensionless number. The following equations are thus proposed for flexural and torsional damage indices respectively, under combined loading:

$$DI_{Flexural,Combined} = \frac{\sum_{i=1}^{M} \Delta E_{hi} \frac{K_{mi}}{K_o} \frac{u_{mi}^2}{u_y^2}}{E_{Flexure}}$$

Eq. 6.7

and

$$DI_{Torsional,\,Combined} = \frac{\sum_{i=1}^{M} \Delta E_{hi,T} \frac{K_{mi,T}}{K_{o,T}} \frac{\theta_{mi,T}^2}{\theta_{y,T}^2}}{E_{Torison}}$$

Eq. 6.8

6.6. VALIDATION OF PROPOSED DAMAGE INDEX MODELS

The proposed damage index model for combined loadings was validated through a research program that evaluated the hysteretic response of RC circular columns according to the test matrix presented in Table 3.1. The main variables considered in the experimental program were (1) the T/M ratio, (2) the column aspect ratio (H/D) to simulate a flexural or shear dominant response, and (3) the level of detailing for high and moderate seismicity as explained in Section 4. The aspect ratio plays an important role in determining the behavior of columns dominated by flexure or by shear. For columns tested in single curvature, as in this study, the aspect ratio is defined as the ratio of the height (M/V=H) to diameter (D) of the column. Columns with higher aspect ratios attract lower seismic load, whereas shorter and stiffer columns attract a much greater portion of the seismic input. The test matrix, therefore, includes circular columns built with two transverse reinforcement ratios, two aspect ratios (H/D=6 and a lower aspect ratio of H/D=3), and five T/M ratios.

6.6.1. Influence of Torsion on Damage Index. Damage indices were calculated for flexural and torsional hysteresis for the columns under combined loading; these are presented in Figure 6.6, which plotted the damage index values derived from the Hwang and Scribner and the Park and Ang models up to the value of ultimate load reached in flexural hysteresis and ultimate torsional moment reached in torsional hysteresis. This figure clearly shows that for both models the progression of damage is amplified with an increase in T/M ratio for flexural hysteresis and with a decrease in T/M ratio for torsional hysteresis.

The damage index values of the Park and Ang approach work as well for torsional hysteresis as for flexure. In both cases, the ultimate limit state reached when the damage index reached one. Also, with the Park and Ang approach, the progression of damage index was linear in both flexure and torsion (Figure 6.6 a,b); because there was less weight on the normalized energy dissipation term. For flexural hysteresis, the damage index for the Hwang and Scribener approach was higher than for the Park and Ang approach; it was lower for torsional hysteresis (Figure 6.6c,d).

The flexural displacement ductility at ultimate state dropped from 17.5 to 4.5 and 4 when the T/M ratio increased from 0 to 0.2 and 0.4 respectively (Figure 6.6 a,c). Further, the torsional twist ductility at ultimate state dropped from 2.5 to 1 when the T/M ratio decreased from ∞ to 0.2 and 0.4. (Figure 6.6d). This observation shows that the transverse spiral reinforcement ratio of 0.73% was not adequate to provide post-yield strength since ultimate state and spiral yielding occurred simultaneously.

Park and Ang Approach
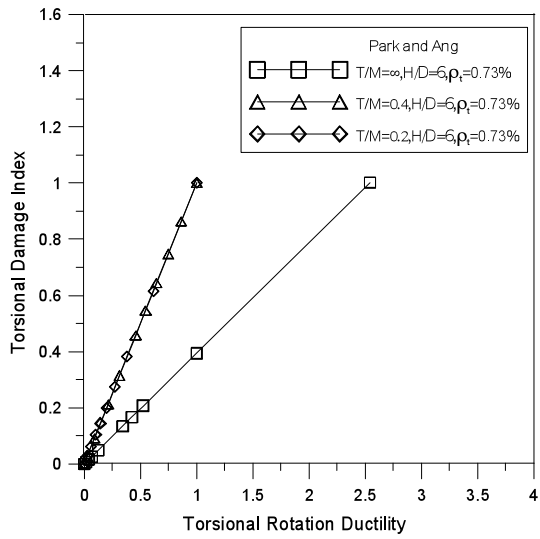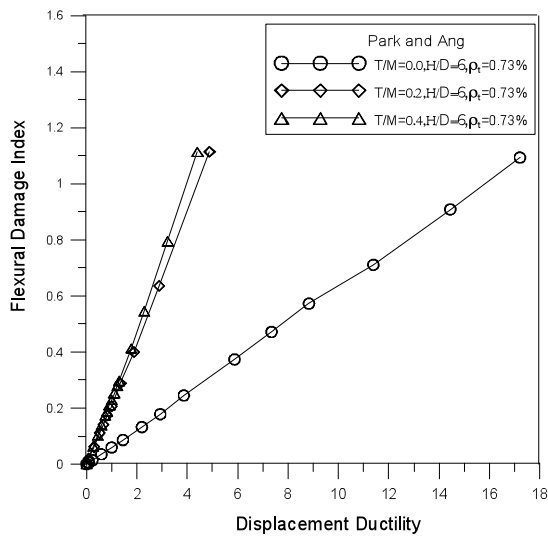
(a) Flexural Damage Index

(b) Torsional Damage Index

Hwang and Scribner Approach

(c) Flexural Damage Index

(d) Torsional Damage Index

Figure 6.6 Effect of Torsion on Damage Index Using Park and Ang and
Hwang and Scribner Approach

For flexural hysteresis, the predictions based on the Hwang and Scribner approach became highly nonlinear after spalling of concrete cover. Similarly, for torsional hysteresis, the predictions using the Hwang and Scribner approach became highly

nonlinear after yielding of the transverse spiral reinforcement. Although parameters are normalized in the Hwang and Scribner approach, the damage index values corresponding to ultimate state in flexural and torsional hysteresis are significantly different.

The ultimate flexural damage indices were 23, 9, and 4 (Figure 6.6c) for T/M ratios of 0, 0.2, and 0.4 respectively. Similarly, the ultimate torsional damage indices were 0.4, 0.3, and 0.1 (Figure 6.6d) for T/M ratios of ∞, 0.4, and 0.2. These indices complicate a one-to-one comparison of the damage level in both flexure and torsion on the same scale for combined loading. However, in flexural and torsional hysteresis, both models clearly show the progression of damage.

6.6.2. Influence of Spiral Reinforcement Ratio on Damage Index. For the columns under combined loading, damage indices for the columns with transverse spiral reinforcement ratios of 0.73% and 1.32% are presented in Figure 6.7. For both types of hysteresis, the progression of damage is clearly contained with an increase in the transverse spiral reinforcement ratio. The ultimate flexural damage index was reached at a displacement ductility of 11 and 7, compared to 4.5 and 4 for a T/M ratio of 0.2 and 0.4 respectively (Figure 6.7a). Similarly, the ultimate torsional damage index was reached at rotation ductility of 2.4 and 1.25, compared to 1 for a T/M ratio of 0.2 and 0.4 respectively, using the Park and Ang approach. These results show that there is an increase in displacement as well as rotational ductility with an increase in the transverse spiral reinforcement ratio.

Park and Ang Approach

(a) Flexural Damage Index

(b) Torsional Damage Index

Hwang and Scribner Approach

(c) Flexural Damage Index

(d) Torsional Damage Index
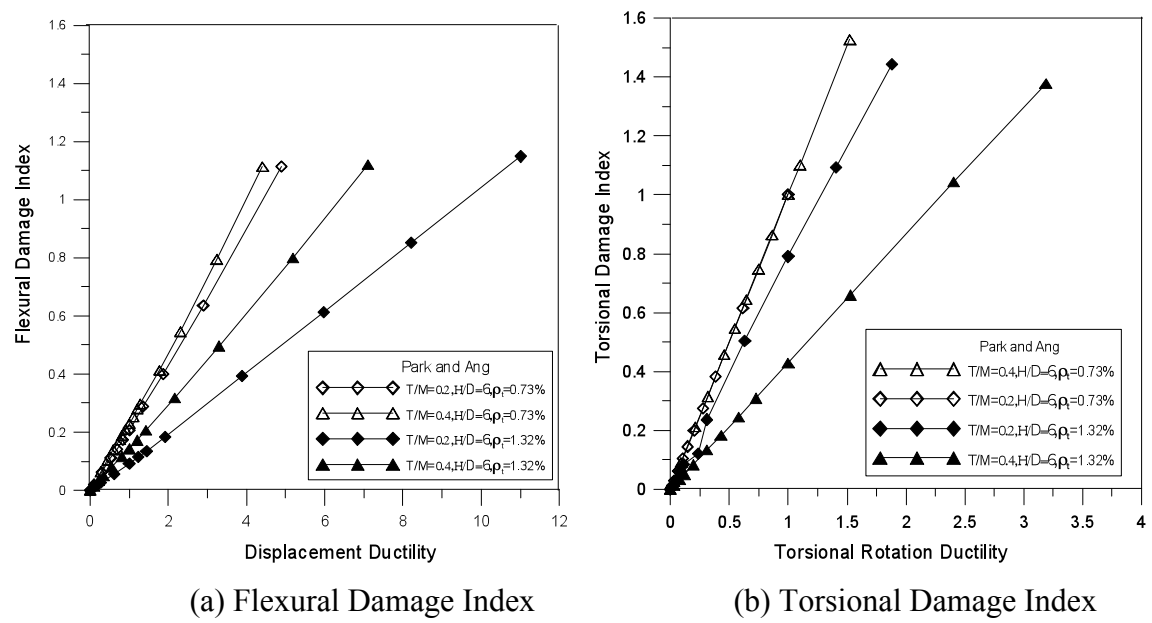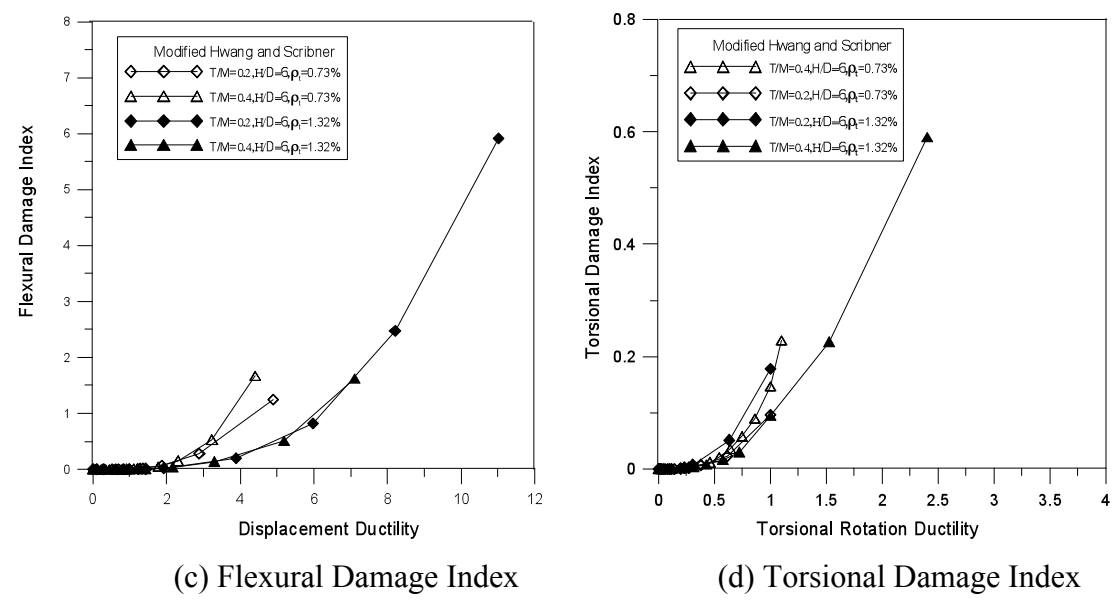
Figure 6.7 Effect of Transverse Spiral Reinforcement Ratio Damage Index using Park and Ang and Hwang and Scribner Approach

Notably, the Hwang and Scribner approach shows that flexural damage index values are higher than torsional damage index. For a T/M ratio of 0.2, flexural damage index values were 1.5 and 6 at ultimate state for transverse reinforcement ratios of 0.73%

and 1.32% respectively. According to the Hwang and Scribner approach, higher damage indices for a column translate into improved performance measured in terms of energy dissipation capacity and strength degradation. This principle was clearly demonstrated with an increase in the spiral reinforcement ratio. However, using the Hwang and Scribner approach, the damage index resulted in no unified value for ultimate state for various levels of torsion (Figure 6.7c,d). Additionally, this approach produced different values depending up on the transverse spiral reinforcement ratios; unlike the model based on the Park and Ang approach.

6.6.3. Influence of Shear Span on Damage Index. Damage indices were calculated for flexural and torsional hysteresis for the columns under combined loading with aspect ratios of 3 and 6 as presented in Figure 6.8. The progression of damage was clearly amplified with the reduction in aspect ratio for both flexural and torsional hysteresis. This amplification is due to the additional effect of increased shear force and flexural and torsional moment with a reduction in aspect ratio. Significantly, due to the reduced aspect ratio, displacement ductility dropped but twist ductility increased for a given T/M ratio when the damage level is constant (Figure 6.8). Flexural displacement ductility at the ultimate damage index dropped from 11 to 5 and from 7 to 4.5, corresponding to T/M ratios of 0.2 and 0.4 with aspect ratios of 6 and 3 respectively (Figure 6.8a) For a T/M ratio of 0.4, torsional twist ductility at the ultimate damage index increased from 2.5 to 4 when the aspect ratio decreased from 6 to 3 (Figure 6.8a). This increase was mainly due to the increase in bending stiffness with reduction in shear span; there was no apparent change in torsional stiffness due to reduction in shear span. Although the damage index values predicted by each approach were different, the trend

in progression of damage was clear. Again, using Hwang and Scribner approach, the damage index values corresponding to ultimate state in torsional and flexural hysteresis were significantly different for various specimens (Figure 6.8c,d).
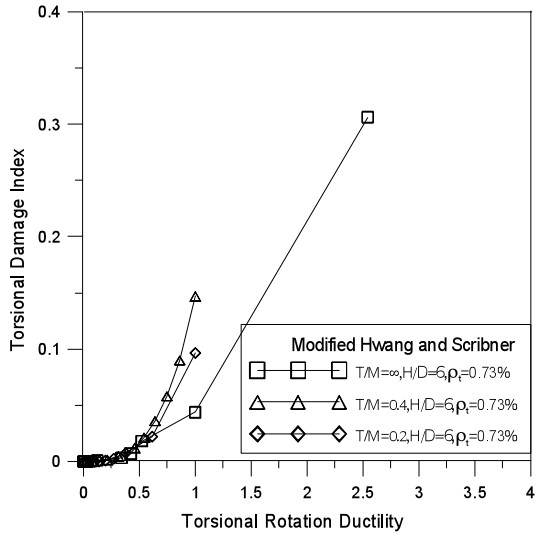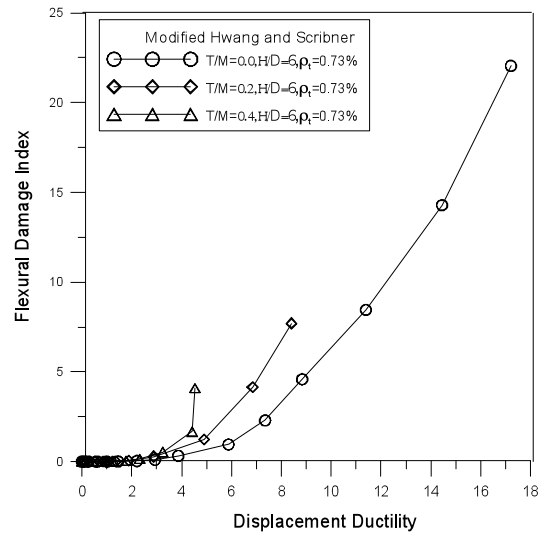
Park and Ang Approach
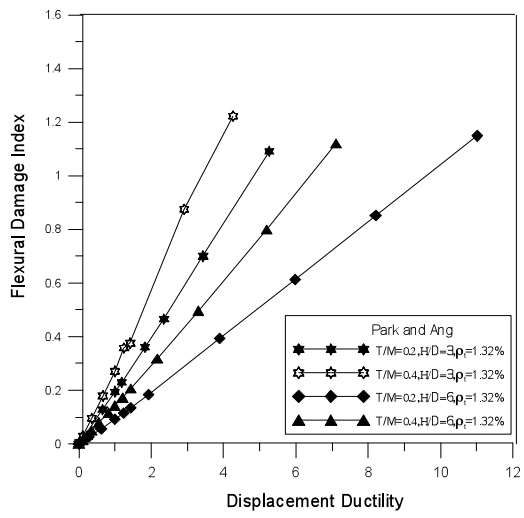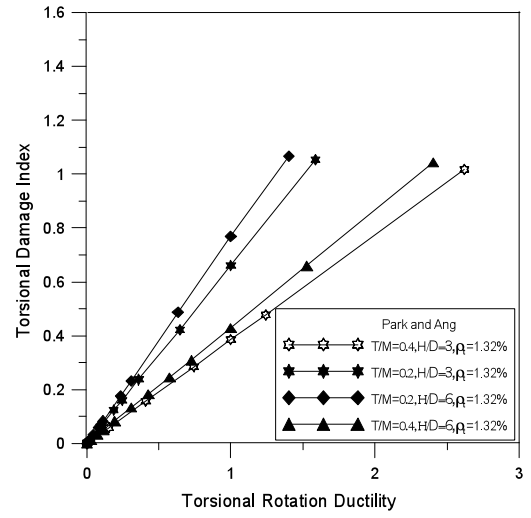
(a) Flexural Damage Index   (b) Torsional Damage Index

Hwang and Scribner Approach
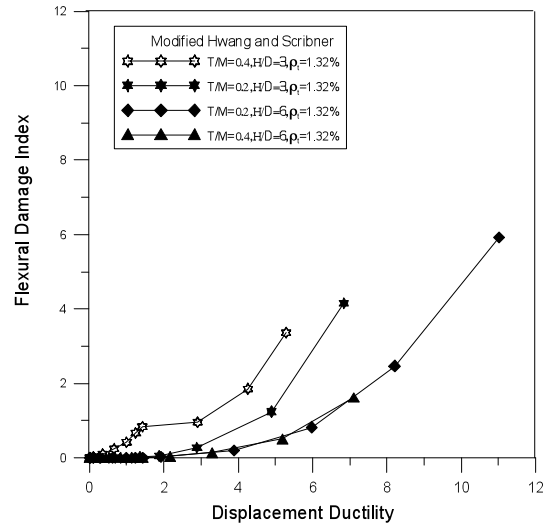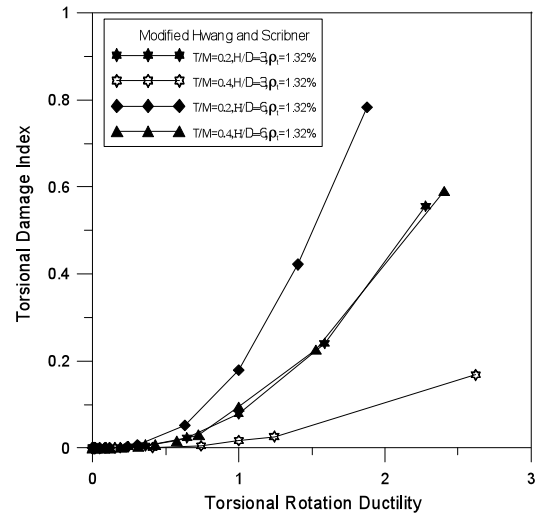
(c) Flexural Damage Index   (d) Torsional Damage Index

Figure 6.8 Effect of Shear Span on Damage Index using Park and Ang and Hwang and Scribner Approach

6.6.4. Interaction of Flexural and Torsional Damage Indices. The predictions based on the Park and Ang approach were physically intuitive in their representation of the damage under combined loading. Hence, they provide the basis for discussion from this point. The damage index values generated from the Park and Ang approach were used to create the diagrams of interaction between flexural and torsional damage indices shown in Figure 6.9c. This interaction can be split into a number of zones, namely, flexural cracking, shear cracking, longitudinal yielding, spiral yielding, and ultimate torsional strength.

The effect of torsion and transverse spiral reinforcement is shown in Figure 5.29a. With a low transverse spiral reinforcement ratio of 0.73%, the columns failed in torsion as the torsional damage index reached the value of '1' before the flexural damage index. The interaction between flexural and torsional moment depended on a number of factors, such as the amount of transverse and longitudinal reinforcement, the aspect ratio of the section, and concrete strength. This relationship shows that a transverse reinforcement ratio that is adequate from a confinement design point of view may not satisfy performance specifications under torsional loadings. Further, even with an increase in the transverse spiral reinforcement ratio, the columns reached the torsional damage index value of '1' just before the flexural damage index reached '1'. However, by containing damage due to increased confinement, the increase in transverse spiral reinforcement ratio made the failure mode less torsional dominant.

In addition, with an increase in the transverse spiral reinforcement ratio, the flexural damage index values and progression of damage were nearly the same for various levels of T/M ratio. The effect of shear span reduction on flexural and torsional

damage index interaction is presented in the Figure 6.9b. This reduction changed the behavior from torsional dominant to flexural dominant. The flexural damage index reached the value of '1' just before the torsional damage index reached the same value.

Using these experimental results, an empirical model was developed to predict the interaction of torsional and flexural damage indices:

$$TDI = \lambda. \left[\left(1.29\rho_t^2 + 7.935\rho_t + 12.39 \right) \frac{T}{M} \right] FDI \qquad \text{Eq. 6.9}$$

where TDI refers torsional damage index, FDI represents the flexural damage index, ρ_t is the spiral reinforcement ratio in percent, λ is a correction factor for the T/M ratio. This factor accommodates a higher spiral reinforcement ratio of 1.32% and varies linearly from 1.5 to 0.8 for T/M ratio from 0.6 to 0. For a spiral reinforcement ratio of less than 1.32%, this factor is 1. Similarly, empirical models could be developed to quantify the flexural damage index and the reduction in ultimate displacement ductility and torsional twist ductility. Using these models, flexural and torsional damage states could be quantified for a given T/M ratio and column sectional details, providing design parameters. The proposed empirical model represents a first step toward development of a damage-based design approach for RC bridge columns under combined loadings. It establishes parameters for spiral reinforcement and T/M ratios. The above empirical equation is applicable only for circular columns. The damage behavior of other sectional shapes will be different (Prakash and Belarbi, 2010; Belarbi et al., 2010). However, such a study needs to be undertaken for various cross sectional shapes such as interlocking, rectangular, and box-sections.
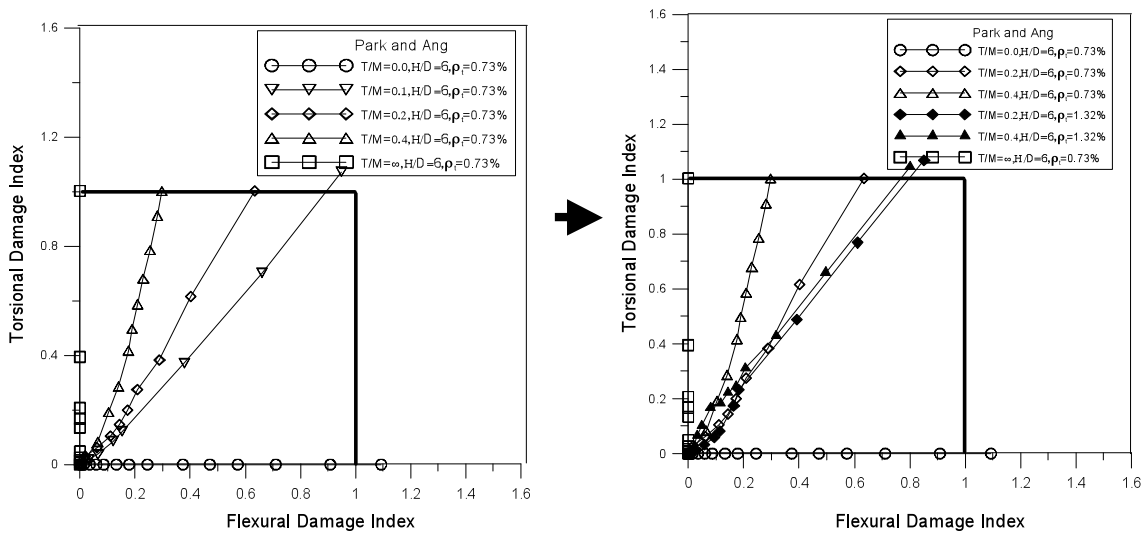
(a) Effect of Transverse Spiral Reinforcement Ratio
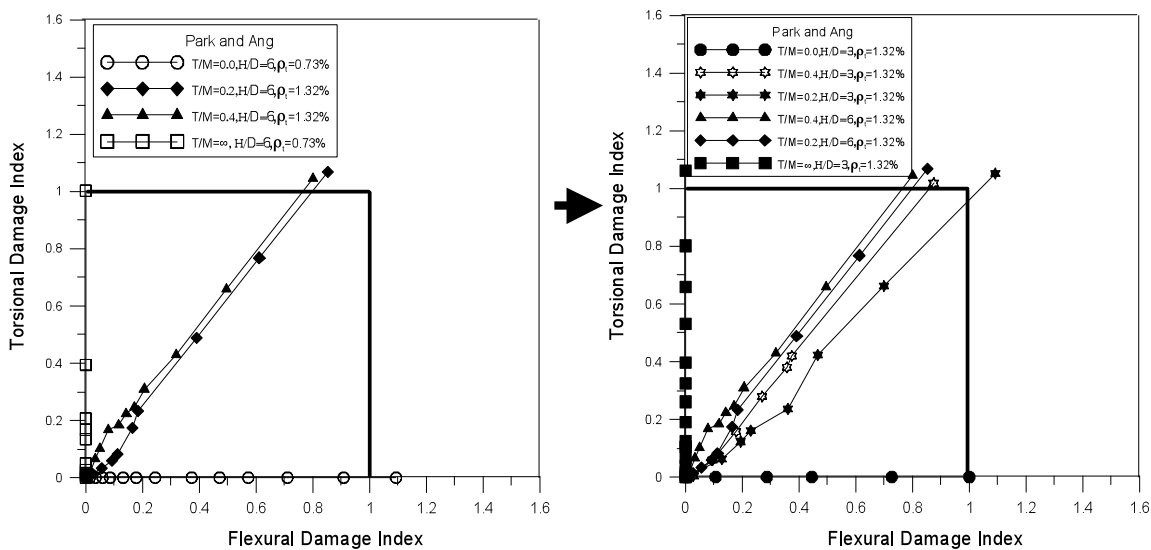
(b) Effect of Aspect Ratio

Figure 6.9 Interaction of Flexural and Torsional Damage Indices
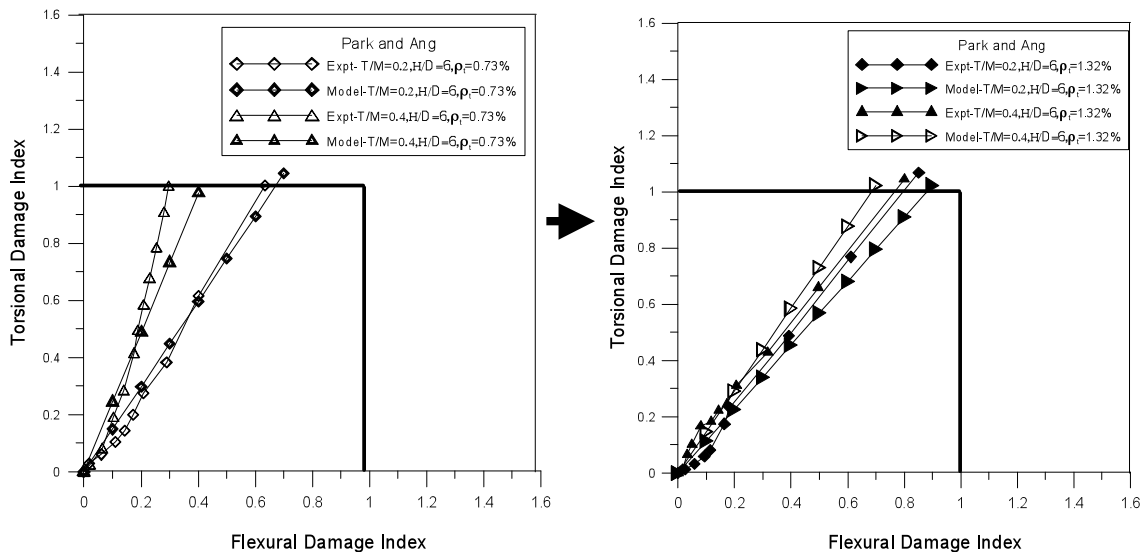
(c) Comparison with the Model

Figure 6.9 (Continued)

Figure 6.9c compares the predictions of the model with the experimental data. The predictions were reasonably accurate for spiral reinforcement ratios of 0.73 and 1.32%. Equation 6.9 clearly shows the increase in the torsional damage index with increases in the T/M ratios. The experimental results demonstrate that the model accurately predicted the change from torsional-dominant behavior to flexural-dominant behavior with an increase in the spiral reinforcement ratio. The failure mode of the columns under combined loadings varied significantly with variations in the longitudinal and spiral reinforcement ratios. The columns used in this study had a constant longitudinal ratio of 2.10%. Thus, the results of the proposed equation are applicable only to those specimens with a longitudinal reinforcement ratio of approximately 2%. The proposed equation could be improved with further experimental and analytical research to include parameters such as concrete strength, concrete cover, bending moment to shear ratio, and so on.

6.7. CORRELATION OF DAMAGE INDEX WITH OBSERVED DAMAGE

The progression of damage index values should be quantified in terms of observed damage. The most important practical aspect of these indices is their ability to give a reliable indication of the failure stages of these columns. Lehman and Moehle (2001) have categorized damage states based on flexural tests on RC columns. The damage states under flexure based on the results of this study are given in Figure 6.10 and explained in Table 6.1. The damage levels were categorized into no damage or localized minor cracking with an index less than 0.15. From a repair and retrofitting design perspective, the occurrence of cracking is of some importance in the context of performance-based design approach. Minor damage or light cracking throughout the column occurred when the damage index was less than 0.2 or higher than 0.15. The spalling of concrete cover indicates the necessity for disruptive repairs. Moderate damage, or severe shear cracking with localized spalling occurred when the damage index was less than 0.4 or higher 0.2. As concrete crushing became more severe, the core concrete was damaged often necessitating more extensive repair measures. This severe damage occurred when the damage index was less than 0.8 or higher 0.4. All these limits, however, must also be quantified in terms of damage index values under pure torsion and combined shear forces, and flexural and torsional moments.

No damage   Minor damage   Moderate damage   Collapse
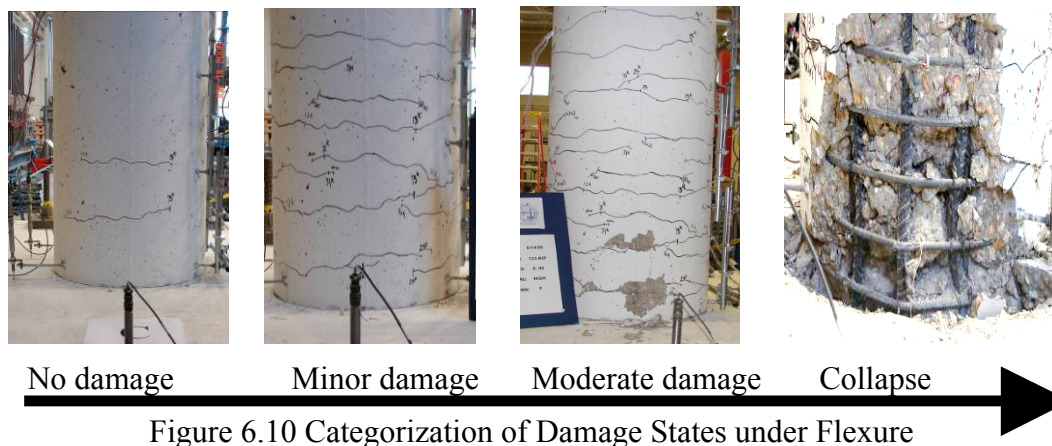
Figure 6.10 Categorization of Damage States under Flexure

Table 6.1 Categorization of Damage States under Flexure

Range of Flexural Damage Index (FDI)	Damage Level
FDI < 0.15	No damage; or localized minor cracking
0.15 < FDI < 0.20	Minor damage: light cracking throughout
0.20 < FDI < 0.40	Moderate damage: severe cracking, yielding of spiral, localized spalling
0.40 < FDI < 1.00	Severe damage: complete spalling of concrete cover, crushing of diagonal strut and core damage
FDI > 1.00	Collapsed: slight buckling of longitudinal bars, severe core damage in the middle of column

Results showing damage states under pure torsion are given in Table 6.2 and illustrated in Figure 6.11. Under pure torsion, when the damage index was less than 0.05, no damage or localized minor shear cracking was observed. This damage index is level far lower than that observed under flexure. Minor damage or light shear cracking throughout the column occurred when the damage index was less than 0.1 and higher than 0.05. A moderate damage level under pure torsion was characterized by severe shear cracking along the whole length of the column, with localized spalling. The spalling of concrete cover was measured by tapping the column with a hammer and listening for a

hollow sound. Spalling occurred at the damage index values between 0.1 and 0.4, indicating that propagation of damage between 0.1 and 0.4 was much faster due to the spread of shear cracking along the whole length of the column. Severe damage was marked by yielding of transverse spiral reinforcement and the complete spalling of concrete cover along the length of the column. The corresponding damage index values were between 0.4 and 0.8, demonstrating that propagation of damage between 0.4 and 0.8 was much faster than the failure sequence under flexure.

Table 6.2 Categorization of Damage States under Pure Torsion

Range of Torsional Damage Index (TDI)	Damage Level
TDI < 0.05	No damage, or localized minor shear cracking
0.05 < TDI < 0.10	Minor damage: light shear cracking throughout
0.10 < TDI < 0.40	Moderate damage: severe shear cracking, localized spalling
0.40 < TDI < 0.80	Severe damage: yielding of spiral, complete spalling of concrete cover along the length of the column
TDI > 0.80	Collapsed: buckling of longitudinal bars, rupture of transverse spiral reinforcement and longitudinal reinforcement

Minor damage   Moderate damage   Severe damage   Collapse
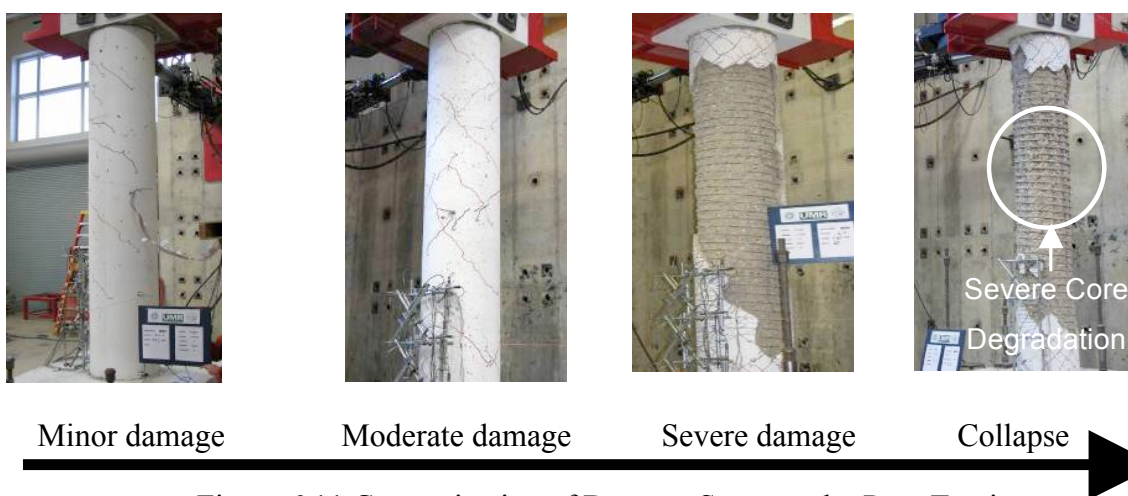
Figure 6.11 Categorization of Damage States under Pure Torsion

The damage states observed under combined bending, shear, and torsion are summarized in Table 6.3 and illustrated in Figure 6.12. No damage or localized minor shear or flexure-shear cracking occurred when the damage index was less than 0.05. Minor damage refers to light flexure-shear cracking throughout the column with a damage index of less than 0.1 or higher than 0.05. Moderate damage occurred with severe flexure-shear cracking, yielding of longitudinal reinforcement, and localized spalling, with damage index values between 0.1 and 0.4. Severe damage showed yielding of transverse spiral reinforcement and complete spalling of concrete cover along more than half the length of column. This damage state showed index values between 0.4 and 0.8.

Table 6.3 Categorization of Damage States under Combined Shear Force and Flexural and Torsional Moment

Range of Flexural Damage Index (FDI)	Range of Torsional Damage Index (TDI)	Damage Level
FDI < 0.10	TDI < 0.05	No damage, or localized minor shear or flexure-shear cracking
0.10 < FDI < 0.20	0.05 < TDI < 0.10	Minor damage: light flexure-shear cracking throughout
0.20 < FDI < 0.40	0.10 < TDI < 0.20	Moderate damage: severe flexure-shear cracking, yielding of longitudinal reinforcement, localized spalling
0.40 < FDI < 0.90	0.40 < TDI < 0.80	Severe damage: yielding of transverse spiral reinforcement, complete spalling of concrete cover along more than half the length of column
FDI > 0.90	TDI > 0.80	Collapsed

| Minor damage | Moderate damage | Severe damage | Collapse |
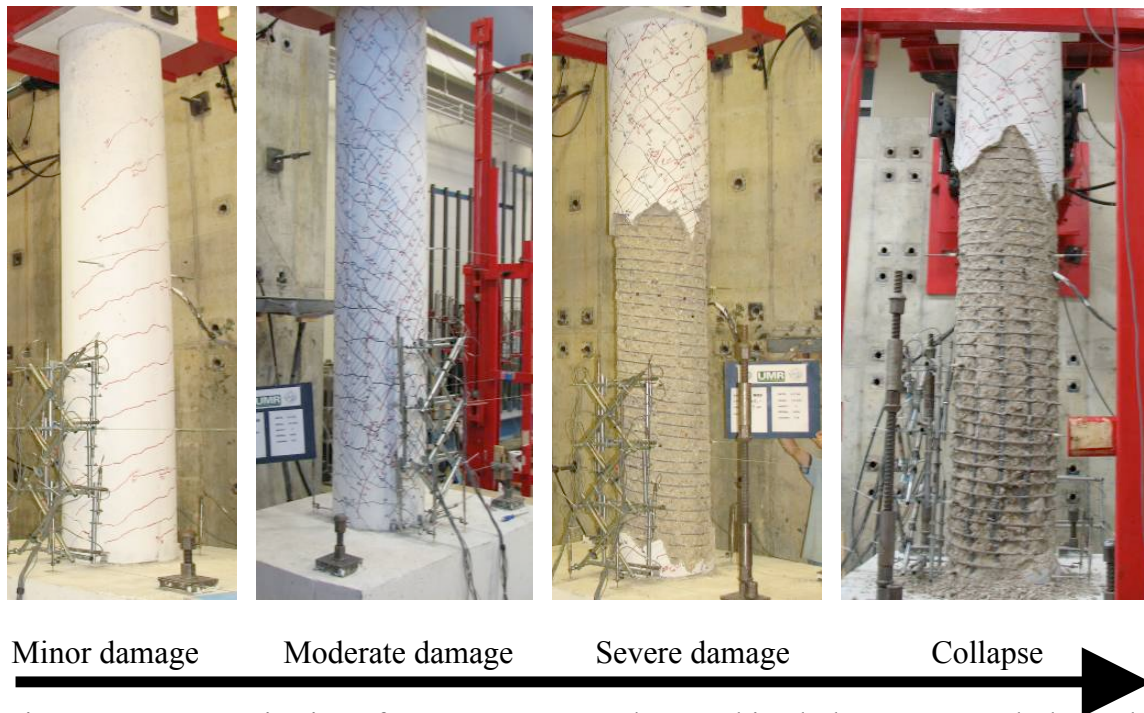
Figure 6.12 Categorization of Damage States under Combined Shear Force and Flexural and Torsional Moment

6.8. CONCLUDING REMARKS

This section has emphasized the importance of a performance-based design of RC bridge columns. Using the concept of damage levels; this study compared such an approach to existing prescriptive design methods. It modified the existing damage index models to study the progression of damage under flexure. It also developed damage index models for pure torsion using the existing approach for flexure. Decoupled damage index models for flexure and pure torsion permitted the study of damage progression under combined loading. Experimental results were used to validate the proposed damage index models.

The work presented here addressed the effects of various changes in design parameters on strength, stiffness, and damage characteristics of RC columns. These changes include increases in the transverse reinforcement and the T/M ratio and a

reduction in shear span. Interaction between flexural and torsional damage index models was studied by interaction diagrams. Using these diagrams, the damages states were defined by specifying the range of damage indices for columns tested under flexure, pure torsion, and combined bending, shear, and torsion. This definition of damage states can be used to quantify the damage to columns subjected to combined loadings. Damage-based design approach for combined loading presented in this study support the following major conclusions:

• The damage index model proposed by Park and Ang was derived essentially from flexure-dominated specimens. It was modified and extended to account for torsional loadings. Damage index models using the Park and Ang approach clearly predicted the progression of damage for both flexure and torsional hysteresis under combined loadings. They were physically intuitive, providing a simple means to quantify the damage from '0', indicating no damage, to '1', indicating near collapse.

• The damage index model proposed by Hwang and Scribner approach was modified by normalizing the model with energy dissipation from bending shear (flexural hysteresis) and pure torsion (torsional hysteresis) results, respectively. Although these models accurately predicted the progression of damage, the damage index values at the ultimate state for flexure and torsion were significantly different.

• Damage indices using the Park and Ang approach under combined bending and torsion correlated well with the experimental data. However, the validation was based on limited test results with a narrow range of parameters. The columns used in the present study were properly detailed according to the code requirements, satisfying confinement requirements from flexural design point of view. However, under combined loadings, the

behavior of columns with low seismic detailing will be significantly different. Thus, the proposed limits on categorization of damage indices apply only to columns that are well detailed or under-reinforced in flexure and torsion.

• Increasing the transverse spiral reinforcement ratio helped increasing the torsional strength and rotational ductility by increasing deformational capacity after yielding. An increase in the spiral ratio resulted in more confinement resulting in a reduction of the damage index for flexure and torsional hysteresis under combined bending moments and torsion.

• A reduction in shear span resulted in decreased energy dissipation and amplified the damage index for both flexural and torsional hysteresis.

• Under combined shear force, flexural and torsional moments, energy dissipation capacity and the equivalent-damping ratio increased with an increase in the transverse spiral reinforcement ratio. However, they decreased with an increase in the T/M ratio and a reduction in the shear span ratio.

7. SUMMARY AND CONCLUSIONS

7.1. SUMMARY

The objective of this investigation was to gain a better understanding of the seismic behavior of circular RC bridge columns under combined loading. The purpose of the experimental investigation was to determine the effects of cyclic torsional moment combined with bending moment, and shear force on behavior of circular RC bridge columns. The analytical investigation focused on the improvement of existing models for flexure, pure torsion and establishment of interaction diagrams from a semi-empirical approach. It also investigated damage index models from a damage-based design point of view.

7.2. CONCLUSIONS

7.2.1. Experimental Investigation. The experimental investigation tested 14 circular RC columns under various T/M ratios and bending moment-to-shear ratios. Sections 4 and 5 described the experimental and analytical investigations and their results. The major conclusions of this work are summarized in the following sections.

7.2.1.1 General conclusions.

- Degradation in the strength of columns under flexure with aspect ratios of six and three occurs by formation of a flexural plastic-hinge at the base of the column, followed by core degradation, and finally by the buckling of longitudinal bars on the compression side.

- Columns subject to pure torsion failed by severe diagonal cracking, leading to the formation of a torsional plastic-hinge near the mid-height of the column.

• The failure of columns under combined loading is due to severe core degradation followed by the buckling of the longitudinal bars. However, the location of the plastic zone shift up from the base of the column according to the increase in T/M ratio.

7.2.1.2 Effect of torsion-to-bending moment ratio.

• The location and length of the plastic-hinge change with specific combinations of bending and torsion, i.e., with changes in the T/M ratio.

• A combination of bending and torsional moments reduces the torsional moment required to cause yielding of the transverse reinforcement and the peak torsional strength.

• Similarly, a combination of bending and torsional moment reduces the bending moment required to cause yielding of the longitudinal reinforcement and the peak flexural strength.

• Under combined torsion and bending, torsional stiffness degrades more rapidly than flexural stiffness with the increments of displacement or twist in columns reinforced with both 0.73% and 1.32% transverse reinforcement.

• Ultimate displacement decreases with a reduction in the flexural energy dissipation capacity accompanied by an increase in the T/M ratio. Similarly, ultimate twist decreases with a reduction in the torsional energy dissipation capacity accompanied by a reduction in the T/M ratio.

7.2.1.3 Effect of spiral reinforcement ratio.

• Degradation in the strength of a column under pure torsion is contained by increasing the spiral reinforcement ratio. Such an increase improves torsional strength

and twist ductility with increase in deformational capacity after spiral reinforcement yielding.

• An increase in the spiral reinforcement ratio provides more confinement to the concrete core and better redistribution of the shear stresses thereby reducing the degradation of bending and torsional strength under combined loading.

• An increase in the spiral reinforcement ratio delays the damage progression corresponding to spiral yielding and peak torsional moment of a column under combined loading when compared to the one with a lower spiral reinforcement ratio.

7.2.1.4 Effect of aspect ratio.

• The shear capacity of columns under flexure increases with a reduction in aspect ratio. This increase is proportional to the reduction in aspect ratio for the columns considered in this study, which failed predominantly in flexure. However, such an increase must be validated for columns that fail predominantly in shear.

• Displacement and twist at ultimate shear and ultimate torsional moment of columns under combined loading decrease significantly with a reduction in shear span or aspect ratio.

• Localized core degradation of concrete occurs at mid-height of columns with a high aspect ratio of six under pure torsion. This effect is due to stress concentration in this region. However, the stress distribution is uniform in columns with a low aspect ratio of three, resulting in no localized failure.

• No appreciable reduction in bending and torsional strength occurs with a reduction in aspect ratio. This effect is attributable to the predominance of the flexural

failure, which was due to low longitudinal reinforcement ratio considered in this study. However, energy dissipation under bending and torsional moments decreases considerably with a reduction in the shear span ratio.

7.2.2. Analytical Investigation.

7.2.2.1 General conclusions.

- Existing plastic-hinge-based model was adapted to predict the behavior of circular RC columns under flexure. The predictions agreed closely with the experimental results. The model used in this study could be extended to predict the behavior of columns under combined loading by adjusting the constitutive models for concrete considering the confinement and softening effect.

- Existing softened truss model is modified to circular sections by removing the variables related to out-of-plane warping and including the tension-stiffening effect. The predictions for columns under pure torsion agreed closely with experimental data.

- The predictions of the interaction diagrams using the semi-empirical formulations as adopted by Elfgren (1972) agreed substantially with the experimental results.

7.2.2.2 Damage-based design approach and damage index models.

- The damage index model proposed by Park and Ang was derived essentially from flexure-dominated specimens. It is modified and extended to account for torsional loading in this study. Damage index models using the Park and Ang approach clearly predicts the progression of damage for both the flexural and torsional hysteresis under combined loading. They are physically intuitive, providing a simple

means to quantify the damage from '0', indicating no damage, to '1', indicating near collapse.

· The damage index model proposed by Hwang and Scribner was modified by normalizing it with energy dissipation from flexure (flexural hysteresis) and pure torsion (torsional hysteresis) results, respectively. Although these models accurately predict the progression of damage, the damage index values at the ultimate state for flexure and torsion are significantly different.

· Damage indices using the Park and Ang approach under combined loading correlate well with the experimental data. However, the validation was based on the limited tests with a narrow range of parameters. The columns used in the present study are properly detailed according to the code requirements, satisfying confinement requirements from a flexural design point of view. However, under combined loading, the behavior of columns with low seismic detailing will be significantly different. Thus, the proposed limits on categorization of damage indices apply only to the columns that are well detailed or under-reinforced in flexure and torsion.

· Increasing the transverse spiral reinforcement ratio increased the torsional strength and twist ductility with the increase of deformational capacity after yielding. An increase in the spiral ratio provides more confinement thereby reducing the damage index for flexure and torsional hysteresis under combined loading.

· A reduction in shear span decreases energy dissipation and amplifies the damage index for both flexural and torsional hysteresis.

· Under combined loading, energy dissipation capacity and the equivalent damping ratio increase with an increase in the transverse spiral reinforcement ratio.

However, they decrease with an increase in the T/M ratio, and a reduction in the shear span ratio. They also indicate the effect of shear in changing the failure modes from ductile to brittle.

7.3. RECOMMENDATIONS FOR FURTHER STUDY

Following are recommendations for future research based on the discussion in previous sections:

• In actual conditions, the bridge columns are subjected to three-dimensional ground motions during an earthquake. Therefore, an experimental study on combined cyclic bilateral bending and torsion would be valuable. The control of actual loading protocol however, could be challenging.

• The effect of torsion on flexural curvature distribution is not yet clearly understood. The significance of torsional loading in plastic-hinge models requires further exploration.

• The loading protocol used in this study was intended to maintain a constant torsion-to-bending moment ratio during the testing. However, it is impossible to control the T/M ratio as a constant value once the flexural or torsional strength is reached. Therefore, control algorithms could be developed based on the outputs of different sensors for a better control on the T/M ratio for future test results.

• An algorithm to control twist-to-displacement as a test parameter is an option for further research. The results of such work would be very useful in establishing a rational relationship between flexural displacement and torsional twist ductility from a displacement-based design point of view.

- Additional full-reversal cyclic tests on RC members are needed to investigate the effects of various T/M ratios, combinations of longitudinal and transverse reinforcement ratios and levels of concrete strength and thus to provide further validation of the experimental and analytical results presented here.

- Axial compression could enhance torsional and bending strength and energy dissipation under combined loading. In the present study, all the columns had a constant axial compression of about 7% of concrete capacity. Future work could study the effects of variation in axial compression on the behavior of columns under combined loading.

- Future work could test columns under combined loading subject to double curvature with a lower aspect ratio or a higher bending moment-to-shear ratio. The results would clarify the shear-dominated behavior under combined loading including torsion.

- The proposed C-TS-STM model could be significantly improved to include the Poisson effect for better prediction of post-peak behavior.

- Parameters affecting the spalling of concrete cover under pure torsion and combined loading including torsion requires further investigation. A parametric study could be conducted to investigate the tensile stresses at the plane of potential spalling formed by stirrups, and to study the effects of various reinforcement ratios and concrete strengths on spalling length.

- The size effect is significant in shear related problems of reinforced concrete. Torsion is a 3-Dimensional shear problem and the size effect could be

significant. At present, there have been no studies conducted on the size effect in problems related with combined loading.

- The shape of the cross section also plays a major role in shaping hear flow characteristics and thereby changing the failure modes of columns under combined loadings. Testing of columns with different cross sectional shapes (e.g., square, rectangular, and interlocking spiral) would address this gap.

- Damage-based design methods adopted in this study could be further developed for the design of RC members under combined loading. Such a project would require experimental work considering a wider range of parameters such as sectional details and loading ratios.

APPENDIX

ADDITIONAL FABRICATION, TEST SETUP AND INSTRUMENTATION

DRAWINGS
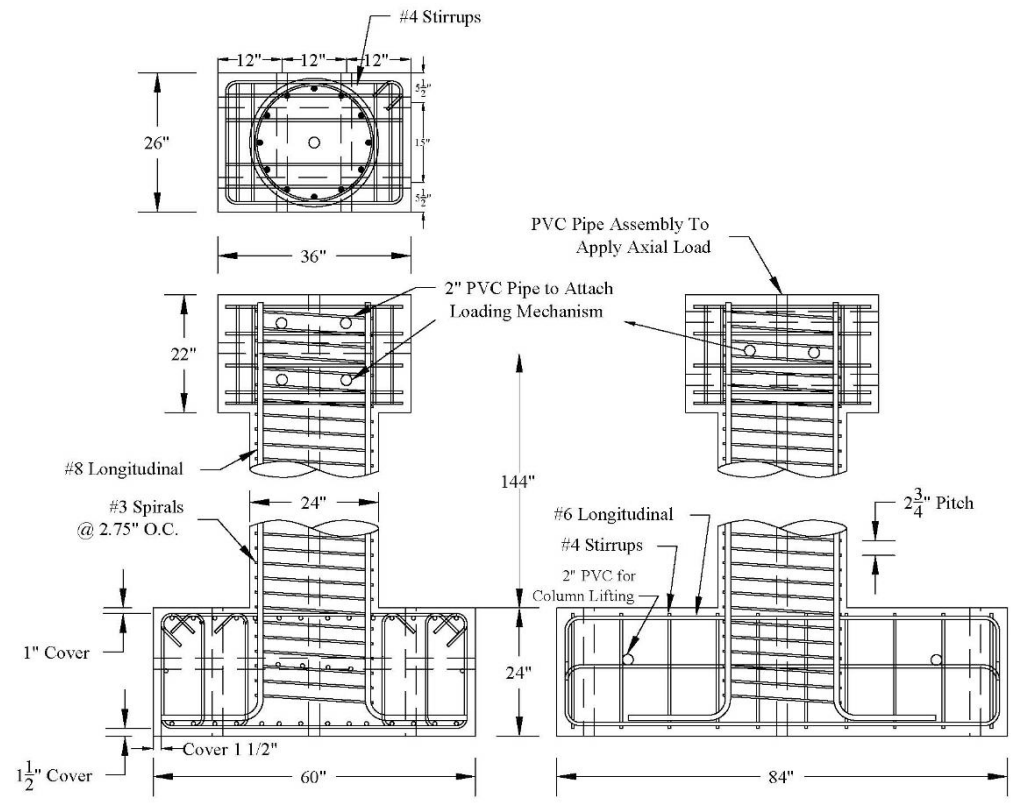
Figure A.1 Specimen Detailing

(All dimensions in inches, 1 inch= 25.4 mm)
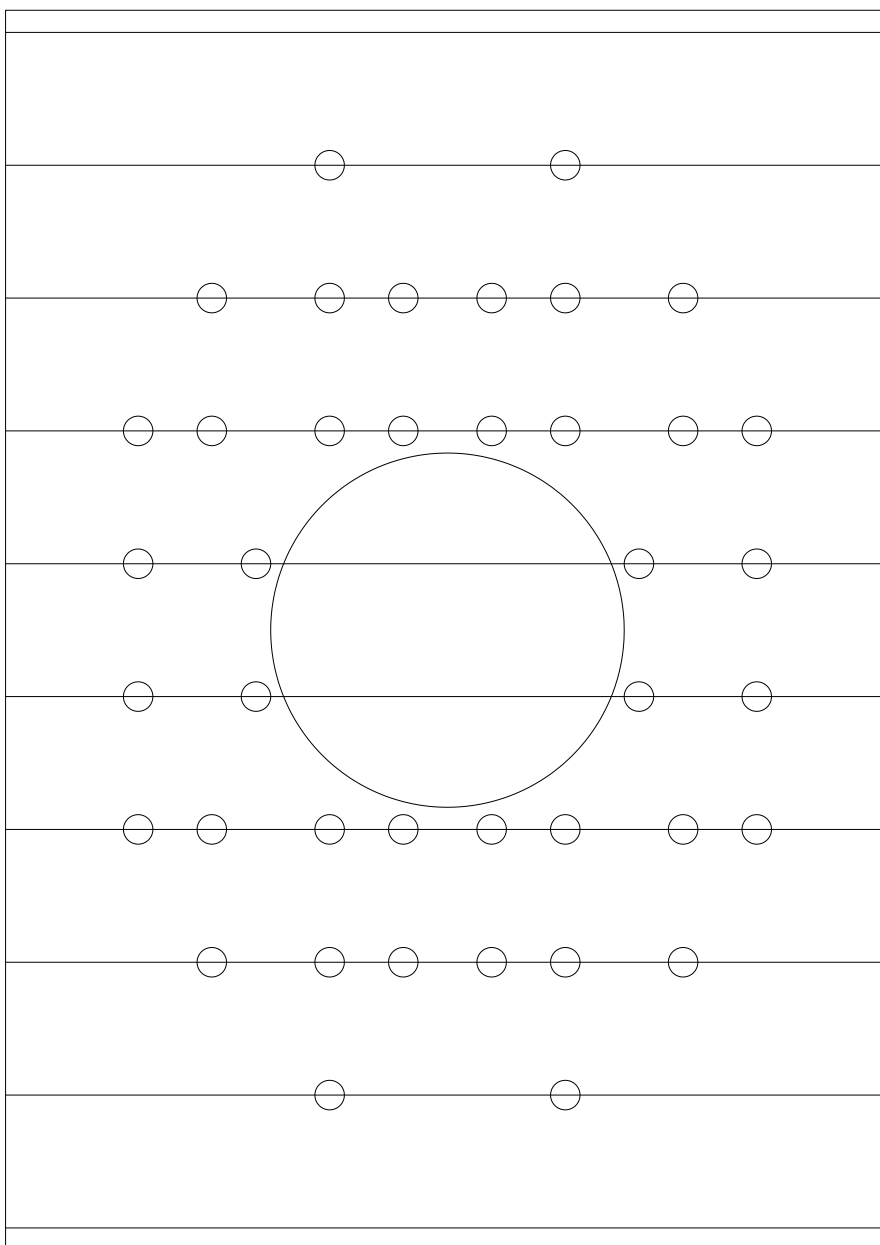
Figure A.2 Location of Shear Legs on the Footing (Plan View)
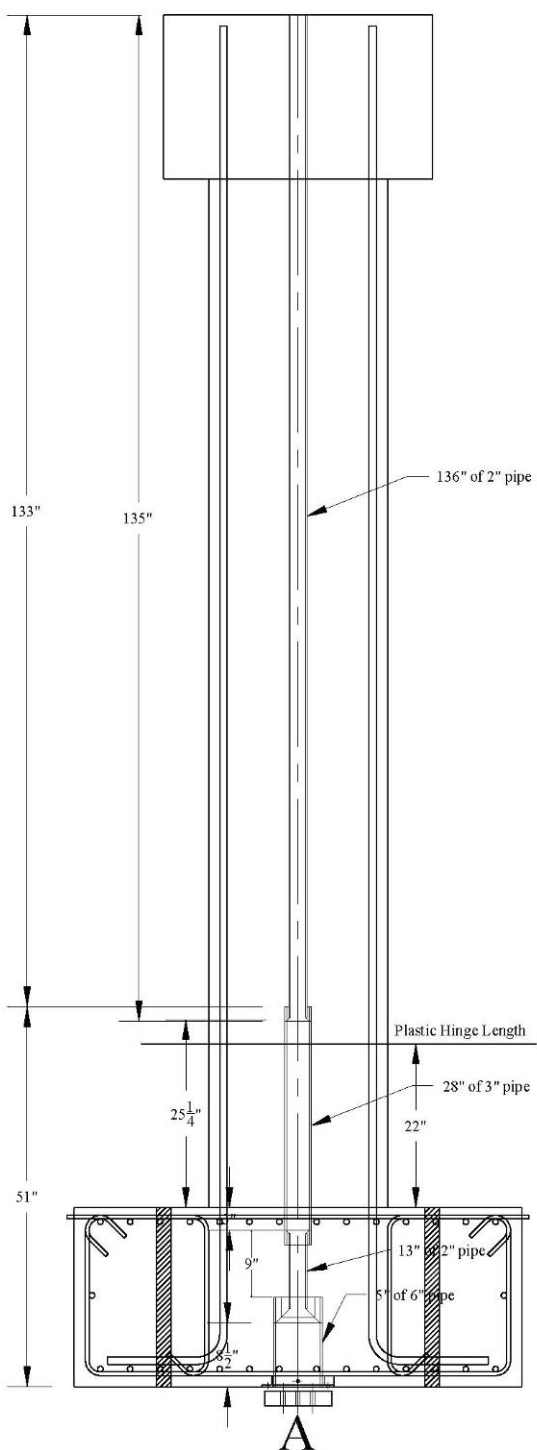
Figure A.3 Elevation of the Column with PVC tubing inside
(All dimensions in inches, 1 inch= 25.4 mm)
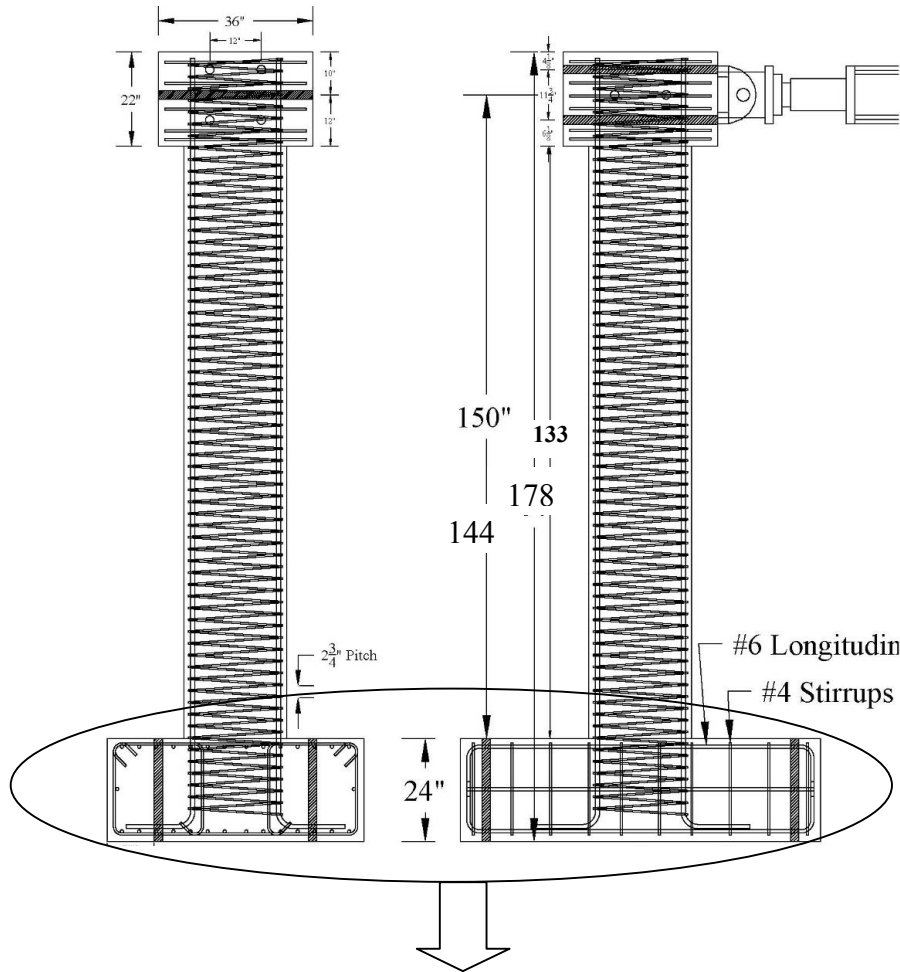
Figure A.4 Column Sectional Detail and Photo of Foundation Reinforcement

(All dimensions in inches, 1 inch= 25.4 mm)
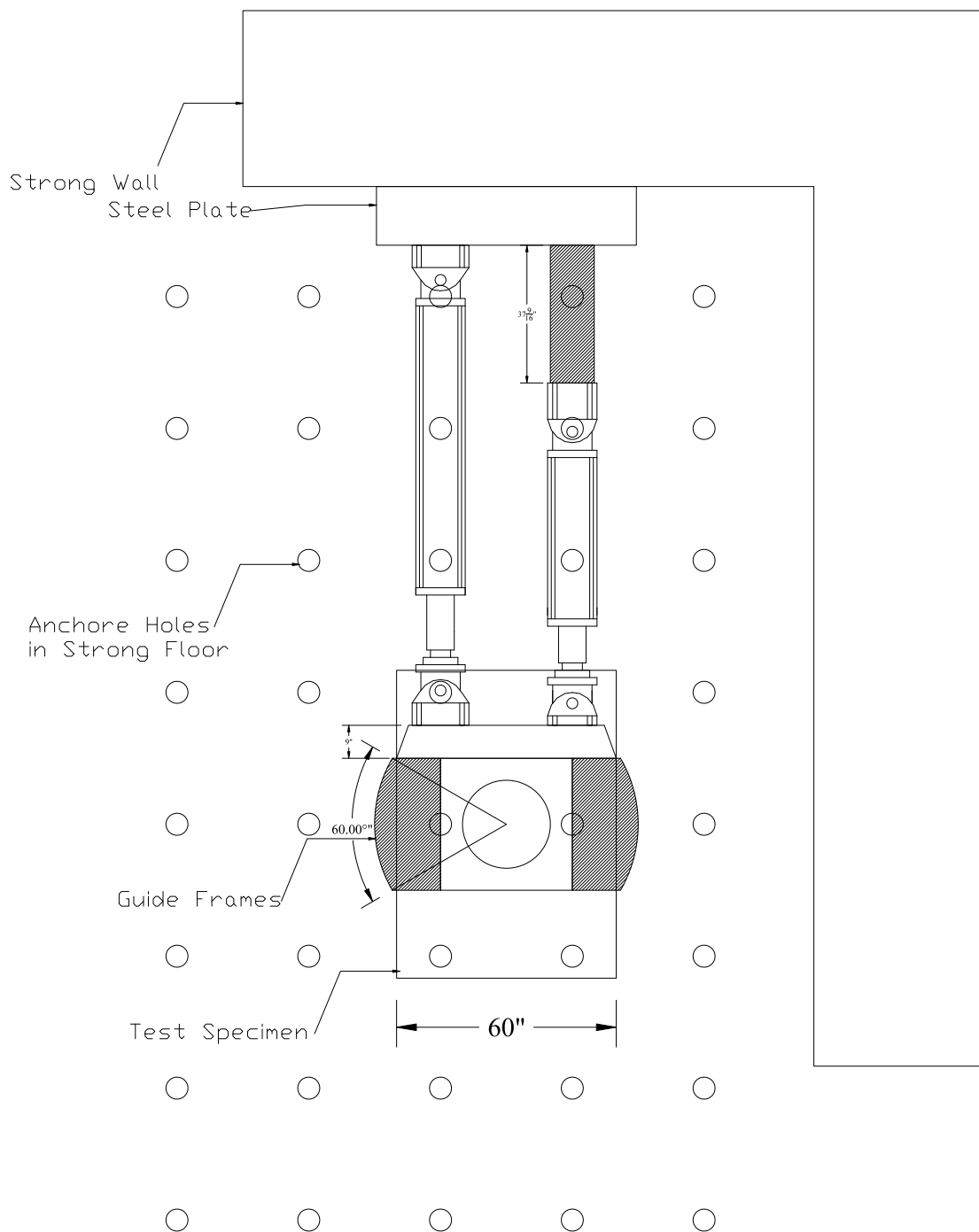
Figure A.5 Plan View of Actuators, Specimen and Floor Holes with Respect to Strong Wall
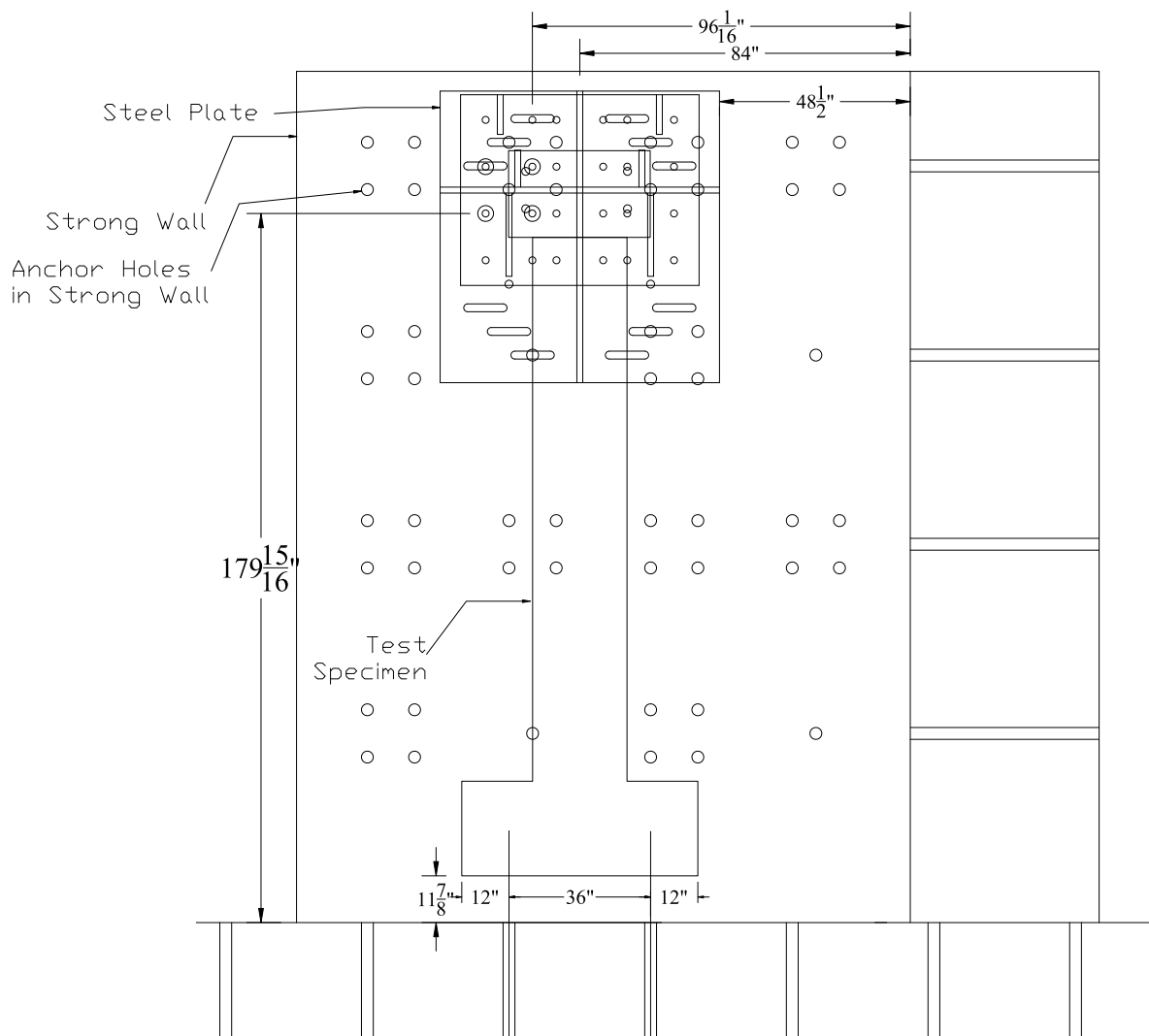
Figure A.6 Arrangement of Steel Plate on Strong Wall

(All dimensions in inches, 1 inch= 25.4 mm)

Gage Position No.	Gage Profile on Long. Bars			
9	A	B	C	D
8	A		C	
7	A	B	C	D
6	A		C	
5	A	B	C	D
4	A		C	
3	A	B	C	D
2				
1				

22 Longitudinal Gages

Gage Position No.	Gage Profile on Long. Bars			
9	A	B	C	D
8	A		C	
7	A	B	C	D
6	A		C	
5	A	B	C	D
4	A		C	
3	A	B	C	D

22 Transverse Gages

210
210
210
210
210
210
210
210
210
190

9
8
7
6
5
4
3
2
1

C
D
B
A
Loading Direction

FACES ON COLUMN

Figure A.7 Strain Gage Locations for Flexure Specimen with Aspect Ratio of 3
(All dimensions in millimeter)

Gage Position No.	Gage Profile on Long. Bars			
9	A	B	C	D
8	A	B	C	D
7	A	B	C	D
6	A	B	C	D
5	A	B	C	D
4	A	B	C	D
3	A	B	C	D
2				
1				

28 Longitudinal Gages
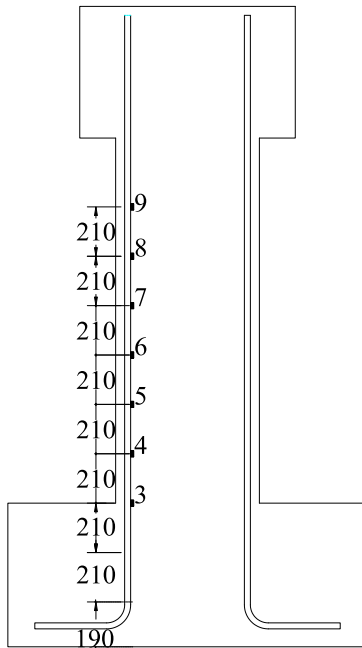
Gage Position No.	Gage Profile on Trans. Bars			
9	A	B	C	D
8	A	B	C	D
7	A	B	C	D
6	A	B	C	D
5	A	B	C	D
4	A	B	C	D
3	A	B	C	D

28 Transverse Gages

210
210
210
210
210
210
210
210
210
190

9
8
7
6
5
4
3

C

D   Loading Direction   B

A
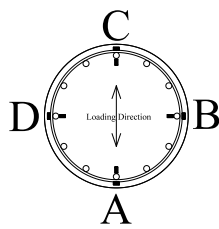
FACES ON COLUMN

Figure A.8 Strain Gage Locations for Pure Torsion with Aspect Ratio of 3
(All dimensions in millimeter)

Gauge No.	Gauge Profile							
9	A	AB	B	BC	C	CD	D	AD
8	A		B		C		D	
7	A	AB	B	BC	C	CD	D	AD
6	A		B		C		D	
5	A	AB	B	BC	C	CD	D	AD
4	A		B		C		D	
3	A	AB	B	BC	C	CD	D	AD

44 Longitudinal Gauges

Gauge No.	Gauge Profile			
9		B		D
8	A	B	C	D
7	A	B	C	D
6	A	B	C	D
5	A	B	C	D
4	A	B	C	D
3	A	B	C	D

26 Transverse Gauges
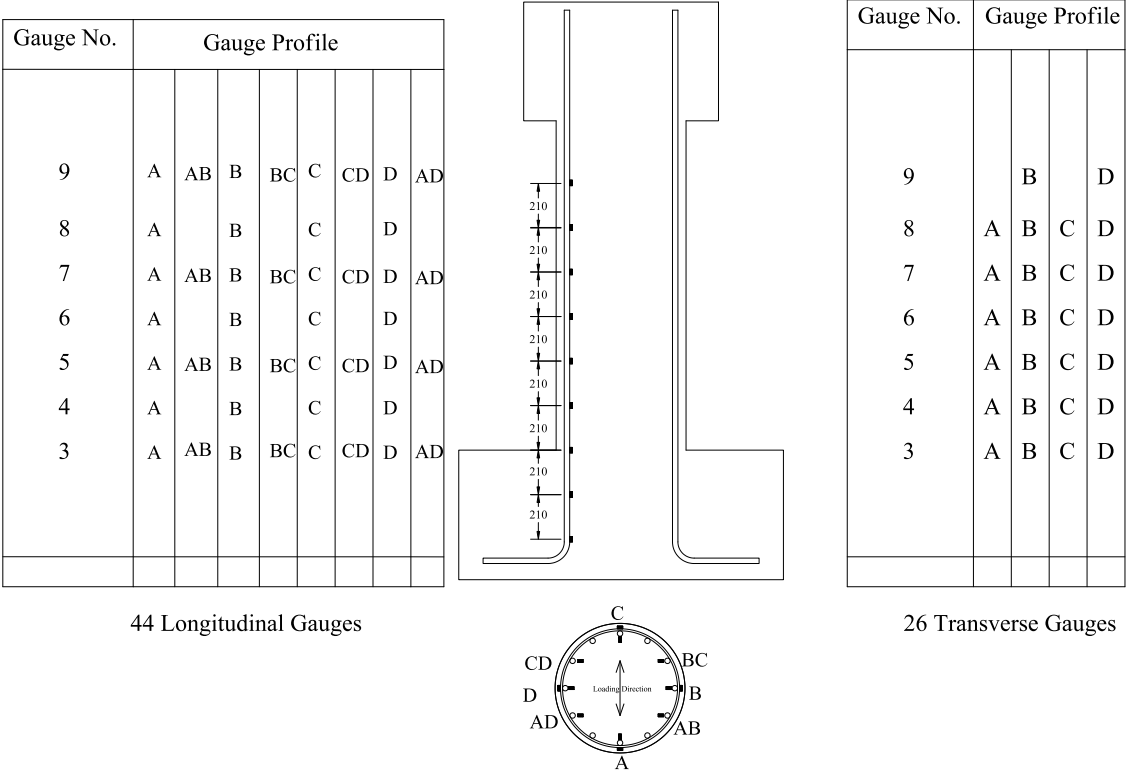
Figure A.9 Strain Gage Locations for Combined Bending and Torsion Specimens with Aspect Ratio of 3
(All dimensions in millimeter)

Gage No.	Gage Profile			
11				
10	A		C	
9				
8	A		C	
7	A		C	
6	A		C	
5	A		C	
4	A	B	C	D
3	A	B	C	D
2	A	B	C	D
1	A		C	

24 Longitudinal Gauges

Gage No.	Gaue Profile			
11				
10		B		D
9		B		D
8	A	B	C	D
7	A	B	C	D
6	A	B	C	D
5	A	B	C	D
4	A	B	C	D
3	A	B	C	D
2				
1				

28 Transverse Gauges
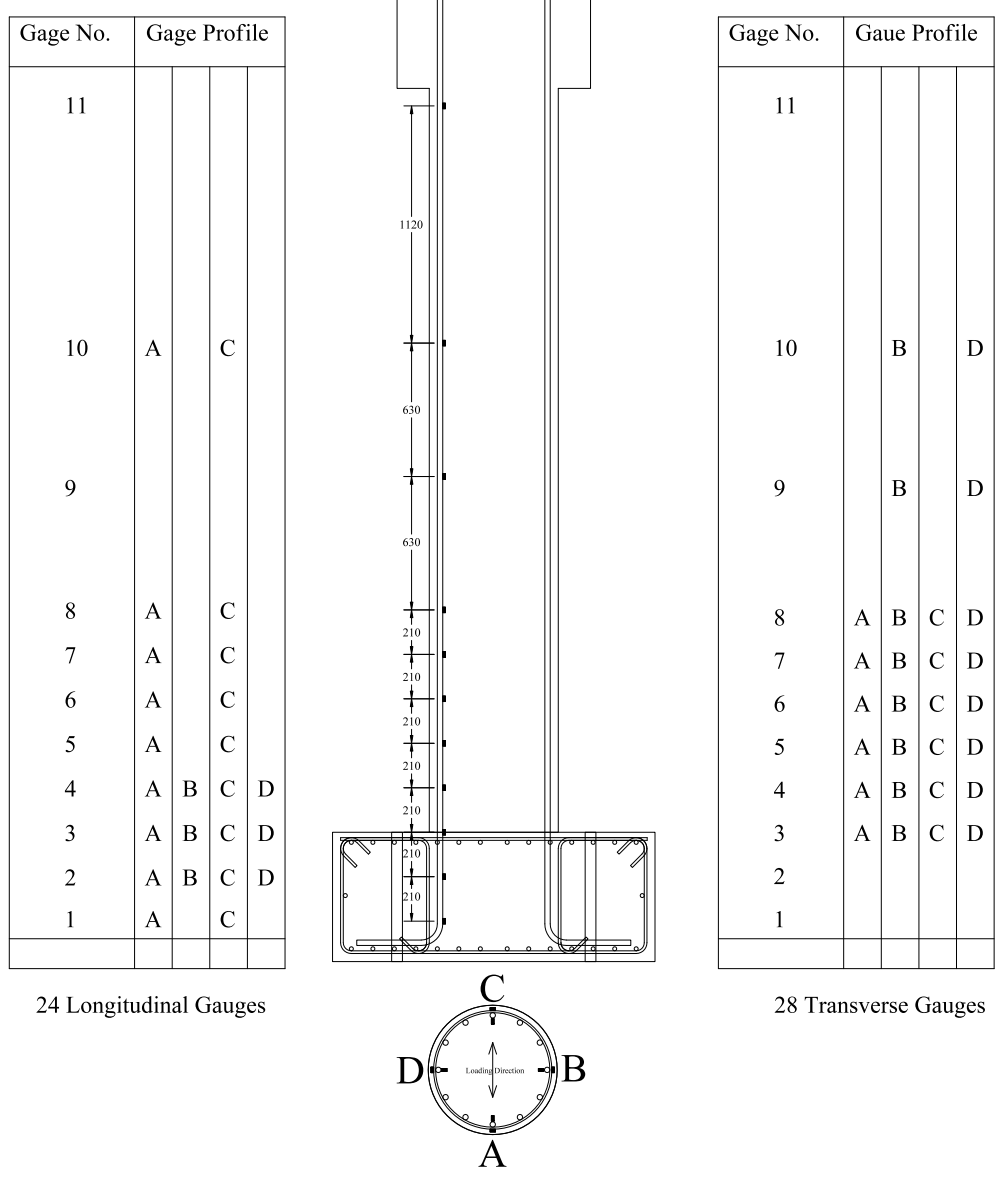
Figure A.10 Strain Gage Locations for Flexure with Aspect Ratio of 6
(All dimensions in millimeter)
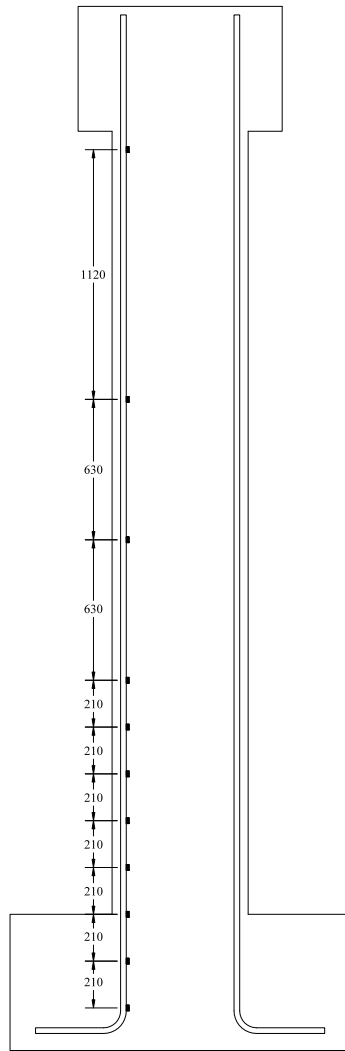
Gauge No.	Gauge Profile		
11			
10			
9			
8	A		C
7			
6	A		C
5	A		C
4			
3	A		C
2			
1			

8 Longitudinal Gauges

1120

630

630

210

210

210

210

210

210

Gauge No.	Gauge Profile		
11			
10			
9			
8	A		C
7			
6	A		C
5	A		C
4			
3	A		C
2			
1			

8 Transverse Gauges

C

D Loading Direction B

A
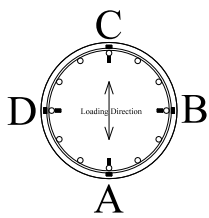
Figure A.11 Strain Gage Locations for Pure Torsion with Aspect Ratio of 6
(All dimensions in millimeter)
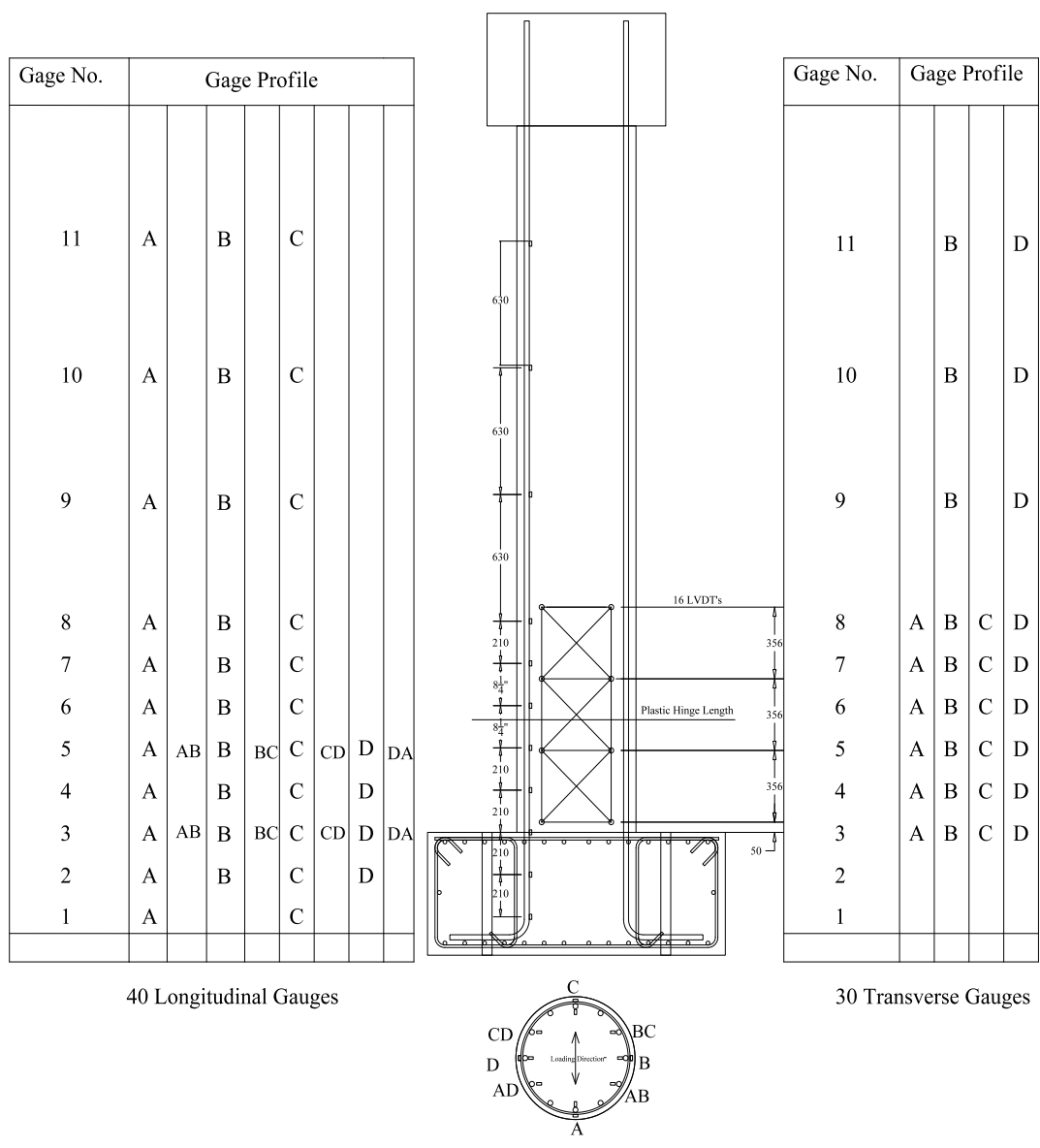
Figure A.12 Strain Gage Locations for Columns with Aspect Ratio of 6 under Combined Bending and Torsion (All dimensions in millimeter)
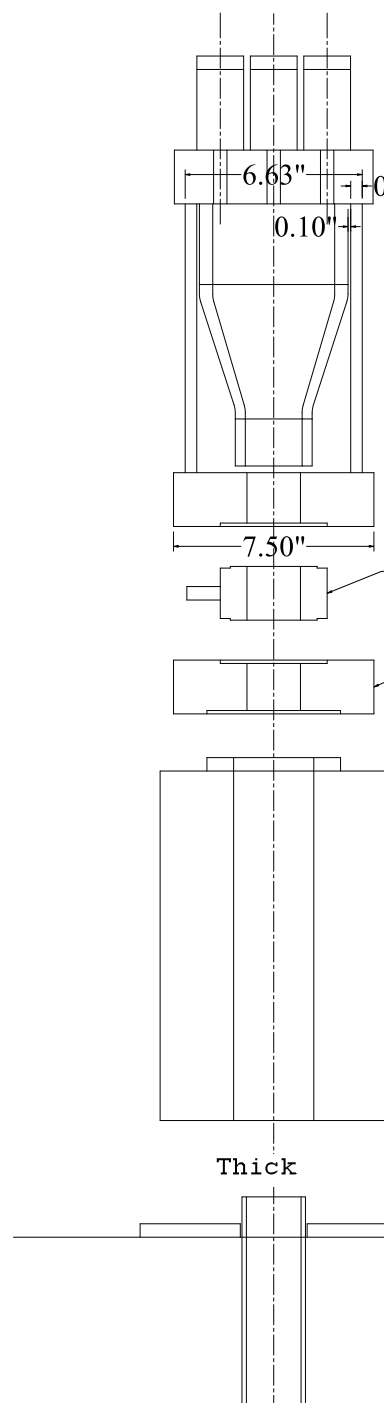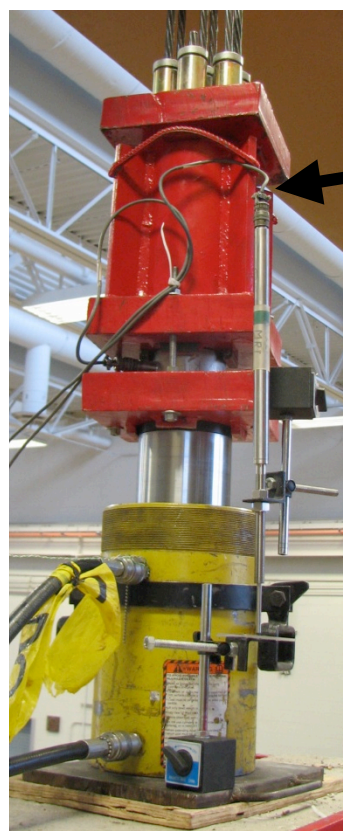
Figure A.13 Arrangment of Loading System at the Top of Loading Stub
(All dimensions in inches, 1 inch= 25.4 mm)
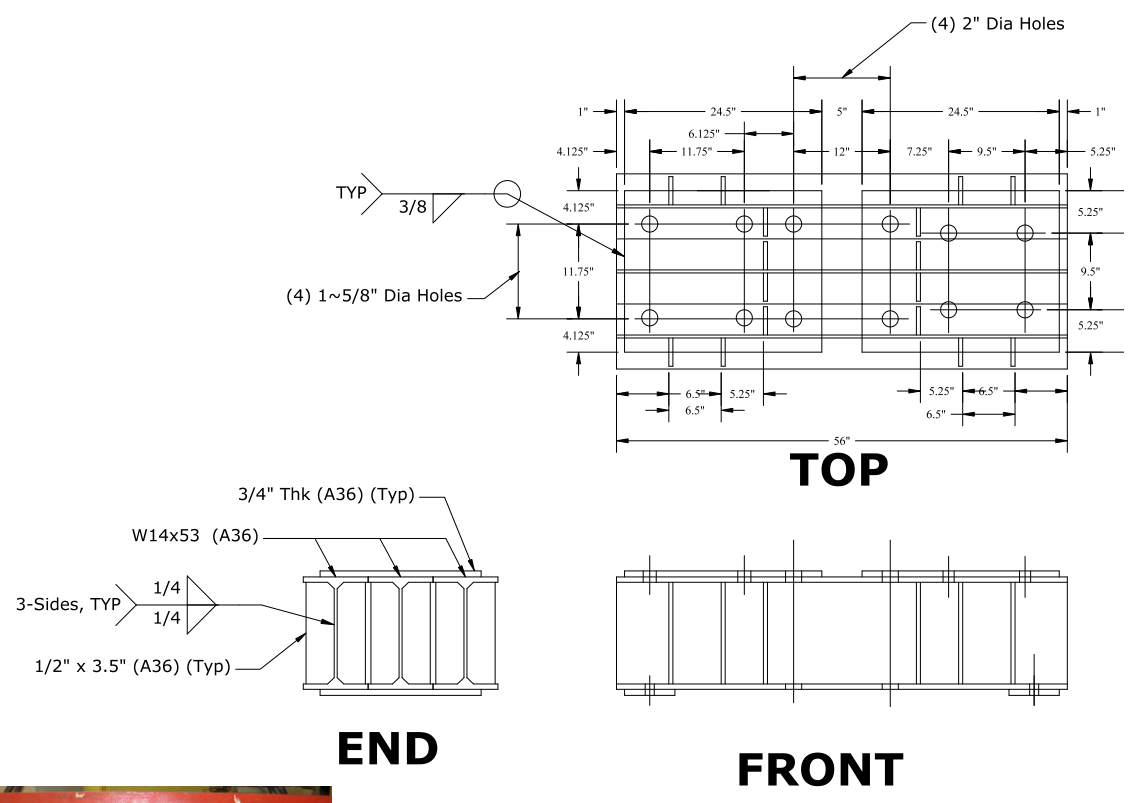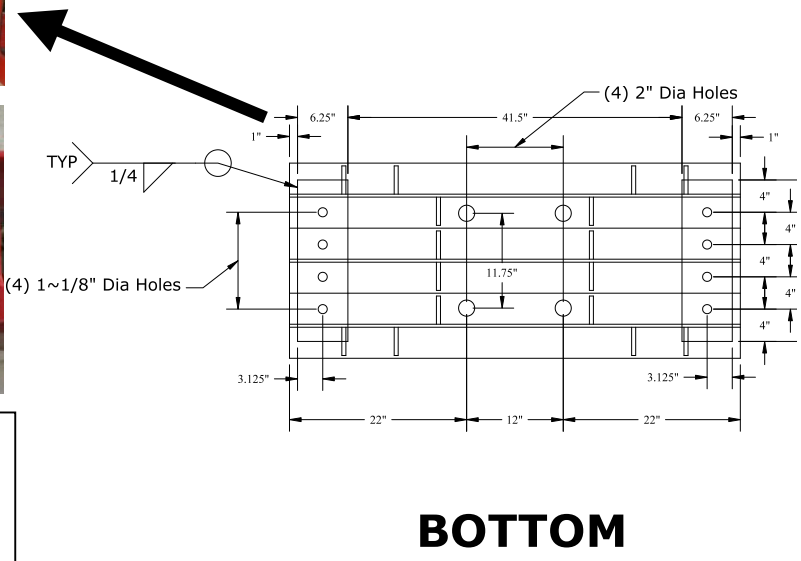
Figure A.14 Loading Beam Details
(All dimensions in inches, 1 inch= 25.4 mm)

3/4" THK (A36) (TYP)

20.25"

3/8
3/8

R39"

Photo of Guiding Frame

TOP

(2) 2" Dia Holes

5.5" 15" 5.5"

2.25"

4"

4" 10"

4" 15.5" 20"

4" 10"

4" 2.25"

1.5" 23" 1.5"

26"

FRONT

9"

16.25" 3/8
3/8

R1.5"

3.75"

(4) 1~1/4" Dia Holes

12.875" 5.125"

18"

SIDE

Photo of the Guiding Frames

Figure A.15 Guiding Frame Details
(All dimensions in inches, 1 inch= 25.4 mm)
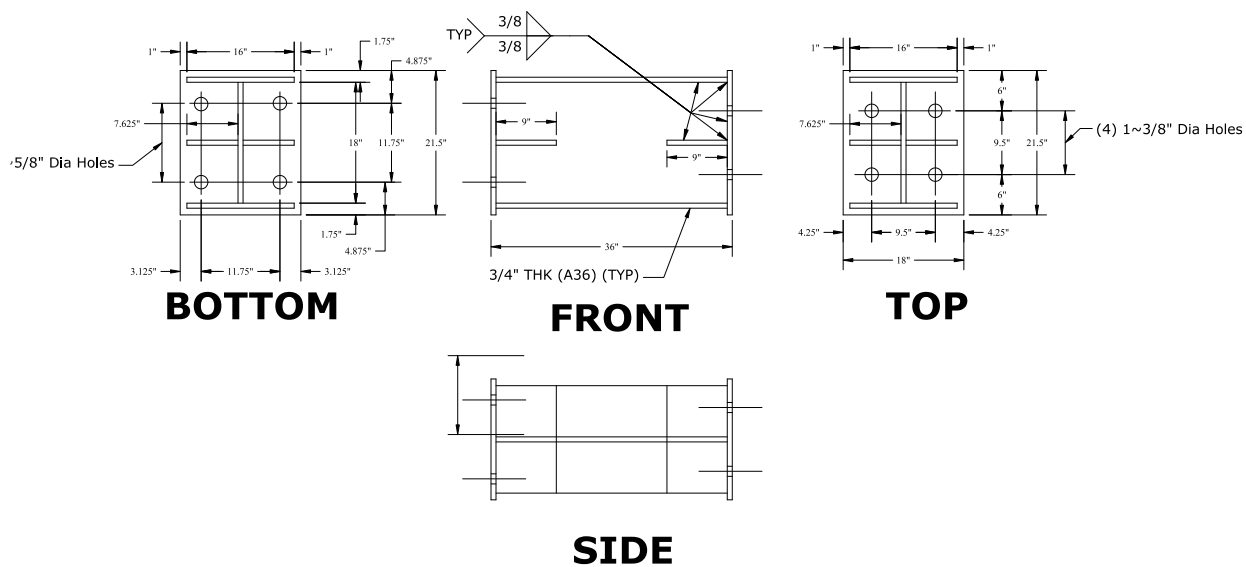
Figure A.16 Column Spacer for Small Actuator

(All dimensions in inches, 1 inch= 25.4 mm)
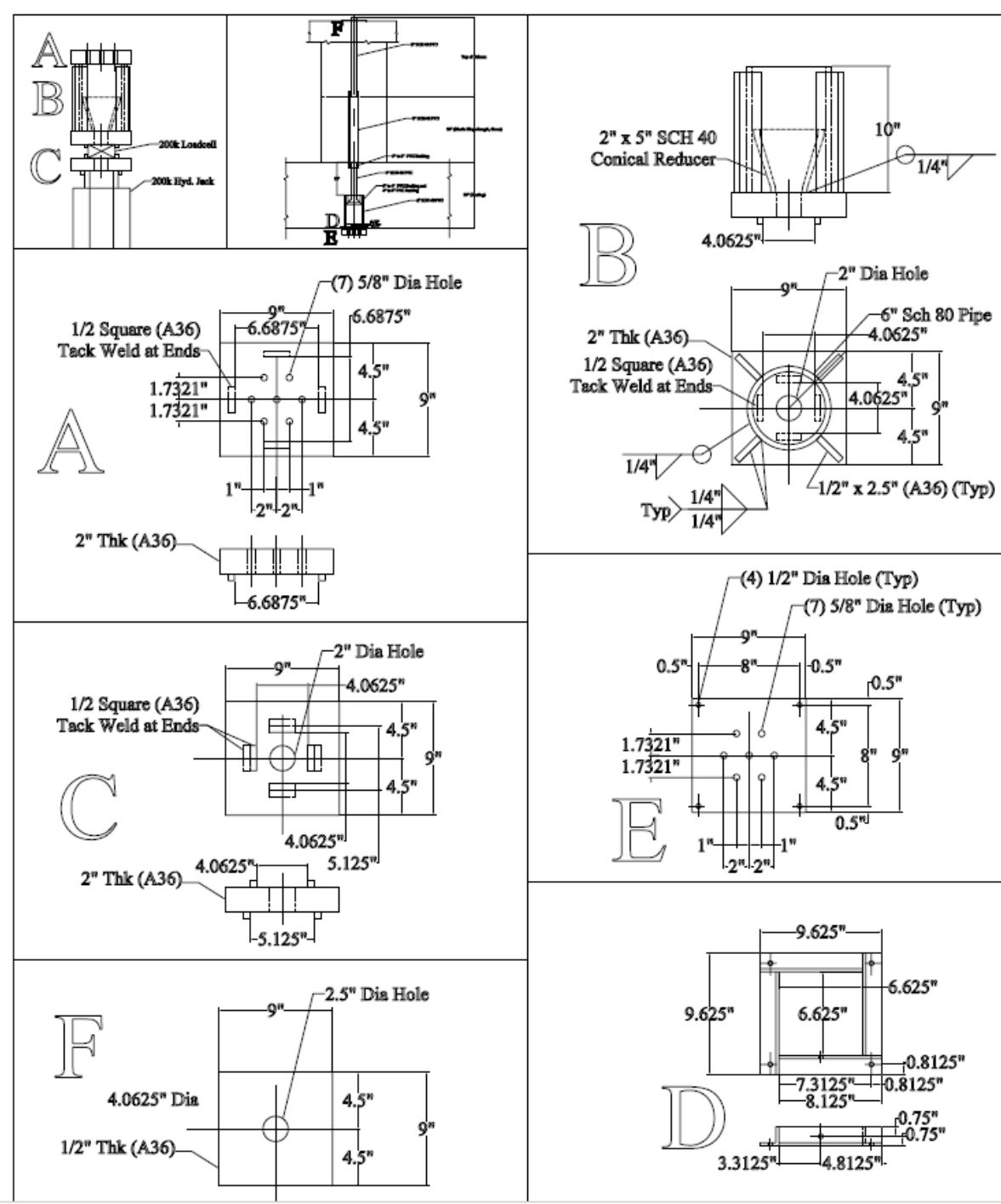
Figure A.17 Steel Elements for Axial Load Setup
(All dimensions in inches, 1 inch= 25.4 mm)

Figure A.18   End Block Detailing
(All dimensions in inches, 1 inch= 25.4 mm)
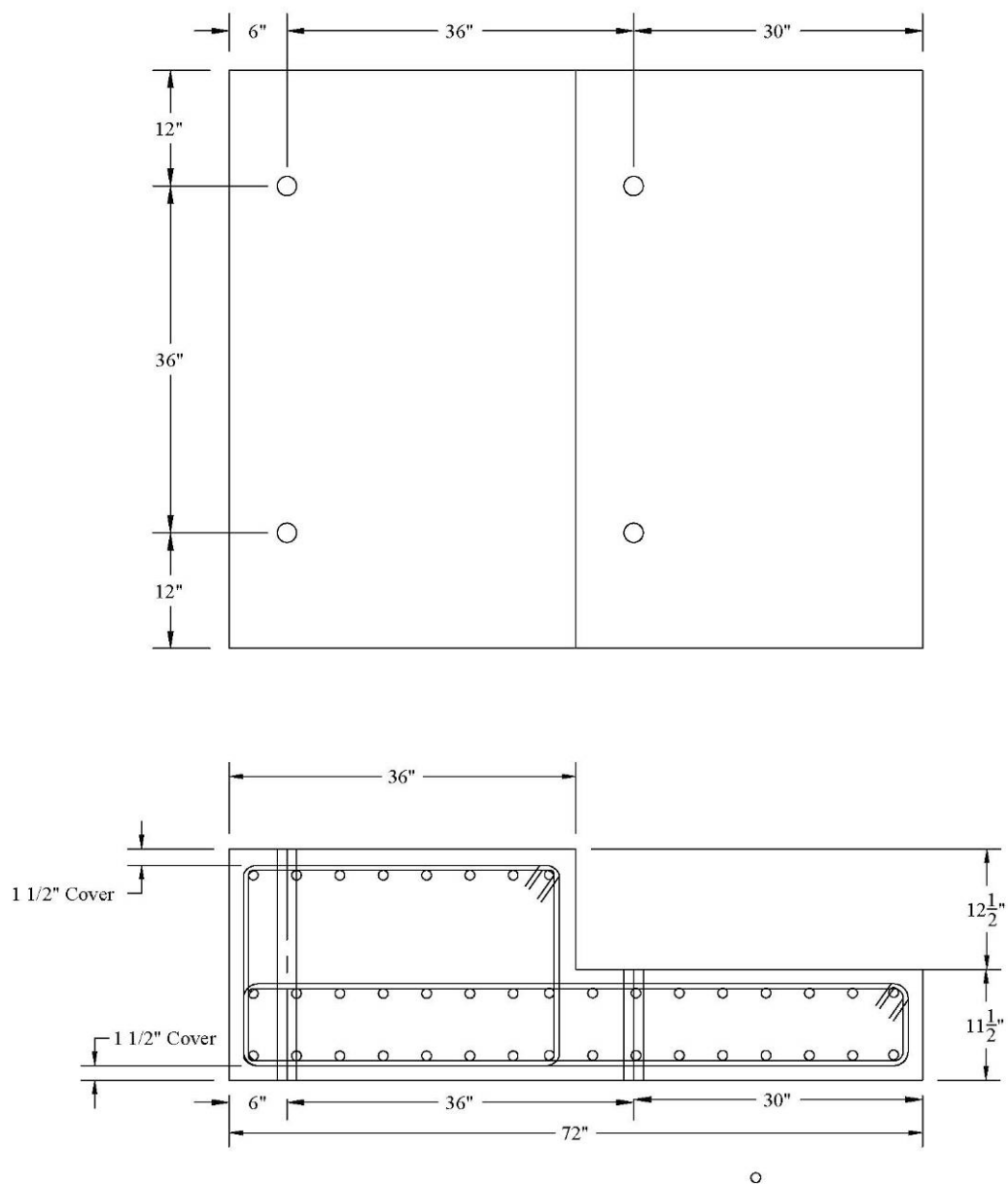
BIBLIOGRAPHY

ACI Committee 318, *Building Code Requirements for Structural Concrete and Commentary (ACI-308-05)*, American Concrete Institute, Detroit, 430 pp, 2008.

ACI Committee 445, *A State of the Art Report on Torsion in Structural Concrete,* American Concrete Institute (in press).

Ahmad, S.H., and Shah, S.P., "Complete Triaxial Stress-Strain Curves for Concrete," *ASCE Journal of the Structural Division,* V. 108, No. ST4, pp. 728-742, 1982.

Alkhrdaji, T. and Belarbi, A., "Shear Flow Zone in Rectangular RC Members subjected to Pure Torsion," *First International Conference on Concrete and Development, Proceedings*, Tehran, Iran, pp. 113-123, 2001.

American Association of State Highway and Transportation Officials, "AASHTO LRFD Bridge Design Specifications and Commentary," SI Units, 2nd Edition, Washington D.C., 1091 pp., 1998.

Ang, B.G., Priestley, M.J.N., and Paulay, T., "Seismic Shear Strength of Circular Reinforced Concrete Columns," *ACI Structural Journal,* V. 86, No. 1, pp. 45-59, 1989.
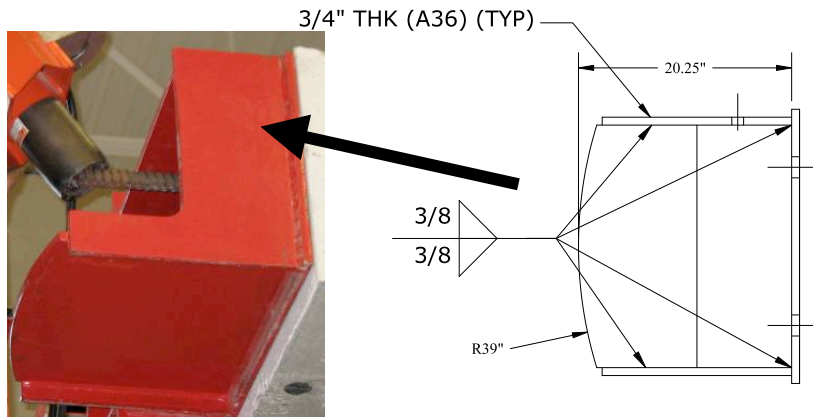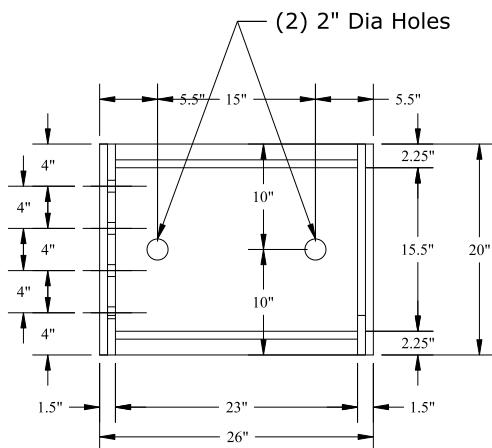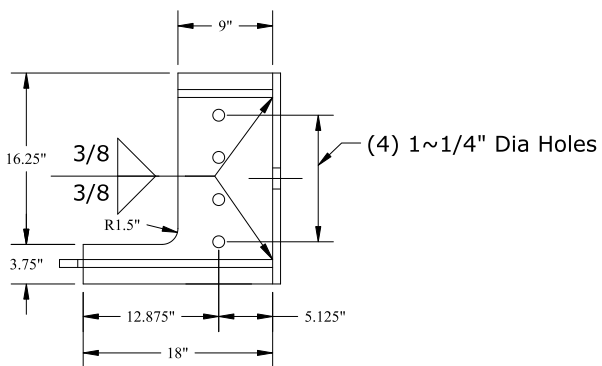
ASCE-ACI Committee 426, "The Shear Strength of Reinforced Concrete Members," *ASCE Journal of the Structural Division,* 99(6), pp. 1091–1187, 1973.

ASTM A 370, *Standard Test Methods and Definitions for Mechanical Testing of Steel Products (ASTM A 370-05)*, ASTM International, West Conshohocken, Pennsylvania, 2005.

ASTM C 31, *Standard Practice for Making and Curing Concrete Test Specimens in the Field (ASTM C 31-03)*, ASTM International, West Conshohocken, Pennsylvania, 2003.

ASTM C 39, *Standard Test Method for Compressive Strength of Cylindrical Concrete Specimens (ASTM C 39-05)*, ASTM International, West Conshohocken, Pennsylvania, 2005.

ASTM C 617, *Standard Practice for Capping Cylindrical Concrete Specimens (ASTM C 617-98)*, ASTM International, West Conshohocken, Pennsylvania, 1998.

Atalay, M.B., Penzien, J., "The Seismic Behavior of Critical Regions of Reinforced Concrete Components Influenced by Moment, Shear and Axial Force," *Report No. EERC 75-19,* Berkley, California: Earthquake Engineering Research Center, University of California, 1975.

ATC 32, "Improved Seismic Design Criteria for California Bridges: Provisional Recommendations," Applied Technology Council, *Report ATC 32*, 1996.

Badawy, H.E.I., "Plastic Analysis of Reinforced Concrete Curved Beams," PhD Thesis, University of Calgary, 238 pp., 1975.

Baker, A.L.L. "Ultimate Load Theory Applied to the Design of Reinforced and Prestressed Concrete Frames," *London: Concrete Publications Ltd*, 1956.

Baker, A.L.L. and Amarakone, A.M.N., "Inelastic Hyper-elastic Frames Analysis," Proceedings of the International Symposium on the Flexural Mechanics of Reinforced Concrete, Miami, Florida, ASCE-ACI, 1973.

Banon, H., Biggs, J.M. and Irvine, H.M., "Seismic Damage in Reinforced Concrete Members," *Journal of Structural Engineering,* ASCE, 107(9), 1713-1729, 1981.

Belarbi, A., "Stress-Strain Relationships of Reinforced Concrete in Biaxial Tension-Compression," *Ph.D. Dissertation*, Department of Civil and Environmental Engineering, University of Houston, 471 pp., 1991.

Belarbi, A., and Hsu, T. T. C., "Constitutive Laws of Concrete in Tension and Reinforcing Bars Stiffened by Concrete," *ACI Structural Journal*, V. 91, No. 4, pp. 465-474, 1994.

Belarbi, A., Prakash, S.S. and Silva, P., "Flexure-Shear-Torsion Interaction of RC Bridge Columns," *Proc. of the Concrete Bridge Conference*, St. Louis, USA, Paper No. 6, 2008.

Belarbi, A., Prakash, S.S. and You, Y.M., "Effect of Transverse Spiral Reinforcement on the Seismic Flexural-Shear-Torsional Behavior of Reinforced Concrete Circular Bridge Columns," *Journal of Structural Engineering and Mechanics,* V. 33, No. 2, 2009.

Belarbi, A., Prakash, S.S. and Silva, P.F. "Incorporation of Decoupled Damage Index Models in the Performance-Based Evaluation of RC Circular and Square Bridge Columns under Combined Loadings," *Special Publication-SP231*, ACI Publications, (Accepted, will be printed in 2010).

Bentz, E.C., "Sectional Analysis of Reinforced Concrete Members," *Ph.D. Thesis,* Department of Civil Engineering, University of Toronto, 2000.

Bhide, S. B. and Collins, M. P., "Influence of Axial Tension on the Shear Capacity of Reinforced Concrete Members," *ACI Structural Journal*, V. 86, No. 5, pp. 570-581, 1989.

Bishara, A., and Peir, J.C., "Reinforced Concrete Rectangular Columns in Torsion," *Journal of Structural Division.* Vol. 94, No. ST 12, pp. 1409-1421, 1973.

Bredt, R., "Kritische Bemerkungen zur Drehungselastizitat," *Zeitschrift des Vereines Deutscher Ingenieure*, Band 40, No. 28, pp. 785-790, No. 29, pp. 813-817, 1896.

Browning, B., Marvel, L. and Hindi, R., "Torsional Ductility of Circular Concrete Bridge Columns," *ASCE Structures Congress 2007,* May 16-19, Long Beach, California, 2007.

Calderone, A.J., Lehman, D.E., and Moehle, J.P., "Behavior of Reinforced Concrete Bridge Columns Having Varying Aspect Ratios and Varying Lengths of Confinement," Pacific Earthquake Engineering Research Center Report 2000/08, 2000.

Caltrans, "Caltrans Bridge Design Specifications," California Department of Transportation, Sacramento, California, 2004.

Chopra, A. K., *Dynamics of Structures*, Prentice Hall, New Jersey, 844 pp., 2001.

Chung, Y.S., and Meyer, C., "Modelling of Concrete Damage," *ACI Structural Journal*, 86 (3), 259-271, 1989.

Collins, M. P., "Torque-Twist Characteristics of Reinforced Concrete Beams," *Inelastic and Non-Linearity in Structural Concrete*, University of Waterloo Press, pp. 211-232, 1972.

Collins, M.P., Bentz, E.C., and Kim, Y.J., "Shear Strength of Circular Reinforced Concrete Columns," SP 197-3, Uzumeri Symposium: Behavior and Design of Concrete Structures for Seismic Performance, Toronto, ACI, Farmington Hills, Michigan, ISBN 0-87031-072-0, pp. 45–86, 2000.

Collins, M.P., Walsh, P.F., Archer, F.E., and Hall, A.S., "Ultimate Strength of Reinforced Concrete Beams Subjected to Combined Torsion and Bending," *Torsion of Structural Concrete, SP18,* American Concrete Institute, Detroit, pp. 279-402, 1968.

Collins, M.P. and Chockalingam, S., "Reinforced Concrete Beams under Reversed Cyclic Torsional Loading," *CEB Symposium, Structural Concrete under Seismic Actions*, Rome, Italy, pp. 181-187, 1979.

Collins, M.P. and Mitchell, D., *Prestressed Concrete Structures*, Response Publications, Canada, 766 pp., 1991.

Corley, W.G., "Rotational capacity of Reinforced Concrete Beams," *Bulletin D108,* Skokie, III: Portland Cement Association, Research and Development Laboratories, 1966.

Cowan, H.J., "The Strength of Plain, Reinforced and Prestressed Concrete Under the Action of Combined Stresses, with Particular Reference to the Combined Bending and Torsion of Rectangular Sections," *Magazine of Concrete Research,* No. 14, pp. 75-86, 1953.

Davey, B.E., "Reinforced Concrete Bridge Piers Under Seismic Loading," Master of Engineering Report, Civil Engineering Department, University of Canterbury, Christchurch, New Zealand, February 1975, 107 pages, December pp. 75-86., 1953.

Elfgren, L., Karlsson, I., and Losberg, A., "Torsion-Bending-Shear Interaction for Concrete Beams," *Journal of Structural Engineering*, ASCE, V. 100, No. ST8, pp.1657-1676, 1974.

Elwood, K.J. and Moehle, J.P., "Drift Capacity of Reinforced Concrete Columns with Light Transverse Reinforcement," *Earthquake Spectra,* 21(1),pp. 71-89, 2005.

Ewida, A.A. and McMullen, A.E. "Concrete Members under Combined Torsion and Shear," *Journal of the Structural Division*, Vol. 108, No. 4, pp. 911-928, 1982.

Floren, A. and Mohammadi, J., "Performance Based Design Approach in Seismic Analysis of bridges," *Journal of Bridge Engineering,* ASCE, 6(1), 37-45, 2001.

Galal, E.K., and Ghobarah, A., "Flexural and Shear Hysteretic Behavior of Reinforced Concrete Columns with Variable Axial Load," *Engineering Structures,* Elsevier, Vol. 25, 1353-1367, 2003.

Gesund, H., and Boston, L.A., "Ultimate Strength in Combined Bending and Torsion of Concrete Beams Containing Only Longitudinal Reinforcement," *Journal of Structural Division,* 61 (11), pp. 1453-1472, 1964.

Ghobarah, A., "Performance Based Design in Earthquake Engineering: State of Development," *Engineering Structures Journal,* Elsevier, 23, pp. 878-884, 2001.

Ghoneim, M.G. and MacGregor, J.G., "Design for Torsion," *ACI Structural Journal,* Vol. 92, No s20, pp. 211-218, 1995.

Greene, G. G., 2006, "Behavior of Reinforced Concrete Girders under Cyclic Torsion and Torsion Combined with Shear: Experimental Investigation and Analytical Models," *Ph.D. thesis,* Department of Civil, Architectural, and Environmental Engineering, University of Missouri at Rolla, Rolla, 227 pp.

Greene, G.G., and Belarbi, A., "Model for RC Members under Torsion, Bending, and Shear: Part 1: Theory," *Journal of Engineering Mechanics*, V. 135, No. 9, American Society of Civil Engineers (in Press), 2009a.

Greene, G.G., and Belarbi, A., "Model for RC Members under Torsion, Bending, and Shear: Part 2: Model Application and Validation," *Journal of Engineering Mechanics*, V. 135, No. 9, American Society of Civil Engineers (in Press), 2009b.

Hachem, M.M., Mahin, S.A. and Moehle, J.P., "Performance of Circular Reinforced Concrete Bridge Columns under Bidirectional Earthquake Loading," Pacific Earthquake Engineering Research Center, *Report No. PEER 2003/06*, University of California, Berkeley, 2003.

Hindi, R., Al-Qattawi, M. and Elsharief, A., "Influence of Different Confinement Patterns on the Axial Behavior of R/C Columns," *Structures Congress*, ASCE, New York, USA, 2005.

Hindi, R.A. and Sexsmith, R.G., "A Proposed Damage Model for RC Bridge Columns under Cyclic Loading," *Earthquake Spectra,* 17(2), pp. 261-290, 2001.

Hognestad, E., "A Study of Combined Bending and Axial Load in Reinforced Concrete Members," *Bulletin Series No. 399*, Engineering Experiment Station, University of Illinois, Urbana, U.S.A, 1951.

Hose, Y.D., Silva, P.F. and Seible, F., "Performance Evaluation of Concrete Bridge Components and Systems under Simulated Seismic Loads," *EERI Earthquake Spectra,* 16(2), pp. 413-442, 2000.

Hsu, H.L and Wang, C.L, "Flexural Torsional Behavior of Steel Reinforced Concrete Members Subjected to Repeated Loading," *Earthquake Engineering and Structural Dynamics Journal,* 29, pp. 667-682, 2000.

Hsu, H.L and Liang, L.L, "Performance of Hollow Composite Members Subjected to Cyclic Eccentric Loading," *Earthquake Engineering and Structural Dynamics Journal*, 32, pp. 433-461, 2003.

Hsu, T. T. C., "Torsion of Structural Concrete – Plain Concrete Rectangular Sections," *Torsion of Structural Concrete, (SP-18)*, American Concrete Institute, Detroit, pp. 203-238, 1968.

Hsu, T. T. C., *Torsion of Reinforced Concrete*, Van Nostrand Reinhold, New York, 516 pp., 1984.

Hsu, T. T. C., *Unified Theory of Reinforced Concrete*, CRC Press, Florida, 313 pp., 1993.

Hsu, T. T. C. and Mo. Y. L., "Softening of Concrete in Torsional Members – Theory and Tests," *ACI Structural Journal*, V. 82, No. 3, pp. 290-303, 1985a.

Hsu, T. T. C. and Mo. Y. L., "Softening of Concrete in Torsional Members – Design Recommendations," *ACI Structural Journal*, V. 82, No. 4, pp. 443-452, 1985b.

Hwang, T.H. and Scribner, C.F., "R/C Member Cyclic Response during Various Loadings," *Journal of Structural Engineering,* ASCE, 110(3), 477-489, 1984.

Iwasaki, T., Kawashima, K., Hagiwara, R., Hasegawa, k., Koyama, T. and Yoshida, T., "Experimental Investigation on Hysteretic Behavior of Reinforced Concrete Columns," *Proceedings of the Second Joint US-Japan Workshop on Performance and Strengthening of Bridge Structures and Research Needs,* San Fransisco, California, 1985.

Jeong, S.H. and Elnashai, A.S, "New Three Dimensional Damage Index for RC Buildings with Planar Irregularities," *Journal of Structural Engineering,* ASCE, 132(9), 1482-1490, 2006.

Kawano, H. and Watanabe, H., "Shear Strength of Reinforced Concrete Columns – Effect of Specimen Size and Load Reversal," *Proceedings, 2nd Italy-Japan Workshop on Seismic Design and Retrofit of Bridges*, 1997.

Kawashima, K., Unjoh, S., and Mukai, H., "Seismic Response of Reinforced Concrete Bridge Piers Subjected to Eccentric Loading," *Proceedings, Fifth U.S. National Conference on Earthquake Engineering*, Chicago, pp. 419-428, 1994.

Kent, D. C., "Inelastic Behavior of Reinforced Concrete Members with Cyclic Loading," *Ph.D. Dissertation*, University of Canterbury, Christchurch, New Zealand, 1969.

Khashaee, P., "Damage-based Seismic Design of Structures," *Earthquake Spectra,* 21(2), 459-468, 2005.

Klus, J., "Ultimate Strength of Reinforced Concrete Beams in Combined Torsion and Shear," *ACI Journal,* Proceedings, V. 65, No. 3, pp. 210-216, 1968.

Koutchoukali, N. E. and Belarbi, A., "Torsion of High-Strength Reinforced Concrete Beams and Minimum Reinforcement Requirement," *ACI Structural Journal*, V. 98, No. 4, pp. 462-469, 2001.

Kowalsky, M.J. and Priestley, M.J.N., "Improved Analytical Model for Shear Strength of Circular Reinforced Concrete Columns in Seismic Regions," *ACI Structural Journal,* Vol. 97, No S42, pp. 388-396, 2000.

Kunnath, S.K., "Cumulative Seismic Damage of Reinforced Concrete Bridge Piers," *NCEER 97-0006 Technical Report,* National Center for Earthquake Engineering Research, Buffalo, N.Y., 1997.

Lampert, P. and Thürlimann, B., "Torsion-Bending Tests of Reinforced Concrete Beams," *Report No. 6506-3*, Intitut für Baustatik, ETH, Zurich, 116 pp., 1969.

Lehman, D.E., Calderone, A.J. and Moehle, J.P., "Behavior and Design of Slender Columns subjected to Lateral Loading," *Proc. of the Sixth U.S. National Conference on Earthquake Engineering,* EERI, Oakland, California, May 31-June 4, Paper No. 87, 1998.

Lessig, N. N., "Determination of Load-Carrying Capacity of Rectangular Reinforced Concrete Elements Subjected to Flexure and Torsion," *Study No. 5*, Institut Betona i Zhelezobetona, Moscow, pp. 5-28, 1959.

Mander, J.B. and Cheng, C.-T., "Seismic Design of Bridge Piers," *Research Report 84-2,* University of Canterbury, Christchurch, New Zealand, 1984.

Mander J.B., Priestley, M.J.N., and Park, R., "Observed Stress-Strain Behavior for Confined Concrete," *Journal of Structural Engineering,* ASCE, 114(8), pp. 1827-1849, 1988.

Mansour, M., Lee, J. Y., and Hsu, T. T. C., "Cyclic Stress-Strain Curves of Concrete and Steel Bars in Membrane Elements," *Journal of Structural Engineering*, ASCE, V. 127, No. 12, pp. 1402-1411, 2001.

Mattock, A.H., Kris, L.B., and Hognestad, E., "Rectangular Concrete Stress Distribution in Ultimate Strength Design," ACI *Journal,* Proceedings, 57(8), pp. 875–928, 1961.

McDaniel, C., "Scale Effects on the Shear Strength of Circular Reinforced Concrete Columns," *M.S Thesis,* University of California, San Diego, 1997.

McMullen, A. E., and El-Degwy, W. M., "Prestressed Concrete Tests Compared with Torsion Theories," *PCI Journal*, V. 30, No. 5, pp. 96-127, 1985.

McMullen, A.E., and Warwaruk, J. M., "Concrete Beams in Bending, Torsion and Shear," *Journal of Structural Engineering*, ASCE, V. 96, No. ST5, pp. 885-903, 1970.

Mitchell, D., "The Behavior of Structural Concrete Beams in Pure Torsion," *Ph.D. Thesis*, Department of Civil Engineering, University of Toronto, Canada, 1974.

Mitchell, D. and Collins, M. P., "Diagonal Compression Field Theory – A Rational Model for Structural Concrete in Pure Torsion," *ACI Structural Journal*, V. 71, pp. 396-408, 1974.

Mo, Y. L. and Yang, R. Y., "Dynamic Response of Box Tubes to Combined Shear and Torsion," *Journal of Structural Engineering*, ASCE, V. 122, No. 1, pp. 47-54, 1996.

Mo, Y.L. and Hsu, T.T.C., "Softening of Concrete in Torsional Members- Design Recommendations*", ACI Structural Journal*, 82(37), 443-452, 1985.

Mörsch, E., 1902, Der *Eisenbetonbau, seine Anwendung und Theorie*, 1st Edition, Wayss and Freytag, A. G., Im Selbstverlag der Firma, Neustadt, a. d. Haardt, 118pp; 2nd Edition, Verlag Von Konrad Wittwer, Stuttgart, 1906, 252pp; 3rd Edition (English Translation by E. P. Goodrich), McGraw-Hill Book Company, New York, 368 pp., 1909.

Mostafaei, H. and Kabeyasawa, T., "Axial-Shear-Flexure Interaction Approach for Reinforced Concrete Columns", *ACI Structural Journal*, 104(2), pp. 218-226, 2007.

Nylander, H., "Torsion and Torsional Restraint by Concrete Structures," *Bulletin D-19*, Statens Kommittee för Byggnadsforskning, Stockholm, 1945.

Onsongo, W. M., "The Diagonal Compression Field Theory for Reinforced Concrete Beams Subjected to Combined Torsion, Flexure and Axial Loads," *Ph.D. Dissertation*, Department of Civil Engineering, University of Toronto, Canada, 246 pp., 1978.

Otsuka, H., Takeshita, E., Yabuki, W., Wang, Y., Yoshimura, T. and Tsunomoto, M., "Study on the Seismic Performance of Reinforced Concrete Columns Subjected to Torsional Moment, Bending Moment and Axial Force," *Proc. of the 13th World Conf. on Earthquake Engineering*, Vancouver, Canada, Paper No. 393, 2004.

Ozcebe, G. and Saatcioglu, M., "Hysteretic Shear Model for Reinforced Concrete Members," *Journal of Structural Engineering, ASCE,* 115(1), pp. 132-148, 1989.

Pandit, G.S. and Mawal, M.B., "Tests of Concrete Columns in Torsion," *Journal of Structural Division,* Vol. 99, No. ST 7, July 1973, pp. 1409-1421, 1973.

Pang, X. B. and Hsu, T.T.C., "Constitutive Laws of Reinforced Concrete in Shear," *Research Report UHCEE 92-1*, Department of Civil and Environmental Engineering, University of Houston, Houston, Texas, 1992.

Park, Y.J. and Ang, A.H.S., "Mechanistic Seismic Damage Model for Reinforced Concrete," *Journal of Structural Engineering,* ASCE, 111(4), pp. 722-739, 1985.

Park, R., and Paulay, T., Reinforced *Concrete Structures*, John Wiley and Sons, New York, 1975.

Paulay, T., and Priestley, M.J.N., Seismic *Design of Reinforced Concrete and Masonry Buildings*, John Wiley and Sons, New York, 1992.

Pontangaroa, R.T., Priestley, M.J.N., and Park, R., "Ductility of Spirally Reinforced Concrete Columns Under Seismic Loading," Report 79-8, Department of Civil Engineering, University of Canterbury, Christchurch, New Zealand, 116 pp., 1979.

Prakash, S.S., and Belarbi, A. "Towards Damage-Based Design Approach for RC Bridge Columns under Combined Loadings using Damage Index Models," *Journal of Earthquake Engineering*, *Taylor & Francis Group Journals* (Accepted, will be published in 2010)

Prakash, S.S., Belarbi, A., and You, Y.M. "Seismic Performance of Circular RC Columns Subjected to Axial, Bending, and Torsion with Low and Moderate Shear," *Journal of Engineering Structures,* Elsevier (Available online from August 2009).

Prakash, S.S., and Belarbi, A. "Bending-Shear-Torsion Interaction Features of RC Circular Bridge Columns-An Experimental Study," *Special Publication-SP265*, Paper No. SP-20, ACI Publications, Symposium in honor of Prof. Tom Hsu, 2009.

Priestly, M.J.N. and Benzoni, G., "Seismic Performance of Circular Columns with Low Longitudinal Reinforcement Ratios," *ACI Structural Journal*, 93(4), pp. 474-485, 1996.

Priestley, M.J.N., Seible, F., and Calvi, G.M., *Seismic Design and Retrofit of Bridges*, John Wiley and Sons, Inc., New York, 686 pp., 1996.

Priestley, M.J.N., Verma, R., and Xiao, Y., "Seismic Shear Strength of Reinforced Concrete Columns," *Journal of Structural Engineering,* ASCE, 120(8), pp. 2310-2329, 1994.

Pritchard, R.G., "Torsion Shear Interaction of Reinforced Concrete Beams," *M.Sc. Thesis*, University of Calgary, Calgary, 1970.

Rabbat, B., "Variable Angle Space Truss Model for Structural Concrete Beams," *Ph.D. Thesis*, Department of Civil Engineering, University of Toronto, 1975.

Rahal, K.N., "The Behavior of Reinforced Concrete Beams Subjected to Combined Shear and Torsion," *Ph.D. Thesis*, Department of Civil Engineering, University of Toronto, 1993.

Rahal, K.N. and Collins, M.P., "Effect of the Thickness of Concrete Cover on the Shear-Torsion Interaction – an Experimental Investigation," *ACI Structural Journal*, V. 92, No. 3, pp. 334-342, 1995a.

Rahal, K.N. and Collins, M.P., "Analysis of Sections Subjected to Combined Shear and Torsion – A Theoretical Model," *ACI Structural Journal*, V. 92, No. 4, pp. 459-469, 1995b.

Rahal, K.N. and Collins, M.P., "Combined Torsion and Bending in Reinforced and Prestressed Concrete Beams," *ACI Structural Journal*, V. 100, No. 2, pp. 157-165, 2003.

Rahal, K.N., "Evaluation of AASHTO-LRFD General Procedure for Torsion and Combined Loading," *ACI Structural Journal,* Vol. 103, No s70, September-October, pp. 683-692, 2006.

Rausch, E., "Design of Reinforced Concrete in Torsion," *Ph.D. Thesis*, Technische Hochschule, Berlin, 53 pp., 1929.

Razvi, S.R., and Saatcioglu, M., "Strength and Deformability of Confined High-Strength Concrete Columns," American Concrete Institute, Structural Journal, Vol. 91, No. 6, pp. 678-687, 1994.

Ritter, W., "Die Bauweise Hennebique," *Schweizerische Bauzeitung*, V. 33, No. 7, Zurich, pp. 59-61, 1899. (Reproduced from SOA ACI 445)

Roufaiel, M.S.L., and Meyer, C., "Analytical Modeling of Hysteretic Behavior of R/C Frames," *Journal of Structural Engineering,* ASCE, Vol.113, No. 3, pp. 429-444, 1987.

Rusch, H., "Research Toward a General Flexural Theory for Structural Concrete," *ACI Journal Proceedings,* Vol. 57, No. 1, pp-1-28; Discussion, Vol. 57, No. 9, March 1961, pp. 1147-1164, 1960.

Saadeghvaziri, M.A., and Fouch, D.A., "Behavior of RC Columns under Non-proportionally Varying Axial load," *Journal of Structural Engineering,* ASCE, V.116, No 7, July 1990, pp. 1835-1856, 1990.

Saint-Venant, B., "Mémoire Sur la Torsion des Prismes," *Mémoires des Savants Étrangers*, Mémoires Présentés par Divers Savants à l'Académie des Sciences, de l'Institut Imperial de France et Imprimé par son Ordre, Paris, Vol. 14, pp. 223-560, 1856.

Sengupta, A. K. and Belarbi, A., "Modeling Effect of Biaxial Stresses on Average Stress-Strain Relationship of Reinforcing Bar in Reinforced Concrete Panels," *ACI Structural Journal*, V. 98, No. 5, pp. 629-637, 2001.

Siess, C. P. and Abbasi, A. F., "Test of Reinforced Concrete Beams with Cadweld Reinforcing Bar Splices," *Report for ERICO Products, Inc.*, University of Illinois, Urbana, 93 pp., 1967.

Sheikh, S.A., and Uzumeri, S.M., "Analytical Model for Concrete Confinement in Tied Columns," *Journal of Structural Division,* ASCE 108 (ST12), 1982.

Sheikh, S.A., and Khoury, S.S., "Confined Concrete Columns with Stubs," *Structural Journal*, V. 90, No. 4, pp. 414–431, 1994.

Stone, W.C. and Cheok, G.S., "Inelastic Behavior of Full Scale Bridge Columns Subjected to Cyclic Loading," *NIST Building Science Report No. 166,* U.S Department of Commerce, National Institute of Standards and Technology, Gaithersburg, MD, 252 pp., 1989.

Taylor, A.W. and Stone, W.C., "Performance Based Seismic Design of Reinforced Concrete Bridge Columns," *Proc. of the 5th US National Conference on Earthquake Engineering, Vol. 1*, Earthquake Engineering Research Institute, Oakland (CA), pp. 459-468, 1994.

Tirasit, P., and Kawashima, K., "Seismic Torsion Response of Skewed Bridge Piers," *JSCE Journal of Earthquake Engineering*, Tokyo Institute of Technology, Tokyo, Japan, pp. 357-364, 2005.

Tirasit, P, and Kawashima, K., "Seismic Performance of Square Reinforced Concrete columns under Combined Cyclic Flexural and Torsional Loadings," *Journal of Earthquake Engineering,* 11, pp. 425-452, 2007.

Tirasit, P, and Kawashima, K., "Effect of Nonlinear Torsion on the Performance of Skewed Bridge Piers," *Journal of Earthquake Engineering*, 12, pp. 980-998, 2008.

Vecchio, F. and Collins, M. P., "Response of Reinforced Concrete to In-Plane Shear and Normal Stresses," *Report No.82-03*, University of Toronto, Toronto, Canada, 1982.

Vecchio, F. J. and Chan, C. C. L., "Reinforced Concrete Membrane Elements with Perforations," *Journal of Structural Engineering*, ASCE, V. 116, No. 9, pp. 2344-2360, 1990.

Vecchio, F. J. and Collins, M. P., "The Modified Compression-Field Theory for Reinforced Concrete Elements Subjected to Shear," *ACI Journal*, V. 83, No. 2, pp. 219-231, 1986.

Vecchio, F.J., "Nonlinear Finite Element Analysis of Reinforced Concrete Membranes," *ACI Structural Journal,* Vol. 86, No. 1, pp. 25-35, 1989.

Vecchio, F. J. and Collins, M. P., "Compression Response of Cracked Reinforced Concrete," *Journal of Structural Engineering*, ASCE, V. 119, No. 12, pp. 3590-3610, 1993.

Vecchio, F.J., and Emara, M.B., "Shear Deformations in Reinforced Concrete Frames," *ACI Structural Journal,* Vol. 89, No. 1, pp. 46–56., 1992.

Vu, N.D., Priestley, M.J.N., Seible, F., Benzoni, G., "Seismic Response of Well Confined Circular Reinforced Concrete Columns with Low Aspect Ratios," *5th Caltrans Seismic Research Workshop,* 1998.

Wang, G.G., and Hsu, C.T., "Complete Biaxial Load-Deformation Behavior of RC Columns," J. Struct. Engrg., ASCE, 118(9), 2590-2609, 1992.

Williams, M.S. and Sexsmith, R.G., "Seismic Damage Indices for Concrete Structures: a State of the Art Review," *Earthquake Spectra*, 11(2), pp. 319-349, 1995.

Williams, M.S., Villemure, I., and Sexsmith, R.G., "Evaluation of Seismic Damage Indices for Concrete Elements Loaded in Combined Shear and Flexure," *ACI Structural Journal*, 6 (1), pp. 37-45, 1997.

Whitney, C.S., "Design of Reinforced Concrete Members under Flexure or Combined Flexure and Direct Compression," *ACI Journal,* March-April, 1937, Proc. V. 33, pp. 483-498, 1937.

Wong, Y.L., Paulay, T., and Priestley, M.J.N, "Squat Circular Bridge Piers under Multidirectional Seismic Attack," Department of Civil Engineering, University of Canterbury, *Report 90-4,* 264 pp., 1990.

Wong, Y.L, Paulay, T., and Priestley, M.J.N, "Response of Circular Columns to Multi-Directional Seismic Attack," *ACI Structural Journal*, V. 90, No. 2, pp. 180-191, 1993.

You, Y. and Belarbi, A., "An Analytical Model to Predict the Behavior of Circular Reinforced Concrete Columns Subjected to Combined Loadings including Torsion," *Proc. of the 14th World Conference on Earthquake Engineering,* Beijing, China. Paper No. 05-01-0299, 2008.

Yudin, V. K., "Determination of the Load-Carrying Capacity of Rectangular Reinforced Concrete Elements Subjected to Combined Torsion and Bending," *Beton i Zhelezobeton*, Moscow, No. 6, pp. 265-269, 1962.

Zahrah, T.F. and Hall, W.J., "Earthquake Energy Absorption in SDOF Structures," *Journal of Structural Engineering,* ASCE, 110(8), pp.1757-1772, 1984.

Zahn, F.A.; Park, R.; and Priestley, M.J.N., "Design of Reinforced Concrete Bridge Columns for Strength and Ductility," *Report 86-7,* Department of Civil Engineering, University of Canterbury, Christchurch, New Zealand, March 380 pp., 1986.

Zhang, J. and Xu, S.Y., "Seismic Response of Simulations of Bridges Considering Shear-Flexural Interaction of Columns. *Proceedings of the 4th International Conference on Advances in Structural Engineering and Mechanics*, May 26-28, Jeju, Korea, pp. 1167-1179, 2008.

VITA

Suriya Prakash was born in Madurai, India, on December 6, 1980. He obtained his undergraduate degree in Civil Engineering with distinction in May 2002 from Thiagrajar College of Engineering affiliated to Madurai Kamaraj University, India. He was a recipient of best outgoing student award for his overall academic performance and extracurricular activities during his bachelor of engineering. After receiving his bachelor degree in civil engineering, he began his graduate studies at the Indian Institute of Technology Madras in August 2002. His research was on understanding the effectiveness of FRP composite retrofitting on behavior of masonry structures. During the graduate studies, he also had a unique opportunity to work at TU-Karlsruhe, Germany through Deutscher Akademischer Austausch Dienst (DAAD) Scholarship sponsored by federal republic of Germany. His research work during his masters involved finite element modeling and experimental studies on masonry walls. He received his Master of Science degree in Civil Engineering with an emphasis in Structures in June 2005.

Then, in August 2005 he came to Missouri S&T to pursue his Ph.D. in Civil Engineering. He worked on a NSF-Network for Earthquake Engineering Simulation (NEES) sponsored project on the behavior of RC bridge columns under combined loadings including torsion for his PhD thesis. He has published several conference and journal papers in domestic and international journals. As a doctoral candidate, he earned the following awards: University Transportation Center Fellowship in 2006, Best Research Poster Award in 2007 from the Council of Graduate Students, Missouri American Concrete Institute Graduate Scholarship in 2008, and Best Research Poster Award in 2009 from the Intelligent Systems Center at Missouri S&T.

Suriya Prakash is a student member in the American Society of Civil Engineers (ASCE) and the American Concrete Institute (ACI). He is also a national member of the Earthquake Engineering Research Institute (EERI) and the Network for Earthquake Engineering Simulation (NEES). He earned his Ph.D. in Civil Engineering from the Missouri University of Science and Technology in December 2009.